UNIVERSIDADE DE LISBOA
FACULDADE DE CIÊNCIAS
DEPARTAMENTO DE QUÍMICA E BIOQUÍMICA

Synthesis of new antibiotic glycosides and computational studies on their interaction with model lipid bilayers

Mestrado em Química
Especialização em Química

Rafael de Santana Nunes

Dissertação orientada por:
Professora Doutora Amélia Pilar Rauter
Doutor Miguel Machuqueiro

2015

Abstract

The search for new antibiotics with innovative mechanisms of action represents a foremost challenge to the scientific community owing to the increasing spread of bacterial resistance to the available therapeutics. In this context, our research group is particularly interested in exploiting the potential usefulness of sugar-based surfactants as antibacterial agents. These molecules are known for their biocompatibility properties and feature low ecotoxicity, making them suitable for several industrial and medicinal applications. In previous work, we reported a series of alkyl 2-deoxy-/2,6-dideoxy-*arabino*-hexopyranosides [**1**–**3**], some of which exhibited potent and selective antibacterial activities against *Bacillus cereus*, *Bacillus subtilis* and, particularly, *Bacillus anthracis*, which is considered a bioterrorism agent. However, the most potent compound, dodecyl 2,6-dideoxy-α-L-*arabino*-hexopyranoside, was also shown to induce acute toxicity towards human lymphocytes. Hence, we were motivated to further optimize this structure with the intent to achieve a potentially non-toxic drug candidate, and to better understand the structural determinants governing bioactive profile. The available data on the surface activity of these compounds and preliminary biological studies suggest a mechanism of action involving aggregation of glycosides into micelles and their interaction with bacterial cell membranes in a detergent-like manner. However, the molecular interactions driving this phenomena are yet to be unraveled. In this research work, we present an interdisciplinary approach to this ongoing investigation, based on (i) the design, synthesis and antibacterial evaluation of deoxy glycoside analogues, and (ii) a computational study focused on their interactions with a model lipid bilayer.

The rationale for design of new dodedyl deoxy glycosides related to the lead compound was conceived aiming at exploring the biological impact of specific structural modifications, namely the replacement of one hydrogen atom at 2-position of the sugar moiety by a hydroxy group (i.e. 6-deoxy glycoside) or by a fluorine atom (i.e. 2,6-dideoxy-2-fluoro glycoside) and, alternatively, the replacement of the methyl group at 6-position by a hydrogen atom (i.e. 2-deoxy pentopyranoside). Accordingly, their preparation was accomplished following distinct approaches. The synthesis of dodecyl α-L-rhamnopyranoside (dodecyl 6-deoxy-α-L-mannopyranoside) succeeded through stereoselective glycosylation of the peracetylated trichloroacetimidate precur-

sor (prepared from L-rhamnose in three steps) catalyzed by trimethylsilyl triflate, followed by deacetylation (85% yield over two steps). Target compounds deoxygenated and/or fluorinated at 2-position of the sugar, in turn, were prepared using glycals as starting materials. New dodecyl 2-deoxy-α- and β-L-*threo*-pentopyranosides were synthesized by reaction of peracetylated L-xylal (obtained from L-xylose in three steps) with dodecanol catalyzed by triphenylphosphane hydrobromide and subsequent deprotection. The glycosylation reaction gave the α- and β-anomers in 23% and 10% isolated yields, respectively, and considerable amounts of 2,3-unsaturated glycosides, arising from acid-catalyzed allylic rearrangement, were also isolated (27% yield). Interestingly, an unusual, solvent-dependent conformational behaviour was found to be assumed by the β-glycoside, as rationalized by combined NMR analysis and DFT calculations. Finally, dodecyl 2,6-dideoxy-2-fluoro glycosides were accessed by one-pot electrophilic fluorination/nucleophilic addition of dodecanol to protected 6-deoxy-L-glucal derivatives mediated by selectfluor, followed by deprotection. Reaction with the readily available acetylated glycal gave the α-L-*gluco*- and α-L-*manno*-glycosides in 37% yield (inseparable mixture), and the β-L-*gluco*-glycoside in 5% yield. When the silylated glycal (prepared from the corresponding acetylated glycal by one-pot deacetylation and silylation) was employed, improved *gluco*-stereoselectivity was achieved, affording the α-L-*gluco*- and β-L-*gluco*-glycosides in 27% yield (inseparable mixture), and the α-L-*manno*-glycoside in 7% yield. With regard to the antibacterial activity using the broth dilution method, the 6-deoxy glycoside and 2-deoxy pentopyranosides were moderately active towards *B. cereus* (MIC = 32 μg mL^{-1}). The 2,6-dideoxy-2-fluoro-α-L-glycosides were the most active compounds, presenting antibacterial activity competitive with that of the lead compound (MIC = 16 μg mL^{-1}), whereas the β-*gluco*-stereoisomer was not active in the range of concentrations tested. The non-fluorinated compounds were further tested against *B. anthracis*, using the agar dilution method, and have been proven to be potent inhibitors of this pathogen (MIC = 8-16 μg mL^{-1}), highlighting their potential in the context of biosecurity as well.

Molecular dynamics (MD) simulations have been widely employed to explore the structural and dynamic properties of a variety of amphiphilic systems, including surfactant micelles and lipid bilayers, as well as to probe relevant intermolecular phenomena such as drug-membrane interactions. Hence, we performed a MD study for this family of alkyl deoxy glycosides, including some of the newly synthesized compounds, looking for insights into their mechanism of action. Our results confirm that these glycosides form stable micelles in solution, in agreement with experimental data on their surface activity. The micelles were shown to interact strongly with a membrane model, and several partition and/or fusion events were observed, indicating a clear preference for the lipidic phase. The direct concentration-dependent effect of these glycosides in the lipid bilayer was also studied, which revealed an increase in the phospholipid hydrocarbon chain ordering, as well as in the membrane thickness. These biophysical alterations, corresponding to a possible decrease in membrane fluidity, may have a significant impact on the structural integrity of a biological membrane. This is particularly relevant since our preliminary results suggest that membrane pore formation/stabilization is not likely to be involved in the mechanism of action for these sugar-based surfactants.

In summary, this work shows that this family of deoxy glycosides comprises very potent membrane-active antibacterial compounds which do not seem to exert their action through commonly known mechanisms. Instead, we suggest a mechanism relying on membrane ordering and stiffening, upon partitioning of these compounds.

Keywords: antibiotics, surfactant glycosides, glycosylation, molecular dynamics, lipid bilayers.

Resumo

A descoberta de novos antibióticos que apresentem mecanismos de ação inovadores representa um dos principais desafios que a comunidade científica enfrenta, sobretudo devido à disseminação crescente de estirpes bacterianas resistentes às terapêuticas disponíveis. Neste contexto, o nosso grupo de investigação está particularmente interessado em explorar a potencial utilidade terapêutica de surfactantes derivados de açúcares enquanto agentes antibacterianos. Estas moléculas são conhecidas pela sua biocompatibilidade e por apresentarem baixa toxicidade ecológica, pelo que se consideram apropriadas para aplicações em medicina e na indústria. Em trabalhos anteriores, descrevemos uma série de 2-desoxi-/2,6-didesoxi-*arabino*-hexopiranósidos de alquilo **[1–3]**, alguns dos quais exibiram actividades antibacterianas potentes e seletivas quando testadas em estirpes de *Bacillus*, nomeadamente *B. cereus*, *B. subtilis* e, em particular, *B. anthracis*, sendo o último considerado um agente de bioterrorismo. No entanto, o composto mais potente, 2,6-didesoxy-*arabino*-hexopiranósido de dodecilo, revelou também induzir toxicidade aguda em linfócitos humanos. Assim, considerámos relevante proceder com a otimização desta estrutura, perspectivando, por um lado, vir a alcançar um candidato a fármaco potencialmente não tóxico e, por outro, aprofundar o nosso conhecimento no que diz respeito às características estruturais que determinam a sua bioactividade. Os dados por nós obtidos sobre a actividade superficial destes compostos, bem como estudos biológicos preliminares que realizámos, sugerem um mecanismo de ação que deverá envolver a associação de glicósidos em agregados micelares em solução e a interação destas estruturas com as membranas celulares bacterianas, de forma semelhante à acção de detergentes. No entanto, as interações moleculares que conduzem a estes fenómenos ainda não foram elucidadas. Neste trabalho, procurámos contribuir para esta investigação em curso por via de uma abordagem interdisciplinar, nomeadamente através do (i) *design*, síntese e subsequente avaliação da actividade antibacteriana de desoxiglicósidos análogos ao composto líder, e de um (ii) estudo computacional centrado na interação dos mesmos compostos com um modelo de bicamada lipídica.

O racional para a síntese de novos desoxiglicósidos de dodecilo relationados com o composto líder foi concebido com o intuito de explorar o eventual impacto biológico de modificações estruturais específicas, nomeadamente a substituição de um átomo de hidrogénio na posição 2 do açúcar

por um grupo hidroxilo (para a formação de um 6-desoxiglicósido) ou por um átomo de flúor (para a formação de 2,6-didesoxi-2-fluoroglicósidos) e, em alternativa, a substituição de grupo metilo na posição 6 por um átomo de hidrogénio (para a formação de 2-desoxipentopiranósidos). Por conseguinte, a sua preparação envolveu necessariamente estratégias distintas. A síntese de α-L-rhamnopiranósido de dodecilo (6-desoxi-α-L-mannopiranósido de dodecilo) foi conseguida através da glicosilação estereoseletiva do precursor tricloroacetimidato peracetilado (que foi obtido de forma simples e eficiente a partir da L-rhamnose, em três passos) catalizada pelo triflato de trimetilsililo, seguida de uma reação de desacetilação (rendimento de 85% para os dois passos). Os compostos-alvo desoxigenados e/ou fluorados na posição 2 do açúcar, por sua vez, foram preparados utilizando glicais como materiais de partida. Assim, novos 2-desoxi-α- e β-L-*threo*-pentopiranósidos de dodecilo foram também sintetizados, desta vez por via da reação do L-xilal peracetilado (obtido a partir da L-xilose em três passos por via de metodologias convencionais) com dodecanol catalisada por hidrobrometo de trifenilfosfónio e subsequente reação de desproteção. A reação de glicosilação originou os correspondentes anómeros α e β com rendimentos de 23% e 10%, respectivamente, e foram ainda isoladas quantidades consideráveis de glicósidos 2,3-insaturados (rendimento total de 27%), que se formam por rearranjo alílico e concomitante eliminação de ácido acético em meio ácido. Esta metodologia merece pois otimização futura com vista a promover a conversão selectiva dos intermediários saturados, por exemplo através da utilização de éteres benzílicos como grupos protetores uma vez que estes são em geral mais estáveis em meio ácido. Curiosamente, verificou-se que o anómero β assume um comportamento conformacional atípico, dependendo do solvente, que foi possível racionalizar combinando análise por NMR e cálculos quânticos (DFT). Finalmente, preparámos vários 2,6-didesoxi-2-fluoroglicósidos de dodecilo através da fluoração eletrófila e simultânea adição nucleófila de dodecanol a derivados protegidos do 6-desoxi-L-glucal, que ocorrem na presença de selectfluor, e subsequente reação de desproteção. Quando a reação foi conduzida usando o glical peracetilado, disponível comercialmente, obtiveram-se os glicósidos exibindo configuração α-L-*gluco* e α-L-*manno* com um rendimento de 37% (sob a forma de uma mistura inseparável de epímeros), e o glicósido exibindo configuração β-L-*gluco* com um rendimento de 5%. Por sua vez, a reação a partir do glical sililado (que foi previamente sintetizado partindo do glical acetilado correspondente por desacetilação e subsequente sililação, num único passo) promoveu a formação preferencial dos estereoisómeros exibindo configuração *gluco*, tendo sido isolados os α-L-*gluco*- e β-L-*gluco*-glicósidos com um rendimento de 27% (desta vez sob a forma de uma mistura inseparável de anómeros), e o α-L-*manno*-glicósido com um rendimento de 7%. No que diz respeito à actividade antibacteriana destes compostos, quando determinada pelo método de diluição em meio líquido, verificou-se que o 6-desoxiglicósido e os 2-desoxipentopiranósidos apresentam actividades moderadas quando testados contra *B. cereus* (CMI = 32 μg mL^{-1}). Por outro lado, os 2,6-didesoxi-2-fluoro-α-L-glicósidos revelaram ser os compostos mais activos, apresentando uma actividade antibacteriana competitiva com a exibida pelo composto líder (CMI = 16 μg mL^{-1}), enquanto que o estereoisómero β-*gluco* não foi de todo activo na gama de concentrações testada. Alguns dos compostos sintetizados, nomeadamente aqueles que não apresentam um átomo de flúor na sua estrutura, foram ainda testados no que se refere à in-

ibição de *B. anthracis*, neste caso utilizando o método de diluição em meio sólido. Verificou-se que todos estes compostos são inibidores potentes deste agente patogénico e, por consequência, consideramos particularmente relevante a sua potencial aplicação também no contexto da segurança biológica.

As simulações de dinâmica molecular têm sido bastante utilizadas enquanto método para explorar as propriedades estruturais e dinâmicas de uma variedade de sistemas amfifílicos, incluindo micelas de surfactantes e bicamadas lipídicas, assim como para investigar fenómenos intermoleculares importantes, tais como interações fármaco-membrana. Neste contexto, realizámos um estudo de dinâmica molecular com o objectivo de estudar esta família de desoxiglicósidos de alquilo, incluindo alguns dos sintetizados no âmbito desta dissertação, na perspectiva contribuir para a elucidação do seu mecanismo de ação. Os nossos resultados confirmam que estes glicósidos formam micelas estáveis em solução aquosa, em concordância com os dados experimentais que se conhecem relativamente à sua actividade superficial. Verificou-se ainda que essas micelas interagem fortemente com um modelo de membrana na sua vizinhança, tendo sido observados vários eventos de partição e/ou fusão micela-membrana, indicando uma preferência clara para a fase lipídica. Também foi estudado o efeito destas moléculas sobre uma bicamada lipídica, em função da sua concentração. Este estudo demonstrou que tanto a ordem das cadeias hidrocarbonadas dos fosfolípidos como a espessura da bicamada aumentam quando a concentração de glicósido é aumentada. Estas alterações biofísicas, que correspondem a uma eventual diminuição da fluidez membranar, poderão ter um impacto significativo na integridade estrutural de uma membrana biológica. Consideramos portanto este resultado particularmente importante, uma vez que estudos preliminares por nós realizados sugerem que o mecanismo de ação destes glicósidos surfactantes não deverá envolver a formação/estabilização de poros membranares.

Em suma, o trabalho realizado demonstra que esta família de desoxiglicósidos inclui vários compostos que apresentam actividades antibacterianas muito potentes e cujo mecanismo de ação deverá ser diferente daqueles que se conhecem para outras classes de antibióticos. Sugerimos pois um mecanismo baseado na ordenação dos fosfolípidos de membrana como consequência da partição de glicósidos.

Palavras-chave: antibióticos, glicósidos surfactantes, glicosilação, dinâmica molecular, bicamadas lipídicas.

Acknowledgments

I would like to start by expressing my gratitude to my supervisors. I am sincerely grateful to Prof. Amélia Pilar Rauter, for all her enthusiasm and sympathy, for encouraging me to explore my ideas, as well as for having provided me with so many opportunities. I am specially thankful to Dr. Miguel Machuqueiro for his guidance and scientific input, but also for all his friendship, patience and encouragement.

I sincerely acknowledge Prof. Maria José Calhorda for welcoming me in her group and for many fruitful discussions throghout the last years.

I wish to thank Diogo Vila-Viçosa ("Mini-Chefe") for his crucial role in this work and for sharing with me his enthusiasm for indoor climbing. I thank Paulo Costa, Vítor Teixeira and Bruno Calçada and Pedro Reis from the modelling group for all their help and companionship. I am also very thankful to all my colleagues and friends from the Carbohydrate Chemistry Group, most specially Dr. Alice Martins, Dr. Nuno Xavier, Ana Marta Matos and Catarina Dias for the nice moments we spent togeter. In particular, I thank João Pedro Pais, not only for his contribution to this work with antimicrobial activity evaluation, but also for the several brainstorming sessions. I also thank Tiago Silva for the many late hours working together on our endless theses.

I should acknowledge all the professors and/or researches that have contributed to this work, namely Prof. Maria José Brito for her valuable help with NMR experiments, Dr. Carlos Cordeiro and Dr. Ana Patrícia Marques for the HRMS spectra, Prof. Carlos Borges for the ESI-MS spectra and for his support along the course, Prof. Christopher Maycock and Dr. Rita Ventura for several NMR experiments carried out at ITQB and for having introduced me to the organic chemistry laboratory a few years ago. My thanks are further extended to Prof. M. Soledade Santos e Prof. Filomena Martins, Prof. Cristina Moiteiro and Prof. Helena Gaspar for helpful discussions, and also to Dr. Ana Pelerito from Instituto Nacional de Saúde Ricardo Jorge for antimicrobial assays on *B. anthracis*.

Above all, I am deeply grateful to my family and friends for their unconditional love and support, regardless of the circumstances.

Contents

List of Figures

List of Schemes

List of Tables

List of Abbreviations

A08	2,6-Dideoxy-α-L-*arabino*-hexopyranoside
A12	2,6-Dideoxy-α-L-*arabino*-hexopyranoside
Ac	Acetyl
Ac_2O	Acetic anhydride
AcOH	Acetic acid
app	apparent
aq.	aqueous
br	broad
Bu	Butyl
c	concentration in g/mL
calcd.	calculated
CIM	Concentração Mínima Inibitória
COSY	Correlation Spectroscopy
$C_{quat.}$	quaternary carbon
D	Lateral self-diffusion coefficient
d	doublet
DBU	1,8-Diazabicyclo[5.4.0]undec-7-ene
dd	doublet of doublets
ddd	doublet of doublets of doublets
DFT	Density Functional Theory
DMAP	4-(Dimethylamino)pyridine
DMF	*N,N*-Dimethylformamide
DMPC	1,2-Dimyristoyl-*sn*-glycero-3-phosphocholine
DMSO	Dimethylsulfoxide
DPPC	1,2-Dipalmitoyl-*sn*-glycero-3-phosphocholine
dq	doublet of quartets
dt	doublet of triplets
Et	Ethyl
EtOAc	Ethyl acetate
ESI	Electrospray Ionization
g	gram
G08	Octyl β-D-glucopyranoside
G12	Dodecyl β-D-glucopyranoside

GL	Glycolipid
h	hour(s)
HMBC	Heteronuclear Multiple Bond Correlation
HMQC	Heteronuclear Multiple Quantum Correlation
HRMS	High Resolution Mass Spectrometry
HSQC	Heteronuclear Single Quantum Correlation
Hz	Hertz
J	Coupling constant
kcal	kilocalory
m	multiplet
MD	Molecular Dynamics
Me	Methyl
$MeNO_2$	Nitromethane
MeOH	Methanol
MBC	Mininum Bactericidal Concentration
MIC	Mininum Inhibitory Concentration
min.	minute(s)
MM	Molecular Mechanics
mmol	milimole
MOI	Moments Of Inertia
m.p.	melting point
MS	Molecular sieves or Mass Spectrometry
MSD	Mean Square Displacement
m/z	mass-to-charge ratio
NaOMe	Sodium methoxide
nm	nanometer
NMR	Nuclear Magnetic Resonance
NOESY	Nuclear Overhauser Effect Spectroscopy
PBC	Periodic Boundary Conditions
PC	Phosphatidylcholine
ppm	parts-per-million
q	quartet
QM	Quantum Mechanics
quint	quintet
R12	Dodecyl α-L-rhamnopyranoside
satd.	saturated
s	singlet
SASA	Solvent Accessible Surface Area
Selectfluor	1-chloromethyl-4-fluorodiazoniabicyclo[2.2.2]-octane bis(tetrafluoroborate)
$\lvert S_{CD} \rvert$	Deuterium order parameter
R_f	Retention factor
r.t.	room temperature
t	triplet
T12	Dodecyl 2-deoxy-α-L-*threo*-pentopyranoside
TBAF	Tetra-*n*-butylammonium fluoride
TBS	*tert*-Butyldimethylsilyl

TBDMSCl	*tert*-Butyldimethylsilyl chloride
THF	Tetrahydrofuran
TLC	Thin-Layer Chromatigraphy
TMS	Tetramethylsilane
TMSOTf	Trimethylsilyl trifluoromethanesulfonate
TPHB	Triphenylphosphane hydrobromide
Å	Angstrom
$[\alpha]_{\boldsymbol{D}}^{\mathbf{20}}$	specific optical rotation
δ	chemical shift

Chapter 1

Introduction

1.1 Bacterial infections and therapeutics

Modern medicine has been dependent on chemotherapeutic agents such as antibiotics [1] for the prevention and/or treatment of infectious diseases since quite a long time. In the nineteenth century, pneumonia, diarrhea and other infections were the main causes of human death. Therefore, the introduction of antibiotics was of of great importance to society in light of its impact on the prevention and/or treatment of these previously life-threatening diseases [**4, 5**]. The most important discovery in the modern era of antimicrobial agents was penincillin, in 1929 [**6**]. Since then, other more effective antibiotics have been discovered and developed, mainly through the elucidation of drug-target interactions and lead optimization approaches [**7**], and also by means of high-throughput screening campaigns exploiting genomics [**8**].

Nowadays, bacterial infections still represent a major public health concern owing to the increasing prevalence of multiple antibiotic-resistant bacterial strains. It has been estimated that at least 25 000 patients die every year in Europe because of bacterial infections that cannot be treated with the available antibiotics [**4, 9**]. Hence, the development of new antimicrobial agents with novel mechanisms of action has emerged as one of the greatest challenges facing modern society and merits innovative strategies from the viewpoint of the scientific community [**10**]. The emergence of antibiotic resistance has also motivated great efforts to unravel the complex mechanims by which the currently available antibiotics mediate bacterial cell death, which have been proven to involve many genetic and biochemical pathways as well as alterations at the ultrastructural level [**7**]. Furthermore, the molecular mechanisms underlying drug-resistance phenomena have been thoroughly investigated likewise. New mechanism are constantly being described, including the prevention of access to drug targets, changes in antibiotic targets by mutation, and direct modification/inactivation of antibiotics [**11, 12**].

[1] The term "antibiotics" earlier referred to compounds produced by microorganisms that are effective against other microorganisms. Nowadays, the definition also includes other antimicrobial compounds of synthetic or semisynthetic origin [**4**].

Antibiotics can be classified based on their respective cellular targets, in addition to being distinguished between bacteriostatic (i.e. those that merely inhibit bacterial cell growth) and bactericidal (i.e. those that induce bacterial cell death) antibiotics. Most bactericidal antibiotics are inhibitors of the synthesis of nucleic acids, cell wall or proteins [**4, 7**]. However, many are known to target bacterial cell membranes. Interestingly, bacterial membrane lipid composition has been shown to play an important role in determining the potency of certain antimicrobial agents, namely antimicrobial peptides [**13–15**] and other polycationic compounds [**16, 17**], some of which are thought to induce the formation of lipid domains/lipid phase separation by clustering negatively charged lipids. Moreover, regulatory processes of membrane lipid homeostasis (i.e. the ability to adjust membrane lipid composition, usually in response to physical/environmental changes) are known to be further involved in antibiotic resistance mechanisms [**18**].

1.2 Carbohydrate-based structures as antibacterial agents

The fact that carbohydrates represent the most abundant, multifunctional and stereochemically rich class of natural products makes them particularly interesting scaffolds for drug discovery. Indeed, not only carbohydrates can be regarded as renewable/environmentally friendly raw materials, but also the increasing knowledge of the many biological processes involving carbohydrates, in particular carbohydrate-protein interactions, provides a unique opportunity for the development of drug candidates that should mimic their function in biological systems, known as glycomimetics, which are a relatively untapped source of therapeutic agents [**19, 20**].

Most carbohydrate-based antibiotics are compounds of natural or semisynthetic origin. They encompass several major classes of compounds that feature distinct mechanisms of action. For instance, aminoglycoside antibiotics (i.e kanamycins, gentamycins, neomycins and apramycins) and macrolide antibiotics (i.e. erythromycin, clarithromycin and azithromycin) act by inhibiting protein synthesis, whereas glycopeptide antibiotics (i.e. vancomycin and teicoplanin) and nucleoside antibiotics (i.e. tunicamycins, mureidomycins and liposidomycins) exert their antibacterial activity through the interruption of bacterial cell wall assembly [**21**].

The design and synthesis of new antibiotic compounds emboding a sugar moitey in their structure has also occupied a prominent place in drug discovery. Inhibition of the biosynthetic pathway of key carbohydrates that are present in bacterial cell walls (i.e. peptidoglycan and lipopolysaccharides) is an attractive approach that has been extensively explored [**21**]. Another important class of synthetic antibiotic compounds includes carbohydrate-based surfactants, which are known for their potential to interact with phospholipid bilayers, eventually leading to the disruption of bacterial cell membranes, as a result of their amphiphilic properties. The synthesis and biological activity of such type of compounds has been reviewed elsewhere [**21**]. Therefore, we will now highlight only the work developed by our research group in the context of this subject.

Amongst several antimicrobial sugar-based surfactants, featuring a long hydrocarbon chain, that have been synthesized in our group, we emphasize a series of (*N*-alkylcarbamoyl)methyl enulosides, and their related pyranoid-conjugated diene esters. Those carrying a dodecyl chain displayed significantly potent antibacterial and/or antifungal activities, namely against the clinically relevant *Bacillus cereus*, *Bacillus subtilis* and *Enterococcus faecalis* bacterial strains, as well as toward the fungal pathogen *Penicillium aurantiogriseum* [**22**].

The synthesis of a new family of alkyl deoxyglycosides has also been undertaken by our group [**1**–**3**]. These are octyl/dodecyl 2-deoxy or 2,6-dideoxy-*arabino*-hexopyranosides (**Figure 1.1**), easily accessed by reaction of fatty alcohols with readily available glycals in the presence of triphenylphosphane hydrobromide, a simple procedure that favors the formation of the α-anomers in high yields, followed by deprotection [**23**]. Their antimicrobial activities were preliminarily evaluated against various pathogens using the paper disk diffusion method, and minimal inhibitory concentrations (MIC) were determined for those that showed relevant activity, in this case using the dilution method.

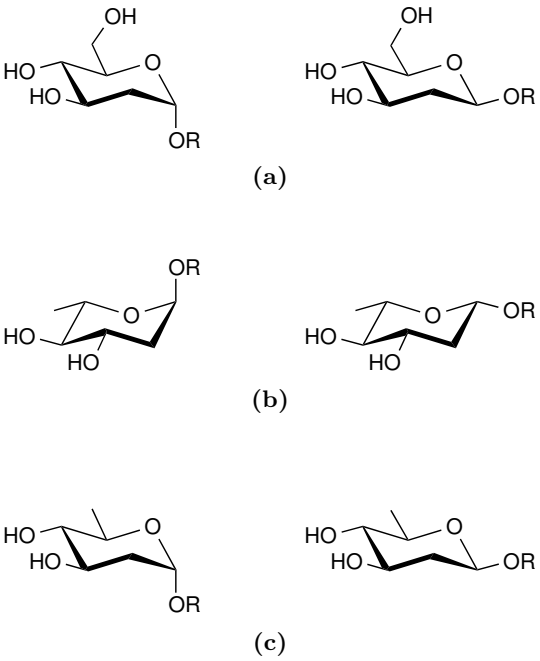

Figure 1.1: Structures of the alkyl deoxyglycosides synthesized by Rauter and co-workers. **(a)** 2-Deoxy-D-*arabino*-hexopyranosides [**2**], **(b)** 2,6-dideoxy-L-*arabino*-hexopyranosides [**1**] and **(c)** 2,6-dideoxy-D-*arabino*-hexopyranosides [**3**]. R = C_8H_{17} or $C_{12}H_{25}$.

Regarding the alkyl 2-deoxy-D-*arabino*-hexopyranosides (**Figure 1.1a**), the most active compounds were the octyl and dodecyl β-glycosides, which exhibited moderate activity against *E. faecalis* (MIC = 31.3 μg mL^{-1}) [**2**]. In the case of the alkyl 2,6-dideoxy-α-L-*arabino*-hexopyranosides (**Figure 1.1b**), the dodecyl α-glycoside proved to be the most active compound, exhibiting very potent activities, particularly against *B. subtillis* and *B. cereus* (MIC = 7.8 μg mL^{-1} in both cases), within the same order of magnitude of those presented by the con-

trol chloramphenicol (MIC = 3.1 μg mL^{-1} and 6.3 μg mL^{-1}, against *B. subtillis* and *B. cereus*, respectively). This compound was also effective against *E. faecalis* (MIC = 15.6 μg mL^{-1}) and *Listeria monocytogenes* (MIC = 31.3 μg mL^{-1}) **[2]**. Despite these promising results regarding bioactivity, this compound was shown to induce acute toxicity toward human lymphocytes at a concentration of 10 μg mL^{-1} **[2]**. Hence, in our ongoing research we have been developing a library of analogues of this compound, in the attempt to achieve a simultaneously bioactive and non-toxic, potential drug candidate. More recently, we synthesized the corresponding alkyl 2,6-dideoxy-D-*arabino*-hexopyranoside stereoisomers (**Figure 1.1c**), using the methodology described above to obtain the intermediate 2-deoxy-D-glycosides followed by regioselective tosylation at 6-position of the sugar and subsequent reductive deoxygenation **[3]**. Furthermore, the results concerning the antibacterial activity of this family of compounds against three strains of *Bacillus anthracis* was also reported therein for the first time. This pathogen is responsible for lethal anthrax infections in humans and livestock, and is a well-known bioterrorism agent **[24]**. Therefore, many efforts have been dedicated to the search for effective inhibitors of this life-threatening pathogen **[25–29]**. The most active compound was again dodecyl 2,6-dideoxy-α-L-*arabino*-hexopyranoside (MIC = 50 μM). Interestingly, the corresponding 2,6-dideoxy-D-glycoside exhibited a lower antibacterial activity (MIC = 25 μM), indicating that configuration of the sugar moiety is able to tune the antibacterial potency displayed by enantiomers for these amphiphilic molecular entities.

1.3 Scope of this work

Following the promising results obtained so far with alkyl deoxyglycosides as antibacterial agents (see **Section 1.2**), our group is now interested in the development of novel sugar-based surfactants that should display improved properties for future application in therapeutics and biosecurity fields (i.e. potent bactericidal activity and low toxicity against human linfocite cells). To achieve such purpose, it is paramount that the structural determinants required for the antibacterial activity of this family of compounds targetting *Bacillus* spp. are deeply studied and their mechanism of action clarified. The herein presented research work combines two distinct contributions to this investigation, relying on a multidisciplinary approach.

In **Part I** (**Chapters 2-5**) of this manuscript, we present the synthesis of a series of new dodecyl deoxyglycosides, starting from commercially available sugars or appropriate glycosyl donors, and the preliminary evalutaion of their antiantibacterial activity, using *B. cereus* as a model microbe due to its genotypic similarity with *B. anthracis* **[30–34]**. Some of the newly synthesized compounds were further tested for their antibacterial activity towards *B. anthracis*.

In **Part II** (**Chapters 6-9**), molecular dynamics (MD) simulations were performed aiming (i) to provide an atomistic description of the aggregates formed by these molecules in aqueous media, (ii) to study their adsorption properties at a model lipid bilayer interface and (iii) to investigate the eventual structural destabilization of model membranes by this family of

surfactant glycosides.

Having introduced the scientific problem in the precedent sections, theoretical and methodologycal aspects relevant to both the experimental and computational studies carried out will also be briefly described further ahead in this manuscript.

I - SYNTHESIS OF NEW DEOXY GLYCOSIDES WITH POTENTIAL ANTIBACTERIAL ACTIVITY

Chapter 2

Brief introduction

2.1 Carbohydrates

Carbohydrates [1] have long been recognized as the most abundant biomolecules in the living world. They occur either as single units (known as monosaccharides, i.e. D-glucose, which is by far the most plentiful of carbohydrates, **Figure 2.1**) or as compounds that consist of multiple sugar residues joined to each other by glycosidic linkages (oligosaccharides and polysaccharides, i.e. sucrose and cellulose, respectively, **Figure 2.1**). Carbohydrates are also structural components of nucleic acids (i.e. deoxyribonucleic acid (DNA), which contains repeated monomeric units of 2-deoxy-D-ribose) and can be found associated with other biomolecules in complex glycoconjugates (i.e. glycolipids, glycopeptides and glycoproteins) that participate in a wide range of biochemical processes. In fact, the primary significance of carbohydrates lies on their major importance in biology [**36**].

Until the end of the twentieth century, however, they were thought to act exclusively as sources of energy storage (i.e. glycogen, the main reservoir of D-glucose in animals) and structural building blocks (i.e. cellulose, cell wall component in plants) [**37**]. Eventually, the great information-carrying potential of carbohydrates came to be recognized, along with the discovery that glycans [2] play key functional roles in triggering biological regulation and recognition events [**38, 39**]. These include intracellular trafficking, cell adhesion, cell growth, disease development, host–pathogen interaction during infection and immune response [**40, 41**]. A multitude of other physiological functions and their implications in human disease continue to be unveiled by the expanding fields of glycobiology and glycomics [**42**–**44**].

[1] The term "carbohydrate" was originally derived in the nineteenth century from the French *hydrate de carbone* and referred only to monosaccharides because their empirical composition could be expressed as $C_n(H_2O)_n$. However, it has been extended to include monosaccharide derivatives (i.e. alditols, deoxysugars and aminosugars, amongst others), their oligomers and polymers [**35**].

[2] "Glycan" generally refers to both polysaccharides and the glycosidic moiety of glycoconjugates [**35**].

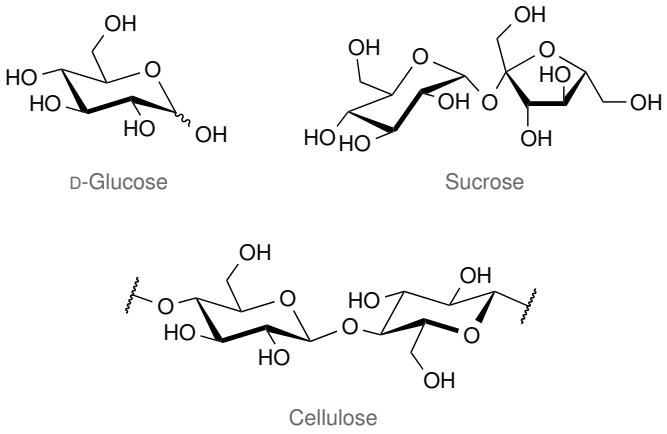

Figure 2.1: Representative structures of monosaccharides (D-glucose), oligosaccharides (sucrose) and polysaccharides (cellulose).

The versatility of carbohydrates in biological systems is undoubtedly a result of the their structural diversity and complexity. Indeed, carbohydrates are highly functionalized and hence stereochemically rich molecules which have been explored by great sugar chemists for over a hundred years. The most remarkable contribution to the field is that of Emil Fischer (1852-1919), who elegantly elucidated the structure of D-(+)-glucose and assigned the relative configurations of the parent monosaccharides in 1891, despite the very limited resources available by the time **[38, 45]**.

Sugars are aliphatic polyhydroxylated aldehydes (generically referred to as aldoses, i.e. D-glucose) or ketones (ketoses, i.e. D-fructose), the later being less common in Nature. The presence of multiple stereogenic centers gives rise to many stereoisomers, and as a consequence several conventions had to be adopted in order to properly name and represent them. The simplest of aldoses is glyceraldehyde, a triose containing only one asymmetric center and therefore occurring as two enantiomeric entities, D- and L-glyceraldehyde. By convention, monosaccharides containing more than three carbon atoms (the commonest being hexoses, i.e. D-mannose and pentoses, i.e. D-xylose) are hence assigned to the D- or L- series according to the absolute configuration (*R* or *S*, respectively, as it is for D- and L-glyceraldehyde) of their configurational atom [3]. The trivial name of the monosaccharide (i.e. "glucose") defines the stereochemistry of the remaining stereocenters relatively to that of the configurational atom **[38]**.

Most monosaccharides exist nearly exclusively as cyclic hemiacetals/hemiketals (generically named lactols), which are formed by means of an intramolecular cyclization reaction involving both hydroxy and carbonyl functionalities. Participation of distinct hydroxy groups leads to rings of different size, the most common being either six- or five-membered (named pyranoses and furanoses, respectively). From this process also arises a new center of chirality (known as anomeric center) and hence two diastereomers, which are designated either α- or β-anomer

[3] The configurational atom is the highest-numbered asymmetric carbon atom **[35]**, i.e. C-5 in glucose.

depending on the relative configurations of the anomeric center and the configurational atom [4].

In solution, reducing sugars [5] can be found as equilibrium anomeric mixtures of the aforementioned cyclic forms, which interconvert via the acyclic polyhydroxyaldehyde/ketone with a concomitant change in optical rotation over time. This process, called *mutarotation*, is illustrated in **Scheme 2.1** for D-glucose in aqueous solution. Equilibration between α-D-glucopyranose and β-D-glucopyranose may occur by hemiacetal hydrolysis in either of the diastereomers, followed by ring-closure of the open-chain form (via intramolecular nucleophilic displacement of the aldehyde by the 5-hydroxy group). The same pathway holds for the α-D-glucofuranose/β-D-glucofuranose equilibrium (though involving the 4-hydroxy group instead). It is worth to mention that hydration - intermolecular addition of water to form a *gem*-diol - is a competing process in aqueous solution, though vestigial for most common hexoses and pentoses [**46**].

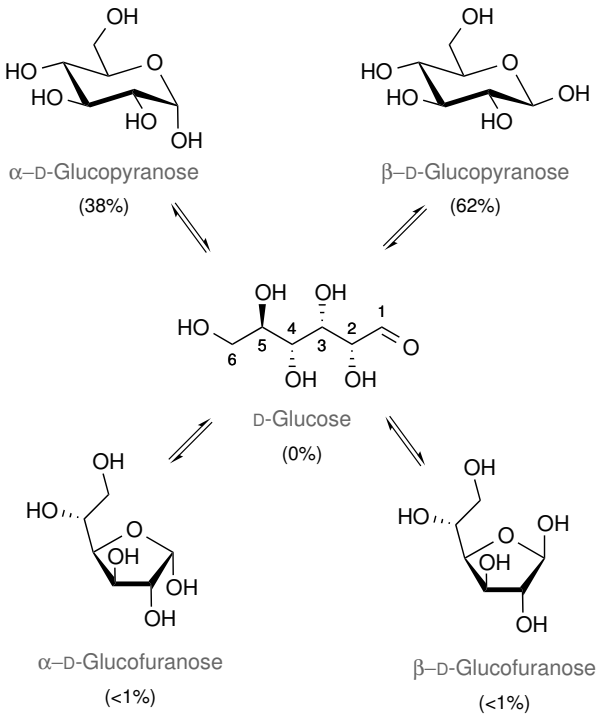

Scheme 2.1: Representation of the equilibrium between the detectable isomers of D-glucose in aqueous solution [**38**].

Equilibrium compositions of carbohydrate solutions are governed by the relative thermodynamic stability of each isomer and their kinetics of formation which depend, in turn, on several effects. For most sugars the 6-membered pyranose structures are strongly stabilized over their

[4] In the current strict definition, the α-anomer is the diasteromer in which the newly formed hydroxy group is *cis* relatively to the oxygen attached to the configurational atom, whereas in the β-anomer they are formally *trans*, in the Fischer projection [**35**]. For most cases, however, the following general rule can be applied: for sugars belonging to the D-series, the anomeric substituent is projected down in α-anomers and up in β-anomers. The opposite applies to the L-series.

[5] The term "reducing" refers to the presence of a free hemiacetal, in opposition to glycosides which present an acetal linkage at the anomeric carbon (see **Section 2.2**).

5-membered furanose counterparts and a chair conformation is usually preferred. Thus, aqueous solutions of D-glucose are composed almost exclusively by pyranose forms in $^4C_1$ conformations [6] as depicted in **Scheme 2.1**. More considerable amounts of furanose forms are observed for other sugars, mostly as a result of the destabilization of the corresponding pyranoses by steric effects [**46**]. The anomeric composition arises, in turn, from a compromise between steric and electronic effects at the anomeric center. In fact, although β-D-glucopyranose is the most populated isomer (c.a. 62%) in equilibrated aqueous solutions of D-glucose, considerable amounts of its corresponding α-anomer are still observed (c.a. 38%), even though it should be energetically destabilized due to steric and solvation considerations. Moreover, the isomer featuring an axial substituent at this position is favored in the case of other monosaccharides (i.e. D-mannose). This result is rationalized in terms of a phenomenon by which the axial orientation of the anomeric substituent in pyranoses and their derivatives is stabilized over its equatorial positioning, named *anomeric effect* [7] by Lemieux [**49**]. The magnitude of this stabilization increases with the electronegativity of the substituent and is usually attenuated with the increased polarity of the solvent [**47, 49, 50**]. However, in the case of positively charged substituents an inversion of this tendency is observed as their equatorial positioning is preferred, owing to the so-called *reverse anomeric effect*.

Though the origins of the anomeric effect(s) are still controversial [**47**–**53**], it has been explained essentially by means of two models. The first is an electrostatic interpretation, based on the interaction of the dipoles formed by (i) the lone-paired electrons of the endocyclic oxygen and (ii) the polarized bond between the anomeric carbon and the exocyclic heteroatom, which is unfavorable in the case of an equatorial substituent (**Figure 2.2a**). In agreement with this interpretation is the aforementioned *reverse anomeric effect*, since it features a reversed dipole in the bond between the anomeric carbon and the exocyclic substituent. According to the other model, which highlights a stereoelectronic component for the anomeric effect, an axial substituent may be stabilized via hyperconjugation, as a result of the *syn*-periplanar arrangement of one of the ring oxygen non-bonding orbitals (n) containing a lone pair of electrons, and the anti-bonding orbital (σ^*) of the anomeric carbon (**Figure 2.2b**). This eventual $n \rightarrow \sigma^*$ interaction is greatly supported by observed variations in bond lengths and angles around the anomeric center.

The anomeric effect is ubiquitous in carbohydrates and has been further recognized in other molecules containing two heteroatoms in a tetrahedral center. It is known for its important implications on conformational preferences and, particularly, in chemical reactivity, as will be highlighted in the next section.

[6] Typically, $^4C_1$ is the most populated chair conformation for D-sugars, whereas their enantiomers commonly assume a $^1C_4$ conformation. For further detail about conformational preferences of carbohydrates, see i.e. ref. [**46**], chapter 2.

[7] The term "*endo*-anomeric" effect is also frequently found in the literature, in order to distinguish the aforementioned effect from the so-called "*exo*-anomeric effect", which is similar in nature but deals with the relative orientation of the sugar ring and the exocyclic substituent. For more insight into the subject see refs. [**47, 48**].

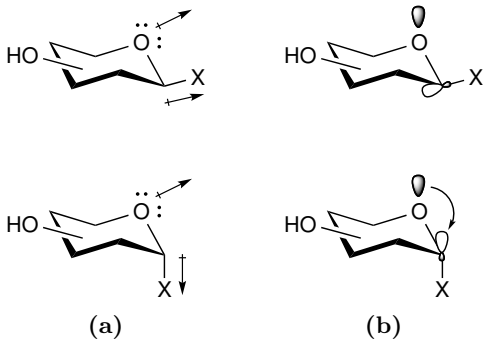

Figure 2.2: Electrostatic **(a)** and stereoelectronic **(b)** interpretations of the anomeric effect. X = generic electronegative substituent.

2.2 Chemical glycosylation

As mentioned earlier in this chapter, most carbohydrates appear in Nature mainly as polysaccharides or associated with other biological macromolecules (i.e. lipids and proteins) in a variety of glycoconjugates. In either case, monosaccharides are linked via glycosidic bonds, which are formed in the following of a glycosylation reaction [**54**]. Living systems feature complex enzymatic machinery and regulatory mechanisms to ensure selectivity and efficiency in this process. In contrast, glycosidic bond formation still poses remarkable challenges to the synthetic chemist, mainly due the unparalleled structural heterogeneity of carbohydrates and glycostructures that may be conceived [**42, 55**]. Since the present work addresses the preparation of glycosides [8], the reader will be provided at this stage with a brief overview of general considerations on chemical glycosylation [9].

Generally, a glycosylation reaction involves the nucleophilic displacement of a leaving group at the anomeric position of a sugar (glycosyl donor) by the hydroxy group (or other nucleophile, by extension [8]) of a second molecule (glycosyl acceptor) usually in the presence of an activator (promoter/catalyst). This process is illustrated in **Scheme 2.2** for the formation of a generic disaccharide. Although conceptually quite simple, glycosylation reactions are actually hampered by a set of specific difficulties that must be taken into account.

The first is the need to temporarily mask the functional groups not intended to participate in the reaction, in order to avoid the formation of complex regioisomeric mixtures. This problem (*regioselectivity*) has been successfully tackled by efficient protection/deprotection strategies and is particularly relevant when the glycosyl acceptor is a sugar, due to the presence of multiple hydroxy groups [**60**].

[8] According to the IUPAC/IUBMB-JCBN recommendations, "*glycosides are mixed acetals formally arising by elimination of water between the hemiacetal or hemiketal hydroxy group of a sugar and a hydroxy group of a second compound*". Yet this definiton has been extended to include compounds in which the anomeric hydroxy group is replaced by other groups, such as -SR, -NR^1R^2 or $CR^1R^2R^3$ [**35**].

[9] For a more in-depth reading, see refs. [**54**] and [**56–59**].

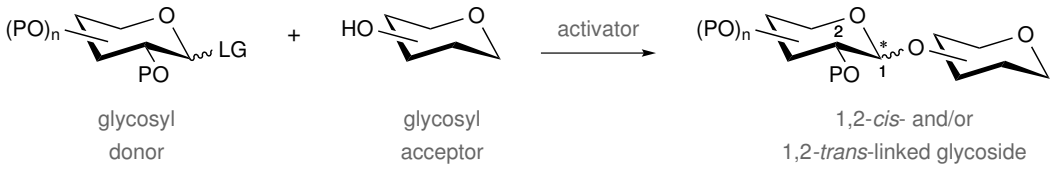

Scheme 2.2: Representation of a generic glycosylation reaction. P = generic protecting group, LG = leaving group.

Another issue deals with the control of *reactivity*, which depends on the nucleophilicity of the glycosyl acceptor and both the leaving-group ability of the glycosyl donor and its stability. In fact, glycosylations with secondary sugar hydroxy groups - which are not particularly good nucleophiles - can often be sluggish and hence low-yielding, as were the first reactions performed at the turn of the twentieth century when only few glycosyl donors (anomeric chlorides/bromides, hemiacetals and, later, acetates) and synthetic methods were available. An important overturn in this area was witnessed during the mid-70's with the development of new anomeric leaving groups, namely glycosyl trichloroacetimidates, thioglycosides and glycosyl fluorides, all of which are broadly used nowadays. Enormous progress has also been made in the last decades, in particular with the introduction of more sophisticated donors such as glycosyl iodides and glycals, amongst many others, and a wave of methodological improvements [**54**].

However, the most important aspect in glycosylation is arguably *stereoselectivity*, once the formation of a glycosidic bond gives rise to a new asymmetric center (**Scheme 2.2**). Control of the stereochemical outcome in these reactions was early noticed to be a considerable challenge, depending on the target glycosidic linkages. These can be usefully distinguished between either 1,2-*cis* linkages, which include those found in α-D-galactosides, α-L-fucosides, β-D-mannosides and α-D-glucosides (**Figure 2.3a**), or 1,2-*trans* linkages such as those presented by β-D-glucosides, β-D-xylosides and α-D-arabinosides (**Figure 2.3b**). The two above-mentioned types of glycosyl residues can be found in a wide variety of natural compounds, along with several deoxygenated derivatives such as 2-deoxyglucosides and sialosides, which can be defined as neither 1,2-*cis*- nor 1,2-*trans*-linked glycosides (**Figure 2.3c**). This distinction is made because while 1,2-*trans* glycosidic linkages are notably easier to prepare by taking advantage of the known effect of neighboring group participation (that is, through the use of acyl protecting groups at 2-position), the stereoselective synthesis of 1,2-*cis*-linked glycosides is not as straightforward, requiring the use of non-participating protecting groups (i.e. benzyl ethers) at 2-position and usually leading to mixtures of anomeric diastereomers [**54**].

Glycosylation is a complex process and several of its mechanistic aspects are still subject to intense debate, namely with respect to the nature of the active intermediates that are involved and the relative contribution of their reactivity to the stereochemical outcome [**42, 61, 62**]. Nevertheless, the commonly accepted rationalization [**56**–**59**] invokes that it often follows unimolecular nucleophilic substitution (S_N1) pathways, as depicted in **Scheme 2.3**.

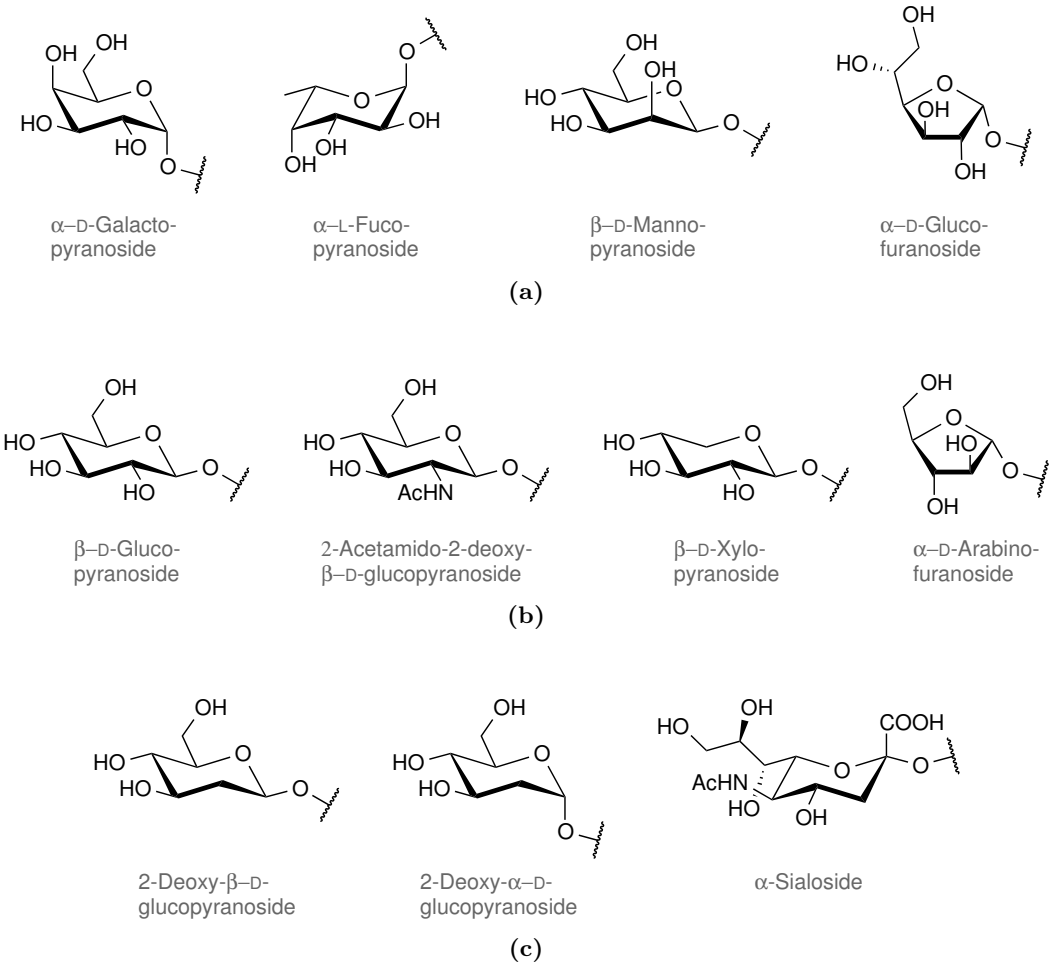

Figure 2.3: Examples of common **(a)** 1,2-*cis*, **(b)** 1,2-*trans* and **(c)** neither 1,2-*cis* nor 1,2-*trans* glycosidic linkages (adapted from ref. [**54**]).

The first step is the departure of the anomeric leaving group, generally mediated by an activator, leading to the formation of a glycosyl cation which is stabilized by resonance to form an oxycarbenium ion. In the case of a glycosyl donor bearing a non-participating group (**Scheme 2.3a**), the nucleophile (glycosyl acceptor) may attack either face of this reactive intermediate and thus both 1,2-*trans* (route a) and 1,2-*cis* (route b) glycosides are possibly formed. Although the 1,2-*cis*-linked thermodynamic product is typically prevalent due to the anomeric effect (i.e. α-glucosides), other factors may significantly influence the stereochemical outcome of a glycosylation reaction (i.e. steric factors, conformation, temperature and solvent, among others). For this reason the stereoselective synthesis of several 1,2-*cis* glycosidic linkages (i.e. β-mannosides) is known to be particularly challenging.

When the glycosyl donor features an acyl-type participating group at 2-position (**Scheme 2.3b**), the glycosyl cation may be intramolecularly stabilized through the participation of the neighboring carbonyl oxygen to form a bicyclic acyloxonium ion. As the nucleophilic attack

on this major intermediate proceeds with inversion of configuration (route c), the 1,2-*trans* glycoside is generally formed with high stereoselectivity, although small amounts of the 1,2-*cis*-linked product may be formed via displacement of the oxycarbenium ion in equilibrium.

Although most glycosylation reactions follow the general mechanisms herein discussed, each type of glycosyl donor has particular features regarding reactivity. Glycals (cyclic enol ether derivatives of pyranoses/furanoses) are worth-mentioning because they are suitable precursors for the preparation of important bioactive 2-deoxyglycosides. They can be either converted into other glycosyl donors or directly employed in glycosylation reactions, which usually proceed via polar addition to the double bond. The regio- and stereochemical outcome of these reactions is mainly governed by the intermediacy of an oxycarbenium ion as well [**54, 63**].

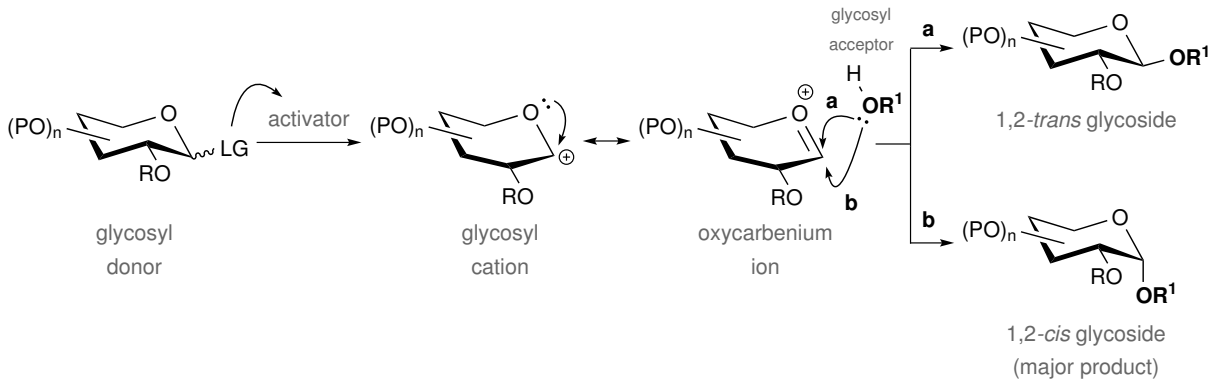

(a)

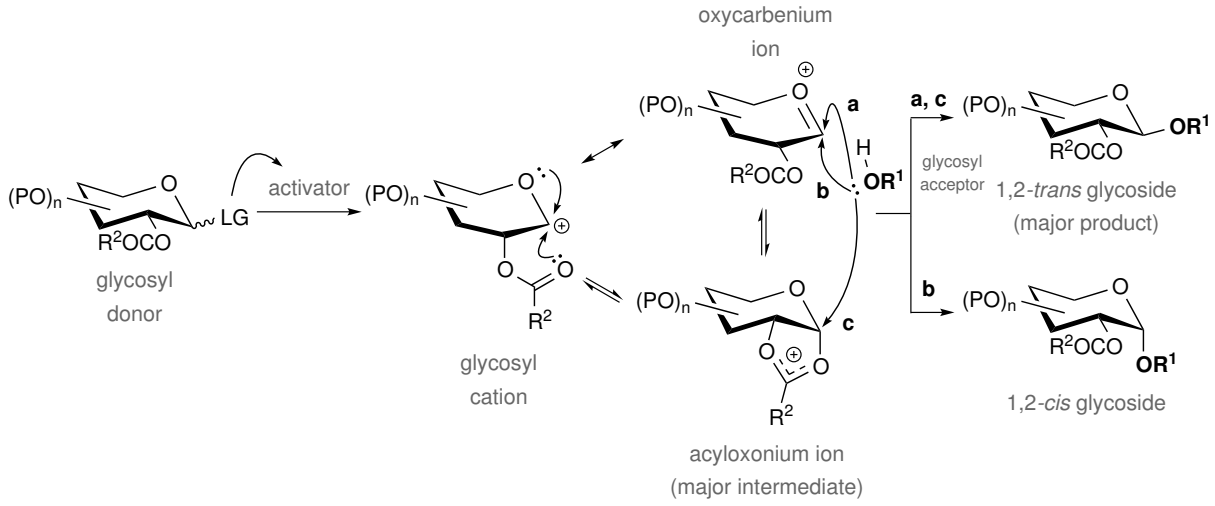

(b)

Scheme 2.3: Mechanisms for glycosylation reactions involving glycosyl donors bearing **(a)** a non-participating group and **(b)** a participating group (adapted from ref. [**54**]). LG = leaving group, P = generic protecting group, R = non-participating group, R^1 = generic aglycone residue, COR^2 = participating group.

2.3 Target compounds and synthetic routes

After having introduced relevant aspects of carbohydrate structure and reactivity, we will now present the target compounds and discuss the synthetic strategies envisaged to access them.

The main goal in this part of the work is the preparation of novel surfactant glycosides with potential antibacterial activity. As described previously (see **Section 1.2**), an original family of alkyl deoxyglycosides displaying antimicrobial activity has been reported by our group [**1**–**3**]. Though the mechanism of action of these compounds is yet to be unraveled, several structure-bioactivity relationships could already be established from the studies carried out so far, namely: (i) the amphiphilic nature of these molecules and their high surface activity is a prerequisite for antimicrobial activity; (ii) bioactivity is tuned by the deoxygenation pattern of the glycosidic moiety, since 2,6-dideoxyglycosides were active towards *Bacillus* spp., *E. faecalis* and *L. monocytogenes* but none of the related 2-deoxyglycosides displayed significant activity; (iii) sugar stereochemistry, in particular anomeric configuration, seems to modulate their antibiotic properties, the most effective compounds being α-anomers and belonging to the L-series; (iv) the nature of the aglycone [10] revealed also to be determinant, as dodecyl glycosides presented higher activity than other glycosylated fatty alcohols ([**1**–**3**] and unpublished results).

Aiming to better understand the importance of key structural features for bioactivity and, ultimately, to achieve a non-toxic potential drug candidate, we disclose now the synthesis (**Section 3.1**) and preliminary antimicrobial activity assessment (**Section 3.2**) of a series of compounds structurally related to dodecyl 2,6-dideoxy-α-L-*arabino*-hexopyranoside **1** , the most potent antibacterial of this family of compounds against *Bacillus* spp. [**1**–**3**]: dodecyl α-L-rhamnopyranoside **2**, dodecyl 2-deoxy-α-L-*threo*-pentopyranoside **3** and dodecyl 2,6-dideoxy-2-fluoro-α-L-gluco/L-mannopyranosides **4**/**5** (**Figure 2.4**).

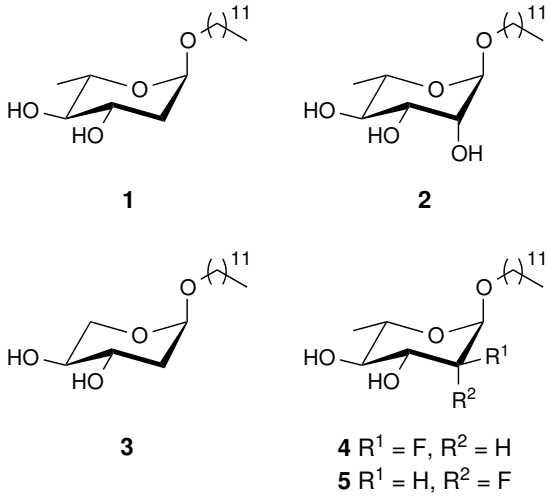

Figure 2.4: Structures of the lead compound **1** and target glycosides **2-5**.

[10] "Aglycone" refers to the compound to which the glycosyl residue ("glycone") has been attached [**35**].

Target glycosides were rationally designed with the intent to explore particular modifications in the sugar moiety of the lead compound **1**, while retaining important characteristic of its bioactive structure, in this case the dodecyl aglycone and the α-L-stereochemistry.

The importance of 2,6-dideoxygenation over 2-deoxygenation has been shown in our previous works [**1**–**3**]. However, the potential of 6-deoxyglycosides as antibacterials targeting *Bacillus* spp. has not been explored yet. Hence, as a starting point for the evaluation of the 6-deoxy pattern we decided to prepare dodecyl α-L-rhamnopyranoside **2**, since it could be easily accessed from L-rhamnose (6-deoxy-L-mannose), through glycosylation of dodecanol with an appropriate peracylated glycosyl donor, i.e. trichloroacetimidate **6** , followed by deprotection (**Scheme 2.4a**). The glycosylation step should proceed with high stereoselectivity using common methods (i.e. Lewis acid catalysis), as a result of neighboring group participation (see **Section 2.2**).

Regarding the synthesis of dodecyl 2-deoxy-α-L-*threo*-pentopyranoside **3** , it was encouraged by promising results meanwhile obtained in our laboratory for D-*threo*-configurated glycosides, which have shown moderate antimicrobial activity and, simultaneously, significantly low toxicity to human cell lines (unpublished data), highlighting the therapeutic potential of pentopyranosyl derivatives. In this context, we considered L-stereoisomers as particular good candidates, based on the superior bioactivity observed for L-*arabino*-hexopyranosides over their enantiomers in our previous works [**1**–**3**]. The synthesis should be readily accomplished by means of triphenylphosphane hydrobromide (TPHB)-catalyzed reaction of dodecanol with protected glycal **7**, which can be obtained from L-xylose by known procedures, and subsequent deprotection (**Scheme 2.4b**). This is an efficient methodology optimized by our group [**23**] that has been applied to the preparation of bioactive 2-deoxy-α-glycosides with high stereoselectivity [**1**–**3**].

Finally, we were also motivated to synthesize 2,6-dideoxy-2-fluoro glycosides **4** /**5** , for two main reasons: (i) it is rather established that the introduction of fluorine in biologically active organic compounds generally leads to beneficial impacts on their pharmacological properties (i.e. modulation of binding affinity, improvement of metabolic stability and pharmacokinetic profile) [**64, 65**]; and (ii) a related 2,6-dideoxy-2-iodo glycoside has been synthesized in our laboratory and exhibited an antibacterial activity competitive with that of the lead compound **1** (unpublished results), suggesting that further modifications at 2-position may be explored. The chosen approach to synthesize target glycosides **4**/**5** was based on regioselective electrophilic fluorination at 2-position of the commercially available glycal **8** and concomitant nucleophilic addition of dodecanol to the anomeric center promoted by selectfluor [**66**], a versatile reagent known for its particular usefulness in the synthesis of 2-deoxy-2-fluoro sugars/glycosides [**67**–**70**]. Once this methodology often leads to mixtures of epimers at 2-position, it is expected that both the desired α-L-*gluco* (**4**) and α-L-*manno* (**5**) stereoisomers may be obtained, after deprotection (**Scheme 2.4c**).

It should be noted at this stage that although the presented synthetic routes have been conceived to access bioactive α-glycosides, whenever β-anomers could be isolated, their antibacterial activity will also be evaluated.

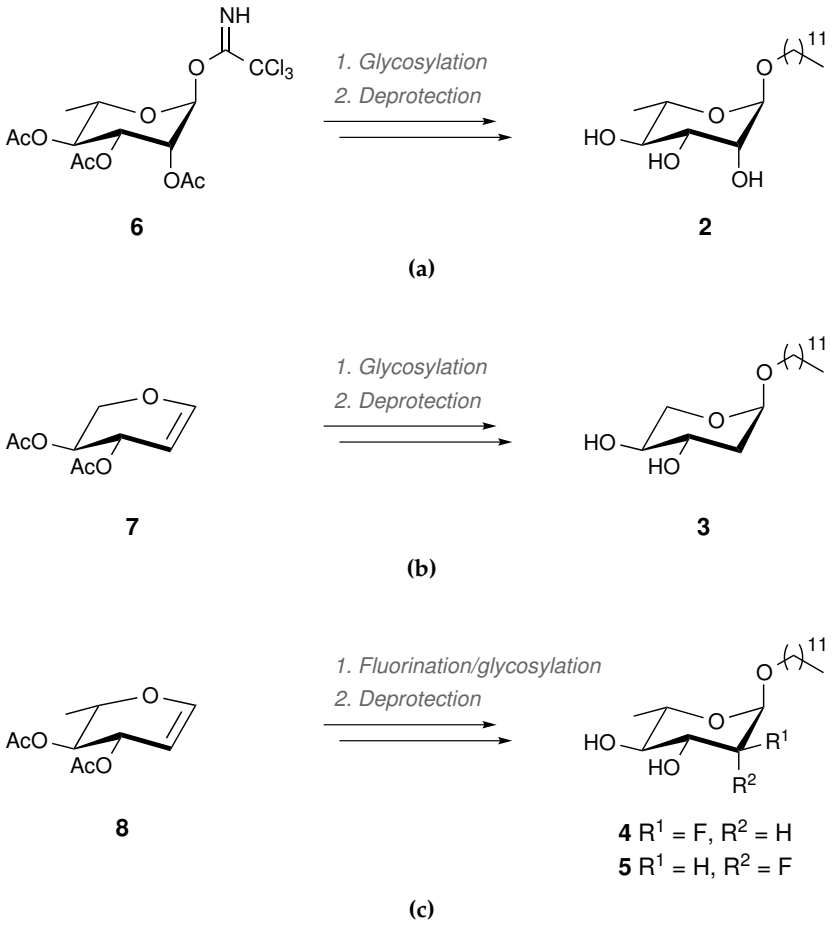

Scheme 2.4: Synthetic strategies towards **(a)** dodecyl α-L-rhamnopyranoside **2**, **(b)** dodecyl 2-deoxy-α-L-*threo*-pentopyranoside **3** and **(c)** dodecyl 2,6-dideoxy-2-fluoro-α-L-gluco/L-mannopyranosides **4**/**5**.

Chapter 3

Results and discussion

3.1 Synthesis

In this section, results obtained for the proposed syntheses (see **Section 2.3**) will be presented, including the preparation of intermediate glycosyl donors, with the exception of those that are commercially available. Evaluation of the antimicrobial activity of the synthesized compounds is provided in **Section 3.2**.

All compounds were characterized by common physical and spectroscopic methods (see **Sections 5.1-5.3** for experimental details and full characterizations). Purity of the final products was confirmed by high resolution mass spectrometry (HRMS) prior to biological assays.

Detailed nuclear magnetic resonance (NMR) analysis was performed through mono- and bidimensional experiments. In most cases, particular emphasis was given to the products obtained directly from the glycosylation reactions, since (i) these are the key synthetic steps in which stereochemistry is defined and mixtures of diastereomers are often resolved; and (ii) final compounds' NMR spectroscopic data usually resembles that presented by their protected precursors. Structural assignments, in particular with respect to the anomeric configuration, were carried out by careful comparison with relevant data reported in the literature, whenever necessary [1]. ^{1}H, ^{13}C and, when applicable, ^{19}F NMR spectra of the final compounds synthesized can be found in **Appendix A**.

In light of the general aspects introduced in **Section 2.2**, glycosylation reaction mechanisms will also be proposed and/or discussed with the intent to rationalize each result with respect to stereoselectivity.

[1] For generic considerations regarding the structural analysis of carbohydrates, in particular by NMR, see i.e. ref. [**71**], chapter 8.

3.1.1 Synthesis of dodecyl α-L-rhamnopyranoside

The synthesis of dodecyl α-L-rhamnopyranoside (dodecyl 6-deoxy-α-L-mannopyranoside) **2** is depicted in **Scheme 3.1**. The first three steps refer to the preparation of the glycosyl donor, 2,3,4-tri-*O*-acetyl-α-L-rhamnopyranosyl trichloroacetimidate **6** [**72**], which was efficiently accomplished in 85% overall yield following conventional methods [**72**–**75**].

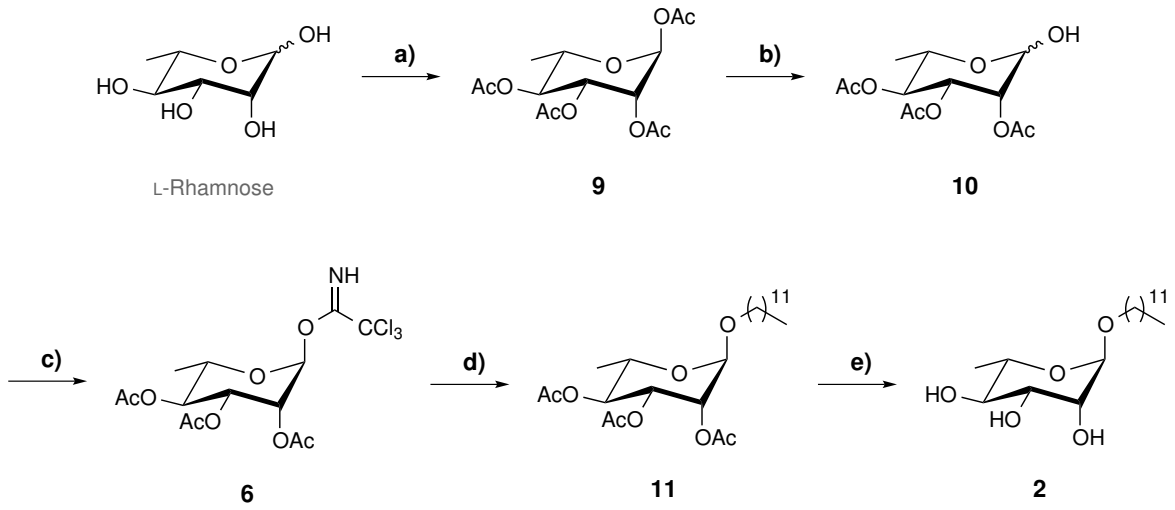

Scheme 3.1: Synthesis of dodecyl α-L-rhamnopyranoside **2**. Reagents and conditions - a) Ac_2O, pyridine, DMAP, 0 °C→r.t.; b) NH_2NH_2·AcOH, DMF, r.t., 95% over two steps; c) Cl_3CCN, DBU, CH_2Cl_2, 0 °C→r.t., 89%; d) dodecanol, TMSOTf, CH_2Cl_2, 4Å MS, 0 °C; e) NaOMe, MeOH, r.t., 71% over two steps.

L-Rhamnose was converted into peracetate **9** via acylation with acetic anhydride in pyridine and in the presence of a catalytic amount of 4-(dimethylamino)pyridine (DMAP) [**71, 72**]. After aqueous work-up and evaporation of the solvent, a crude residue was obtained which did not require further purification by column chromatography since it was remarkably pure, as shown by NMR. Interestingly, this procedure afforded exclusively one of the possible diastereomers. The correspondent anomeric proton appeared in the ^{1}H NMR spectrum at lower field ($\delta = 6.02$ ppm) than the remaining sugar ring signals, as expected, and as a broad doublet due to the very small coupling constant with H-2 ($^3J_{1,2} = 1.1$ Hz), in agreement with L-*manno* configuration in a typical $^1C_4$ conformation. It is well known that for mannopyranoses/pyranosides (as well as other pyranose systems containing an axial substituent at 2-position) the coupling constant $^3J_{1,2}$ is not indicative of the anomeric configuration, because it is expected to be of the same order of magnitude for both α- and β-anomers [**46, 71, 76**]. Therefore, the α-anomeric configuration was assigned mainly taking into account the established thermodynamic control by the anomeric effect. Attribution of the remaining sugar ring signals was easily accomplished through inspection of both ^{1}H and ^{13}C NMR spectra, and supported by bidimentional correlation experiments (COSY, HMQC). The H-2 signal was observed in the ^{1}H NMR spectrum as a broad doublet of doublets, as a result of different coupling constants with H-1 and H-3 ($^3J_{2,3} =$

2.9 Hz), and with a chemical shift of $\delta = 5.25$ ppm. At lower field ($\delta = 5.30$ ppm) appeared the H-3 signal, also as a doublet of doublets but presenting a large, typical *trans*-diaxial coupling constant with H-4 ($^3J_{3,4} = 9.9$ Hz), which in turn could be observed as a triplet due to similar coupling with both H-3 and H-5 ($^3J_{4,5} = 9.9$ Hz) at $\delta = 5.13$ ppm. H-5 was found at $\delta =$ 3.94 ppm, as a doublet of quartets due to different coupling constants with H-4 and the three protons at 6-position ($^3J_{5,6} = 6.2$ Hz). Finally, the latter referred protons were observed as a doublet at considerably higher field ($\delta = 1.24$ ppm), which is characteristic for methyl groups. Regarding carbon signals, a chemical shift of $\delta = 90.6$ ppm was found for the anomeric carbon and all other sugar ring signals were observed at higher field in the ^{13}C NMR spectrum. Also important to note is the presence of four singlets in the ^{1}H NMR spectrum, with chemical shifts ranging from $\delta = 2.01$ ppm to $\delta = 2.17$ ppm and integrating three protons each, corresponding to the protons from the acetyl groups. Accordingly, their carbon signals could also be easily assigned in the ^{13}C NMR spectrum.

Selective anomeric deacetylation of **9** proceeded smoothly in the presence of hydrazine acetate, an established procedure **[72, 73, 75]** that afforded the desired hemiacetal **10** in high yield (95% from L-rhamnose) and purity after recrystallization. With respect to its structural characterization, it was mainly accomplished through inspection of the ^{1}H NMR spectrum, in which the H-1 signal of the major α-anomer could be observed, as expected, at higher field ($\delta = 5.17$ ppm) when compared to its percursor containing an electron withdrawing acetyl group at the anomeric position. The coupling constant $^3J_{1,2}$ could not be determined since both H-1 and H-2 resonances were observed as poorly resolved signals. Also key indicator of successful regioselective deacetylation was (i) the fact that only three acetyl groups could be detected and (ii) the presente of the signal of the anomeric hydroxy proton, which in the case of the α-anomer could be observed at $\delta = 3.20$ ppm, as a doublet due to coupling with the respective H-1 ($^3J_{1(\alpha),\mathrm{OH}}$ = 3.9 Hz). Only trace amounts (<10%) of the β-anomer could be detected by ^{1}H NMR in chloroform-*d*. Its anomeric proton appeared at higher field ($\delta = 4.95$ ppm) when compared to its α-stereoisomer, as a well-defined doublet due to the presence of a large coupling constant with the respective hydroxy group proton ($^3J_{1(\beta),\mathrm{OH}} = 9.4$ Hz), which in turn was visible at $\delta =$ 3.54 ppm, also as a doublet. The remaining ^{1}H NMR signals were found to be similar to those presented by **9**, as was also the case for the carbon signals observed in the ^{13}C NMR spectrum.

Treatment of **10** with trichloroacetonitrile and 1,8-diazabicyclo[5.4.0]undec-7-ene (DBU) **[71–75]** gave known peracetylrhamnopyranosyl trichloroacetimidate **6** **[72]** in 89% yield. The exclusive formation of the α-anomer (thermodynamic product) was expected in these conditions, due to the reversibility of the base-catalyzed addition of the anomeric hydroxy group to trichloroacetonitrile. In fact, it is established that when a strong base (i.e. DBU) is employed, trichloroacetimidation occurs faster than mutarotation and, as a result, thermodynamic control can be achieved. In contrast, the use of weak bases (i.e. K_2CO_3) often favours the formation of kinetically controlled products (β-anomers) **[37, 54, 71]**. The ^{1}H NMR spectrum presented a singlet at $\delta = 8.74$ ppm, without correlation in the COSY spectrum, corresponding to the imine proton. A deshielding in the chemical shift of the anomeric proton ($\delta = 6.20$ ppm) due

to the presence of a highly electon withdrawing group at this position could also be observed, as expected. Regarding ^{13}C NMR spectroscopic data, the most important signals were those corresponding to the two quaternary carbons of the aglycone, which could be observed at δ = 159.9 ppm (C=NH) and δ = 90.6 ppm (CCl_3). The remaining carbon and proton signals were in accordance with those of precursors **9** and **10**.

Glycosyl trichloroacetimidates have been widely used in the preparation of glycosides and complex oligosaccharides since their introduction by Schmidt and co-workers in 1980, as a result of their outstanding donor properties. First, as we have already seen, they can be easily prepared. They also present good stability and, most importantly, balanced reactivity. In fact, they strong glycosyl donors and, simultaneously, require mild activation conditions, most commonly Lewis acid catalysis (i.e trimethylsilyl triflate, TMSOTf), leading to good reaction yields and stereocontrol. Hence, the synthesis of dodecyl α-L-rhamnopyranoside **2** was accomplished through glycosylation of dodecanol, employing trichloroacetimidate **6** as glycosyl donor and in the presence of a catalytic amount of TMSOTf [**72**–**75**], followed by deacetylation using sodium methoxide in methanol, known as Zemplén procedure [**71**].

Initial attempts to purify peracetylated glycoside **11** directly from the glycosylation reaction mixture by column chromatography proved to be inefficient, as a result of two major drawbacks: (i) separation of **11** from unreacted dodecanol was remarkably difficult due to the very similar retention factors (R_f) presented by both compounds; and (ii) a considerable amount of deacetylated products (that is, a regioisomeric mixture of dodecyl glycosides bearing different positions deprotected) could be detected on the reaction mixture by thin layer chromatography (TLC) and also by NMR (in this case after isolation by column chromatography), indicating that the acetyl protecting groups were labile in these conditions. Nevertheless, a small amount of protected glycoside **11** (major product of the glycosylation reaction) could be isolated pure (see **Section 5.3** for further detail) and its structure was unambiguously confirmed. The anomeric proton was visible in the ^{1}H NMR spectrum as a doublet ($^3J_{1,2}$ = 1.7 Hz) at higher field (δ = 4.71 ppm) when compared to trichloroacetimidate **6**, a result of the electron donating character of the alkyl substituent. While the remaining sugar ring protons (and carbons) appeared to be rather similar to those displayed by their percursors, several characteristic signals from the dodecyl chain could be observed, in accordance with literature data [**1**–**3**]. Hence, the non-equivalent H-1'a and H-1'b protons were observed at δ = 3.66 ppm and δ = 3.42 ppm, respectively, both as typical doublets of triplets (dt) presenting a geminal coupling constant with each other ($^2J_{1'a,1'b}$ = 9.6 Hz) and a vicinal coupling constant with H-2'a and H-2'b (i.e. $^3J_{1'a,2'a} = {}^3J_{1'a,2'b}$ = 6.6 Hz). At higher field were found the signals due to H-2'a,b (δ = 1.54-1.62 ppm, multiplet) and H-3'a,b to H-11'a,b (δ = 1.24-1.37 ppm, multiplet), followed by the three protons of the 12'-methyl group (δ = 0.88 ppm) which was visible as a triplet ($^3J_{12',11'}$ = 6.8 Hz). Regarding the carbon signals of the dodecyl moiety, these were found in the ^{13}C NMR spectrum at δ = 68.3 ppm (C-1'), δ = 22.7-31.9 ppm (C-2' to C-11') and δ = 14.1 (C-12'). Importantly, the α-anomeric configuration could be confirmed due to the presence of key correlations in the NOESY spectrum, namely those of H-2'a,b with H-5 and H-2. The observed

α-stereoselectivity was already expected, since it should be promoted by neighbouring group participation (**Scheme 3.2**). The proposed mechanism follows the general pathway discussed in **Section 2.2**: activation of trichloroacetimidate **6** and concomitant departure of the anomeric leaving group leads to the formation of a glycosyl cation, which is in resonance with an oxycarbenium ion; intramolecular stabilization of this intermediate, assited by the acetyl group at 2-position, then leads to a bicyclic acyloxonium ion, which is attacked by the nucleophile (in this case dodecanol) in S_N2-fashion to afford only the 1,2-*trans*-linked α-glycoside **11**. Alternatively to this major route, nucleophic attack may take place on the intermediate oxycarbenium ion to afford **11** (thermodynamic product) as the major diastereomer, although the 1,2-*cis*-linked β-glycoside (kinetic product) could also arise from this pathway.

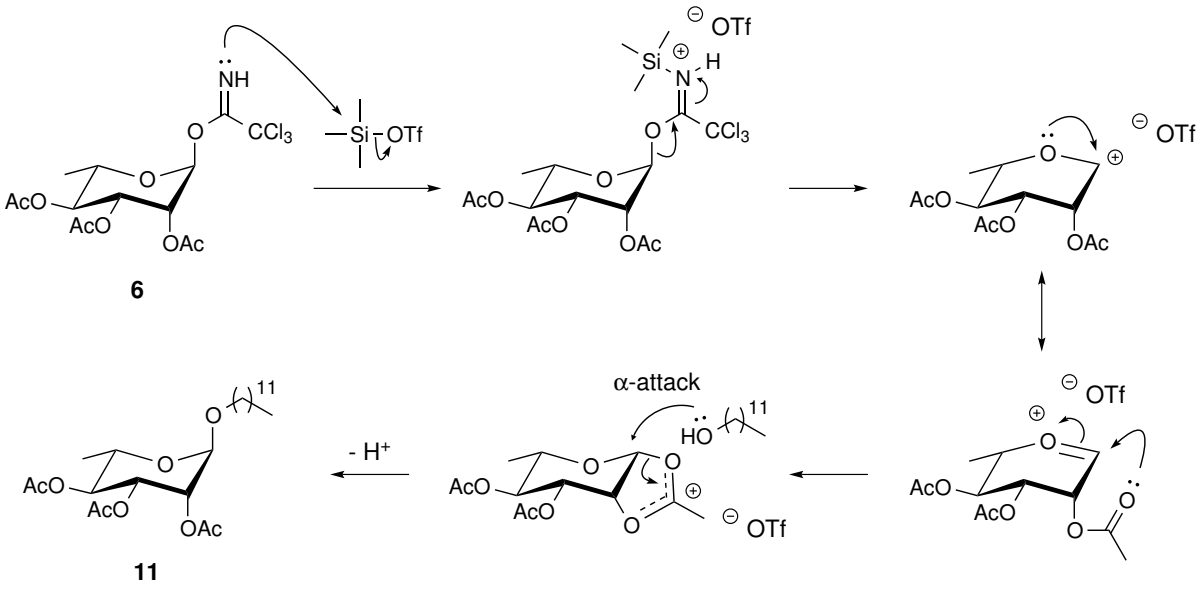

Scheme 3.2: Mechanism for the TMSOTf-catalysed activation of trichloroacetimidate **6** and subsequent formation of α-glycoside **11** through neighbouring group participation.

Taking into account the reaction stereocontrol and being aware that the previously referred methodological difficulties would probably lead to a decrease in the reaction yield (based on the amount of **11** isolated), we decided to perform glycosylation and subsequent deprotection in one-pot. Thus, the reaction mixture obtained from the glycosylation step was neutralized, concentrated and immediately subjected to deacetylation, a procedure that efficiently afforded target deprotected glycoside **2** in 71% overall yield (**Scheme 3.1**). Although in this case trace amounts (<7%) of its corresponding β-anomer could be detected by NMR (in some of the fractions collected from column chromatography), it could not be isolated pure and, consequently, was not characterized. NMR data of final compound **2** was in agreement with that of protected glycoside **11**, the most relevant differences being the significant shielding in the signals due to H-2 (δ = 5.23 ppm to δ = 3.81 ppm), H-3 (δ = 5.30 ppm to δ = 3.66 ppm) and H-4 (δ = 5.06 ppm to δ = 3.39 ppm) observed in the ^{1}H NMR spectrum, as well as the disappearance of the signals corresponding to the acetyl groups after deprotection, in both ^{1}H and ^{13}C NMR spectra.

3.1.2 Synthesis and conformational *in silico* study of dodecyl 2-deoxy-L-*threo*-pentopyranosides

The first task in the synthetic route towards dodecyl 2-deoxy-α-L-*threo*-pentopyranoside **3** was the preparation of the glycosyl donor, 3,4-di-*O*-acetyl-L-xylal **7**, which is not commercially available. Although several modern protocols have been developed over the years for the synthesis of glycals [**54, 63**], these are commonly obtained by variations of the traditional method based on elimination of peracetylated glycosyl halides in reductive media, since this is a straightforward and generally efficient procedure. Hence, preparation of **7** was easily carried out in 54% overall yield (**Scheme 3.3**), via peracetylation of L-xylose [**71**] followed by convertion of peracetyl xylopyranose **12** into bromide **13** by a conventional procedure [**77**] and subsequent Zinc-promoted reductive elimination involving the latter compound, as described elsewhere [**78**].

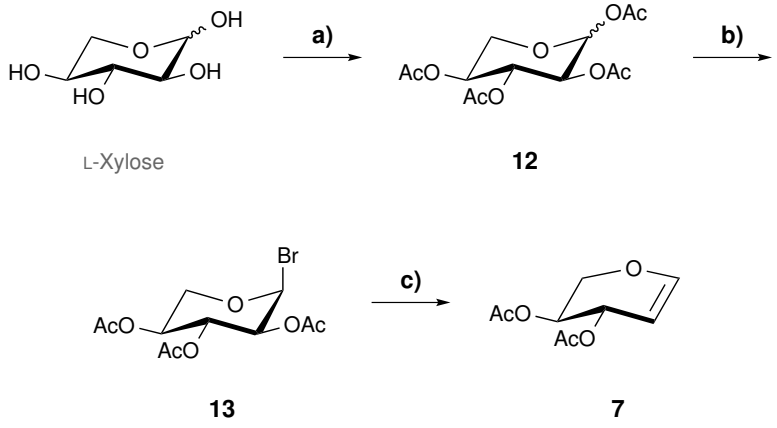

Scheme 3.3: Synthesis of 3,4-di-*O*-acetyl-L-xylal **7**. Reagents and conditions - a) Ac_2O, pyridine, DMAP, r.t., quantitative; b) HBr/AcOH 33 wt.%, Ac_2O, CH_2Cl_2, 0 °C→r.t., 93%; c) $NaH_2PO_4{\cdot}2H_2O$, Zn, acetone, H_2O, r.t., 58%.

Acetylation of L-xylose (as described in **Section 3.1.1** for L-rhamnose) gave peracetate **12** as a mixture of anomers (α/β = 1:0.15) in quantitative yield and sufficient purity to proceed to the next step. Structural characterization was mainly accomplished by NMR and, in the case of the β-anomer, matched literature data for its enantiomer [**77**]. The two diastereomers could be distinguised by differences is their respective anomeric signals. As expected, the equatorially-oriented H-1 of the α-anomer apperared in the ^{1}H NMR spectrum at lower field (δ = 6.26 ppm) when compared to the axial anomeric proton of the β-stereoisomer (δ = 5.72 ppm). Both signals could be observed as doublets, but while the α-anomer presented a small coupling constant ($^3J_{1(\alpha),2} \approx 4$ Hz) due to the *cis*-relative orientation of H-1 and H-2, a large coupling constant ($^3J_{1(\beta),2} \approx 7$ Hz) was found for the β-anomer, consistent with a *trans*-diaxial positioning in the latter case. Inspection of the remaining sugar ring proton resonances (with the exception of H-2 and H-4 of both diastereomers, which were collapsed whithin the same multiplet) allowed the unambiguous confirmation of the xylopyranosyl skeleton. In both cases,

H-3 (δ = 5.47 ppm for the α-anomer and 5.21 ppm for the β-anomer) was observed as a triplet due to the similar *trans*-diaxial coupling constants with H-2 and H-4 ($^3J_{3,2} \approx {}^3J_{3,4}$ = 9.8 Hz for the α anomer and 8.4 Hz for the β-anomer). The signals due to H-5a,e were visible as typical AB systems, with the equatorial protons resonating at lower field (δ = 3.94 ppm for the α-anomer and 4.15 ppm for the β-anomer) relatively to their axial counterparts (δ = 3.72 ppm for the α-anomer and 3.53 ppm for the β-anomer). Moreover, H-5e were invariably observed as doublets of doublets, as a result of their different geminal and vicinal coupling constants ($^2J_{5e,5a}$ = 11 Hz for the α-anomer and 12 Hz for the β-anomer, $^3J_{5e,4}$ = 5.8 Hz for the α-anomer and 4.9 Hz for the β-anomer). In turn, H-5a signals presented different multiplicity: a triplet was observed for the α-anomer, due to similar coupling with both H-5e and H-4 ($^2J_{5a,5e} \approx {}^3J_{5a,4}$ = 11 Hz), whilst in the case of the β-anomer a doublet of doublets was found, as a result of differences in these coupling constants ($^2J_{5a,5e}$ = 12 Hz, $^3J_{5a,4}$ = 8.4 Hz). With respect to the anomeric carbon signals, these were found in the ^{13}C NMR spectrum at δ = 82.3 ppm for the α-anomer and 92.0 ppm for the β-anomer, as expected, and at lower field when compared to the remaining sugar ring carbons. The acetyl groups were assigned in both ^{1}H and ^{13}C NMR spectra similarly to those of the rhamnopyranosyl derivative **9** (see **Section 3.1.1**).

The next step was the preparation of bromide **13**, which was accomplished in 94% yield by treatment of **12** with hydrobromic acid (33 wt.% in acetic acid) and a catalytic amount of acetic anhydride, in dichloromethane and under low temperature [**77**]. Althought requiring rather harsh conditions, this conventional procedure proved to be efficient since bromide **13** could be easily isolated in good purity after aqueous work-up and solvent evaporation. Product recrystallization, as reported in the literature for the D-stereoisomer [**77**], was attempted in small scale and found to be possible. However, we decided not to purify the residue following evaporation of the solvent because rapid decomposition was observed during air exposure. The recently reported protocol based on *in situ* generation of hydrobromic acid from acetyl bromide and methanol in acetic acid [**79**] was also preliminarily applied and gave yields of the same order of magnitude. Despite the milder reaction conditions, this methodology proved not to be advantageous since work-up (prolonged evaporation of acetic acid/hydrobromic acid under low pressure and room temperature) was extremely difficult to carry out. The α-anomer (thermodynamic product owing to the anomeric effect) was the only stereoisomer formed in this reaction, as confirmed by NMR data, which was similar to that reported literature for its enantiomer [**77**]. In fact, the H-1 signal could be observed in the ^{1}H NMR spectrum at δ = 6.59 ppm (lower field when compared to its percursor) as a doublet and with a small coupling constant with H-2 ($^3J_{1,2}$ = 3.9 Hz). The anomeric carbon was found in the ^{13}C NMR spectrum at δ = 87.6 ppm. The remaining carbon and proton signals were similar to those of acetate **12**, except for the fact that only three acetyl groups were detected. However, in this case the H-2 and H-4 signals could be clearly assigned in the ^{1}H NMR spectrum: the first was visible as a doublet of doublets due to different couplings with H-1 and H-3 ($^3J_{2,3}$ = 9.8 Hz) and the latter as a double double doublet (ddd), presenting different coupling constants with H-3 ($^3J_{4,3}$ = 9.8 Hz), H-5a ($^3J_{4,5a}$ = 11.2 Hz) and H-5e ($^3J_{4,5e}$ = 6.1 Hz). Glycal **7** was finally accessed by treatment of the previously

prepared peracetylxylopyranosyl bromide **13** with Zn-saturated sodium dihydrogen phosphate solution at room temperature. This protocol has been reported to offer several advantages over classical methods, such as usually higher reaction yields, the use of mild and environmentally friendly conditions and the fact that no aditional reagents (i.e. Cu(II) salts [**63**]) are required for the activation of zinc dust, since it has been shown to present high activity in phosphate buffer [**78**]. Although satisfactory, the moderate yield obtained (58%) could not reproduce the higher conversion efficiency (76%) reported in the literature for its known D-stereoisomer [**78**], a presumed result of the unexpected difficulties experienced when performing aqueous work-up of the reaction mixture. In agreement with ^{1}H NMR data for 3,4-di-*O*-acetyl-D-xylal [**78**], the anomeric proton was visible as a doublet ($^{3}J_{1,2} \approx 6$ Hz) at low field ($\delta = 6.61$ ppm), followed by the signals of H-2, H-3 and H-4 ($\delta = 4.95$-2.00 ppm, multiplet). The H-5a,b signals could be observed at $\delta = 4.20$ ppm (H-5a) and $\delta = 3.98$ ppm (H-5b) as apparent doublets, since only their geminal coupling constant ($^{2}J_{5a,5b} = 12.3$ Hz) could be observed in the spectrum. The typical double bond signals due to C-1 and C-2 could be clearly assigned in the ^{13}C NMR spectrum at $\delta = 148.0$ ppm and $\delta = 97.4$ ppm, respectively. Also key indicator of the success of the elimination reaction carried out was the presence of only two acetyl groups, as observed in both ^{1}H and ^{13}C NMR spectra.

As mentioned in **Chapter 2**, glycals are versatile structures that have been widely used as synthons for the preparation of biologically relvant 2-deoxyglycosides. We have reported the synthesis of antibiotic alkyl 2-deoxy/2,6-dideoxy-*arabino*-hexopyranosides, through reaction of fatty alcohols with commercially available glycals in the presence of TPHB [**1**–**3, 23**], a procedure that usually leads to high selectivity for the α-anomers, which present greater bioactivity. The mechanism of this reaction should be briefly discussed at this stage, since it does not follow the general pathway introduced in **Section 2.2**. Instead, it proceeds a via polar addition to the cyclic enol ether (**Scheme 3.4**, route a), which is commonly regiospecific because the introduction of the electrophile (H^{+}) at 2-position is directed by the endocyclic oxygen [**63**]. As a consequence, a resonance-stabilized glycosyl cation is produced, which is subsequently attacked by the nucleophile (i.e. alcohol) to deliver anomeric mixtures of saturated 2-deoxyglycosides. Although stereoselectivity at the anomeric position is dependent on the reaction conditions and the specific glycal/acceptor system [**23**], the α-stereoisomers are expected to predominate owing to the anomeric effect, as has been shown for several reactions performed in the presence of TPHB or other protonic acids [**23, 63**]. A drawback of these acid-catalyzed addition reactions is the fact that glycals may undergo concurrent reactions, namely those leading to rearrangement products. As exemplified in **Scheme 3.4** (route b), elimination of the allylic substituent at 3-position results in the formation of a delocalized cation, named allyloxycarbenium ion. From the nucleophilic attack on this reactive intermediate may arise, for instance 2,3-unsaturated glycosides. Allylically-rearranged glycosides of this type, however, are usually produced through Lewis acid activation of acetylated glycals [**63**] and their formation is in general avoided by the use of glycals bearing alkyl substituents at 3-position, which have been described to undergo Ferrier rearrangement only under harsh acidic conditions (i.e. zeolites [**23**]).

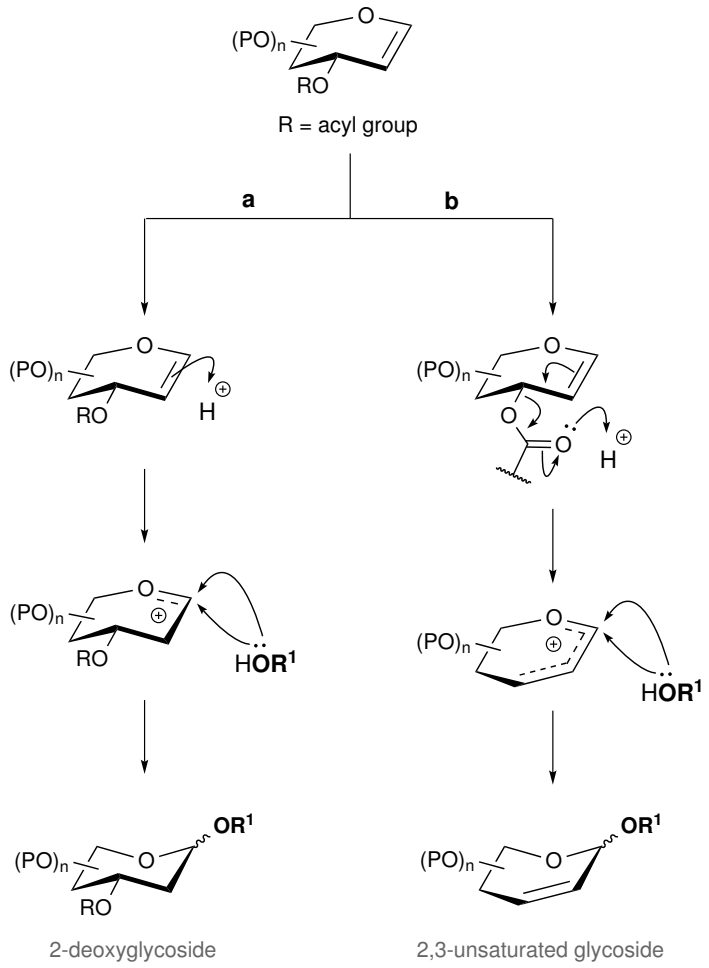

Scheme 3.4: General mechanisms for the acid-catalyzed convertion of glycals into 2-deoxyglycosides and 2,3-unsaturated glycosides. P = generic protecting group, R^1 = generic aglycone residue.

To our experience, however, rearrangement products are only isolated in very low yield ($\leq$ 10%) in TPHB-mediated reactions of alcohols with acetylated glycals [**1, 2, 23**]. Hence, we decided to employ the same procedure in the reaction of pentopyranose-derived peracetylated glycal **7** with dodecanol, which was conducted following the previously optimized conditions [**2**]. Surprisingly, a complex mixture of 2-deoxyglycosides **14-15** (total 33%) and 2,3-unsaturated glycosides **16-17** (total 27%) was obtained (**Scheme 3.5**), in a ratio of 1:0.82 (based on isolated yields). A decrease on the anomeric stereoselectivity was also evident, with α/β ratios of 1:0.44 for 2-deoxyglycosides **14-15** and 1:0.35 for 2,3-unsaturated glycosides **16-17**. In fact, although it has been reported that Ferrier rearrangement of hex-1-enitols leads to the exclusive formation of α-anomers [**1, 2, 23**], a significant amount (7%) of the β-configurated 2,3-unsaturated glycoside **17** was obtained in this case. We may only rationalize these overall results in light of the particularly different reactivity of pent-1-enitol **7** under these conditions, which should be further investigated.

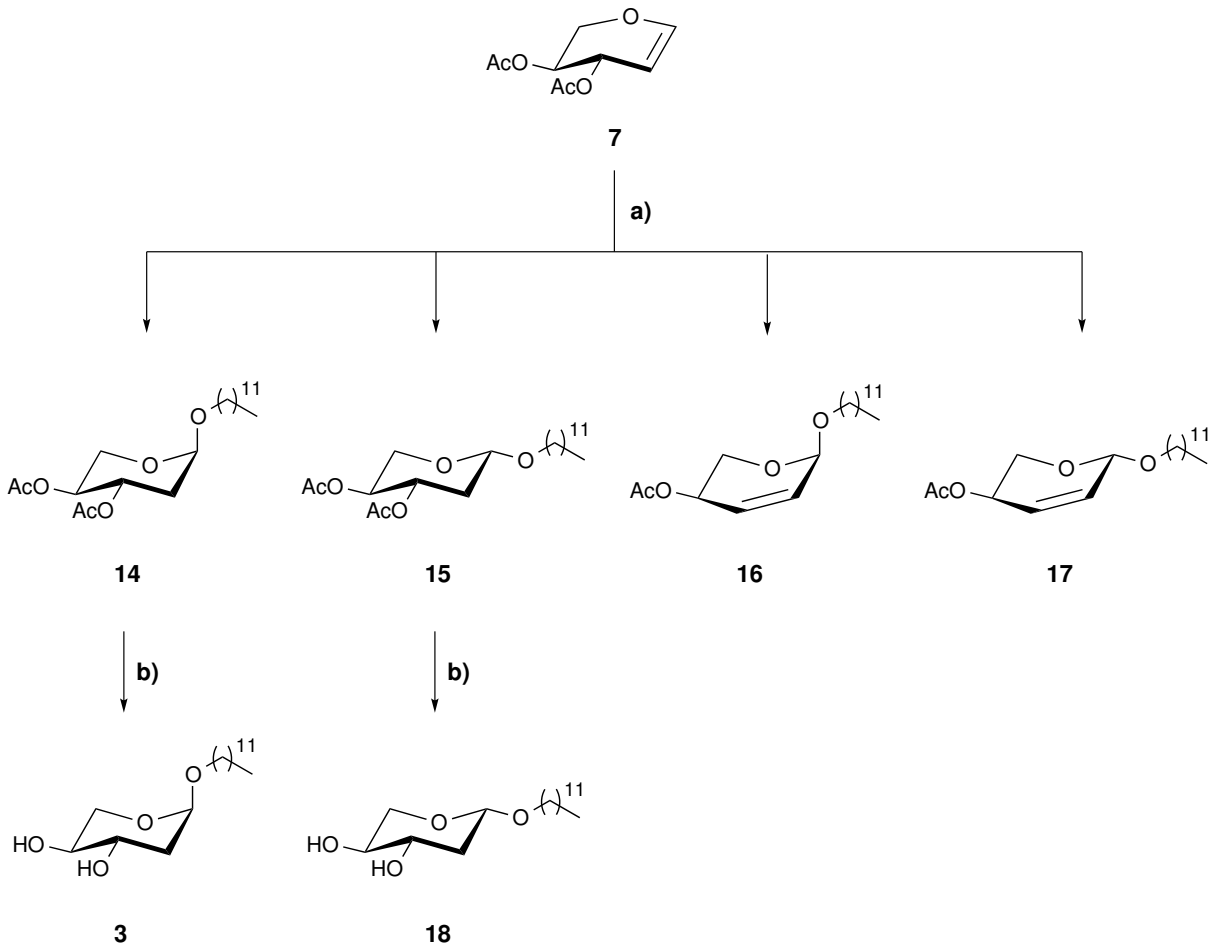

Scheme 3.5: Synthesis of dodecyl 2-deoxy-L-*threo*-pentopyranosides **3** and **18**. Reagents and conditions - a) dodecanol, $PPh_3 \cdot HBr$, CH_2Cl_2, r.t., 23% for **14**, 10% for **15**, 20% for **16**, 7% for **17**; b) NaOMe, MeOH, r.t., 64% for **3** and 99% for **18**.

Nevertheless, the four products **14-17** could be isolated pure (despite worth noting difficulties regarding the separation of **15** from unreacted dodecanol) for characterization purposes and the 2-deoxy pentopyranosyl glycosides **14** and **15** were subjected to deprotection as described previously, affording target α-glycoside **3** and β-glycoside **18**, respectively, which were both evaluated for their potential antimicrobial activity (see **Section 3.2**).

Dodecyl 3,4-di-*O*-acetyl-2-deoxy-α-L-*threo*-pentopyranoside **14** was the major product of the glycosylation reaction and could be isolated in 23% yield. The H-3 and H-4 resonances were observed at higher field (δ = 5.27 ppm and δ = 4.86 ppm, respectively) than the remaining signals in the ^{1}H NMR spectrum, due to their functionalization with electron withdrawing acetyl groups. Both presented a ddd pattern (apparent triplet of doublets) as a result of the different coupling constants with each other ($^3J_{3,4}$ = 8.5 Hz) and with the H-2a,e ($^3J_{3,2a}$ = 10.1 Hz, $^3J_{3,2e}$ = 4.8 Hz) or H-5a,e ($^3J_{4,5a}$ = 9.2 Hz, $^3J_{4,5e}$ = 5.0 Hz) methylene protons, respectively. The anomeric proton was visible at δ = 4.82 ppm as an apparent broad triplet, due to the very similar coupling constants with H-2a ($^3J_{1,2a}$ = 3.2 Hz) and H-2e ($^3J_{1,2e}$ = 2.8 Hz), which in fact

could be distinguised. H-5e was visible at $\delta = 3.77$ ppm as a doublet of doublets due to different geminal ($^2J_{5e,5a} = 11.1$ Hz) and vicinal coupling constants, followed by the signals due to H-5a and H-1'a (δ = 3.62-3.69 ppm, multiplet). H-1'b, in turn, could be observed as a typical dt ($^2J_{1'b,1'a} = 9.3$ Hz, $^3J_{1'b,2'a} = {}^3J_{1'b,2'b} = 6.7$ Hz) at $\delta = 3.35$ ppm. More importantly, the signals of non-equivalent H-2e (broad ddd) and H-2a (broad ddd) were found at high field (δ = 2.18 ppm and $\delta = 1.76$ ppm, respectively), presenting a large geminal coupling constant ($^2J_{2e,2a} = 13$ Hz) and different vicinal couplings with H-1 and H-3 (see above). The protons corresponding to the two acetyl groups were clearly observed as singlets at δ = 2.04-2.05 ppm and the remaining signals from the alkyl chain were assigned in similarly to those of other dodecyl glycosides (i.e. compound **11** and refs. [**1**–**3, 23**]). In the ^{13}C NMR spectrum, the anomeric carbon was found at $\delta = 97.0$ ppm and the remaining carbons could be assigned accordingly.

Although data obtained for the β-anomer **15** (isolated in 10% yield) was very similar to that of compound **14**, key differences allowed the unambiguous assignment of its opposite stereochemistry at the anomeric position. H-1 resonance was found at higher field ($\delta = 4.62$ ppm), as expected, and as a broad doublet of doublets presenting a large coupling constant with H-2a ($^3J_{1,2a} = 6.3$ Hz) and a smaller coupling with H-2e ($^3J_{1,2e} = 2.7$ Hz). In agreement, the resonance of the anomeric carbon was slightly deshielded ($\delta = 98.2$ ppm) with respect to the correspondent signal of its stereoisomer **14**.

The 2,3-unsaturated α-glycoside **16** was obtained in 20% yield and identified by careful comparison with literature data for Ferrier products derived from hex-1-enitols [**1, 2, 23**]. The olefinic H-2 and H-3 signals were found in the ^{1}H NMR spectrum at low field (δ = 6.04-6.07 ppm, multiplet), followed by the anomeric proton ($\delta = 4.99$ ppm) which was observed as a singlet, in agreement with its supposed *quasi*-equatorial orientation [**1, 2, 23**]. H-4 was detected as a broadened signal at $\delta = 4.95$ ppm and the resonance of the two protons at 5-position were visible at $\delta = 4.17$ ppm and $\delta = 3.83$ ppm, as a doublet of doublets ($^2J_{5a,5b} = 13.0$ Hz, $^3J_{5a,4} = 2.0$ Hz) and as a doublet, respectively, because the vicinal coupling constant with H-4 could only be observed for one of these protons. A singlet corresponding to the acetyl group at 4-position could be observed at $\delta = 2.10$ ppm, and the usual dodecyl chain resonances were visible as well. The C-2 and C-3 resonances appeared in the ^{13}C NMR spectrum at $\delta = 131.1$ ppm and $\delta = 124.9$ ppm (assigned as permutable signals since their ressonances were collapsed in the ^{1}H NMR spectrum and thus could not be distinguised by HMQC), and the anomeric carbon was found at $\delta = 93.0$ ppm.

Regarding the β-configurated Ferrier product **17**, the corresponding H-2 and H-3 resonances were also observed at lower field than the remaining signals in the ^{1}H NMR spectrum, but in this case they could be distinguished at chemical shifts of $\delta = 5.87$ ppm and $\delta = 5.94$ ppm, respectively, and both as doublets due to vicinal coupling with each other ($^3J_{2,3} = 10.3$ Hz). H-1 was observed again as a singlet, at $\delta = 4.93$ ppm. The signals due to C-2 and C-3 were clearly assigned in the ^{3}C NMR spectrum at $\delta = 129.4$ ppm and $\delta = 128.7$ ppm, respectively, and the anomeric carbon was found at a chemical shift of $\delta = 94.3$ ppm.

The final step was deprotection of the acetyl groups from 2-deoxyglycosides **14** and **15** which afforded, respectively, target compound **3** in 64% yield and its β-steroisomer **18** in nearly quantitative yield (**Scheme 3.5**).

Structural characterization of the α-glycoside **3** was unambiguous. As expected, no significant differences were observed with respect to the anomeric proton and carbon resonances, which were found at chemical shifts of $\delta = 4.84$ ppm and $\delta = 97.6$ ppm, respectively. However, in this case H-1 was observed as a broad double doublet presenting different coupling constants with the two methylene protons at 2-position ($^3J_{1,2a} = 3.3$ Hz, $^3J_{1,2e} = 1.7$ Hz). These coupling constants could be confirmed through inspection of the H-2e and H-2a resonances which were found at $\delta = 2.11$ ppm and $\delta = 1.64$ ppm, respectively, and displayed similar multiplicity to that of the acetylated percursor **14** (br ddd), as well as coupling constants of the same order of magnitude ($^2J_{2e,2a} = 12.8$ Hz, $^3J_{2e,3} = 4.1$ Hz, $^3J_{2a,3} = 10.9$ Hz). In contrast, the resonance corresponding to H-3 appeared as a poorly resolved, broadened signal (therefore assigned as a multiplet) and with a low chemical shift ($\delta = 3.88$-3.96 ppm) when compared with its funtionalized percursor. Accordingly, the signal due to H-4 was also observed at higher field ($\delta = 3.46$-3.59 ppm, within a multiplet with H-5a). Also relevant is the fact that the acetyl groups could no longer be detected in both ^{1}H and ^{13}C NMR spectra. Instead, two broad singlets due to the hydroxy protons at 3- and 4-positions were clearly observed at $\delta = 2.51$ ppm and $\delta = 1.72$ ppm.

Assignment of the resonances obtained for the β-anomer **18** was not as straightforward. In fact, the anomeric proton and carbon signals were found at chemical shifts of $\delta = 4.80$ ppm and $\delta = 98.1$ ppm, respectively, which are surprisingly similar to those obtained for its α-steroisomer (see above). Moreover, the H-1 resonance was observed as a broad triplet, indicating a low coupling with both H-2e and H-2a ($^3J_{1,2e} \approx {}^3J_{1,2a} = 3.5$ Hz), which in turn were both found as broad double triplets ($\delta = 2.21$ ppm and $\delta = 1.78$ ppm, assigned as permutable signals) as a result of their large geminal coupling constant ($^2J_{2e,2a} = 14.2$ Hz) and small vicinal coupling constants with both H-1 and H-3 ($^3J_{2e,3} \approx {}^3J_{2a,3} = 3.5$ Hz). It is also relevant to note that none of the typically large, *trans*-diaxial coupling constants (i.e. $^3J_{2a,3}$) could be detected, even taking into consideration the poorly resolved ^{1}H NMR spectrum obtained in deuterated chloroform. Altogether, these resuls were clearly not in agreement with the expected equatorial orientation of the anomeric substituent and, consequently, with the supposed $^1C_4$ conformation for β-glycoside **18**. Instead, they suggested that an unusual $^4C_1$ conformation, featuring all substituents of the pentopyranosyl ring in axial disposition (**Figure 3.1**), might be assumed by this compound in chloroform. Although presumed to be energetically unfavored, such eventual conformational preference would explain the NMR data so far obtained, namely: (i) the similarity between the chemical shifts observed for the anomeric protons and carbons of both diastereomers (since an axial orientation of the anomeric substituent would be featured by both, in that case); (ii) the small vicinal coupling constants of H-2e,a with H-1 found for both α- an β-anomers; and (iii) the absence of other expected *trans*-diaxial vicinal coupling constants ($^3J_{Ha,Ha}$) in the case of the β-anomer.

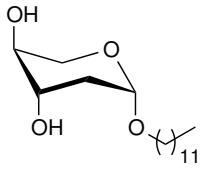

18

Figure 3.1: Proposed chair conformation for dodecyl 2-deoxy-β-L-*threo*-pentopyranoside **18** based on NMR data obtained in chloroform-*d*.

Being aware of the known influence of solvent effects on the conformational preferences of carbohydrates and their derivatives **[36, 47, 49, 50, 80]**, we decided to acquire NMR spectra for the two stereoisomers in methanol-d_4, anticipating an eventually different conformational behaviour in the more polar, protic solvent. For comparison purposes, data obtained in both chloroform-*d* (discussed above) and methanol-d_4 are given together in **Tables 3.1-3.4**.

^{1}H NMR data obtained for the α-anomer **3** in chloroform-*d* and methanol-d_4 were rather similar (**Table 3.1**), the most significant difference probably being the fact that the acidic hydroxy protons were not observed in the protic solvent, as expected. Nevertheless, the information obtained from the two experiments was to some extent complementary once distinct signals could be fully assigned in each spectrum, due to differences in chemical shifts and resolution.

In the case of the β-anomer **18**, in turn, relevant differences in ^{1}H NMR data were identified in the two solvents (**Table 3.2**). In methanol-d_4, the anomeric proton was visible at δ = 4.53 ppm, which is a considerably lower chemical shift when compared to that obtained for its α-stereoisomer in the same solvent environment (δ = 4.80 ppm, **Table 3.1**). Moreover, the resonance due to H-1 was visible as a double doublet and different coupling constants with H-2e,a could be clearly distinguished: while a small coupling was observed between H-1 and H-2e ($^3J_{1,2e}$ = 1.7 Hz), a large coupling of H-1 with H-2a ($^3J_{1,2a}$ = 8.4 Hz) was found, indicating an axial disposition for the proton at the anomeric position. The signals due to H-2e and H-2a were observed at δ = 2.11 ppm (ddd) and δ = 1.48 ppm (ddd), respectively, displaying a typical geminal coupling constant ($^2J_{2e,2a}$ = 12.8 Hz) and, in the latter case, a *trans*-diaxial vicinal coupling constant with H-3 ($^3J_{2a,3}$ = 10.2 Hz) was presented, a result that allowed confirmation of the equatorial orientation for the substituent at 3-position. From the observation of key coupling constants in the H-3, H-4 and H-5e,a resonances (i.e. $^3J_{3,4}$ = 8.1 Hz, $^3J_{4,5a}$ = 9.0 Hz), an equatorial disposition for the hydroxy group at 4-position could also be assigned. It is relevant to mention that, in agreement, correlations of H-1 with H-3 and H-5a could be clearly observed in the NOESY spectrum. ^{13}C NMR chemical shifts obtained for the anomeric carbons of both diastereomers are provided in **Tables 3.3** and **3.4**. In methanol-d_4, C-1 was found at 99.0 ppm for the α-anomer and at 101.5 ppm for the β-anomer. In contrast to the very similar values determined in chloroform-*d* ($\Delta\delta$ = 0.5 ppm), this much more significant difference ($\Delta\delta$ = 2.5 ppm) in methanol-d_4 also supports an equatorial orientation for the alcoxy substituent at the anomeric position, in the case of the β-stereoisomer.

Table 3.1: ^{1}H NMR data for dodecyl 2-deoxy-α-L-*threo*-pentopyranoside **(3)**.

	^{1}**H NMR** δ/ ppm [a]	
Position	**chloroform-*d***	**methanol-d_4**
1	4.84 (br dd) ($^{3}J_{1,2a}$ = 3.3, $^{3}J_{1,2e}$ = 1.7)	4.80 (br dd) ($^{3}J_{1,2a}$ = 3.5, $^{3}J_{1,2e}$ = 1.7)
2e	2.11 (br ddd) ($^{2}J_{2e,2a}$ = 12.8, $^{3}J_{2e,3}$ = 4.1, $^{3}J_{2e,1}$ = 1.7)	2.02 (ddd) ($^{2}J_{2e,2a}$ = 12.9, $^{3}J_{2e,3}$ = 4.9, $^{3}J_{2e,1}$ = 1.7)
2a	1.64 (br ddd) ($^{2}J_{2a,2e}$ = 12.8, $^{3}J_{2a,3}$ = 10.9, $^{3}J_{2a,1}$ = 3.3)	1.52-1.62 (m) [d]
3	3.88-3.96 (m) [b]	3.76 (br ddd) ($^{3}J_{3,2a}$ = 10.8, $^{3}J_{3,4}$ = 8.1, $^{3}J_{3,2e}$ = 4.9)
4	3.46-3.59 (m) [c]	3.32-3.42 (m) [e]
5e	3.69 (dd) ($^{2}J_{5e,5a}$ = 9.9, $^{3}J_{5e,4}$ = 4.1)	3.59 (dd) ($^{2}J_{5e,5a}$ = 10.1, $^{3}J_{5e,4}$ = 4.5)
5a	3.46-3.59 (m) [c]	3.44 (t) ($^{2}J_{5a,5e}$ = $^{3}J_{5a,4}$ = 10.1)
1'a	3.63 (dt) ($^{2}J_{1'a,1'b}$ = 9.3, $^{3}J_{1'a,2'a}$ = $^{3}J_{1'a,2'b}$ = 6.8)	3.63 (dt) ($^{2}J_{1'a,1'b}$ = 9.3, $^{3}J_{1'a,2'a}$ = $^{3}J_{1'a,2'b}$ = 6.7)
1'b	3.34 (dt) ($^{2}J_{1'b,1'a}$ = 9.3, $^{3}J_{1'b,2'a}$ = $^{3}J_{1'b,2'b}$ = 6.8)	3.32-3.42 (m) [e]
2'	1.52-1.60 (m)	1.52-1.62 (m) [d]
3'-11'	1.21-1.38 (m)	1.24-1.41 (m)
12'	0.88 (t) ($^{3}J_{12',11'}$ = 6.7)	0.90 (t) ($^{3}J_{12',11'}$ = 6.7)
OH	2.51 (br s)	-
OH	1.72 (br s)	-

[a] In parenthesis are the multiplicity and coupling constant(s) (J/ Hz) for each resonance.
[b] Multiplicity could not be extracted since a complex, broadened signal was observed.
[c] H-4 and H-5a were observed within the same multiplet.
[d] H-2a and H-2'a,b were observed within the same multiplet.
[e] H-4 and H-1'b were observed within the same multiplet.

Table 3.2: ^{1}H NMR data for dodecyl 2-deoxy-β-L-*threo*-pentopyranoside **(18)**.

	^{1}**H NMR** δ/ ppm [a]	
Position	**chloroform-*d***	**methanol-d_4**
1	4.80 (br t) ($^3J_{1,2a} = {}^3J_{1,2e} = 3.5$)	4.53 (dd) ($^3J_{1,2a} = 8.4$, $^3J_{1,2e} = 1.9$)
2e	2.21 (br dt) [b] ($^2J_{2e,2a} = 14.2$, $^3J_{2e,1} = {}^3J_{2e,3} = 3.5$)	2.11 (ddd) ($^2J_{2e,2a} = 12.8$, $^3J_{2e,3} = 4.8$, $^3J_{2e,1} = 1.9$)
2a	1.78 (br dt) [b] ($^2J_{2a,2e} = 14.2$, $^3J_{2a,1} = {}^3J_{2a,3} = 3.5$)	1.48 (ddd) ($^2J_{2a,2e} = 12.8$, $^3J_{2a,3} = 10.2$, $^3J_{2a,1} = 8.4$)
3	3.72-3.80 (m) [c]	3.52 (ddd) ($^3J_{3,2a} = 10.2$, $^3J_{3,4} = 8.1$, $^3J_{2e,3} = 4.8$)
4	3.63-3.68 (m) [d]	3.38 (ddd) ($^3J_{4,5a} = 9.0$, $^3J_{4,3} = 8.1$, $^3J_{4,5e} = 4.7$)
5e	4.15 (br dd) [e] ($^2J_{5e,5a} = 12.5$, $^3J_{5e,4} = 1.7$)	3.90 (dd) ($^2J_{5e,5a} = 11.5$, $^3J_{5e,4} = 4.7$)
5a	3.36-3.50 (m) [e,f]	3.17 (dd) ($^2J_{5a,5e} = 11.5$, $^3J_{5a,4} = 9.0$)
1'a	3.72-3.80 (m) [c]	3.78 (dt) ($^2J_{1'a,1'b} = 9.4$, $^3J_{1'a,2'a} = {}^3J_{1'a,2'b} = 6.7$)
1'b	3.36-3.50 (m) [f]	3.44 (dt) ($^2J_{1'b,1'a} = 9.4$, $^3J_{1'b,2'a} = {}^3J_{1'b,2'b} = 6.7$)
2'	1.56-1.63 (m)	1.53-1.60 (m)
3'-11'	1.22-1.37 (m)	1.25-1.37 (m)
12'	0.88 (t) ($^3J_{12',11'} = 6.7$)	0.90 (t) ($^3J_{12',11'} = 6.7$)
3-OH	3.36-3.50 (m) [f]	-
4-OH	2.03-2.11 (m) [g]	-

[a] In parenthesis are the multiplicity and coupling constant(s) (J/ Hz) for each resonance.
[b] H-2e,a were assigned as permutable signals.
[c] H-3 and H-1'a were observed within the same multiplet.
[d] Multiplicity could not be extracted since a complex, broadened signal was observed.
[e] H-5e,a were assigned as permutable signals.
[f] H-5a/H-5e, OH-3 and H-1'b were observed within the same multiplet.
[g] A complex multiplet was observed.

Table 3.3: ^{13}C NMR data for dodecyl 2-deoxy-α-L-*threo*-pentopyranoside **(3)**.

	^{13}C NMR δ/ ppm	
Position	**chloroform-*d***	**methanol-d_4**
1	97.6	99.0
2	37.3	38.5
3	69.6	69.9
4	72.1	72.5
5	62.1	63.6
1'	67.6	68.4
2'-11'	22.7-31.9	23.7-34.1
12'	14.1	14.4

Table 3.4: ^{13}C NMR data for dodecyl 2-deoxy-β-L-*threo*-pentopyranoside **(18)**.

	^{13}C NMR δ/ ppm	
Position	**chloroform-*d***	**methanol-d_4**
1	98.1	101.5
2	32.3	38.8
3	67.9	71.7
4	69.1	72.1
5	60.8	66.1
1'	68.6	70.1
2'-11'	22.7-31.9	23.8-33.1
12'	14.1	14.5

The above-discussed experimental results provide strong evidence that the solvent environment is able to modulate the conformer populations of β-glycoside **18** in solution. However, solvent effects seem not to be relevant in the case of the α-anomer **3**. Indeed, as depicted in **Scheme 3.6a**, no different conformational behaviour could be detected for the α-stereoisomer **3** in chloroform-d and methanol-d_4, since only the supposed $^1C_4$ conformation could be observed. In contrast, with respect to the β-stereoisomer **18**, whereas in methanol-d_4 the expected $^1C_4$ conformation could be clearly assigned by means of NMR, an atypical $^4C_1$ conformer seems to be assumed in chloroform-d (**Scheme 3.6b**). This is a rather unusual result since most pyranose sugars (and their derivatives, i.e. pyranoid glycosides) belonging to the L-series are known to commonly assume $^1C_4$ conformations.

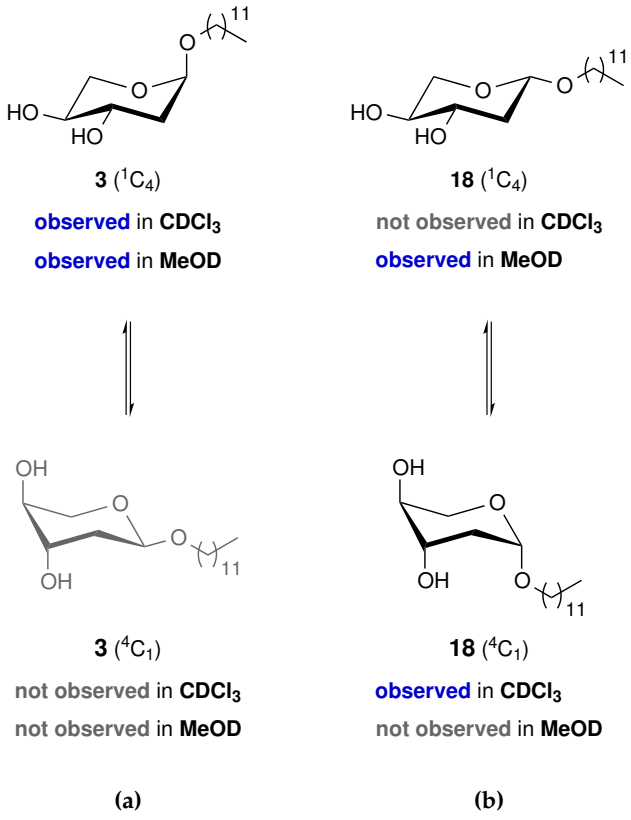

Scheme 3.6: Representation of the chair conformations observed by NMR in chloroform-d and methanol-d_4 for **(a)** dodecyl 2-deoxy-α-L-*threo*-pentopyranoside **3** and **(b)** dodecyl 2-deoxy-β-L-*threo*-pentopyranoside **18**.

With the intent to further analyze the proposed conformational preferences, theoretical calculations were performed at the density functional theory (DFT) [**81**] level. Hence, the structures of the two possible chair conformations of α- (**3**) and β- (**18**) glycosides were geometrically optimized in both chloroform and methanol by using an implicit solvation model in the calculations (see **Section 5.5** for detailed methods). The computed free energy differences [**82**] between each conformer ($\Delta G\ ^4C_1 \rightarrow\ ^1C_4$) are provided in **Table 3.5**.

Table 3.5: DFT-calculated free energy differences between the chair conformations of dodecyl 2-deoxy-α-L-*threo*-pentopyranoside **(3)** and dodecyl 2-deoxy-β-L-*threo*-pentopyranoside **(18)** using an implicit solvent model.

	$\Delta G\ ^{4}C_1 \rightarrow\ ^{1}C_4$/ kcal mol^{-1}	
Solvent	**α-anomer (3)**	**β-anomer (18)**
chloroform	-4.2	1.0
methanol	-3.2	0.2

In agreement with experimental observations, the considerable free energy differences obtained for the α-glycoside **3** (-4.2 and -3.2 kcal mol^{-1} in chloroform and methanol, respectively) suggest a clear preference for the $^1C_4$ conformer in solution, regardless of the solvent environment (see **Scheme 3.6a**). This is not a surprising result owing to both electronic and steric considerations: in fact, the axial orientation of the alcoxy substituent at the anomeric center is expected to be stabilized by the anomeric effect and, on the other hand, steric factors should promote an equatorial arrangement for the bulky hydroxy groups at 3- and 4-positions.

Distinct energetic preferences were evident with regard to the β-anomer **18**. In opposition to the free energy difference of -4.2 kcal mol^{-1} obtained for the α-anomer **3** in chloroform, a difference of 1.0 kcal mol^{-1} was found between the two optimized geometries of the β-anomer **18**, pinpointing a positive energy difference and, consequently, higher stability for the $^4C_1$ form in the same solvent (see **Scheme 3.6b**). Accounting for the unfavourable non-bonding steric interactions between 1,3-*cis*-arranged axial groups in the pentopyranosyl ring (that is, those involving oxygen atoms from the hydroxy groups and axially-oriented protons from the sugar ring), this thermodynamic preference for the $^4C_1$ conformer may be explained by a prevalence of the anomeric effect (over the aforementioned destabilizing steric factors), which is probably exacerbated in the less polar media. In fact, it has been widely recognized that chair conformations displaying a large number of substituents in axial orientation may be significantly stabilized owing to the influence of the anomeric effect, most commonly in non-polar solvents, as has been shown for several pyranose/pyranoside systems [**36, 47, 49, 50, 80**]. On the other hand, it should also be stressed that other particular structural features of 2-deoxy-*threo*-pentopyranoside **18** may contribute to the greater stability of the $^4C_1$ conformation. First, because the two vicinal hydroxy groups are *trans*-diaxially-arranged, no relevant repulsive interaction is thought to arise between them (i.e. unfavorable electrostatic interaction involving the two carbon-oxygen dipoles). Moreover, the destabilizing steric effects that would be exerted by further hydroxy and hydroxymethyl groups at 2- and 5-positions, respectively, are also not accounted in this case [**38, 80**].

In addition to the stereoelectronic influences already discussed and considering the particular structural flexibility of **18** (promoted by the methylene groups at 2- and 5-positions), a plausible driving force towards the lower energy calculated for the $^4C_1$ conformer in chloroform is a weak hydrogen bond involving the 3-hydroxy group and the exocyclic oxygen atom (2.8 Å). Notwithstanding the distortion in the O−H$\cdots$O bond angle ($\approx$ 143 °) presented by the geometrically optimized structure (**Figure 3.2**), the stabilizing effect of this intramolecular interaction may account for the unusual conformational behaviour of β-glycoside **18** in the weakly hydrogen bonding solvent.

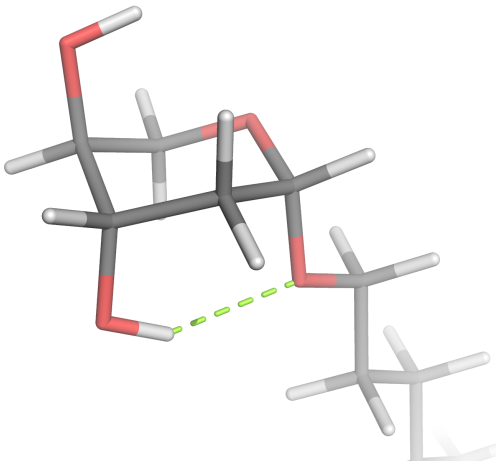

Figure 3.2: Structure of the $^4C_1$ conformer of dodecyl 2-deoxy-β-L-*threo*-pentopyranoside **18** obtained from DFT calculations in chloroform. The observed intramolecular hydrogen bond is depicted in green dashes. Image was rendered using PyMOL [**83**].

With respect to the calculations performed for **18** in methanol, a very neglectible free energy difference of 0.2 kcal mol^{-1} between the two conformations was obtained, even though experimental data provides unambiguous evidence that only the $^1C_4$ conformer is populated in the protic solvent. A replacement of the previously referred intramolecular hydrogen bond by intermolecular interactions with the solvent (and concomitant stabilization of the "all-equatorial" $^1C_4$ conformer) could be anticipated, owing to the strong hydrogen bonding abitily featured by methanol and the decreased influence of the anomeric effect in the more polar media. Thus, the calculated energy difference probably accounts for an overestimation of the intramolecular hydrogen bond, in this case. This result may be rationalized in terms of a poor description of solvation effects by the implicit model, in which the solvent is represented as a continuum dielectric medium [**84**].

3.1.3 Synthesis of dodecyl 2,6-dideoxy-2-fluoroglycosides

For the synthesis of deoxyfluoroglycosides **4** and **5**, 1-chloromethyl-4-fluorodiazoniabicyclo[2.2.2]-octane bis(tetrafluoroborate) (Selectfluor) was employed as fluorinating agent and the commercially available 3,4-di-*O*-acetyl-6-deoxy-L-glucal **8** was directly engaged as the glycosyl donor in the glycosylation reaction. Selectfluor is a versatile reagent with vast application in electrophilic fluorination reactions and many other transformations leading to bioactive molecular entities of therapeutic relevance. Incorporation of fluorine into organic compounds can be efficiently achieved under mild conditions due to the exceptional properties exhibited by this reagent, namely its good stability, high reactivity and safety. In fact, the development of selectfluor represented a major improvement in electrophilic fluorination, which traditionally required the use of extremely toxic reagents (i.e. molecular fluorine). **[66]**

The usefulness of this reagent in synthetic carbohydrate chemistry was first reported by Wong and co-workers **[67]**, who demostrated that selectfluor reacts regioselectively with glycals in the presence of nucleophiles to afford 2-deoxy-2-fluorosugars and glycosides in high yields. This one-pot procedure circumvents the inefficiency of previous methodologies based on time-consuming protecting group manipulations followed by selective nucleophilic fluorination at 2-position and subsequent activation of the 2-deoxy-2-fluoro sugar derivatives, which often present poor reactivity because of the inductive effect exerted by the 2-fluoro group **[67, 69]**. Selectfluor can also be used as fluorinating agent for the preparation of glycosyl fluorides and in glycosylation reactions as activator of thioglycosyl donors. All these selectfluor-mediated carbohydrate transformations have been extensively investigated in the past **[67–70]**. In particular, the referred electrophilic fluorination-nucleophilic addition reaction involving glycals and nucleophiles was subjected to a detailed mechanistic study, undertaken by Vincent al., in order to gain insight into the sterocontrol of both carbon-fluorine bond formation and anomeric functionalization **[69]**. Improved yields were shown to be obtained when reactions are performed following a stepwise procedure: (i) initial reaction of the glycal with selectfluor at room temperature and (ii) addition of the nucleophile under reflux conditions. Hence, the reaction mechanism may be separated into the two stages of this procedure, which have been studied independently. ^{1}H and ^{19}F NMR time-course reaction monitoring was carried out in deuterated nitromethane (an appropriate solvent for these transformations) for the electrophilic fluorination of 3,4-di-*O*-acetyl-L-fucal **19** in the presence of selectfluor (**Scheme 3.7**). Protected L-fucal derivative **19** was chosen because of its excellent diastereoselectivity with respect to the fluorination step, leading to the exclusive formation of equatorially fluorinated products (a general feature of glycals bearing axial/pseudo-axial groups at 4-position, i.e. also D-galactal derivatives **[67–69]**). The triflate counterion of selectfluor was used instead of the more common tetrafluoroborate salt, since it proved to dramatically increase reaction yields and decrease the formation of side-products (i.e. 1,2-difluoro sugar derivatives). It was demonstrated that the attack of selectfluor upon the glycal occurs following a pure *syn*-addition (in this case from the opposite face of the axial group, due to steric reasons), from which arises an α-intermediate (**20**) that instantaneously

equilibrates to a more thermodynamically stable conformation (**21**) presenting the positively charged anomeric substituent in equatorial disposition, a result of the reverse-anomeric effect. This intermediate adduct was shown to then slowly anomerize to the more stable β-stereoisomer (**22**). In an independent experiment, the mechanism of the second step (nucleophilic attack) was adressed through addition of benzyl alcohol to the reactive intermediates **21** and **22** separately, both yielding anomeric mixtures of benzyl 3,4-di-*O*-acetyl-2-deoxy-2-fluoro-L-fucopyranose **23**. It was found that adducts **21** and **22** do not display the same reactivity and stability (as supported by hydrolysis studies), leading to different outcomes with regard to diastereoselectivity. Overall, it was concluded that higher α-anomeric selectivity can be achieved if (i) the initial *syn*-adduct (**21**) is allowed to epimerize to the thermodynamically more stable steroisomer (**22**), and (ii) the glycosylation step is conducted at higher temperature (**Scheme 3.7**). Several other factors were shown to influence the stereocontrol in these reactions, including the protecting group pattern of the glycal and the steric hinderance of the glycosyl acceptor [**66, 69, 70**]. Nevertheless, it could be clearly concluded from these experiments that the stereochemistry of the carbon-fluorine bond is determined prior to the nucleophilic attack and, as a consequence, independently [**69**].

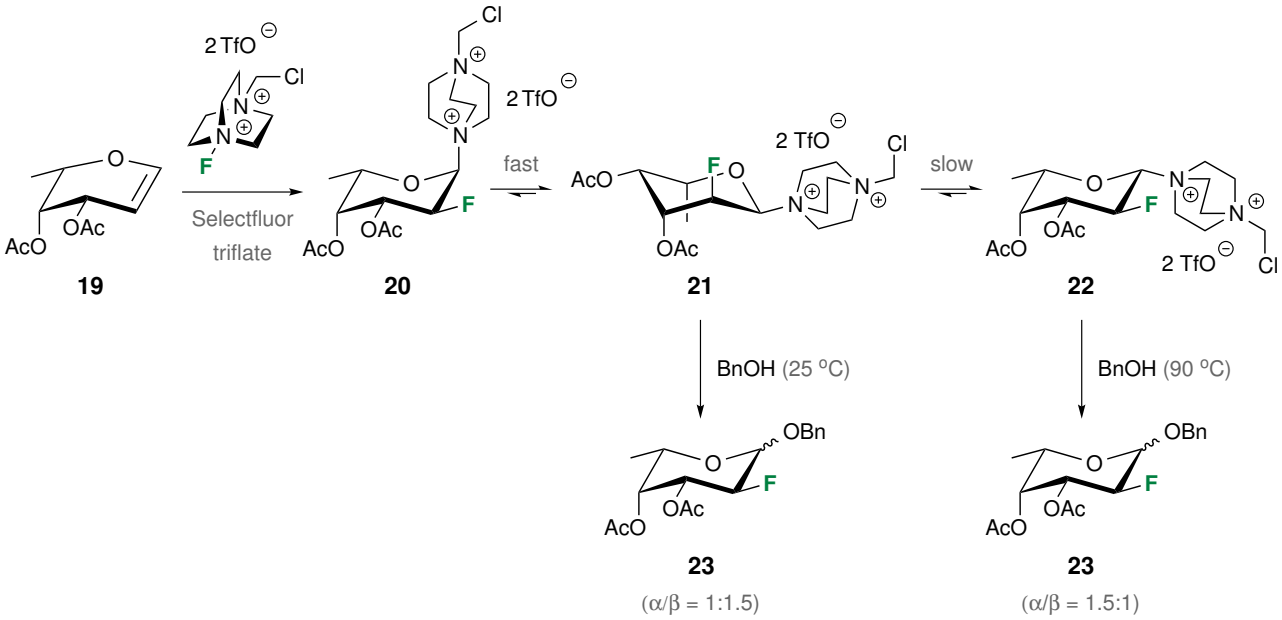

Scheme 3.7: Mechanism for the selectfluor triflate-promoted electrophilic fluorination-nucleophilic addition reaction of 3,4-di-*O*-acetyl-L-fucal **19** with benzyl alcohol proposed after ^{1}H and ^{19}F NMR time-course reaction monitoring in CD_3NO_2 (adapted from refs. [**66, 69**]).

Although in the fucose and galactose series the stereochemistry of fluorine addition is directed by the axial group at 4-position and its functionalization, low-to-moderate diastereoselectivies are usually observed when "all-equatorial" glycals are employed [**67–70**]. Thus, mixtures of epimers at 2-position are expected to arise from reaction of a protected L-glucal derivative with selectfluor in the presence of a nucleophile (i.e. alcohol). Also, taking into account the stereochemistry at the anomeric center, four diastereoisomers (bearing α/β-L-*gluco* and/or α/β-

L-*manno* configuration) can be formed in the following of this polar addition reaction **[54, 63]**, as illustrated in **Scheme 3.8**. At this stage, however, no particular stereoselectivity was required with regard to the carbon-fluorine bond formation, since we intended to obtain both L-*gluco* (**4**) and L-*manno* (**5**) stereoisomers for biological activity screening purposes.

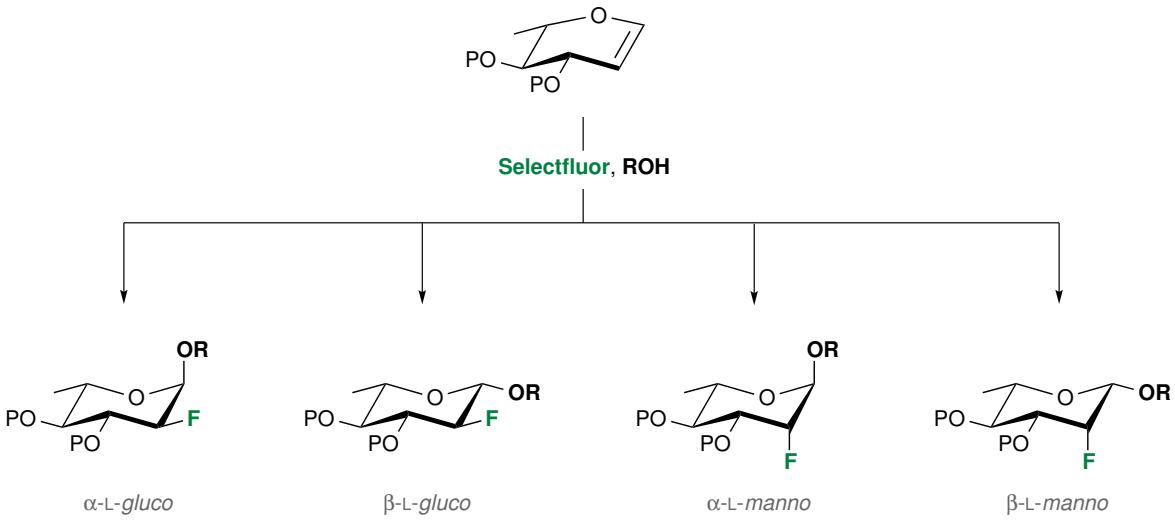

Scheme 3.8: Generic representation of the four possible stereoisomers arising from reaction of a protected L-glucal derivative with an alcohol in the presence of selectfluor. P = generic protecting group, R = generic aglycone residue.

The synthetic route towards target dodecyl deoxyfluoroglycosides **4** and **5** is outlined in **Scheme 3.9**. Peracetylated 6-deoxy-L-glucal **8** and selectfluor bis(tetrafluoroborate) were allowed to react smoothly in nitromethane at room temperature, as described by Wong and co-workers **[69]**. After total consumption of the starting material, dodecanol was added and the reaction was carried out under reflux conditions, which was reported to promote increased α-stereoselectivity. It should be noted that the liquid fatty alcohol and the solvent displayed poor miscibility at room temperature, a problem that was surpassed upon heating. Notwithstanding, acetylated 2,6-dideoxy-2-fluoroglycosides **24-26** could be isolated in only moderate overall yield (42%). Even though the desired α-L-*gluco* (**24**) and α-L-*manno* (**25**) stereoisomers were the major products of this reaction (37% yield, *gluco*/*manno* $\approx$ 0.8:1), separation of the two epimers could not be achieved by conventional column chromatography. Indeed, mixtures of axially- and equatorially-fluorinated epimers which are either inseparable or extremely difficult to resolve have been previously reported in the literature for related 2-deoxy-2-fluorosugars/glycosides **[67, 69, 70]**. Nevertheless, the two stereoisomers were deprotected by methanolysis, affording target α-L-*gluco*- (**4**) and α-L-*manno*-configurated (**5**) glycosides in excelent yield (89%), also as an inseparable mixture of epimers which was afterwards subjected to biological evaluation. The β-L-*gluco*-configurated glycoside **26** was the minor product of this reaction (5% yield) and could be easily purified from the crude mixture. However, it was not engaged in the deacetylation step because the very small amount obtained was required for full physical and spectroscopic

characterization. Finally, no β-L-*manno* stereoisomer could be isolated, in agreement with literature data according to which, in general, only minor proportions of β-*manno*-configurated 2-deoxy-2-fluoroglycosides are obtained **[69, 70]**.

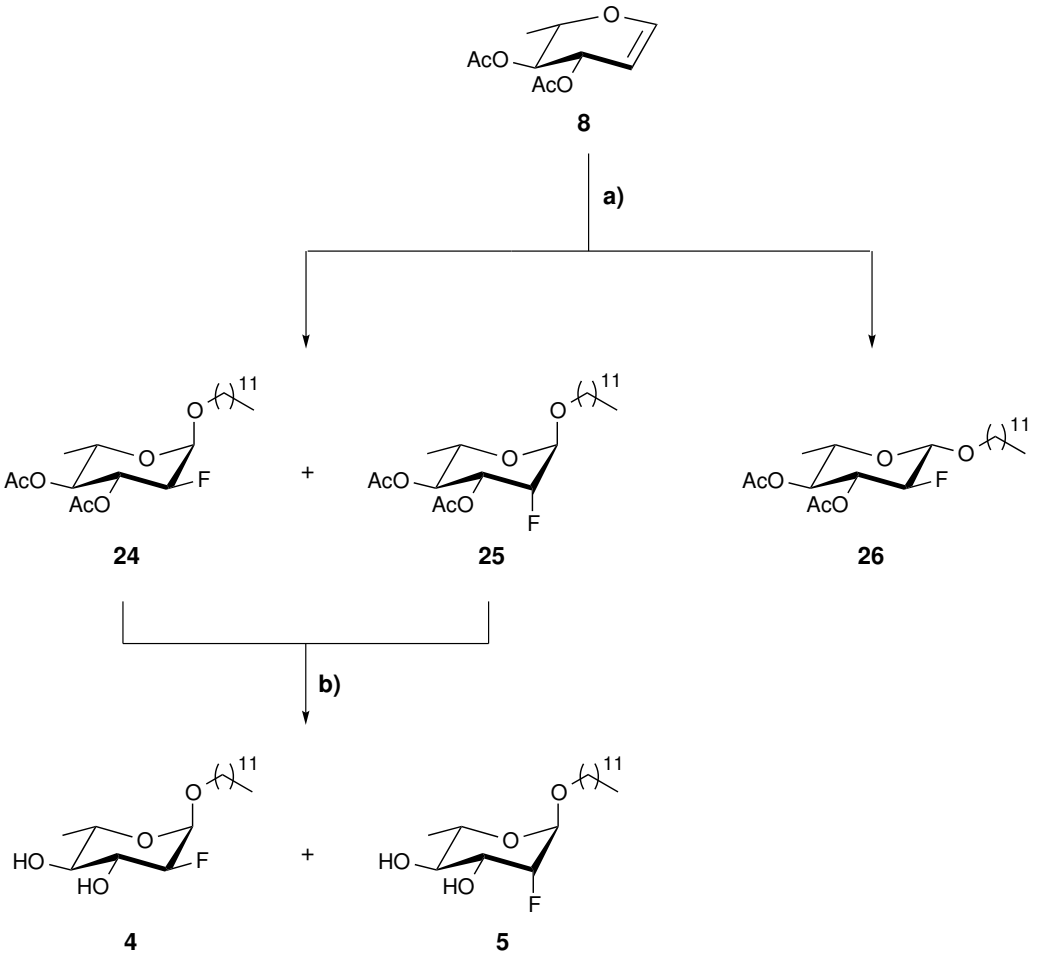

Scheme 3.9: Synthesis of dodecyl 2,6-dideoxy-2-fluoroglycosides **4** and **5**. Reagents and conditions - a) i) selectfluor, $MeNO_2$, 4Å MS, 0 °C→r.t., ii) dodecanol, 90 °C, reflux, 37% for **24**/**25**, 5% for **26**; b) NaOMe, MeOH, r.t., 89%.

Structural characterization of the compounds was mainly accomplished by means of ^{1}H, ^{13}C and ^{19}F NMR, and required careful inspection of literature data for other fluorinated carbohydrate derivatives **[67–70, 85]**. In the case of inseparable mixtures of stereoisomers, multiplet analysis was supported by homonuclear *J*-resolved spectroscopy [2] to allow the interpretation of complex/overlapping multiplets, as well as the unambiguous discrimination between homonuclear (^{1}H-^{1}H) and heteronuclear (^{1}H-^{19}F) spin-spin couplings. For stereochemical assignment purposes, particular emphasis was given to the acetylated intermediates **24-26**, for which selected NMR data is given together in **Tables 3.6** and **3.7**.

[2] *J*-resolved **[86–88]** is a two-dimensional NMR technique which allows separation of spin-spin couplings from chemical shifts. It is most commonly applied to (i) provide accurate measurement of coupling constants and/or (ii) display chemical shifts without spin-coupling fine-structure (i.e. "proton-decoupled" proton spectra).

Table 3.6: Selected ^{1}H and ^{19}F NMR data for acetylated 2,6-dideoxy-2-fluoroglycosides **24-26** in chloroform-*d*.

	^{1}H and ^{19}F NMR δ/ ppm [a]		
Position	**α-L-*gluco* (24)** [b]	**α-L-*manno* (25)** [b]	**β-L-*gluco* (26)**
1	4.97 (d) ($^{3}J_{1,2} = 3.8$)	4.90 (dd) ($^{3}J_{1,F} = 7.5$, $^{3}J_{1,2} = 1.6$)	4.52 (dd) ($^{3}J_{1,2} = 7.7$, $^{3}J_{1,F} = 2.7$)
2	4.46 (ddd) ($^{2}J_{2,F} = 49.6$, $^{3}J_{2,3} = 9.7$, $^{3}J_{2,1} = 3.8$)	4.72 (ddd) [c] ($^{2}J_{2,F} = 50.2$, $^{3}J_{2,3} = 2.6$, $^{3}J_{2,1} = 1.6$)	4.26 (br ddd) ($^{2}J_{2,F} = 50.8$, $^{3}J_{2,3} = 9.3$, $^{3}J_{2,1} = 7.7$)
3	5.50 (dt) ($^{3}J_{3,F} = 12.0$, $^{3}J_{3,2} = {}^{3}J_{3,4} = 9.7$)	5.22 (ddd) ($^{3}J_{3,F} = 28.8$, $^{3}J_{3,4} = 10.1$, $^{3}J_{3,2} = 2.6$)	5.26 (dt) ($^{3}J_{3,F} = 14.6$, $^{3}J_{3,4} = {}^{3}J_{3,2} = 9.3$)
4	4.73 (t) ($^{3}J_{4,3} = {}^{3}J_{4,5} = 9.7$)	5.10 (t) ($^{3}J_{4,5} = 9.7$)	4.76 (t) ($^{3}J_{4,5} = 9.6$)
5	3.92 (dq) ($^{3}J_{5,4} = 9.7$, $^{3}J_{5,6} = 6.3$)	3.87 (dq) ($^{3}J_{5,4} = 9.7$, $^{3}J_{5,6} = 6.3$)	3.57 (dq) ($^{3}J_{5,4} = 9.6$, $^{3}J_{5,6} = 6.3$)
6	1.17 (d) ($^{3}J_{6,5} = 6.3$)	1.22 (d) ($^{3}J_{6,5} = 6.3$)	1.23 (d) ($^{3}J_{6,5} = 6.3$)
2-F	-201.2 (dd) ($^{2}J_{F,2} = 49.6$, $^{3}J_{F,3} = 12.0$)	-204.1 (ddd) ($^{2}J_{F,2} = 50.2$, $^{3}J_{F,3} = 28.8$, $^{3}J_{F,1} = 7.5$)	-199.4 (app dd) [d] ($^{2}J_{F,2} = 50.8$, $^{3}J_{F,3} = 14.6$)

[a] In parenthesis are the multiplicity and coupling constant(s) (J/ Hz) for each resonance.
[b] Extracted data from spectra obtained for the inseparable mixture of epimers.
[c] The signal was observed as an apparent doublet of triplets, due to the very similar values of $^{3}J_{2,1}$ and $^{3}J_{2,3}$. However, both multiplicity and coupling constants could be confirmed by J-resolved experiments and extracted from the H-3 and H-1 signals.
[d] The signal was observed as an apparent doublet of doublets, although a vicinal couping constant with H-1 ($^{3}J_{F,1} = 2.7$ Hz) could be observed in the ^{1}H NMR spectrum and confirmed by J-resolved experiments.

Table 3.7: Selected ^{13}C NMR data for acetylated 2,6-dideoxy-2-fluoroglycosides **24-26** in chloroform-*d*.

	^{13}C NMR δ/ ppm [a]		
Position	**α-L-*gluco* (24)** [b]	**α-L-*manno* (25)** [b]	**β-L-*gluco* (26)**
1	95.8 (d) ($^2J_{1,F} = 20.2$)	97.0 (d) ($^2J_{1,F} = 28.8$)	100.2 (d) ($^2J_{1,F} = 22.0$)
2	87.7 (d) ($^1J_{2,F} = 194.5$)	87.5 (d) ($^1J_{2,F} = 178.6$)	89.8 (d) ($^1J_{2,F} = 190.6$)
3	70.8 (d) ($^2J_{3,F} = 19.2$)	70.1 (d) ($^2J_{3,F} = 16.6$)	73.0 (d) ($^2J_{3,F} = 19.5$)
4	73.6 (d) ($^3J_{4,F} = 7.0$)	71.0	73.2 (d) ($^3J_{4,F} = 7.2$)
5	65.0	66.3	69.9
6	17.2	17.3	17.3

[a] In parenthesis are the multiplicity and coupling constants (J/ Hz) for each resonance, when applicable.
[b] Extracted data from spectra obtained for the inseparable mixture of epimers.

Although the α-L-*gluco*- and α-L-*manno*-configurated glycosides **24** and **25** were obtained as an inseparable mixture, full spectroscopic characterization and unambiguous assignment of absolute configuration was easily accomplished, since most of the relevant resonances were remarkably well-resolved in the aquired NMR spectra.

With respect to the α-*gluco* stereoisomer (**24**), successful fluorination at 2-position was confirmed by the presence of a resonance at δ = -201.2 ppm in the ^{19}F NMR spectrum, observed as a doublet of doublets presenting a very large, heteronuclear geminal coupling constant with H-2 ($^2J_{F,2}$ = 49.6 Hz) and a smaller vicinal coupling with H-3 ($^3J_{F,3}$ = 12.0 Hz), both of which could also be observed in the ^{1}H NMR spectrum. This data is in aggreement with characteristic information reported in the literature for related 2-deoxy-2-fluoroglucopyranoses/pyranosides **[67–70, 85]** [3,4]. Moreover, no vicinal coupling between the fluorine atom at 2-position and H-1 could be detected, indicating an axial disposition for the anomeric alcoxy group and, consequently, α-*gluco* stereochemistry [5]. Accordingly, the resonance corresponding to the anomeric proton was visible at δ = 4.97 ppm in the ^{1}H NMR spectrum, as a doublet due to the presence of a small, homonuclear coupling constant with H-2 ($^3J_{1,2}$ = 3.8 Hz). The signal due to H-2 was observed at δ = 4.46 ppm, presentig a ddd pattern as a result of very different couplings with the fluorine atom, the anomeric proton and the *trans*-arranged H-3 ($^3J_{2,3}$ = 9.7 Hz), which in turn appeared at lower field (δ = 5.50 ppm) due to the presence of an electron withdrawing acetyl group at this position. The resonance was observed as a double triplet owing to similar coupling constants with H-2 and H-4 ($^3J_{3,4}$ = 9.7 Hz), but different coupling with the 2-fluoro group. ^{1}H NMR data for the remaining resonances (i.e. H-4, H-5, H-6, signals due to the alkyl moiety and the two acetyl groups) clearly resembled those of other peracetylated dodecyl 6-deoxy-hexopyranosides previously described (see **Sections 3.1.1-3.1.2**), as well as literature data **[1–3]**, given the absence of heteronuclear spin couplings with the fluorine atom. Regarding ^{13}C NMR data, the anomeric carbon was visible at δ = 95.8 ppm, as a doublet due to coupling with the fluorine atom ($^2J_{1,F}$ = 20.2 Hz). Similar multiplicity was also observed for the C-2 ($^1J_{2,F}$ = 194.5 Hz), C-3 ($^2J_{3,F}$ = 19.2 Hz) and C-4 ($^3J_{4,F}$ = 7.0 Hz) resonances, consistently with data reported in the literature for other 2-deoxy-2-fluoroglucosides **[67–70, 85]**. The remaining carbon signals were assigned accordingly, without particularities worth noting.

In the case of the α-*manno* diastereomer (**25**), slight differences in spectroscopic data were indicative of opposite stereochemistry at 2-position. The signal due to the fluorine atom was now visible at δ = -204.1 ppm and as a ddd in the ^{19}F NMR spectrum, displaying a typical geminal coupling constant with H-2 ($^2J_{F,2}$ = 50.2 Hz) [3], and vicinal coupling constants with both the *trans*-arranged H-3 ($^3J_{F,3}$ = 28.8 Hz) and the *cis*-related H-1 ($^3J_{F,1}$ = 7.5 Hz) [6]. Accordingly, all these heteronuclear spin couplings were also observed in the ^{1}H NMR spectrum. The anomeric proton was observed as a double doublet at δ = 4.90 ppm due to different couplings with the

[3] Typically, $^2J_{F,2} \approx$ 50 Hz for 2-deoxy-2-fluoropyranoses/pyranosides.

[4] Typically, $^3J_{F,3} \approx$ 10-15 Hz for *gluco*-configurated epimers.

[5] Typically, $^3J_{F,1} <$ 0.5 Hz for α-*gluco*-configurated stereoisomers and $^3J_{F,1} \approx$ 2-4 Hz for their β-anomers.

[6] Typically, $^3J_{F,3} \approx$ 27-30 Hz for *manno*-configurated epimers, $^3J_{F,1} \approx$ 6-8 Hz for their α-anomers and $^3J_{F,1} \approx$ 18-20 Hz for their β-anomers.

fluorine atom and the proton at 2-position ($^3J_{1,2}$ = 1.6 Hz). H-2 appeared at δ = 4.72 ppm, presenting ddd (apparent double triplet) multiplicity as a result of different couplings with the fluorine atom, H-1 and H-3 ($^3J_{2,3}$ = 2.6 Hz). The signal corresponding to H-3 was visible also as a ddd owing to different couplings with the fluorine atom, H-2 and the *trans*-arranged H-4 ($^3J_{3,4}$ = 10.1 Hz), with a chemical shift of δ = 5.22 ppm. The remaining proton resonances were assigned similarly to those of its α-*gluco*-configurated epimer (**24**). The anomeric carbon was observed as a doublet ($^2J_{1,F}$ = 28.8 Hz) in the ^{13}C NMR spectrum, at a chemical shift of δ = 97.0 ppm. No relevant dissimilarities were found between the remaining carbon resonances and those of compound **24**, except for the signal due to C-4, which was observed as a singlet at δ = 70.1 ppm. The absence of heteronuclear vicinal coupling between the carbon atom at 4-position and the 2-fluoro group is a common spectroscopic feature presented by 2-deoxy-2-fluoro-α-mannosides, as described in the literature [**67–70, 85**].

Regarding the acetylated product bearing β-*gluco*-configuration (**26**), the fluorine resonance was observed at δ = -199.4 ppm in the ^{19}F NMR spectrum, as a double doublet owing to heteronuclear coupling constants with the protons at 2- and 3-positions ($^2J_{F,2}$ = 50.8 Hz and $^3J_{F,3}$ = 14.6 Hz, respectively), in aggreement with its supposed equatorial orientation [3,4]. As expected, the anomeric proton was visible in the ^{1}H NMR spectrum at higher field (δ = 4.52 ppm) when compared to its correspondent α-stereoisomer (**24**), indicating an equatorial positioning for the anomeric substituent as well. Accordingly, the signal was also observed as a double doublet due to the presence of a typical *trans*-diaxial coupling constant with the vicinal H-2 ($^3J_{1,2}$ = 7.7 Hz) and a small coupling with the fluorine at the same position ($^3J_{1,F}$ = 2.7 Hz) [5,7]. Spectroscopic data for the remaining proton resonances greatly resembled those obtained for the α-anomer (**24**), as was also the case for most of the carbon signals observed in the ^{13}C NMR spectrum, with the exception of the anomeric carbon which was found at significantlty lower field (δ = 100.2 ppm), reinforcing the assigned anomeric configuration. Also important is the fact that NOESY experiments supported these results, as they revealed key correlations of H-1 with the 1,3-*cis*-related H-3 and H-5 resonances.

The desired dodecyl 2,6-dideoxy-2-fluoroglycosides **4** and **5** were finally assessed by deprotection. Although in this case much more complex spectra was obtained (because of considerable signal overlapping), the most relevant NMR spectroscopic data could be fully extracted from *J*-resolved experiments. As could be anticipated, no major differences were observed when comparing data obtained for each compound with its corresponding acetylated percursor, with the exception of (i) the signals due to H-3 and H-4, which were observed at higher field for the non-functionalized glycosides **4** and **5** in the ^{1}H NMR spectrum, as well as (ii) the fact that the signals due to the acetyl groups could no longer be detected (in turn, hydroxy group-protons were now visible at $\delta \approx$ 2-3 ppm in the ^{1}H NMR spectrum).

[7] Most commonly, β-*gluco*-configurated stereoisomers present very small coupling constants between the fluorine at 2-position and the anomeric proton ($^3J_{1,F}$), that usually are not resolved in ^{19}F NMR but can be detected by ^{1}H NMR, unlike their corresponding α-anomers.

Even though the target deoxyfluroglycosides **4** and **5** could be prepared with reasonable efficiency (33% overall yield from **8**), the usefulness of the applied synthetic methodology is greatly limited by the fact that the two stereoisomers could not be separated by conventional column chromatography. In fact, biological evaluation of the obtained epimeric mixture may lead to ambiguous results arising from eventual synergism/antagonism effects. Anticipating such a problem, we considered paramount the development of diastereoselective approaches to the synthesis of each potentially bioactive compound.

As we have already discussed, the protecting group pattern of the glycal in known to direct the stereoselectivity of these reactions. Regarding the stereochemistry of the carbon-fluorine bond, in particular, it has been shown that increasing the steric hinderance of the protecting groups in "all-equatorial" glycals dramatically influences the *gluco*/*manno* selectivity favoring the formation of equatorially fluorinated products [**69, 70**]. Hence, it is possible to obtain high levels of *gluco*-stereoselectivity by simply modifying the protecting group strategy. Recently, Vincent and co-workers reported an optimized procedure for the fluorophosphorylation of protected D-glucals and L-heptosylglycals as a key step for the stereoselective synthesis of a fluorinated analogue of ADP-L-*glycero*-β-D-*manno*-heptopyranose, an important intermediate of the lipopolysaccharide biosynthesis in Gram-negative bacteria [**89**]. Exclusive formation of the β-*gluco* stereoisomer could be achieved when sterically hindered *tert*-butyldimethylsilyl ether protecting groups were employed and the reaction temperature was lowered. Therefore, we considered applying these conditions to our system as a promising strategy for the synthesis of the desired α-*gluco*-configurated glycoside **4**, although an eventual decrease in anomeric selectivity could be anticipated. Biological evaluation of this molecular entity, together with the mixture containing also its stereoisomer, should provide valuable insight into the relevance of the carbon-fluorine bond stereochemistry.

As depicted in **Scheme 3.10**, preparation of the persilylated 6-deoxy-L-glucal derivative **27** was easily accomplished in high yield (82%), following a two-step one-pot procedure [**89**] involving (i) methanolysis of the acetylated percursor **8** and subsequent (ii) silylation of the glycal by treatment with *tert*-butyldimethylsilyl chloride and imidazole in *N,N*-dimethylformamide, as first described by Corey and Venkateswarlu [**90, 91**].

The structure of **27** was easily confirmed by means of ^{1}H and ^{13}C NMR spectroscopic data. The anomeric proton was visible as a doublet at a chemical shift of $\delta = 6.28$ ppm, presenting a coupling constant with the proton at 2-position ($^{3}J_{1,2} = 6.1$ Hz), as expected. The H-2 resonance, in turn, was observed at $\delta = 6.65$ ppm, as a broad double doublet due to different couplings with H-1 and H-3 ($^{3}J_{2,3} = 3.1$ Hz). The signal corresponding to H-3 appeared as a poorly resolved, broadened signal (therefore assigned as a multiplet) at $\delta = 4.06$-4.10 ppm, followed by H-5 which was observed as an apparent quintet at $\delta = 3.93$ ppm, owing to relatively similar couplings with H-4 ($^{3}J_{5,4} = 7.1$ Hz) and the equivalent protons at 6-position ($^{3}J_{5,6} = 6.6$ Hz). H-4 was found at $\delta = 3.56$ ppm, as a broad triplet owing to similar couplings with the protons at 3- and 5-positions ($^{3}J_{4,3} \approx {}^{3}J_{4,5} = 7.1$ Hz), and the CH_3-6 resonance was visible at

δ = 1.31 ppm, as a doublet due to coupling with H-5. The signals corresponding to the silyl ether *tert*-butyl and methyl protons were visible as singlets at δ = 0.90 ppm and δ = 0.10-0.11 ppm, respectively. With regard to carbon resonances, the olefinic C-1 and C-2 signals were found at δ = 143.1 ppm and δ = 102.9 ppm, respectively, and the remaining sugar ring carbons appeared at higher field, as expected. The signals due to the *tert*-butyl carbons from the silyl ether protecting groups were visible at δ = 25.9-26.0 ppm (primary carbons) and δ = 18.0-18.1 ppm (quaternary carbons). In turn, the resonances corresponding to the silanoxymethyl groups were observed at very high field ($\delta \leq$ -3.7 ppm) due to the shielding effect exerted by the silicon nucleus.

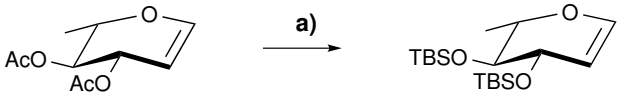

8 **27**

Scheme 3.10: Conversion of acetylated glycal **8** into silylated glical **27**. Reagents and conditions - a) i) NaOMe, MeOH, r.t., ii) TBDMSCl, imidazole, DMF, r.t., 82%.

Finally, selectfluor-mediated electrophilic fluorination-nucleophilic addition reaction of **27** with dodecanol was performed (**Scheme 3.11**). In the attempt to reproduce the conditions described in the literature [**89**], the addition step was first conducted at moderate temperature (45 °C). However, because the reaction was very sluggish, it was allowed to proceed for further 24 h at increased temperature (90 °C). Following this procedure, silylated 2,6-dideoxy-2-fluoroglycosides **28-30** were obtained in slightly lower overall yield (34%) when compared to their acetylated counterparts (see **Scheme 3.9**). As expected, a significantly improved *gluco*-diastereoselectivity was observed, since the α-L-*gluco*- (**28**) and β-L-*gluco*-configurated (**29**) diastereomers were the major products of the reaction (27% yield, $\alpha/\beta \approx$ 1:1.3). The α-L-*manno* (**30**) stereoisomer was isolated in only 7% yield and could be easily purified in this case, due to the different physical properties exhibited by the silylated glycosides **28-30** (i.e. comparing to those of acetylated glycosides **24-26**). However, glycoside **30** was not isolated in sufficient amount to proceed to the next step. It is important to note that glycosides **28** and **29** where obtained as an inseparable anomeric mixture. Nevertheless, after removal of the silyl ether protecting groups, which was accomplished in excellent yield (95%) by fluorolysis using tetra-*n*-butylammonium fluoride in tetrahydrofuran [**90, 91**], target α-L-*gluco*-configurated glycoside **4** and its β-anomer **31** could be easily separated.

Regarding the structural characterization of the new 2,6-dideoxy-2-fluoroglycosides, most of the NMR spectroscopic data which was relevant for stereochemicalassignment purposes was similar to that described above. Selected ^{1}H, ^{19}F and ^{13}C NMR data for protected glycosides **28-30** is listed in **Tables 3.8** and **3.9**.

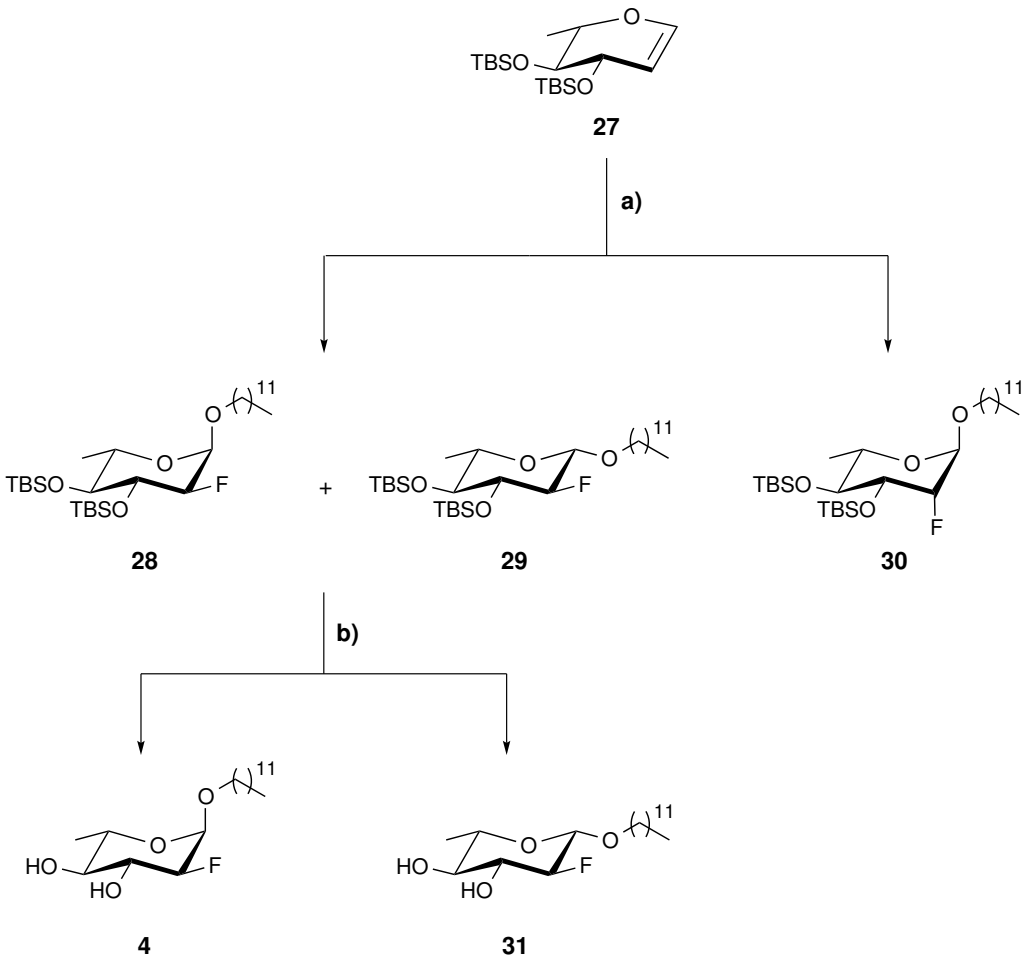

Scheme 3.11: Synthesis of dodecyl 2,6-dideoxy-2-fluoro-L-glucopyranosides **4** and **31**. Reagents and conditions - a) i) selectfluor, $MeNO_2$, 4Å MS, 0 °C→r.t., ii) dodecanol, 45 °C→90 °C, reflux, 27% for **28**/**29**, 7% for **30**; b) TBAF, THF, r.t., 35% for **4**, 60% for **31**.

Table 3.8: Selected ^{1}H and ^{19}F NMR data for silylated 2,6-dideoxy-2-fluoroglycosides **28-30** in chloroform-*d*.

	^{1}H and ^{19}F NMR δ/ ppm [a]		
Position	**α-L-*gluco* (28)** [b]	**β-L-*gluco* (29)** [b]	**α-L-*manno* (30)**
1	4.85 (d) ($^{3}J_{1,2}$ = 3.8)	4.42 (dd) ($^{3}J_{1,2}$ = 7.7, $^{3}J_{1,F}$ = 2.9)	4.81 (dd) ($^{3}J_{1,F}$ = 7.3, $^{3}J_{1,2}$ = 2.4)
2	4.16 (ddd) ($^{2}J_{2,F}$ = 48.7, $^{3}J_{2,3}$ = 9.3, $^{3}J_{2,1}$ = 3.8)	4.02 (ddd) ($^{2}J_{2,F}$ = 50.4, $^{3}J_{1,2}$ = 7.7, $^{3}J_{2,3}$ = 8.6)	4.53 (br dt) ($^{2}J_{2,F}$ = 49.5, $^{3}J_{2,3}$ = $^{3}J_{2,1}$ = 2.4)
3	4.01 (ddd) ($^{3}J_{3,F}$ = 10.5, $^{3}J_{3,2}$ = 9.3, $^{3}J_{3,4}$ = 8.2)	3.71 (ddd) ($^{3}J_{3,F}$ = 14.4, $^{3}J_{3,2}$ = 8.6, $^{3}J_{3,4}$ = 7.9)	3.89 (ddd) ($^{3}J_{3,F}$ = 28.3, $^{3}J_{3,4}$ = 8.3, $^{3}J_{3,2}$ = 2.4)
4	3.16 (dd) [c] ($^{3}J_{4,5}$ = 9.4, $^{3}J_{4,3}$ = 8.2)	3.24 (dd) [c] ($^{3}J_{4,5}$ = 8.8, $^{3}J_{4,3}$ = 7.9)	3.53-3.64 (m) [g]
5	3.62-3.70 (m) [d]	3.30 (dq) ($^{3}J_{5,4}$ = 8.8, $^{3}J_{5,6}$ = 6.2)	3.53-3.64 (m) [g]
6	1.20 (d) ($^{3}J_{6,5}$ = 6.5)	1.26 (d) [e] ($^{3}J_{6,5}$ = 6.2)	1.25 (d) [h] ($^{3}J_{6,5}$ = 6.3)
2-F	-195.8 (dd) ($^{2}J_{F,2}$ = 48.7, $^{3}J_{F,3}$ = 10.5)	-192.7 (app dd) [f] ($^{2}J_{F,2}$ = 50.4, $^{3}J_{F,3}$ = 14.4)	-204.5 (ddd) ($^{2}J_{F,2}$ = 49.5, $^{3}J_{F,3}$ = 28.3, $^{3}J_{F,1}$ = 7.3)

[a] In parenthesis are the multiplicity and coupling constant(s) (J/ Hz) for each resonance.
[b] Extracted data from spectra obtained for the inseparable mixture of anomers.
[c] H-4 was observed as an apparent triplet in the ^{1}H NMR spectrum, due to the very similar values of $^{3}J_{4,3}$ and $^{3}J_{4,5}$. However, both multiplicity and coupling constants could be extracted from the J-resolved spectrum.
[d] H-5 was observed overlapped with H-1'a in a multiplet.
[e] CH_3-6 resonance was observed overlapped with H-3'a,b - H-11'a,b in a multiplet (δ = 1.22-1.38). However, both chemical shift and coupling constants could be extracted from the J-resolved spectrum.
[f] The signal was observed as an apparent doublet of doublets, although a vicinal couping constant with H-1 ($^{3}J_{F,1}$ = 2.9 Hz) could be observed in the ^{1}H NMR spectrum and confirmed by J-resolved experiments.
[g] H-4 and H-5 were observed overlapped in a multiplet.
[h] CH_3-6 resonance was observed overlapped with H-3'a,b - H-11'a,b in a multiplet (δ = 1.22-1.34). However, both chemical shift and coupling constants could be extracted from the J-resolved spectrum.

Table 3.9: Selected ^{13}C NMR data for silylated 2,6-dideoxy-2-fluoroglycosides **28-30** in chloroform-*d*.

	^{13}C NMR δ/ ppm [a]		
Position	**α-L-*gluco* (28)** [b]	**β-L-*gluco* (29)** [b]	**α-L-*manno* (30)**
1	96.2 (d) ($^2J_{1,F} = 21.5$)	100.1 (d) ($^2J_{1,F} = 24.1$)	97.2 (d) ($^2J_{1,F} = 29.3$)
2	90.8 (d) ($^1J_{2,F} = 190.8$)	93.1 (d) ($^1J_{2,F} = 186.6$)	90.7 (d) ($^1J_{2,F} = 177.2$)
3	73.3 (d) ($^2J_{3,F} = 16.1$)	76.9 [c]	72.6 (d) ($^2J_{3,F} = 17.1$)
4	76.9 [c]	76.2 (d) ($^3J_{4,F} = 7.5$)	73.9
5	68.3	72.7	69.7
6	18.1	18.1	18.0

[a] In parenthesis are the multiplicity and coupling constants (J/ Hz) for each resonance, when applicable.
[b] Extracted data from spectra obtained for the inseparable mixture of anomers.
[c] The chemical shift was inferred from HMQC, because the signal was overlapped with the solvent residual peak.

3.2 Antibacterial activity

A preliminary screening of the antibacterial activity of the newly synthesized compounds was assessed through determination of minimum inhibitory concentrations (MIC) and mininum bactericidal concentrations (MBC) against *Bacillus cereus*, using an adaptation of the broth microdilution method [**92, 93**] (see **Section 5.4** for detailed methods). *Bacillus cereus* was employed as model microbe due its well-known genotypic similarity with *Bacillus anthracis* [**30–34**], the pathogen responsible for anthrax infections [**24**] and ultimate target of our research on innovative sugar-based bactericidal agents towards biosecurity.

Results obtained for the final compounds (**2**, **3**, **18**, **4**/**5**, **4** and **31**) and for the positive controls (ciprofloxacin and dodecyl 2,6-dideoxy-α-L-*arabino*-hexopyranoside **1**) are provided in **Table 3.10**. An important observation is the invariable correspondence between MIC and MBC values for all the tested compounds. In fact, this is a common feature whithin this family of antimicrobial deoxyglycosides which is indicative that, in addition to inhibiting bacterial cell growth, the mode of action of these molecules implies a bactericidal effect.

Dodecyl α-L-rhamnopyranoside **2** was synthesized with the intent to evaluate the potential antibacterial activity of surfactant 6-deoxyglycosides. In previous work, we have shown that while 2,6-dideoxygenation leads to potent antimicrobial glycosides (i.e. compound **1**), no relevant activity is featured by the related 2-deoxyglycosides bearing a hydroxy group at 6-position [**1–3**]. However, the effect of exclusive 6-deoxygenation has not been investigated so far. Although glycoside **2** exhibited a bioactive profile, it was only effective at higher concentrations (MIC = 32 μg mL^{-1}) when compared to the lead compound **1** (MIC = 16 μg mL^{-1}). This result strongly indicates that a decrease in hydrophobicity, in this case promoted by the presence of a hydroxy group at 2-position, gives rise to inferior antimicrobial properties.

The α-L-*threo*-configurated glycoside **3** presented also moderate antibacterial activity, since it inhibited bacterial cell growth and exerted bactericidal effect at a concentration of 32 μg mL^{-1}. Surprisingly, the β-stereoisomer **18** was also active at the same concentration. This result was unexpected owing to the significantly superior bioactivity reported for α-*arabino*-hexopyranosides over their β-anomers, as described in previous studies performed by our research group [**1–3**], and suggests that the enhanced structural flexibility exhibited by pentopyranosides **3** and **18** may be able to modulate the biological behaviour of these molecules. Also worth noting is the fact that the antibacterial activities obtained are similar to those determined for related D-*threo* glycosides (MIC = 32 μg mL^{-1}) in preliminary work performed in our laboratory [8]. Hence, in contrast to what has been reported for *arabino*-hexopyranosides [**1–3**], the D/L-stereochemistry seems not to be paramount in determining the potency of the antimicrobial action in the case of *threo*-pentopyranosides.

[8] Patrícia Serra, João Pais and Amélia P. Rauter *et al.*, unpublished results.

Regarding the 2-fluorinated deoxyglycosides **4**, **5** and **31**, considerably different results were obtained. The epimeric mixture of α-L-*gluco*- (**4**) and α-L-*manno*-configurated (**5**) glycosides (**4**/**5** ≈ 1:3) presented an antibacterial activity competitive with that of the lead compound **1** (MIC = 16 μg mL^{-1}). Moreover, the stereochemically pure α-glucoside **4** (minor component in the above-referred mixture) was also active at the same concentration, suggesting that the two epimers may be equally potent as antimicrobials. Nevertheless, the stereoselective synthesis of the α-mannoside **5** is required to fully address an eventual influence of the stereochemistry at the fluorinated position on the bioactive profile of these molecular entities. It should also be noted that, as mentioned in **Section 2.3**, similar antimicrobial activity was displayed by an iodinated analogue (dodecyl 2,6-dideoxy-2-iodo-α-L-mannopyranoside) in preliminary assays performed in our laboratory [9]. Altogether, these results reinforce that increased hydrophobicity at 2-position leads to improved antimicrobial activity (cf. discussion above on the 6-deoxyglycoside **2**). The β-L-*gluco*-configurated glycoside **31**, in turn, was inactive upon screening for its potential antibacterial activity (MIC > 128 μg mL^{-1}). Thus, with respect to biological behaviour, the dodecyl 2,6-dideoxy-2-fluoro-L-glycosides herein disclosed greatly resemble the corresponding 2,6-dideoxy-L-*arabino*-hexopyranosides previously synthesized by our group [**1**–**3**].

More recently, we had the opportunity to further evaluate some of the newly synthesized deoxyglycosides (compounds **2**, **3** and **18**) for their potential as inhibitors of *B. anthracis* growth. MIC values were determined in this case using the agar dilution method (in solid media), against three different strains - *B. anthracis (pathogenic)*, *B. anthracis (vacinal)* and *B. anthracis (ovince)*. The results are summarized in **Table 3.11**, showing that all compounds presented potent antibacterial activity, being effective at concentrations ranging from 8 to 16 μg mL^{-1}, depending on the bacterial strain tested. More importantly, in certain cases the activity exhibited was identical to that presented by the lead compound (MIC = 8 μg mL^{-1}), emphasizing the strong therapeutic potential of this new family of lead structures that we have generated.

[9] João Pais and Amélia P. Rauter *et al.*, unpublished results.

Table 3.10: Antibacterial activities expressed as MIC and MBC against *B. cereus* determined by the broth microdilution method [a] **[92, 93]**.

#	Compound	MIC *B. cereus*/ μg mL^{-1}	MBC *B. cereus*/ μg mL^{-1}
-	Ciprofloxacin [b]	≤ 2	≤ 2
1 [a]	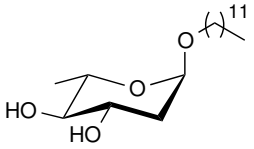	16	16
2	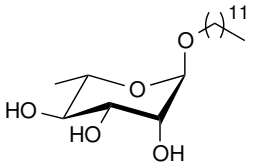	32	32
3	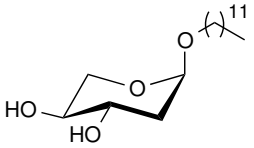	32	32
18	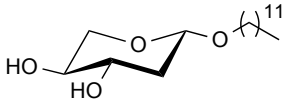	32	32
4/**5** [c]	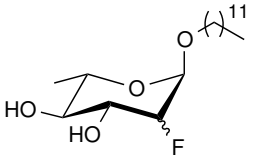	16	16
4	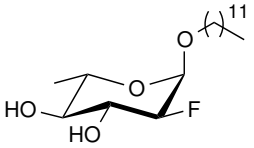	16	16
31	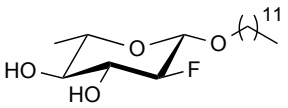	>128	>128

[a] The tested concentrations ranged from 4 to 128 μg mL^{-1}.
[b] The standard antibiotic ciprofloxacin and dodecyl 2,6-dideoxy-α-L-*arabino*-hexopyranoside (**1**) were used as positive controls.
[c] Final α-L-*gluco* (**4**)/α-L-*manno* (**5**) ratio tested was 1:3 (assessed by ^{1}H and ^{19}F NMR spectroscopy).

Table 3.11: Antibacterial activities expressed as MIC against three strains of *B. anthracis* determined by the agar dilution method [a] **[3]**.

#	**Compound**	**MIC** *B. anthracis (pathogenic)*/ μg mL^{-1}	**MIC** *B. anthracis (vacinal)*/ μg mL^{-1}	**MIC** *B. anthracis (ovine)*/ μg mL^{-1}
-	Ciprofloxacin [b]	≤ 8	≤ 8	≤ 8
1 [a]	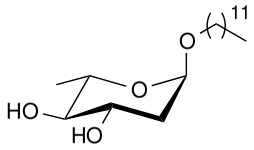	8	8	8
2	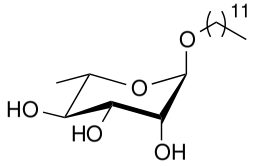	16	8	16
3	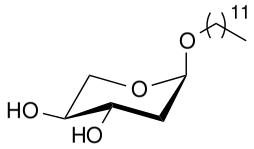	8	8	16
18	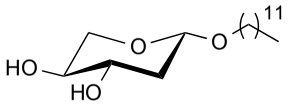	16	8	16

[a] The tested concentrations were 8 and 16 μg mL^{-1}.
[a] The standard antibiotic ciprofloxacin and dodecyl 2,6-dideoxy-α-L-*arabino*-hexopyranoside (**1**) were used as positive controls.

Chapter 4

Conclusion

New carbohydrate-based surfactants deoxygenated in the sugar headgroup have been successfully accessed by appropriate synthetic methodologies and preliminarily screened for their antibacterial activity against *Bacillus cereus* and, for some of the compounds, also against *B. anthracis*. Several promising results were achieved in the following of this exploratory research ultimately intended at establishing structure-bioactivity relationships, which should provide valuable insights for further lead optimization towards a potentially non-toxic drug candidate.

The synthesis of dodecyl α-L-rhamnopyranoside (dodecyl 6-deoxy-α-L-mannopyranoside) **2** was accomplished in very good overall yield (60%) following established methodologies. L-Rhamnose was efficiently converted into known trichloroacetimidate **6** via peracetylation, selective anomeric deprotection mediated by hydrazine acetate, and trichloroacetimidation (85% for three steps). Glycosylation of dodecanol with trichloroacetimidate **6** proceeded with high α-stereoselectivity in the presence of catalytic trimethylsilyl triflate, and subsequent removal of the acetyl protecting groups by methanolysis afforded the desired 6-deoxyglycoside **2** (71% yield over two steps).

Evaluation of the microbial susceptibility of *B. cereus* to **2** gave rise to only moderate antibacterial activity (MIC = 32 μg mL^{-1}) when compared to the lead compound **1** (MIC = 16 μg mL^{-1}). This result was rationalized by the presence of a hydroxy group at 2-position and consequent increase in the hydrophilic character featured by **2**, given the known importance of aggregation phenomena in tuning the bioactivity for this family of surfactant glycosides [**1**–**3**]. This compound was also found to be a potent inhibitor of *B. anthracis* (MIC = 8-16 μg mL^{-1}, depending on the bacterial strain tested).

Dodecyl 2-deoxy-L-*threo*-pentopyranosides bearing α- (**3**) and β- (**18**) configuration were prepared following a more expedient synthetic route. Starting from L-xylose, the non-commercially available 3,4-di-*O*-acetyl-L-xylal **7** was accessed by acetylation, anomeric bromination and reductive elimination (54% overall yield). Addition of dodecanol to glycal **7** in the presence of triphenylphosphane hydrobromide afforded the acetylated 2-deoxy-α-glycoside **14** in 23% yield

and its β-stereoisomer **15** in 10% yield. Surprisingly, the 2,3-unsaturated α- and β-glycosides **16** and **17**, arising from allylic rearrangement, were also produced in significant yield (20% and 7%, respectively). Hence, further optimization should be carried out in order to improve the overall conversion efficiency into the desired saturated intermediates, i.e. via employing the corresponding perbenzylated glycal due to its presumably superior stability under acidic conditions. The 2-deoxyglycosides **3** and **18** were finally obtained through Zémplen deacetylation of **14** (64%) and **15** (99%), respectively. Interestingly, nuclear magnetic resonance data and theoretical calculations revealed that an unusual "all-axial" chair conformation may be assumed by the β-glycoside **18** in chloroform, but not in methanol, probably due to an exacerbated influence of the anomeric effect, and energetic stabilization by intramolecular hydrogen bonding, in the less polar solvent.

Regarding antibacterial activity, both stereoisomers **3** and **18** were active at the same concentration (MIC = 32 μg mL^{-1}), in contrast to the different biological behaviour presented by α- and β-*arabino*-hexopyranosides previously reported by our group [**1**–**3**], thus pinpointing that the increased flexibility of the pentopyranosyl ring structures may be able to modulate their antimicrobial properties. The two compounds were further effective towards *B. anthracis* (MIC = 8-16 μg mL^{-1}, depending on the bacterial strain tested).

Preparation of 2,6-dideoxy-2-fluoroglycosides analogous to the lead compound **1** was carried out based on electrophilic fluorination-nucleophilic addition reaction of dodecanol with appropriate glycal derivatives, and using selectfluor as fluorinating agent. When the commercially available 3,4-di-*O*-acetyl-6-deoxy-L-glucal **8** was employed, intermediate glycosides bearing α-L-*gluco*- (**24**), α-L-*manno*- (**25**) and β-L-*gluco*- (**26**) configuration could be isolated in only moderate overall yield (42%), probably due to the poor miscibility featured by the dodecanol/nitromethane system and consequently decreased reactivity of the alcohol in this preliminary reaction, which merits further optimization. The α-glycosides **24** and **25** were the major products of the reaction (37% overall yield) and were obtained as an inseparable mixture, which was subjected to deacetylation to afford target dodecyl 2,6-dideoxy-2-fluoro-α-L-*gluco*- (**4**) and α-L-*manno*-configurated (**5**) glycosides in high yield (89%), also as an inseparable mixture. The minor β-L-*gluco*-configurated glycoside **26** (5% yield), in turn, was not isolated in sufficient quantity to proceed to the next step. In order to study the relevance of the stereochemistry at the fluorinated position for bioactivity, a new approach was attempted aiming at manipulating the *gluco*/*manno*-stereoselectivity. For that purpose, persilylated glycal **27** was prepared in high yield (82%) through one-pot deacetylation of **8** followed by silylation. Reaction of **27** with selectfluor and dodecanol gave rise to improved *gluco*-diastereoselectivity, as intended, delivering silylated glycosides bearing α-L-*gluco*- (**28**) and β-L-*gluco*-configuration (**29**) in moderate yield (27%), although a decrease in α-diastereoselectivity was also observed. The α-L-*manno*-configurated (**30**) glycoside was produced in only minor proportions (7% yield) and thus could not be employed in the following step. Removal of the silyl ether protecting groups from the mixture containing **28** and **29** afforded the easily separable dodecyl 2,6-dideoxy-2-fluoro-α-L- (**4**) and β-L- (**31**) glucosides in nearly quantitative overall yield (95%).

The epimeric mixture containing glycosides **4** and **5** (**4**/**5** ≈ 1:3) was effective at a concentration competitive with that presented by the lead compound **1** (MIC = 16 μg mL^{-1}) and the same antibacterial activity was obseved for pure α-glucoside **4**. While these results put forward a similar biological behaviour for the two epimers, a diastereoselective synthetic route towards α-mannoside **5** is paramount to clarify such hypotesis. In agreement with known data for *arabino*-hexopyranosides [**1**–**3**], the β-anomer **31** was inactive in the range of concentrations tested. The very potent antibacterial activity displayed by the α-anomers strongly encourage the further evaluation of the microbial susceptibility of *B. anthracis* to these compounds, which will be undertaken in the near future. To our knowledge, this is the first example of both synthesis and microbial susceptibility evaluation of alkyl 2,6-dideoxy-2-fluoroglycosides. Taking into account the promising results obtained so far, further inspection of the impact of deoxygenation and fluorination at different positions (i.e. 2,6-dideoxy-6-fluoro pattern and/or 2,6-dideoxy-2,6-difluoro pattern) may eventually lead to molecular entities displaying optimized antimicrobial action.

Finally, it is worth noting that the results herein disclosed, in particular concerning the active compounds, encourage further assessement of their eventual citotoxicity since it is key to understand their therapeutic potential. In particular, the relevant antibacterial activities obtained against *B. anthracis* for some of the compounds encourage further optimization of these lead structures that we have disclosed herein. We consider also important the evaluation of the surface-active properties of the newly synthesized surfactant glycosides, in order to better understand the relationship between key structural features and bioactivity, particularly with respect to the deoxyfluoroglycosides since the fluorination of related carbohydrate-based surfactants has been shown to dramatically influence their physical properties [**94**].

Chapter 5

Experimental section

5.1 General methods and materials

All reagents and solvents were of analytical grade and were purchased from commercial suppliers. Unless otherwise mentioned, reagents were used as provided by the manufacturer without further purification. Amberlite IR-120 (H^+ active) resin was washed with MeOH prior to use. Anhydrous THF was freshly distilled from Na/bezophenone. Other anhydrous solvents were dried prior to use over a bed of activated 3 Å (MeOH) or 4 Å (other solvents) molecular sieves.

Reactions were carried out under N_2 atmosphere, except when aqueous solutions were present in the reaction media. Solutions were concentrated under reduced pressure using rotary evaporators (models R-200 and R-210, Büchi) and below 40 °C. Whenever necessary, compound dissolution was promoted by sonication using an ultrasonic bath (Ultrasonic Cleaner, VWR). A mechanical stirrer (VOS 14, VWR) was used on indicated experiments.

Reaction monitoring was performed by thin layer chromatography (TLC) on aluminium sheets precoated with 0.2 mm of silica gel 60 F_{254} (Merck). Detection was accomplished by exposure to UV radiation (254 nm) and immersion of the plates in a 10% ethanolic solution of H_2SO_4, followed by heating at 120 °C.

Products were purified either by flash column chromatography using silica gel 60 G (0.040-0.063 mm or 0.015-0.040 mm, Merck) applying low external pressure, or by preparative TLC on 20 × 20 cm plates precoated with silica gel 60 F_{254} (Merck).

Melting points (m.p.) were measured on a SMP 30 capillary apparatus (Stuart Scientific, Bibby) and were not corrected.

Specific rotations ($[\alpha]_D^{20}$) were measured on a Perkin-Elmer 343 digital polarimeter using a thermostated cell (1 dm path length). Sample concentrations (c) are expressed as g/100 mL of given solvent.

NMR spectra (^{1}H, ^{13}C and ^{19}F nuclei) were recorded using a Bruker Avance 400 spectrometer operating at 25 °C. Assignements were supported by bidimensional experiments (COSY, HMQB, HSQC, HMBC, NOESY and *J*-resolved). Chemical shifts (δ) are given in ppm, either using TMS as internal standard (for ^{1}H and ^{13}C NMR spectra aquired in chloroform-*d*) or relative to the deuterated solvent residual signal (for other solvents). Coupling constants (J) are reported in Hertz (Hz). Data for ^{1}H and ^{19}F NMR spectra are reported as follows: chemical shift, [multiplicity, coupling constant(s), integration, assignement]. Multiplicities are indicated as follows: s (singlet), d (doublet), t (triplet), q (quartet), quint. (quintet), dd (doublet of doublets), br s (broad singlet), app t (apparent triplet), etc. Data processing and analysis was performed using Brucker TopSpin^{TM} software package (version 3.2).

MS spectra were obtained on a LCQ DUO ion trap mass spectrometer from Thermo Scientific, equipped with an ESI ion source. Xcalibur^{TM} software package (version 1.2) was used for data analysis. HRMS spectra were acquired on a Apex Ultra FT-ICR mass spectrometer equipped with an external Apollo II Dual ESI/MALDI ion source from Bruker Daltonics, and a 7T actively shielded superconducting magnet from Magnex Scientific.

5.2 Compound index

#	Compound	Name	Experiment(s)	Page(s)
9	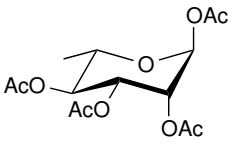	1,2,3,4-Tetra-*O*-acetyl-α-L-rhamnopyranose	1	-
10	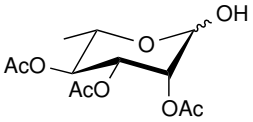	2,3,4-Tri-*O*-acetyl-L-rhamnopyranose	1	-
6	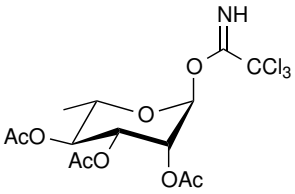	2,3,4-Tri-*O*-acetyl-α-L-rhamnopyranosyl trichloroacetimidate	2	-
11	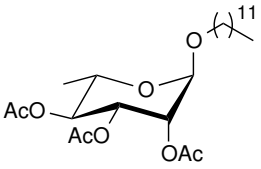	Dodecyl 2,3,4-tri-*O*-acetyl-α-L-rhamnopyranoside	3	-
2	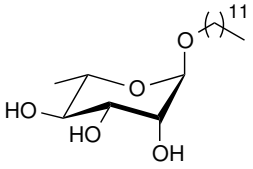	Dodecyl α-L-rhamnopyranoside	3	-

Continued on next page

Continued from previous page

#	Compound	Name	Experiment(s)	Page(s)
12	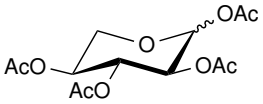	1,2,3,4-Tetra-*O*-acetyl-β-L-xylopyranose	4	-
13	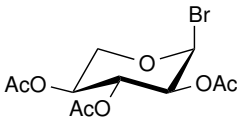	2,3,4-Tetra-*O*-acetyl-α-L-xylopyranosyl bromide	5	-
7	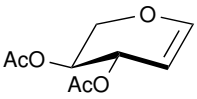	3,4-Di-*O*-acetyl-1,5-anhydro-2-deoxy-L-*threo*-pent-1-enitol	6	-
14	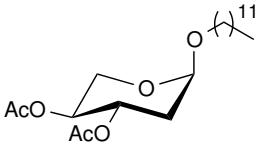	Dodecyl 3,4-di-*O*-acetyl-2-deoxy-α-L-*threo*-pentopyranoside	7	-
15	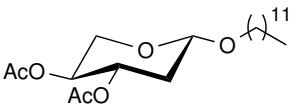	Dodecyl 3,4-di-*O*-acetyl-2-deoxy-β-L-*threo*-pentopyranoside	7	-

Continued on next page

Continued from previous page

#	Compound	Name	Experiment(s)	Page(s)
16	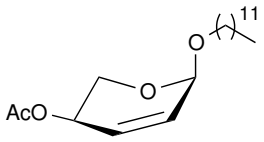	Dodecyl 4-*O*-acetyl-2,3-dideoxy-α-L-*glycero*-pent-2-enopyranoside	7	-
17	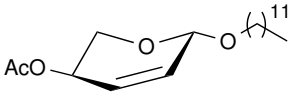	Dodecyl 4-*O*-acetyl-2,3-dideoxy-β-L-*glycero*-pent-2-enopyranoside	7	-
3	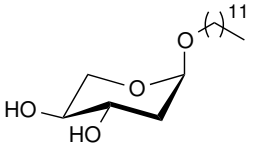	Dodecyl 2-deoxy-α-L-*threo*-pentopyranoside	8	-
18	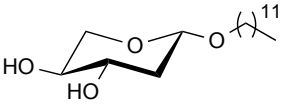	Dodecyl 2-deoxy-β-L-*threo*-pentopyranoside	9	-
24	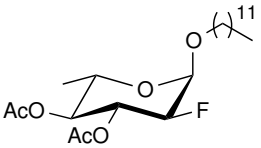	Dodecyl 3,4-di-*O*-acetyl-2,6-dideoxy-2-fluoro-α-L-glucopyranoside	10	-

Continued on next page

Continued from previous page

#	Compound	Name	Experiment(s)	Page(s)
25	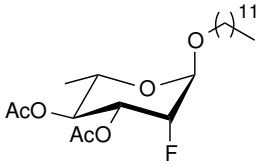	Dodecyl 3,4-di-*O*-acetyl-2,6-dideoxy-2-fluoro-α-L-mannopyranoside	10	-
26	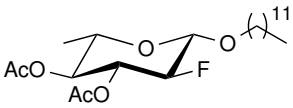	Dodecyl 3,4-di-*O*-acetyl-2,6-dideoxy-2-fluoro-β-L-glucopyranoside	10	-
4	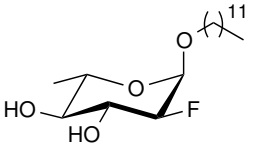	Dodecyl 2,6-dideoxy-2-fluoro-α-L-glucopyranoside	11, 14	-
5	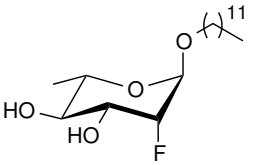	Dodecyl 2,6-dideoxy-2-fluoro-α-L-mannopyranoside	11	-
27	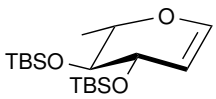	1,5-Anhydro-3,4-di-*O*-*tert*-butyldimethylsilyl-2,6-dideoxy-L-*arabino*-hex-1-enitol	12	-

Continued on next page

Continued from previous page

#	Compound	Name	Experiment(s)	Page(s)
28	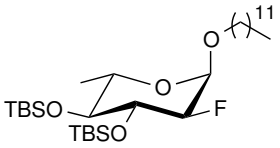	Dodecyl 3,4-di-*O*-*tert*-butyldimethylsilyl-2,6-dideoxy-2-fluoro-α-L-glucopyranoside	13	-
29	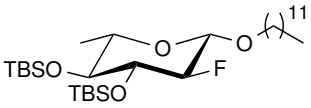	Dodecyl 3,4-di-*O*-*tert*-butyldimethylsilyl-2,6-dideoxy-2-fluoro-β-L-glucopyranoside	13	-
30	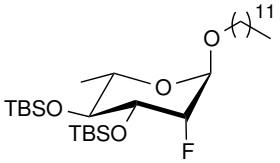	Dodecyl 3,4-di-*O*-*tert*-butyldimethylsilyl-2,6-dideoxy-2-fluoro-α-L-mannopyranoside	13	-
31	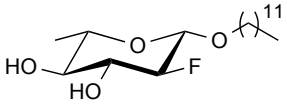	Dodecyl 2,6-dideoxy-2-fluoro-β-L-glucopyranoside	14	-

5.3 Synthesis

Experiment 1

1,2,3,4-Tetra-*O*-acetyl-α-L-rhamnopyranose **(9)**;
2,3,4-Tri-*O*-acetyl-L-rhamnopyranose **(10)**

Commercial L-(+)-rhamnose monohydrate (1.0 g, 5.5 mmol) was dissolved in pyridine (10 mL) and acetic anhydride (6.9 mL, 73.1 mmol) was added dropwise at 0 °C, followed by a catalytic amount of 4-(dimethylamino)pyridine. The reaction was allowed to reach room temperature and stirred overnight. CH_2Cl_2 was then added and the solution was washed with a 2M HCl aq. solution and brine, the combined organic layers dried ($MgSO_4$), filtered and concentrated under reduced pressure to yield a very viscous colourless oil of **9**, which was pure by NMR. The residue obtained was directly engaged in the next step without further purification.

$\boldsymbol{R_f} = 0.42$ (*n*-hexane/EtOAc, 2:1).

$[\alpha]_D^{\mathbf{20}} = -55°$ (*c* 0.98, $CHCl_3$).

^{1}H NMR (400 MHz, $CDCl_3$): $\delta = 6.02$ (br d, $^3J_{1,2} = 1.1$ Hz, 1H, H-1), 5.30 (dd, $^3J_{3,2} = 2.9$ Hz, $^3J_{3,4} = 9.9$ Hz, 1H, H-3), 5.25 (br dd, $^3J_{2,1} = 1.1$ Hz, $^3J_{2,3} = 2.9$ Hz, 1H, H-2), 5.13 (t, $^3J_{4,3} = {}^3J_{4,5} = 9.9$ Hz, 1H, H-4), 3.94 (dq, $^3J_{5,4} = 9.9$ Hz, $^3J_{5,6} = 6.2$ Hz, 1H, H-5), 2.17 (s, 3H, OAc), 2.16 (s, 3H, OAc), 2.07 (s, 3H, OAc), 2.01 (s, 3H, OAc), 1.24 (d, $^3J_{6,5} = 6.2$ Hz, 3H, CH_3-6).

^{13}C NMR (100 MHz, $CDCl_3$): $\delta = 170.1$, 169.9, 169.8, 168.4 (4 × $C_{quat.}$ OAc), 90.6 (C-1), 70.4 (C-4), 68.8 (C-3), 68.7 (C-5), 68.6 (C-2), 20.9, 20.8, 20.8, 20.7 (4 × CH_3 OAc), 17.4 (C-6).

MS (ESI): $m/z = 354.9$ $[M+Na]^+$.

To a solution the product of the previous step in anhydrous DMF (20 mL) was added hydrazine acetate (1.77 g, 19.2 mmol) at room temperature. The reaction was stirred until complete consumption of the starting material (96 h) and quenched by adding EtOAc. The solution was washed with brine and water, dried ($MgSO_4$), filtered and concentrated under reduced pressure to afford hemiacetal **10** as a white powder, after recristalization from EtOAc/*n*-hexane (1.36 g, 95% for two steps).

$\boldsymbol{R_f} = 0.21$ (*n*-hexane/EtOAc, 2:1).

$[\alpha]_D^{\mathbf{20}} = -26°$ (*c* 1.01, $CHCl_3$).

^{1}H NMR (400 MHz, $CDCl_3$): $\delta = 5.37$ (dd, $^3J_{3,2} = 3.4$ Hz, $^3J_{3,4} = 10.1$ Hz, 1H, H-3), 5.28 (br s, 1H, H-2), 5.17 (br s, 1H, H-1(α)), 5.09 (t, $^3J_{4,3} = {}^3J_{4,5} = 10.1$ Hz, 1H, H-4), 4.95 (d,

$^3J_{1(\beta),OH}$ = 9.4 Hz, H-1(β)) [1], 4.14 (dq, $^3J_{5,4}$ = 10.1 Hz, $^3J_{5,6}$ = 6.3 Hz, 1H, H-5), 3.54 (d, $^3J_{OH,1(\beta)}$ = 9.4 Hz, 1H, OH(β)) [1], 3.20 (d, $^3J_{OH,1(\alpha)}$ = 3.9 Hz, 1H, OH(α)), 2.16 (s, 3H, OAc), 3.06 (s, 3H, OAc), 2.00 (s, 3H, OAc), 1.23 (d, $^3J_{6,5}$ = 6.3 Hz, 3H, CH_3-6).

^{13}C NMR (100 MHz, $CDCl_3$): δ = 170.3, 170.2, 170.1 (3 × $C_{quat.}$ OAc), 92.6 (C-1(β))[1], 92.5 (C-1(α)), 71.1 (C-4), 70.2 (C-2), 68.8 (C-3), 66.4 (C-5), 21.0, 20.9, 20.8 (3 × CH_3 OAc), 17.5 (C-6).

MS (ESI): m/z = 313.1 $[M+Na]^+$.

Experiment 2

2,3,4-Tri-*O*-acetyl-α-L-rhamnopyranosyl trichloroacetimidate **(6)**

A solution of hemiacetal **10** (100 mg, 0.35 mmol) and trichloroacetonitrile (104 μL, 1.04 mmol) in anhydrous CH_2Cl_2 (1 mL) was cooled to 0 °C. 1,8-Diazabicyclo[5.4.0]undec-7-ene (16 μL, 0.11 mmol) was then added and the reaction was allowed to reach room temperature. After 2 h over stirring, the solution was concentrated under reduced pressure and the residue was purified by flash column chromatography on silica gel (*n*-hexane/EtOAc, 3:1 to 2:1) to give trichloroacetimidate **6** (133 mg, 89%) as a slightly yellow foam. NMR spectroscopic data was in agreement with the literature **[72]**.

$\boldsymbol{R_f}$ = 0.59 (*n*-hexane/EtOAc, 2:1).

^{1}H NMR (400 MHz, $CDCl_3$): δ = 8.74 (s, 1H, NH), 6.20 (br d, $^3J_{1,2}$ = 1.6 Hz, 1H, H-1), 5.46 (br dd, $^3J_{2,1}$ = 1.6 Hz, $^3J_{2,3}$ = 3.2 Hz, 1H, H-2), 5.37 (dd, $^3J_{3,2}$ = 3.2 Hz, $^3J_{3,4}$ = 10.1 Hz, 1H, H-3), 5.18 (t, $^3J_{4,3}$ = $^3J_{4,5}$ = 10.1 Hz, 1H, H-4), 4.09 (dq, $^3J_{5,4}$ = 10.1 Hz, $^3J_{5,6}$ = 6.2 Hz, 1H, H-5), 2.19 (s, 3H, OAc), 2.08 (s, 3H, OAc), 2.01 (s, 3H, OAc), 1.27 (d, $^3J_{6,5}$ = 6.2 Hz, 3H, CH_3-6).

^{13}C NMR (100 MHz, $CDCl_3$): δ = 169.9, 169.9, 169.8 (3 × $C_{quat.}$ OAc), 159.9 (C-1'), 94.6 (C-1), 90.6 (C-2'), 70.3 (C-4), 69.3 (C-5), 68.8 (C-3), 68.4 (C-2), 20.8, 20.8, 20.7 (3 × CH_3 OAc), 17.5 (C-6).

[1] Only trace amounts (<10%) of the β-anomer could be detected by NMR in $CDCl_3$.

Experiment 3

Dodecyl 2,3,4-tri-*O*-acetyl-α-L-rhamnopyranoside **(11)**;
Dodecyl α-L-rhamnopyranoside **(2)**

A solution of trichloroacetimidate **6** (68 mg, 0.16 mmol) and dodecanol (40 μL, 0.18 mmol) in anhydrous CH_2Cl_2 (2 mL) was stirred in the presence of activated 4 Å molecular sieves (100 mg) at room temperature for 30 min. The reaction was then cooled to 0 °C and trimethylsilyl triflate (3 μL, 0.02 mmol) was added. After 2 h at 0 °C, triethylamine was added dropwise until neutral pH and the solution was concentrated under vacuum. The residue containing glycoside **11** and several deacetylated products was immediately used in the next step. [2]

$\boldsymbol{R_f}$ = 0.72 (*n*-hexane/EtOAc, 3:2).

$[\alpha]_{\boldsymbol{D}}^{\mathbf{20}}$ = −48° (*c* 1.00, $CHCl_3$).

^{1}H NMR (400 MHz, $CDCl_3$): δ = 5.30 (dd, $^3J_{3,2}$ = 3.5 Hz, $^3J_{3,4}$ = 10.0 Hz, 1H, H-3), 5.23 (dd, $^3J_{2,1}$ = 1.7 Hz, $^3J_{2,3}$ = 3.5 Hz, 1H, H-2), 5.06 (t $^3J_{4,3}$ = $^3J_{4,5}$ = 10.0 Hz, 1H, H-4), 4.71 (d, $^3J_{1,2}$ = 1.7 Hz, 1H, H-1), 3.87 (dq,$^3J_{5,4}$ = 10.0 Hz, $^3J_{5,6}$ = 6.3 Hz, 1H, H-5), 3.66 (dt, $^2J_{1'a,1'b}$ = 9.6 Hz, $^3J_{1'a,2'a}$ = $^3J_{1'a,2'b}$ = 6.6 Hz, 1H, H-1'a), 3.42 (dt, $^2J_{1'b,1'a}$ = 9.6 Hz, $^3J_{1'b,2'a}$ = $^3J_{1'b,2'b}$ = 6.6 Hz, 1H, H-1'b), 2.15 (s, 3H, OAc), 2.05 (s, 3H, OAc), 1.99 (s, 3H, OAc), 1.62-1.54 (m, 2H, H-2'a,b), 1.37-1.24 (m, 18H, H-3'a,b - H-11'a,b), 1.22 (d, $^3J_{6,5}$ = 6.3 Hz, 3H, CH_3-6), 0.88 (t, $^3J_{12',11'}$ = 6.8 Hz, 3H, CH_3-12').

^{13}C NMR (100 MHz, $CDCl_3$): δ = 170.2, 170.1, 170.0 (3 × $C_{quat.}$ OAc), 97.4 (C-1), 71.2 (C-4), 70.0 (C-2), 69.2 (C-3), 68.3 (C-1'), 66.2 (C-5), 31.9, 29.7, 29.6, 29.6, 29.6, 29.4, 29.4, 29.3, 26.1, 22.7 (C-2' - C-11'), 21.0, 20.8, 20.8 (3 × CH_3 OAc), 17.4 (C-6), 14.1 (C-12').

MS (ESI): *m/z* = 481.2 $[M+Na]^+$.

The crude mixture obtained as described above was dissolved in anhydrous MeOH (0.5 mL). A 1M solution of sodium methoxide in MeOH (160 μL) was slowly added under vigorous stirring, and the reaction was allowed to proceed at room temperature overnight. The solution was neutralized by adding Amberlite IR-120, filtered and the solvent was evaporated under reduced pressure. Purification by flash column chromatography on silica gel (EtOAc) gave the desired glycoside **2** (37 mg, 71% over two steps) as a white powder, and its β-isomer (3 mg, 6% over two steps), which could not be isolated pure.

$\boldsymbol{R_f}$ = 0.49 (EtOAc).

m.p. = 48.8−49.7 °C.

[2] The residue obtained from another reaction following the same procedure as described above (starting from 100 mg of **6**) was subjected to purification by flash column chromatography on silica gel (CH_2Cl_2/MeOH, 99:1, several runs) to afford acetylated glycoside **11** as a colourless oil for characterization purposes.

$[\alpha]_D^{20} = -52°$ (c 1.00, $CHCl_3$).

^{1}H NMR (400 MHz, MeOD): δ = 4.68 (d, $^3J_{1,2}$ = 1.6 Hz, 1H, H-1), 3.81 (dd, $^3J_{2,1}$ = 1.6 Hz, $^3J_{2,3}$ = 3.4 Hz, 1H, H-2), 3.69 (dt, $^2J_{1'a,1'b}$ = 9.6 Hz, $^3J_{1'a,2'a}$ = $^3J_{1'a,2'b}$ = 6.4 Hz, 1H, H-1'a), 3.66 (dd, $^3J_{3,2}$ = 3.4 Hz,$^3J_{3,4}$ = 9.5 Hz, 1H, H-3), 3.60 (dq, $^3J_{5,4}$ = 9.5 Hz, $^3J_{5,6}$ = 6.3 Hz, 1H, H-5), 3.43 (dt, $^2J_{1'b,1'a}$ = 9.6 Hz, $^3J_{1'b,2'a}$ = $^3J_{1'b,2'b}$ = 6.4 Hz, 1H, H-1'b), 3.39 (t, $^3J_{4,3}$ = $^3J_{4,5}$ = 9.5 Hz, 1H, H-4), 1.65-1.57 (m, 2H, H-2'a,b), 1.42-1.31 (m, 18H, H-3'a,b - H-11'a,b), 1.29 (d, $^3J_{6,5}$ = 6.3 Hz, 3H, CH_3-6), 0.93 (t, $^3J_{12',11'}$ = 6.8 Hz, 3H, CH_3-12').

^{13}C NMR (100 MHz, MeOD): δ = 101.6 (C-1), 73.9 (C-4), 72.4 (C-3), 72.3 (C-2), 69.7 (C-5), 68.5 (C-1'), 33.0, 30.8, 30.7, 30.7, 30.7, 30.6, 30.5, 30.5, 27.3, 23.7 (C-2' - C-11'), 18.0 (C-6), 14.4 (C-12').

HRMS (ESI): m/z = calcd. for $C_{18}H_{36}NaO_5$ $[M+Na]^+$ 355.24549, found 355.24550.

Experiment 4

1,2,3,4-Tetra-*O*-acetyl-L-xylopyranose **(12)**

To a solution of commercial L-(-)-xylose (2.0 g, 13.3 mmol) in pyridine (20 mL) was added acetic anhydride (10.1 mL, 106.8 mmol), followed by a catalytic amount of 4-(dimethylamino)pyridine. The reaction mixture was stirred overnight at room temperature and then queched by careful addition of a 2M HCl aq. solution under ice bath. The mixture was extracted with CH_2Cl_2, the combined organic layers washed with satd. aq. $NaHCO_3$ solution and brine, dried ($MgSO_4$), filtered and concentrated under reduced pressure affording a very viscous colourless oil of peracetate **12** (4.23 g, quantitative) as a mixture of anomers (α/β = 1:0.15), which was used in the next step without further purification.

R_f = 0.42 (petroleum ether/EtOAc, 2:1).

MS (ESI): m/z = 341.0 $[M+Na]^+$.

Extracted data for the α-anomer:

^{1}H NMR (400 MHz, $CDCl_3$): δ = 6.26 (d, $^3J_{1,2}$ = 3.6 Hz, 1H, H-1), 5.47 (t, $^3J_{3,2}$ = $^3J_{3,4}$ = 9.8 Hz, 1H, H-3), 5.06-5.00 (m, 2H, H-2, H-4), 3.94 (dd, $^3J_{5e,4}$ = 5.8 Hz, $^2J_{5e,5a}$ = 11.0 Hz, 1H, H-5e), 3.72 (t, $^3J_{5a,4}$ = $^2J_{5a,5e}$ = 11.0 Hz, 1H, H-5a), 2.18 (s, 3H, OAc), 2.05 (s, 6H, 2 × OAc), 2.02 (s, 3H, OAc).

^{13}C NMR (100 MHz, $CDCl_3$): δ = 170.1, 169.8, 169.7, 169.0 (4 × $C_{quat.}$ OAc), 82.3 (C-1), 69.4, 69.4 (C-2, C-3), 68.7 (C-4), 60.7 (C-5), 20.9, 20.7, 20.7, 20.5 (4 × CH_3 OAc).

Extracted data for the β-anomer [3]:

^{1}H NMR (400 MHz, $CDCl_3$): δ = 5.72 (d, $^3J_{1,2}$ = 6.9 Hz, 1H, H-1), 5.21 (t, $^3J_{3,2} = {}^3J_{3,4}$ = 8.4 Hz, 1H, H-3), 5.08-4.94 (m, 2H, H-2, H-4), 4.15 (dd, $^3J_{5e,4}$ = 4.9 Hz, $^2J_{5e,5a}$ = 12.0 Hz, 1H, H-5e), 3.53 (dd, $^3J_{5a,4}$ = 8.4 Hz, $^2J_{5a,5e}$ = 12.0 Hz, 1H, H-5a), 2.11 (s, 3H, OAc), 2.06 (s, 3H, OAc), 2.05 (s, 6H, 2 × OAc).

^{13}C NMR (100 MHz, $CDCl_3$): δ = 169.9, 169.8, 169.1, 169.1 (4 × $C_{quat.}$ OAc), 92.0 (C-1), 80.0 (C-3), 69.5, 68.3, (C-2, C-4), 62.8 (C-5), 20.8, 20.7, 20.6, 20.5 (4 × CH_3 OAc).

Experiment 5

2,3,4-Tetra-*O*-acetyl-α-L-xylopyranosyl bromide **(13)**

Peracetate **12** (1.60 g, 5.0 mmol) was dissolved in anhydrous CH_2Cl_2 (11 mL) and acetic anhydride (0.32 mL, 3.4 mmol) was added. The solution was then cooled to 0 °C and a solution of hydrobromic acid (3.2 mL, 33 wt.% in AcOH) was added dropwise. The reaction was stirred for 1 h at 0 °C and for further 1 h at room temperature. The mixture was then diluted with CH_2Cl_2 (40 mL) and washed with water (15 mL), satd. aq. $NaHCO_3$ solution (2 × 15 mL) and brine (15 mL), and the combined organic phases were dried ($MgSO_4$). After filtration and evaporation of the solvent at room temperature, bromide **13** [3] (1.59 g, 93%) was obtained as a white solid, which was immediately used in the next step without additional purification.

$\boldsymbol{R_f}$ = 0.64 (petroleum ether/EtOAc, 2:1).

$[\alpha]_D^{20} = -178°$ (*c* 1.00, $CHCl_3$).

^{1}H NMR (400 MHz, $CDCl_3$): δ = 6.59 (d, $^3J_{1,2}$ = 3.9 Hz, 1H, H-1), 5.57 (t, $^3J_{3,2} = {}^3J_{3,4}$ = 9.8 Hz, 1H, H-3), 5.04 (ddd, $^3J_{4,3}$ = 9.8 Hz, $^3J_{4,5a}$ = 11.2 Hz, $^3J_{4,5e}$ = 6.1 Hz, 1H, H-4), 4.77 (dd, $^3J_{2,1}$ = 3.9 Hz, $^3J_{2,3}$ = 9.8 Hz, 1H, H-2), 4.06 (dd, $^3J_{5e,4}$ = 6.1 Hz, $^2J_{5e,5a}$ = 11.2 Hz, 1H, H-5e), 3.88 (t, $^3J_{5a,4} = {}^2J_{5a,5e}$ = 11.2 Hz, 1H, H-5a), 2.11 (s, 3H, OAc), 2.06 (s, 6H, 2 × OAc).

^{13}C NMR (100 MHz, $CDCl_3$): δ = 169.9, 169.9, 169.8 (3 × $C_{quat.}$ OAc), 87.6 (C-1), 70.9 (C-2), 69.6 (C-3), 68.1 (C-4), 62.5 (C-5), 20.7, 20.7, 20.6 (3 × CH_3 OAc).

MS (ESI): *m/z* = 360.0 $[M+Na]^+$, 362.0 $[M+2+Na]^+$.

[3] See ref. **[77]** for data regarding its enantiomer.

Experiment 6

3,4-Di-*O*-acetyl-1,5-anhydro-2-deoxy-L-*threo*-pent-1-enitol **(7)**

To a solution of bromide **13** (1.59 g, 4.69 mmol) in acetone (23 mL) under vigorous mechanical stirring was successively added solid sodium dihydrogen phosphate dihyrate (8.07 g, 51.8 mmol) and zinc powder (2.31 g, 35.3 mmol). After 10 min at room temperature, water (2.3 mL) was added, and the reaction was stirred for further 50 min. The solution was then diluted with EtOAc and filtered over a pad of celite. The filtrate was washed with satd. aq. $NaHCO_3$ solution (3 ×) and brine. The combined organic phases were dried ($MgSO_4$), filtered and concentrated under vacuum. The residue was purified by flash column chromatography on silica gel (petroleum ether/EtOAc, 4:1 to 3:1) to give glycal **7** [4] (0.54 g, 58%) as a colourless liquid.

$\boldsymbol{R_f} = 0.76$ (petroleum eter/EtOAc, 3:1).

^{1}H NMR (400 MHz, $CDCl_3$): $\delta = 6.61$ (d, $^3J_{1,2} = 5.6$ Hz, 1H, H-1), 5.00-4.95 (m, 3H, H-2, H-3, H-4), 4.20 (app d, $^2J_{5a,5b} = 12.3$ Hz, 1H, H-5a), 3.98 (app d, $^2J_{5b,5a} = 12.3$ Hz, 1H, H-5b), 2.10 (s, 3H, OAc), 2.07 (s, 3H, OAc).

^{13}C NMR (100 MHz, $CDCl_3$): $\delta = 169.9$, 169.8 (2 × $C_{quat.}$ OAc), 148.0 (C-1), 97.4 (C-2), 67.2 (C-4), 63.6 (C-5), 63.4 (C-3), 21.1, 21.0 (2 × CH_3 OAc).

MS (ESI): $m/z = 222.9$ $[M+Na]^+$.

Experiment 7

Dodecyl 3,4-di-*O*-acetyl-2-deoxy-α-L-*threo*-pentopyranoside **(14)**;
Dodecyl 3,4-di-*O*-acetyl-2-deoxy-β-L-*threo*-pentopyranoside **(15)**;
Dodecyl 4-*O*-acetyl-2,3-dideoxy-α-L-*glycero*-pent-2-enopyranoside **(16)**;
Dodecyl 4-*O*-acetyl-2,3-dideoxy-β-L-*glycero*-pent-2-enopyranoside **(17)**

A solution of dodecanol (592 mg, 3.18 mmol) and triphenylphosphane hydrobromide (98 mg, 0.29 mmol) in anhydrous CH_2Cl_2 (2 mL) was added to a stirred solution of glycal **7** (530 mg, 2.65 mmol) in anhydrous CH_2Cl_2 (2 mL). After 4 h at room temperature, the reaction mixture was diluted with CH_2Cl_2 and washed with satd. aq. $NaHCO_3$ solution. The combined organic layers were dried ($MgSO_4$), filtered and concentrated under vaccum. Purification of the residue by flash column chromatography on silica gel (*n*-hexane/EtOAc, 95:5, several runs) led to the

[4] See ref. [**78**] for data regarding its enantiomer.

isolation of the desired 2-deoxyglycosides **14** (237 mg, 23%) and **15** (103 mg, 10%) as colourless oils, as well as the 2,3-unsaturated glycosides **16** (163 mg, 20%) and **17** (55 mg, 7%) as a white solid and a colourless oil, respectively.

Dodecyl 3,4-di-*O*-acetyl-2-deoxy-α-L-*threo*-pentopyranoside **(14)**:

$\boldsymbol{R_f}$ = 0.55 (*n*-hexane/EtOAc, 6:1).

$[\alpha]_{\boldsymbol{D}}^{\mathbf{20}}$ = −58° (*c* 1.02, $CHCl_3$).

^{1}H NMR (400 MHz, $CDCl_3$): δ = 5.27 (br ddd, $^3J_{3,4}$ = 8.5 Hz, $^3J_{3,2a}$ = 10.1 Hz, $^3J_{3,2e}$ = 4.8 Hz, 1H, H-3), 4.86 (br ddd, $^3J_{4,3}$ = 8.5 Hz, $^3J_{4,5a}$ = 9.2 Hz, $^3J_{4,5e}$ = 5.0 Hz, 1H, H-4), 4.82 (app br t, $^3J_{1,2a}$ = 3.2 Hz, $^3J_{1,2e}$ = 2.8 Hz, 1H, H-1), 3.77 (dd, $^2J_{5e,5a}$ = 11.1 Hz, $^3J_{5e,4}$ = 5.0 Hz, 1H, H-5e), 3.69-3.62 (m, 2H, H-5a, H-1'a), 3.35 (dt, $^2J_{1'b,1'a}$ = 9.3 Hz, $^3J_{1'b,2'a}$ = $^3J_{1'b,2'b}$ = 6.7 Hz, 1H, H-1'b), 2.18 (br ddd, $^2J_{2e,2a}$ = 13.0 Hz, $^3J_{2e,3}$ = 4.8 Hz, $^3J_{2e,1}$ = 2.8 Hz, 1H, H-2e), 2.05 (s, 3H, OAc), 2.04 (s, 3H, OAc), 1.76 (br ddd, $^2J_{2a,2e}$ = 13.0 Hz, $^3J_{2a,3}$ = 10.1 Hz, $^3J_{2a,1}$ = 3.2 Hz, 1H, H-2a), 1.61-1.54 (m, 2H, H-2'a,b), 1.36-1.23 (m, 18H, H-3'a,b - H-11'a,b), 0.88 (t, $^3J_{12',11'}$ = 6.8 Hz, 3H, CH_3-12').

^{13}C NMR (100 MHz, $CDCl_3$): δ = 170.2, 170.1 (2 × $C_{quat.}$ OAc), 97.0 (C-1), 69.6 (C-4), 68.6 (C-3), 68.0 (C-1'), 59.8 (C-5), 34.6 (C-2), 31.9, 29.7, 29.6, 29.6, 29.6, 29.5, 29.5, 29.4, 26.2, 22.7 (C-2' - C-11'), 21.1, 20.9 (2 × CH_3 OAc), 14.1 (C-12').

MS (ESI): *m/z* = 409.2 $[M+Na]^+$.

Dodecyl 3,4-di-*O*-acetyl-2-deoxy-β-L-*threo*-pentopyranoside **(15)**:

$\boldsymbol{R_f}$ = 0.48 (*n*-hexane/EtOAc, 6:1).

$[\alpha]_{\boldsymbol{D}}^{\mathbf{20}}$ = +52° (*c* 1.00, $CHCl_3$).

^{1}H NMR (400 MHz, $CDCl_3$): δ = 4.94 (br ddd, $^3J_{3,4}$ = 6.5 Hz, $^3J_{3,2a}$ = 8.7 Hz, $^3J_{3,2e}$ = 4.6 Hz, 1H, H-3), 4.84 (br ddd, $^3J_{4,3}$ = 6.5 Hz, $^3J_{4,5a}$ = 7.3 Hz, $^3J_{4,5e}$ = 3.9 Hz, 1H, H-4), 4.62 (br dd, $^3J_{1,2a}$ = 6.3 Hz, $^3J_{1,2e}$ = 2.7 Hz, 1H, H-1), 4.12 (dd, $^2J_{5e,5a}$ = 12.1 Hz, $^3J_{5e,4}$ = 3.9 Hz, 1H, H-5e), 3.76 (dt, $^2J_{1'a,1'b}$ = 9.2 Hz, $^3J_{1'a,2'a}$ = $^3J_{1'a,2'b}$ = 6.8 Hz, 1H, H-1'a), 3.43-3.35 (m, 2H, H-5a, H-1'b), 2.23 (br ddd, $^2J_{2e,2a}$ = 13.3 Hz,$^3J_{2e,3}$ = 4.6 Hz,1H, H-2e), 2.07 (s, 3H, OAc), 2.06 (s, 3H, OAc), 1.79 (br ddd, $^2J_{2a,2e}$ = 13.3 Hz, $^3J_{2a,3}$ = 8.7 Hz, $^3J_{2a,1}$ = 6.3 Hz, $^3J_{2a,1}$ = 6.3 Hz, 1H, H-2a), 1.61-1.53 (m, 2H, H-2'a,b), 1.35-1.21 (m, 18H, H-3'a,b - H-11'a,b), 0.88 (t, $^3J_{12',11'}$ = 6.5 Hz, 3H, CH_3-12').

^{13}C NMR (100 MHz, $CDCl_3$): δ = 170.2, 170.1 (2 × $C_{quat.}$ OAc), 98.2 (C-1), 69.1 (C-4), 68.9 (C-1'), 68.6 (C-3), 60.9 (C-5), 33.3 (C-2), 31.9, 29.7, 29.7, 29.6, 29.6, 29.6, 29.4, 29.4, 26.1, 22.7 (C-2' - C-11'), 21.1, 21.0 (2 × CH_3 OAc), 14.1 (C-12').

MS (ESI): *m/z* = 409.1 $[M+Na]^+$.

Dodecyl 4-*O*-acetyl-2,3-dideoxy-α-L-*glycero*-pent-2-enopyranoside **(16)**:

$\boldsymbol{R_f}$ = 0.71 (*n*-hexane/EtOAc, 6:1).

m.p. = 40.4−41.1 °C.

$[\alpha]_{\boldsymbol{D}}^{\mathbf{20}}$ = −96° (*c* 1.00, $CHCl_3$).

^{1}H NMR (400 MHz, $CDCl_3$): δ = 6.07-6.04 (m, 2H, H-3, H-2), 4.99 (s, 1H, H-1), 4.95 (br s, 1H, H-4), 4.17 (dd, $^2J_{5a,5b}$ = 13.0 Hz, $^3J_{5a,4}$ = 2.0 Hz, 1H, H-5a), 3.83 (d, $^2J_{5b,5a}$ = 13.0 Hz, 1H, H-5b), 3.77 (dt, $^2J_{1'a,1'b}$ = 9.4 Hz, $^3J_{1'a,2'a}$ = $^3J_{1'a,2'b}$ = 6.7 Hz, 1H, H-1'a), 3.48 (dt, $^2J_{1'b,1'a}$ = 9.4 Hz, $^3J_{1'b,2'a}$ = $^3J_{1'a,2'b}$ = 6.7 Hz, 1H, H-1'b), 2.10 (s, 3H, OAc), 1.63-1.55 (m, 2H, H-2'a,b), 1.37-1.23 (m, 18H, H-3'a,b - H-11'a,b), 0.88 (t, $^3J_{12',11'}$ = 6.8 Hz, 3H, CH_3-12').

^{13}C NMR (100 MHz, $CDCl_3$): δ = 170.7 ($C_{quat.}$ OAc), 131.1, 124.9 (C-3, C-2), 93.0 (C-1), 68.7 (C-1'), 63.4 (C-4), 61.2 (C-5), 31.9, 29.7, 29.7, 29.6, 29.6, 29.6, 29.4, 29.4, 26.2, 22.7 (C-2' - C-11'), 21.1 (CH_3 OAc), 14.1 (C-12').

MS (ESI): *m/z* = 349.2 $[M+Na]^+$.

Dodecyl 4-*O*-acetyl-2,3-dideoxy-β-L-*glycero*-pent-2-enopyranoside **(17)**:

$\boldsymbol{R_f}$ = 0.78 (*n*-hexane/EtOAc, 6:1).

$[\alpha]_{\boldsymbol{D}}^{\mathbf{20}}$ = −51° (*c* 1.05, $CHCl_3$).

^{1}H NMR (400 MHz, $CDCl_3$): δ = 5.94 (br d, $^3J_{3,2}$ = 10.3 Hz, 1H, H-3), 5.87 (br d, $^3J_{2,3}$ = 10.3 Hz, 1H, H-2), 5.28 (br s, 1H, H-4), 4.93 (s, 1H, H-1), 3.88-3.74 (m, 3H, H-1'a, H-5a,b), 4.47 (dt, $^2J_{1'b,1'a}$ = 9.3 Hz, $^3J_{1'b,2'a}$ = $^3J_{1'b,2'b}$ = 6.7 Hz, 1H, H-1'b), 2.07 (s, 3H, OAc), 1.65-1.56 (m, 2H, H-2'a,b), 1.39-1.21 (m, 18H, H-3'a,b - H-11'a,b), 0.88 (t, $^3J_{12',11'}$ = 6.7 Hz , 3H, CH_3-12').

^{13}C NMR (100 MHz, $CDCl_3$): δ = 170.6 ($C_{quat.}$ OAc), 129.4 (C-2), 128.7 (C-3), 94.3 (C-1), 68.9 (C-1'), 65.0 (C-4), 60.2 (C-5), 31.9, 29.8, 29.7, 29.7, 29.6, 29.6, 29.4, 29.4, 26.2, 22.7 (C-2' - C-11'), 21.0 (CH_3 OAc), 14.1 (C-12').

MS (ESI): *m/z* = 349.3 $[M+Na]^+$.

Experiment 8

Dodecyl 2-deoxy-α-L-*threo*-pentopyranoside **(3)**

Acetylated glycoside **14** (201 mg, 0.52 mmol) was dissolved in anhydrous MeOH (2 mL). A 1M solution of sodium methoxide in MeOH (55 μL) was slowly added under vigorous stirring. After 1 h 15 min at room temperature, the reaction was neutralized by adding Amberlite IR-120, filtered and the solvent was evaporated under reduced pressure. Purification of the residue

by flash column chromatography on silica gel (*n*-hexane/EtOAc, 4:1 to EtOAc) gave the desired glycoside **3** (101 mg, 64%) as a white powder.

$\boldsymbol{R_f}$ = 0.43 (EtOAc/*n*-hexane, 3:1).

m.p. = 52.8−54.2 °C.

$[\alpha]_{\boldsymbol{D}}^{\boldsymbol{20}}$ = −62° (*c* 1.00, $CHCl_3$).

^{1}H NMR (400 MHz, $CDCl_3$): δ = 4.84 (br dd, $^3J_{1,2a}$ = 3.3 Hz, $^3J_{1,2e}$ = 1.7 Hz, 1H, H-1), 3.96-3.88 (m, 1H, H-3), 3.69 (dd, $^2J_{5e,5a}$ = 9.9 Hz, $^3J_{5e,4}$ = 4.1 Hz, 1H, H-5e), 3.63 (dt, $^2J_{1'a,1'b}$ = 9.3 Hz, $^3J_{1'a,2'a}$ = $^3J_{1'a,2'b}$ = 6.8 Hz, 1H, H-1'a), 3.59-3.46 (m, 2H, H-4, H-5a), 3.34 (dt, $^2J_{1'b,1'a}$ = 9.3 Hz, $^3J_{1'b,2'a}$ = $^3J_{1'b,2'b}$ = 6.8 Hz, 1H, H-1'b), 2.51 (br s, 1H, OH), 2.11 (br ddd, $^2J_{2e,2a}$ = 12.8 Hz, $^3J_{2e,3}$ = 4.1 Hz, $^3J_{2e,1}$ = 1.7 Hz, 1H, H-2e), 1.72 (br s, 1H, OH), 1.64 (br ddd, $^2J_{2a,2e}$ = 12.8 Hz, $^3J_{2a,3}$ = 10.9 Hz, $^3J_{2a,1}$ = 3.3 Hz, 1H, H-2a), 1.60-1.52 (m, 2H, H-2'a,b), 1.38-1.21 (m, 18H, H-3'a,b - H-11'a,b), 0.88 (t, $^3J_{12',11'}$ = 6.7 Hz, 3H, CH_3-12').

^{13}C NMR (100 MHz, $CDCl_3$): δ = 97.6 (C-1), 72.1 (C-4), 69.6 (C-3), 67.6 (C-1'), 62.1 (C-5), 37.3 (C-2), 31.9, 29.7, 29.6, 29.6, 29.6, 29.6, 29.5, 29.4, 26.2, 22.7 (C-2' - C-11'), 14.1 (C-12').

^{1}H NMR (400 MHz, MeOD): δ = 4.80 (br dd, $^3J_{1,2a}$ = 3.5 Hz, $^3J_{1,2e}$ = 1.7 Hz, 1H, H-1), 3.76 (br ddd, $^3J_{3,2a}$ = 10.8 Hz, $^3J_{3,4}$ = 8.1 Hz, $^3J_{3,2e}$ = 4.9 Hz, 1H, H-3), 3.63 (dt, $^2J_{1'a,1'b}$ = 9.3 Hz, $^3J_{1'a,2'a}$ = $^3J_{1'a,2'b}$ = 6.7 Hz, 1H, H-1'a), 3.59 (dd, $^2J_{5e,5a}$ = 10.1 Hz, $^3J_{5e,4}$ = 4.5 Hz, 1H, H-5e), 3.44 (t, $^2J_{5a,5e}$ = $^3J_{5a,4}$ = 10.1 Hz, 1H, H-5a), 3.42-3.32 (m, 2H, H-4, H-1'b), 2.02 (ddd, $^2J_{2e,2a}$ = 12.9 Hz, $^3J_{2e,3}$ = 4.9 Hz, $^3J_{2e,1}$ = 1.7 Hz, 1H, H-2e), 1.62-1.52 (m, 3H, H-2'a,b, H-2a), 1.41-1.24 (m, 18H, H-3'a,b - H-11'a,b), 0.90 (t, $^3J_{12',11'}$ = 6.7 Hz, 3H, CH_3-12').

^{13}C NMR (100 MHz, MeOD): δ = 99.0 (C-1), 72.5 (C-4), 69.9 (C-3), 68.4 (C-1'), 63.6 (C-5), 38.5 (C-2), 34.1, 30.8, 30.7, 30.7, 30.7, 30.7, 30.6, 30.5, 27.4, 23.7 (C-2' - C-11'), 14.4 (C-12').

HRMS (ESI): *m/z* = calcd. for $C_{17}H_{34}NaO_4$ $[M+Na]^+$ 325.23493, found 325.23488.

Experiment 9

Dodecyl 2-deoxy-β-L-*threo*-pentopyranoside **(18)**

Acetylated glycoside **15** (229 mg, 0.59 mmol) and dodecanol (471 mg, 2.53 mmol) were dissolved in anhydrous MeOH (5.6 mL). A 1M solution of sodium methoxide in MeOH (154 μL) was slowly added under vigorous stirring. After 3 h at room temperature, the reaction was neutralized by adding Amberlite IR-120, filtered and the solvent was evaporated under reduced pressure. Purification by flash column chromatography on silica gel (*n*-hexane/EtOAc, 1:1 to 1:4) gave the desired glycoside **18** (178 mg, 99%) as a white powder.

$\boldsymbol{R_f}$ = 0.43 (EtOAc/*n*-hexane, 3:1).

m.p. = 68.3−68.8 °C.

$[\alpha]_D^{20}$ = +72° (*c* 1.00, $CHCl_3$).

^{1}H NMR (400 MHz, $CDCl_3$): δ = 4.80 (br t, $^3J_{1,2a} = {}^3J_{1,2e}$ = 3.5 Hz, 1H, H-1), 4.15 (br dd, $^2J_{5e,5a}$ = 12.5 Hz, $^3J_{5e,4}$ = 1.7 Hz, 1H, H-5e [5]), 3.80-3.72 (m, 2H, H-3, H-1'a), 3.68-3.63 (m, 1H, H-4), 3.50-3.36 (m, 3H, H-5a [5], OH-3, H-1'b), 2.21 (br dt, $^2J_{2e,2a}$ = 14.2 Hz, $^3J_{2e,1} = {}^3J_{2e,3}$ = 3.5 Hz, 1H, H-2e [6]), 2.11-2.03 (m, 1H, OH-4), 1.78 (br dt, $^2J_{2a,2e}$ = 14.2 Hz, $^3J_{2a,1} = {}^3J_{2a,3}$ = 3.5 Hz, 1H, H-2a [6]), 1.63-1.56 (m, 2H, H-2'a,b), 1.37-1.22 (m, 18H, H-3'a,b - H-11'a,b), 0.88 (t, $^3J_{12',11'}$ = 6.7 Hz, 3H, CH_3-12').

^{13}C NMR (100 MHz, $CDCl_3$): δ = 98.1 (C-1), 69.1 (C-4), 68.6 (C-1'), 67.9 (C-3), 60.8 (C-5), 32.3 (C-2), 31.9, 29.7, 29.6, 29.6, 29.6, 29.5, 29.4, 29.4, 26.2, 22.7 (C-2' - C-11'), 14.1 (C-12').

^{1}H NMR (400 MHz, MeOD): δ = 4.53 (dd, $^3J_{1,2a}$ = 8.4 Hz, $^3J_{1,2e}$ = 1.9 Hz, 1H, H-1), 3.90 (dd, $^2J_{5e,5a}$ = 11.5 Hz, $^3J_{5e,4}$ = 4.7 Hz, 1H, H-5e), 3.78 (dt, $^2J_{1'a,1'b}$ = 9.4 Hz, $^3J_{1'a,2'a} = {}^3J_{1'a,2'b}$ = 6.7 Hz, 1H, H-1'a), 3.52 (ddd, $^3J_{3,2a}$ = 10.2 Hz, $^3J_{3,4}$ = 8.1 Hz, $^3J_{2e,3}$ = 4.8 Hz, 1H, H-3), 3.44 (dt, $^2J_{1'b,1'a}$ = 9.4 Hz, $^3J_{1'b,2'a} = {}^3J_{1'b,2'b}$ = 6.7 Hz, 1H, H-1'b), 3.38 (ddd, $^3J_{4,5a}$ = 9.0 Hz, $^3J_{4,3}$ = 8.1 Hz, $^3J_{4,5e}$ = 4.7 Hz, 1H, H-4), 3.17 (dd, $^2J_{5a,5e}$ = 11.5 Hz, $^3J_{5a,4}$ = 9.0 Hz, 1H, H-5a), 2.11 (ddd, $^2J_{2e,2a}$ = 12.8 Hz, $^3J_{2e,3}$ = 4.8 Hz, $^3J_{2e,1}$ = 1.9 Hz, 1H, H-2e), 1.60-1.53 (m, 2H, H-2'a,b), 1.48 (ddd, $^2J_{2a,2e}$ = 12.8 Hz, $^3J_{2a,3}$ = 10.2 Hz, $^3J_{2a,1}$ = 8.4 Hz, 1H, H-2a), 1.37-1.25 (m, 18H, H-3'a,b - H-11'a,b), 0.90 (t, $^3J_{12',11'}$ = 6.7 Hz, 3H, CH_3-12').

^{13}C NMR (100 MHz, MeOD): δ = 101.5 (C-1), 72.1 (C-4), 71.7 (C-3), 70.1 (C-1'), 66.1 (C-5), 38.8 (C-2), 33.1, 30.8, 30.8, 30.8, 30.7, 30.7, 30.5, 30.5, 27.2, 23.8 (C-2' - C-11'), 14.5 (C-12').

HRMS (ESI): *m/z* = calcd. for $C_{17}H_{34}NaO_4$ $[M+Na]^+$ 325.23493, found 325.23485.

Experiment 10

Dodecyl 3,4-di-*O*-acetyl-2,6-dideoxy-2-fluoro-α-L-glucopyranoside **(24)**;
Dodecyl 3,4-di-*O*-acetyl-2,6-dideoxy-2-fluoro-α-L-mannopyranoside **(25)**;
Dodecyl 3,4-di-*O*-acetyl-2,6-dideoxy-2-fluoro-β-L-glucopyranoside **(26)**

A solution of commercial 3,4-di-*O*-acetyl-6-deoxy-L-glucal **8** (650 mg, 3.03 mmol) in anhydrous $MeNO_2$ (25 mL) was stirred in the presence of activated 4 Å molecular sieves (200 mg) at room temperature for 30 min. Selectfluor bis(tetrafluoroborate) (1.29 g, 3.64 mmol) was then added and the mixtured was stirred overnight. A solution of dodecanol (1.24 g, 6.68 mmol) in anhydrous $MeNO_2$ was added and the reaction mixture was warmed to 90 °C. After 48 h, the mixture was poured into CH_2Cl_2, filtered over a pad of celite and concentrated under reduced

[5] H-5e,a were assigned as permutable signals.
[6] H-2e,a were assigned as permutable signals.

pressure. The resulting residue was purified by flash column chromatography on silica gel (*n*-hexane/EtOAc, 10:1 to 5:1) to give *α-gluco* glycoside **24** and *α-manno* glycoside **25** (469 mg, 37% total yield) as an inseparable mixture of epimers (0.8:1), and the *β-gluco* glycoside **24** (68 mg, 5%) as light brown needles, after crystallization from methanol.

Extracted data for dodecyl 3,4-di-*O*-acetyl-2,6-dideoxy-2-fluoro-α-L-glucopyranoside **(24)**:

$\boldsymbol{R_f}$ = 0.68 (*n*-hexane/EtOAc, 4:1).

^{1}H NMR (400 MHz, $CDCl_3$): δ = 5.50 (dt, $^3J_{3,F}$ = 12.0 Hz, $^3J_{3,2} = {}^3J_{3,4}$ = 9.7 Hz, 1H, H-3), 4.97 (d, $^3J_{1,2}$ = 3.8 Hz, 1H, H-1), 4.73 (t, $^3J_{4,3} = {}^3J_{4,5}$ = 9.7 Hz, 1H, H-4), 4.46 (ddd, $^2J_{2,F}$ = 49.6 Hz, $^3J_{2,3}$ = 9.7 Hz, $^3J_{2,1}$ = 3.8 Hz, 1H, H-2), 3.92 (dq, $^3J_{5,4}$ = 9.7 Hz, $^3J_{5,6}$ = 6.3 Hz, 1H, H-5), 3.71 (dt, $^2J_{1'a,1'b}$ = 9.5 Hz, $^3J_{1'a,2'a} = {}^3J_{1'a,2'b}$ = 6.6 Hz, 1H, H-1'a), 3.49 (dt, $^2J_{1'b,1'a}$ = 9.5 Hz, $^3J_{1'b,2'a} = {}^3J_{1'b,2'b}$ = 6.6 Hz, 1H, H-1'b), 2.06 (s, 3H, OAc), 2.05 (s, 3H, OAc), 1.70-1.55 (m, 2H, H-2'a,b), 1.38-1.24 (m, 18H, H-3'a,b - H-11'a,b), 1.17 (d, $^3J_{6,5}$ = 6.3 Hz, 1H, CH_3-6), 0.88 (t, $^3J_{12',11'}$ = 6.8 Hz, 3H, CH_3-12').

^{13}C NMR (100 MHz, $CDCl_3$): δ = 170.2, 170.0 (2 × $C_{quat.}$ OAc), 95.8 (d, $^2J_{1,F}$ = 20.2 Hz, C-1), 87.7 (d, $^1J_{2,F}$ = 194.5 Hz, C-2), 73.6 (d, $^3J_{4,F}$ = 7.0 Hz, C-4), 70.8 (d, $^2J_{3,F}$ = 19.2 Hz, C-3), 68.8 (C-1'), 65.0 (C-5), 31.9, 29.7, 29.6, 29.6, 29.6, 29.4, 29.4, 29.4, 26.0, 22.7 (C-2' - C-11'), 20.8, 20.7 (2 × CH_3 OAc), 17.2 (C-6), 14.1 (C-12').

^{19}F NMR (376 MHz, $CDCl_3$): δ = −201.2 (dd, $^2J_{F,2}$ = 49.6 Hz, $^3J_{F,3}$ = 12.0 Hz).

MS (ESI): *m/z* = 441.3 $[M+Na]^+$.

Extracted data for dodecyl 3,4-di-*O*-acetyl-2,6-dideoxy-2-fluoro-α-L-mannopyranoside **(25)**:

$\boldsymbol{R_f}$ = 0.68 (*n*-hexane/EtOAc, 4:1).

^{1}H NMR (400 MHz, $CDCl_3$): δ = 5.22 (ddd, $^3J_{3,F}$ = 28.8 Hz, $^3J_{3,4}$ = 10.1 Hz, $^3J_{3,2}$ = 2.6 Hz, 1H, H-3), 5.10 (t, $^3J_{4,5}$ = 9.7 Hz, 1H, H-4), 4.90 (dd, $^3J_{1,F}$ = 7.5 Hz, $^3J_{1,2}$ = 1.6 Hz, 1H, H-1), 4.72 (ddd, $^2J_{2,F}$ = 50.2 Hz, $^3J_{2,3}$ = 2.6 Hz, $^3J_{2,1}$ = 1.6 Hz, 1H, H-2) [7], 3.87 (dq, $^3J_{5,4}$ = 9.7 Hz, $^3J_{5,6}$ = 6.3 Hz, 1H, H-5), 3.70 (dt, $^2J_{1'a,1'b}$ = 9.6 Hz, $^3J_{1'a,2'a} = {}^3J_{1'a,2'b}$ = 6.7 Hz, 1H, H-1'a), 3.45 (dt, $^2J_{1'b,1'a}$ = 9.6 Hz, $^3J_{1'b,2'a} = {}^3J_{1'b,2'b}$ = 6.7 Hz, 1H, H-1'b), 2.09 (s, 3H, OAc), 2.05 (s, 3H, OAc), 1.70-1.55 (m, 2H, H-2'a,b), 1.38-1.24 (m, 18H, H-3'a,b - H-11'a,b), 1.22 (d, $^3J_{6,5}$ = 6.3 Hz, 1H, CH_3-6), 0.88 (t, $^3J_{12',11'}$ = 6.8 Hz, 3H, CH_3-12').

^{13}C NMR (100 MHz, $CDCl_3$): δ = 170.3, 169.8 (2 × $C_{quat.}$ OAc), 97.0 (d, $^2J_{1,F}$ = 28.8 Hz, C-1), 87.5 (d, $^1J_{2,F}$ = 178.6 Hz, C-2), 71.0 (C-4), 70.1 (d, $^2J_{3,F}$ = 16.6 Hz, C-3), 68.4 (C-1'), 66.3 (C-5), 31.9, 29.7, 29.6, 29.6, 29.6, 29.4, 29.4, 29.3, 26.0, 22.7 (C-2' - C-11'), 20.8, 20.8 (2 × CH_3 OAc), 17.3 (C-6), 14.1 (C-12').

[7] The signal was observed as an apparent doublet of triplets, due to the very similar values of $^3J_{2,1}$ and $^3J_{2,3}$. However, both multiplicity and coupling constants could be confirmed by *J*-resolved experiments and extracted from the H-3 and H-1 signals.

^{19}F NMR (376 MHz, $CDCl_3$): $\delta = -204.1$ (ddd, $^2J_{F,2} = 50.2$ Hz, $^3J_{F,3} = 28.8$ Hz, $^3J_{F,1} = 7.5$ Hz).

MS (ESI): $m/z = 441.3$ $[M+Na]^+$.

Dodecyl 3,4-di-*O*-acetyl-2,6-dideoxy-2-fluoro-β-L-glucopyranoside **(26)**:

$\boldsymbol{R_f} = 0.59$ (*n*-hexane/EtOAc, 4:1).

m.p. = 62.7−63.8 °C.

$[\alpha]_{\boldsymbol{D}}^{\mathbf{20}} = -22°$ (*c* 1.00, $CHCl_3$).

^{1}H NMR (400 MHz, $CDCl_3$): $\delta = 5.26$ (dt, $^3J_{3,F} = 14.6$ Hz, $^3J_{3,4} = {}^3J_{3,2} = 9.3$ Hz, 1H, H-3), 4.76 (t, $^3J_{4,5} = 9.6$ Hz, 1H, H-4), 4.52 (dd, $^3J_{1,2} = 7.7$ Hz, $^3J_{1,F} = 2.7$ Hz, 1H, H-1), 4.26 (br ddd, $^2J_{2,F} = 50.8$ Hz, $^3J_{2,3} = 9.3$ Hz, $^3J_{2,1} = 7.7$ Hz, 1H, H-2), 3.88 (dt, $^2J_{1'a,1'b} = 9.3$ Hz, $^3J_{1'a,2'a} = {}^3J_{1'a,2'b} = 6.7$ Hz, 1H, H-1'a), 3.57 (dq, $^3J_{5,4} = 9.6$ Hz, $^3J_{5,6} = 6.3$ Hz, 1H, H-5), (dt, $^2J_{1'b,1'a} = 9.3$ Hz, $^3J_{1'b,2'a} = {}^3J_{1'b,2'b} = 6.7$ Hz, 1H, H-1'b), 2.07 (s, 3H, OAc), 2.04 (s, 3H, OAc), 1.68-1.56 (m, 2H, H-2'a,b), 1.38-1.24 (m, 18H, H-3'a,b - H-11'a,b), 1.23 (d, $^3J_{6,5} = 6.3$ Hz, 1H, CH_3-6), 0.88 (t, $^3J_{12',11'} = 6.8$ Hz, 3H, CH_3-12').

^{13}C NMR (100 MHz, $CDCl_3$): $\delta = 170.2$, 169.8 (2 × $C_{quat.}$ OAc), 100.2 (d, $^2J_{1,F} = 22.0$ Hz, C-1), 89.8 (d, $^1J_{2,F} = 190.6$ Hz, C-2), 73.2 (d, $^3J_{4,F} = 7.2$ Hz, C-4), 73.0 (d, $^2J_{3,F} = 19.5$ Hz, C-3), 70.4 (C-1'), 69.9 (C-5), 31.9, 29.7, 29.6, 29.6, 29.5, 29.5, 29.4, 29.4, 25.8, 22.7 (C-2' - C-11'), 20.8, 20.7 (2 × CH_3 OAc), 17.3 (C-6), 14.1 (C-12').

^{19}F NMR (376 MHz, $CDCl_3$): $\delta = -199.4$ (app dd, $^2J_{F,2} = 50.8$ Hz, $^3J_{F,3} = 14.6$ Hz) [8].

MS (ESI): $m/z = 441.1$ $[M+Na]^+$.

Experiment 11

Dodecyl 2,6-dideoxy-2-fluoro-α-L-glucopyranoside **(4)**;
Dodecyl 2,6-dideoxy-2-fluoro-α-L-mannopyranoside **(5)**

A mixture of epimeric glycosides **24** and **25** (435 mg, 1.04 mmol, ratio 1:0.8) was dissolved in anhydrous MeOH (4 mL) and the solution was stirred at room temperature. A 1M solution of sodium methoxide in MeOH (480 μL) was then slowly added. After 3 h 30 min the reaction was neutralized by adding Amberlite IR-120, filtered and the solvent was evaporated under reduced pressure. Purification by flash column chromatography on silica gel (petroleum ether/EtOAc, 2:1 to 100% EtOAc) gave a mixture of the target glycosides **4** and **5** as a very clear colourless oil (310 mg, 89%) that turned into a white powder upon crystallization from petroleum ether.

[8] The signal was observed as an apparent doublet of doublets, although a vicinal couping constant with H-1 ($^3J_{F,1} = 2.7$ Hz) could be observed in the ^{1}H NMR spectrum and confirmed by *J*-resolved experiments.

HRMS (ESI): m/z = calcd. for $C_{18}H_{35}FNaO_4$ $[M+Na]^+$ 357.24116, found 357.24121.

Extracted data for dodecyl 2,6-dideoxy-2-fluoro-α-L-mannopyranoside **(5)** [9]:

$\boldsymbol{R_f}$ = 0.44 (petroleum ether/EtOAc, 2:1).

^{1}H NMR (400 MHz, $CDCl_3$): δ = 4.89 (dd, $^3J_{1,F}$ = 7.7 Hz, $^3J_{1,2}$ = 1.7 Hz, 1H, H-1), 4.66 (ddd, $^2J_{2,F}$ = 50.2 Hz, $^3J_{2,3}$ = 2.8 Hz, $^3J_{2,1}$ = 1.7 Hz, 1H, H-2) [10], 3.86-3.65 (m, 3H, H-3, H-5, H-1'a), 3.47 (t, $^3J_{4,3} = {}^3J_{4,5}$ = 9.4 Hz, 1H, H-4), 3.42 (dt, $^2J_{1'b,1'a}$ = 9.6 Hz, $^3J_{1'b,2'a} = {}^3J_{1'b,2'b}$ = 6.5 Hz, 1H, H-1'b), 2.37 (br s, 1H, OH-4), 2.22 (br s, 1H, OH-3), 1.67-2.53 (m, 2H, H-2'a,b), 1.36.1.23 (m, 21H, H-3'a,b - H-11'a,b, CH_3-6) [11], 0.88 (t, $^3J_{12',11'}$ = 7.2 Hz, 3H, CH_3-12').

^{13}C NMR (100 MHz, $CDCl_3$): δ = 97.1 (d, $^2J_{1,F}$ = 29.2 Hz, C-1), 89.8 (d, $^1J_{2,F}$ = 173.2 Hz, C-2), 73.7 (C-4), 71.2 (d, $^2J_{3,F}$ = 17.7 Hz, C-3), 68.0 (C-1'), 67.9 (C-5), 31.9, 29.7, 29.6, 29.6, 29.6, 29.4, 29.4, 29.4, 26.0, 22.7 (C-2' - C-11'), 17.4 (C-6), 14.1 (C-12').

^{19}F NMR (376 MHz, $CDCl_3$): δ = −206.5 (ddd, $^2J_{F,2}$ = 50.2 Hz, $^3J_{F,3}$ = 29.9 Hz, $^3J_{F,1}$ = 7.7 Hz) .

Experiment 12

1,5-Anhydro-3,4-di-*O*-*tert*-butyldimethylsilyl-2,6-dideoxy-L-*arabino*-hex-1-enitol **(27)**

Sodium methoxide (24 mg, 0.44 mmol) was added to a stirred solution of commercial 3,4-di-*O*-acetyl-6-deoxy-L-glucal **8** (566 mg, 2.64 mmol) in anhydrous MeOH (5 mL). After 1 h at room temperature, the solvent was evaporated under reduced pressure. The residue was resuspended in anhydrous DMF (20 mL) and the solution was cooled to 0 °C. Imidazole (1.80 g, 26.4 mmol) and *tert*-butyldimethylsilyl chloride (3.98 g, 26.4 mmol) were added successively and the mixture was allowed to reach room temperature. After 48 h, the solution was poured into brine and the aqueous phase was extracted with EtOAc (3 ×). The combined organic layers were washed with satd. aq. $NaHCO_3$ solution, then brine, and dried ($MgSO_4$). After filtration and evaporation of of the solvent under vacuum, the crude product was purified by flash column chromatography on silica gel (*n*-hexane/EtOAc, 95:5 to 9:1) to give silylated glycal **27** (780 mg, 82%) as a very clear colourless liquid.

$\boldsymbol{R_f}$ = 0.82 (*n*-hexane/EtOAc, 95:5).

$[\alpha]_{\boldsymbol{D}}^{\mathbf{20}}$ = +45° (*c* 1.16, $CHCl_3$).

[9] Full physical and spectroscopic characterization of dodecyl 2,6-dideoxy-2-fluoro-α-L-glucopyranoside **(4)** is provided in **Experiment 17**.

[10] The signal was observed as an apparent doublet of triplets, due to the very similar values of $^3J_{2,1}$ and $^3J_{2,3}$. However, both multiplicity and coupling constants could be extracted from the *J*-resolved spectrum.

[11] The H-6 signal could be observed as a doublet at 1.33 ppm ($^3J_{6,5}$ = 6.3 Hz, extracted from the *J*-resolved spectrum).

^{1}H NMR (400 MHz, $CDCl_3$): δ = 6.28 (d, $^3J_{1,2}$ = 6.1 Hz, 1H, H-1), 6.65 (br dd, $^3J_{2,1}$ = 6.1 Hz, $^3J_{2,3}$ = 3.1 Hz, 1H, H-2), 4.10-4.06 (m, 1H, H-3), 3.93 (app quint., $^3J_{5,4}$ = 7.1 Hz, $^3J_{5,6}$ = 6.6 Hz, 1H, H-5), 3.56 (br t, $^3J_{4,3} \approx {}^3J_{4,5}$ = 7.1 Hz, 1H, H-4), 1.31 (d, $^3J_{6,5}$ = 6.6 Hz, 3H, CH_3-6), 0.90 (s, 18H, 2 × *t*-BuSi), 0.11 (s, 3H, CH_3Si), 0.10 (br s, 9H, 3 × CH_3Si).

^{13}C NMR (100 MHz, $CDCl_3$): δ = 143.1 (C-1), 102.9 (C-2), 75.2 (C-5), 74.7 (C-4), 69.4 (C-3), 26.0, 25.9 (2 × $(CH_3)_3$ *t*-BuSi), 18.1, 18.0 (2 × $C_{quat.}$ *t*-BuSi), 17.2 (C-6), -3.7, -3.9, -4.2, -4.3 (4 × CH_3Si).

MS (ESI): m/z = 381.2 $[M+Na]^+$.

Experiment 13

Dodecyl 3,4-di-*O*-*tert*-butyldimethylsilyl-2,6-dideoxy-2-fluoro-α-L-glucopyranoside **(28)**;
Dodecyl 3,4-di-*O*-*tert*-butyldimethylsilyl-2,6-dideoxy-2-fluoro-β-L-glucopyranoside **(29)**;
Dodecyl 3,4-di-*O*-*tert*-butyldimethylsilyl-2,6-dideoxy-2-fluoro-α-L-mannopyranoside **(30)**

A solution of glycal **27** (750 mg, 2.09 mmol) in anhydrous $MeNO_2$ (30 mL) was stirred in the presence of activated 4 Å molecular sieves (1 g) at room temperature for 2 h. The solution was then cooled to 0 °C and selectfluor bis(tetrafluoroborate) (1.11 g, 3.14 mmol) was added very quickly. The mixture was allowed to reach room temperature and stirred for 20 h. Dodecanol (0.56 mL, 2.51 mmol) was then added and the reaction was stirred at 45 °C for 24 h and at 90 °C for further 24h. The mixture was then poured into EtOAc, filtered over a pad of celite and concentrated under reduced pressure. The resulting residue was purified by flash column chromatography on silica gel (*n*-hexane/CH_2Cl_2, 4:1 to 2:1) to give glycosides **28** and **29** (313 mg, 27% total yield) as an inseparable mixture of anomers (α/β = 1:1.3), and the α-*manno* glycoside **30** (77 mg, 7%) as a colourless oil.

Extracted data for dodecyl 3,4-di-*O*-*tert*-butyldimethylsilyl-2,6-dideoxy-2-fluoro-α-L-glucopyranoside **(28)**:

$\boldsymbol{R_f}$ = 0.53 (*n*-hexane/CH_2Cl_2, 3:1).

^{1}H NMR (400 MHz, $CDCl_3$): δ = 4.85 (d, $^3J_{1,2}$ = 3.8 Hz, 1H, H-1), 4.16 (ddd, $^2J_{2,F}$ = 48.7 Hz, $^3J_{2,3}$ = 9.3 Hz, $^3J_{2,1}$ = 3.8 Hz, 1H, H-2), 4.01 (ddd, $^3J_{3,F}$ = 10.5 Hz, $^3J_{3,2}$ = 9.3 Hz, $^3J_{3,4}$ = 8.2 Hz, 1H, H-3), 3.70-3.62 (m, 2H, H-1'a, H-5), 3.43 (dt, $^2J_{1'b,1'a}$ = 9.5 Hz, $^3J_{1'b,2'a} = {}^3J_{1'b,2'b}$ = 6.7 Hz, 1H, H-1'b), 3.16 (dd, $^3J_{4,5}$ = 9.4 Hz, $^3J_{4,3}$ = 8.2 Hz, 1H, H-4) [12], 1.68-1.54 (m, 2H, H-2'a,b), 1.38-1.22 (m, 18H, H-3'a,b - H-11'a,b), 1.20 (d, $^3J_{6,5}$ = 6.5 Hz, 1H, CH_3-6), 0.91 (s, 9H, *t*-BuSi), 0.90 (s, 9H, *t*-BuSi), 0.88 (t, $^3J_{12',11'}$ = 7.2 Hz, 3H, CH_3-12'), 0.13-0.08 (m, 12H, 4 × CH_3Si).

[12] H-4 was observed as an apparent triplet in the ^{1}H NMR spectrum, due to the very similar values of $^3J_{4,3}$ and $^3J_{4,5}$. However, both multiplicity and coupling constants could be extracted from the *J*-resolved spectrum.

^{13}C NMR (100 MHz, $CDCl_3$): δ = 96.2 (d, $^2J_{1,F}$ = 21.5 Hz, C-1), 90.8 (d, $^1J_{2,F}$ = 190.8 Hz, C-2), 76.9 (C-4) [13], 73.3 (d, $^2J_{3,F}$ = 16.1 Hz, C-3), 68.3 (C-5), 68.1 (C-1'), 31.9, 29.7, 29.7, 29.7, 29.6, 29.6, 29.5, 29.4, 26.4, 26.1, 26.0, 22.7 (C-2' - C-11', 2 × $(CH_3)_3$ *t*-BuSi), 18.6, 18.4 (2 × $C_{quat.}$ *t*-BuSi), 18.1 (C-6), 14.1 (C-12'), -2.5, -2.6, -3.5, -3.8 (4 × CH_3Si).

^{19}F NMR (376 MHz, $CDCl_3$): δ = −195.8 (dd, $^2J_{F,2}$ = 48.7 Hz, $^3J_{F,3}$ = 10.5 Hz).

MS (ESI): *m/z* = 585.4 $[M+Na]^+$.

Extracted data for dodecyl 3,4-di-*O*-*tert*-butyldimethylsilyl-2,6-dideoxy-2-fluoro-β-L-glucopyranoside **(29)**:

$\boldsymbol{R_f}$ = 0.53 (*n*-hexane/CH_2Cl_2, 3:1).

^{1}H NMR (400 MHz, $CDCl_3$): δ = 4.42 (dd, $^3J_{1,2}$ = 7.7 Hz, $^3J_{1,F}$ = 2.9 Hz, 1H, H-1), 4.02 (ddd, $^2J_{2,F}$ = 50.4 Hz, $^3J_{1,2}$ = 7.7 Hz, $^3J_{2,3}$ = 8.6 Hz, 1H, H-2), 3.86 (dt, $^2J_{1'a,1'b}$ = 9.4 Hz, $^3J_{1'a,2'a}$ = $^3J_{1'a,2'b}$ = 7.0 Hz, 1H, H-1'a), 3.71 (ddd, $^3J_{3,F}$ = 14.4 Hz, $^3J_{3,2}$ = 8.6 Hz, $^3J_{3,4}$ = 7.9 Hz, 1H, H-3), 3.52 (dt, $^2J_{1'b,1'a}$ = 9.4 Hz, $^3J_{1'b,2'a}$ = $^3J_{1'b,2'b}$ = 7.0 Hz, 1H, H-1'b), 3.30 (dq, $^3J_{5,4}$ = 8.8 Hz, $^3J_{5,6}$ = 6.2 Hz, 1H, H-5), 3.24 (dd, $^3J_{4,5}$ = 8.8 Hz, $^3J_{4,3}$ = 7.9 Hz, 1H, H-4) [12], 1.68-1.54 (m, 2H, H-2'a,b), 1.38-1.22 (m, 21H, H-3'a,b - H-11'a,b, CH_3-6) [14], 0.91 (s, 9H, *t*-BuSi), 0.90 (s, 9H, *t*-BuSi), 0.88 (t, $^3J_{12',11'}$ = 7.2 Hz, 3H, CH_3-12'), 0.13-0.08 (m, 12H, 4 × CH_3Si).

^{13}C NMR (100 MHz, $CDCl_3$): δ = 100.1 (d, $^2J_{1,F}$ = 24.1 Hz, C-1), 93.1 (d, $^1J_{2,F}$ = 186.6 Hz, C-2), 76.9 (C-3) [13], 76.2 (d, $^3J_{4,F}$ = 7.5 Hz, C-4), 72.7 (C-5), 70.0 (C-1'), 31.9, 29.7, 29.7, 29.7, 29.6, 29.6, 29.4, 29.4, 26.4, 26.1, 25.9, 22.7 (C-2' - C-11', 2 × $(CH_3)_3$ *t*-BuSi), 18.6, 18.4 (2 × $C_{quat.}$ *t*-BuSi), 18.1 (C-6), 14.1 (C-12'), -2.5, -2.6, -3.5, -3.8 (4 × CH_3Si).

^{19}F NMR (376 MHz, $CDCl_3$): δ = −192.7 (app dd, $^2J_{F,2}$ = 50.4 Hz, $^3J_{F,3}$ = 14.4 Hz) [15].

MS (ESI): *m/z* = 585.4 $[M+Na]^+$.

Dodecyl 3,4-di-*O*-*tert*-butyldimethylsilyl-2,6-dideoxy-2-fluoro-α-L-mannopyranoside **(30)**:

$\boldsymbol{R_f}$ = 0.41 (*n*-hexane/CH_2Cl_2, 3:1).

$[\alpha]_{\boldsymbol{D}}^{\boldsymbol{20}}$ = −34° (*c* 1.01, $CHCl_3$).

^{1}H NMR (400 MHz, $CDCl_3$): δ = 4.81 (dd, $^3J_{1,F}$ = 7.3 Hz, $^3J_{1,2}$ = 2.4 Hz, 1H, H-1), 4.53 (br dt, $^2J_{2,F}$ = 49.5 Hz, $^3J_{2,3}$ = $^3J_{2,1}$ = 2.4 Hz, 1H, H-2), 3.89 (ddd, $^3J_{3,F}$ = 28.3 Hz, $^3J_{3,4}$ = 8.3 Hz, $^3J_{3,2}$ = 2.4 Hz, 1H, H-3), 3.68 (dt, $^2J_{1'a,1'b}$ = 9.5 Hz, $^3J_{1'a,2'a}$ = $^3J_{1'a,2'b}$ = 6.6 Hz, 1H, H-1'a), 3.64-3.53 (m, 2H, H-5, H-4) [16], 3.39 (dt, $^2J_{1'b,1'a}$ = 9.5 Hz, $^3J_{1'b,2'a}$ = $^3J_{1'b,2'b}$ =

[13] The chemical shift was inferred from HMQC, because the signal was overlapped with the solvent residual peak.

[14] CH_3-6 could be observed as a doublet at 1.26 ppm ($^3J_{6,5}$ = 6.2 Hz, extracted from the *J*-resolved spectrum).

[15] The signal was observed as an apparent doublet of doublets, although a vicinal couping constant with H-1 ($^3J_{F,1}$ = 2.9 Hz) could be observed in the ^{1}H NMR spectrum and confirmed by *J*-resolved experiments.

[16] H-4 could be observed as a triplet at 3.55 ppm ($^3J_{4,3} \approx {}^3J_{4,5}$ = 8.5 Hz, extracted from the *J*-resolved

6.6 Hz, 1H, H-1'b), 1.62-1.53 (m, 2H, H-2'a,b), 1.34-1.22 (m, 21H, H-3'a,b - H-11'a,b, CH_3-6) [17], 0.93 (s, 9H, *t*-BuSi), 0.90 (s, 9H, *t*-BuSi), 0.88 (t, $^3J_{12',11'}$ = 7.3 Hz, 3H, CH_3-12'), 0.13 (s, 3H, CH_3Si), 0.12 (s, 3H, CH_3Si), 0.11 (s, 3H, CH_3Si), 0.09 (s, 3H, CH_3Si).

^{13}C NMR (100 MHz, $CDCl_3$): δ = 97.2 (d, $^2J_{1,F}$ = 29.3 Hz, C-1), 90.7 (d, $^1J_{2,F}$ = 177.2 Hz, C-2), 73.9 (C-4), 72.6 (d, $^2J_{3,F}$ = 17.1 Hz, C-3), 69.7 (C-5), 67.9 (C-1'), 31.9, 29.7, 29.7, 29.6, 29.6, 29.4, 29.4, 26.1, 26.1, 26.1, 26.1, 22.7 (C-2' - C-11', 2 × $(CH_3)_3$ *t*-BuSi), 18.4, 18.4 (2 × $C_{quat.}$ *t*-BuSi), 18.0 (C-6), 14.1 (C-12'), -3.0, -3.4, -4.1, -4.5 (4 × CH_3Si).

^{19}F NMR (376 MHz, $CDCl_3$): δ = −204.5 (ddd, $^2J_{F,2}$ = 49.5 Hz, $^3J_{F,3}$ = 28.3 Hz, $^3J_{F,1}$ = 7.3 Hz).

MS (ESI): m/z = 585.3 $[M+Na]^+$.

Experiment 14

Dodecyl 2,6-dideoxy-2-fluoro-α-L-glucopyranoside **(4)**;
Dodecyl 2,6-dideoxy-2-fluoro-β-L-glucopyranoside **(31)**

To a solution of glycosides **28** and **29** (280 mg, 0.50 mmol, α/β = 1:1.3) in anhydrous THF (4 mL) was added a 1M solution of tetra-*n*-butylammonium fluoride in THF (4.5 mL, 4.5 mmol). The solution was stirred overnight at room temperature, and then quenched by diluting with EtOAc followed by dropwise addition of satd. aq. NH_4Cl solution. The aqueous phase was saturated with NaCl, exaustively extracted with EtOAc and the combined organic layers were dried ($MgSO_4$). After filtration and evaporation of the solvent, the crude mixture was purified by flash column chromatography on silica gel (petroleum ether/EtOAc, 2:1 to 100% EtOAc) to give **4** (58 mg, 35%) as a colourless oil and **31** (100 mg, 60%) as a white solid.

Dodecyl 2,6-dideoxy-2-fluoro-α-L-glucopyranoside **(4)**:

$\boldsymbol{R_f}$ = 0.42 (petroleum ether/EtOAc, 2:1).

$[\alpha]_D^{20}$ = −68° (*c* 0.96, $CHCl_3$).

^{1}H NMR (400 MHz, $CDCl_3$): δ = 4.93 (d, $^3J_{1,2}$ = 3.2 Hz, 1H, H-1), 4.31 (ddd, $^2J_{2,F}$ = 50.2 Hz, $^3J_{2,3}$ = 9.2 Hz, $^3J_{2,1}$ = 3.2 Hz, 1H, H-2), 4.04 (dt, $^3J_{3,F}$ = 12.5 Hz, $^3J_{3,4}$ = $^3J_{3,2}$ = 9.2 Hz, 1H, H-3), 3.78-3.67 (m, 2H, H-5, H-1'a), 3.46 (dt, $^2J_{1'b,1'a}$ = 9.1 Hz, $^3J_{1'b,2'a}$ = $^3J_{1'b,2'b}$ = 6.8 Hz, 1H, H-1'b), 3.21 (t, $^3J_{4,3}$ = $^3J_{4,5}$ = 9.2 Hz, 1H, H-4), 2.69-2.39 (m, 2H, OH-3, OH-4), 1.69-1.56 (m, 2H, H-2'a,b), 1.37-1.22 (m, 21H, H-3'a,b - H-11'a,b, CH_3-6) [18], 0.88 (t, $^3J_{12',11'}$ = 6.8 Hz, 3H, CH_3-12').

spectrum).

[17] CH_3-6 could be observed as a doublet at 1.25 ppm ($^3J_{6,5}$ = 6.3 Hz, extracted from the *J*-resolved spectrum).

[18] CH_3-6 could be observed as a doublet at 1.29 ppm ($^3J_{6,5}$ = 6.3 Hz, extracted from the *J*-resolved spectrum).

^{13}C NMR (100 MHz, $CDCl_3$): δ = 96.0 (d, $^2J_{1,F}$ = 20.3 Hz, C-1), 90.4 (d, $^1J_{2,F}$ = 188.9 Hz, C-2), 75.4 (d, $^3J_{4,F}$ = 6.8 Hz, C-4), 72.3 (d, $^2J_{3,F}$ = 17.9 Hz, C-3), 68.4 (C-1'), 66.9 (C-5), 31.9, 29.7, 29.6, 29.6, 29.6, 29.4, 29.4, 29.4, 26.1, 22.7 (C-2' - C-11'), 17.4 (C-6), 14.1 (C-12').

^{19}F NMR (376 MHz, $CDCl_3$): δ = −202.2 (dd, $^2J_{F,2}$ = 50.2 Hz, $^3J_{F,3}$ = 12.5 Hz).

HRMS (ESI): *m/z* = calcd. for $C_{18}H_{35}FNaO_4$ $[M+Na]^+$ 357.24116, found 357.24127.

Dodecyl 2,6-dideoxy-2-fluoro-β-L-glucopyranoside **(31)**:

$\boldsymbol{R_f}$ = 0.31 (petroleum ether/EtOAc, 2:1).

m.p. = 85.4−86.8 °C.

$[\alpha]_D^{20}$ = +20° (*c* 1.00, $CHCl_3$).

^{1}H NMR (400 MHz, $CDCl_3$): δ = 4.46 (dd, $^3J_{1,2}$ = 7.7 Hz, $^3J_{1,F}$ = 2.0 Hz, 1H, H-1), 4.14 (br ddd, $^2J_{2,F}$ = 51.6 Hz, $^3J_{2,3}$ = 9.0 Hz, $^3J_{2,1}$ = 7.7 Hz, 1H, H-2), 3.88 (dt, $^2J_{1'a,1'b}$ = 9.0 Hz, $^3J_{1'a,2'a}$ = $^3J_{1'a,2'b}$ = 7.0 Hz, 1H, H-1'a), 3.70 (dt, $^3J_{3,F}$ = 15.1 Hz, $^3J_{3,4}$ = $^3J_{3,2}$ = 9.0 Hz, 1H, H-3), 3.54 (dt, $^2J_{1'b,1'a}$ = 9.0 Hz, $^3J_{1'b,2'a}$ = $^3J_{1'b,2'b}$ = 7.0 Hz, 1H, H-1'b), 3.39 (dq, $^3J_{5,4}$ = 9.0 Hz, $^3J_{5,6}$ = 6.1 Hz, 1H, H-5), 3.27 (t, $^3J_{4,5}$ = 9.0 Hz, 1H, H-4), 2.70 (br s, 1H, OH), 2.50 (br s, 1H, OH), 1.69-1.57 (m, 2H, H-2'a,b), 1.35 (d, $^3J_{6,5}$ = 6.3 Hz, 1H, CH_3-6), 1.33-1.22 (m, 18H, H-3'a,b - H-11'a,b), 0.88 (t, $^3J_{12',11'}$ = 6.8 Hz, 3H, CH_3-12').

^{13}C NMR (100 MHz, $CDCl_3$): δ = 100.1 (d, $^2J_{1,F}$ = 22.0 Hz, C-1), 92.4 (d, $^1J_{2,F}$ = 184.8 Hz, C-2), 75.6 (d, $^2J_{3,F}$ = 18.0 Hz, C-3), 75.0 (d, $^3J_{4,F}$ = 7.1 Hz, C-4), 71.5 (C-5), 70.2 (C-1'), 31.9, 29.7, 29.6, 29.6, 29.6, 29.6, 29.4, 29.4, 25.9, 22.7 (C-2' - C-11'), 17.4 (C-6), 14.1 (C-12').

^{19}F NMR (376 MHz, $CDCl_3$): δ = −200.3 (app dd, $^2J_{F,2}$ = 51.6 Hz, $^3J_{F,3}$ = 15.1 Hz) [19].

HRMS (ESI): *m/z* = calcd. for $C_{18}H_{35}FNaO_4$ $[M+Na]^+$ 357.24116, found 357.24119.

[19] The signal was observed as an apparent doublet of doublets, although a vicinal couping constant with H-1 ($^3J_{F,1}$ = 2.0 Hz) could be observed in the ^{1}H NMR spectrum and confirmed by *J*-resolved experiments.

5.4 Antibacterial activity

All procedures used in the biological activity assessment are according to the Clinical Laboratory and Standards Institute (CLSI) specifications [**92, 93**].

The mininum inhibitory concentration (MIC) and mininum bactericidal concentration (MBC) of compounds **2**, **3**, **18**, **4**/**5** (1:3), **4** and **31** against *B. cereus* from the American Type Culture Collection (ATCC 14579) were determined using an adaptation of the microdilution method. Strains were preserved as frozen cell cultures in MH-glycerol mixture, at -80 °C. Pre-inoculums were performed before each assay: microorganisms were growth in Muller-Hinton medium (MH; Fluka, 90922) with cation-adjusted content, in an incubator at 30 °C and stirring at 200 rpm, overnight.

Muller-Hinton medium was freshly prepared following the instructions of the manufacturer, dissolving 22 g of dry MH medium in 1 L of purified water (Milli-Q). The medium was then sterilized at 121 °C during 15 min. Muller-Hinton Agar medium (MHA) was prepared dissolving 22 g of dry MH medium and 15 g of agar in 1 L of purified water (Milli-Q). Stock solutions of the tested compounds, as well as the controls, were prepared in DMSO to a final concentration of 4 mg mL^{-1}. The standard antibiotic ciprofloxacin and dodecyl 2,6-dideoxy-α-L-*arabino*-hexopyranoside (**1**) were used as positive controls.

Broth microdilution testing for MIC determination was performed in 96-well, flat-bottom microtiter plates with automated data acquisition. Each plate included positive controls (bacteria only), negative controls (medium only), and serial two-fold dilutions of each of the tested compounds, in cation-adjusted MH medium. Compound-containing wells included final concentrations ranging from 4 to 128 μg mL^{-1}. The inoculum density was standardized by diluting cultures of the bacterial strains to the absorbance of 0.08 to 0.10 (equivalent to 0.5 McFarland units) at 600 nm, using sterilized medium as reference. Then, a solution was prepared, diluting the standardized solution in sterile medium by 1:10 and the microplate previously prepared with the compound-containing and positive control was inoculated by addition of 10 μL of this bacterial solution, containing 2×10^6 CFU mL^{-1}. The plate was sealed with parafilm, placed in the microplate reading apparatus (Anthos Zenith 3100 Microplate Multimode Detector) and readings were taken at 595 nm, every 10 min, with agitation before each reading, at the temperature of 35 °C during 24 h. Data was collected by Beckman Coulter Multimode Detection Software (V 2.1.0.17). MIC was recorded as the lowest concentration used that did not result in observed optical density (OD) at 595 nm higher than its respective control with compound after 24 h of incubation.

After 24 h of incubation, a spotting assay was performed in order to evaluate MBC. Plates were prepared using solid medium (MHA), dried on laminar flux chamber and inoculated with 10 μL of the content of each microplate well. Plates were incubated at 35 °C overnight. MBC was recorded as the lowest concentration used that did not result in observable bacterial colonies in solid medium after 24 h of incubation.

The microbial susceptibility of *B. anthracis* to compounds **2**, **3** and **18** was evaluated using three strains (*pathogenic* - human pathogen; *vacinal* - vaccine strain; *ovine* - sheep origin) from the collection of the Instituto Nacional de Saúde Doutor Ricardo Jorge, INSA (Portugal). The standard antibiotic ciprofloxacin and dodecyl 2,6-dideoxy-α-L-*arabino*-hexopyranoside (**1**) were again used as positive controls. The assays were carried out in a biosafety level 3 laboratory, using the agar dilution method in solid medium (MHA) medium (in triplicate), as we have described previously [**3**].

5.5 Computational details

The structures of each appropriate conformer of dodecyl 2-deoxy-α-L-*threo*-pentopyranoside (**3**) and dodecyl 2-deoxy-β-L-*threo*-pentopyranoside (**18**) were built by using PyMOL^{TM} Molecular Graphics System (version 1.4.1) [**83**].

Prior to geometry optimizations, each structure was energy minimized with Avogadro software [**95**], using the steepest descent algorithm and the MMFF94s force field [**96**].

DFT calculations were performed with Gaussian 09 software [**97**]. The Perdew– Burke–Ernzerhof functional (PBE0), which uses 25% exchange and 75% correlation weighting, was used in all calculations [**98**]. Geometries were optimized without symmetry constraints and obtained using the 6-311G** basis set in all atoms [**99**]. Frequency calculations were performed to assess the nature of optimized geometries, and zero imaginary frequency was obtained for all minima. All geometries were optimized in the corresponding media (chloroform or methanol), using the polarizable continuum solvation model (IEFPCM) [**100**] on the electronic density (SMD) [**84**]. Dielectric constants (bulk relative permittivities) of ε=4.711 (for chloroform) and ε=32.613 (methanol) were used for solvent specification.

Analysis and processing of the geometrically optimized structures were performed using Chemcraft (version 1.6) [**101**] software package and PyMOL [**83**].

II - MODELLING THE INTERACTION OF ANTIBIOTIC GLYCOSIDES WITH LIPID BILAYERS

Chapter 6

Molecular modeling

Molecular modelling techniques are key tools for the study of complex biochemical systems and processes at the microscopic level. Computer simulations, in particular molecular mechanics/molecular dynamics (MM/MD) methodologies, are specially important due to the limited molecular resolution provided by most experimental techniques. In recent years, with technological development rapidly improving the available calculation power, their applications have extended to considerably large molecular systems and significantly longer time-scales. The aim of the following section is to provide the reader with a brief description of the theoretical foundations underlying the MM/MD methods [1] used in this work.

6.1 Molecular mechanics/molecular dynamics (MM/MD)

Molecular modelling approaches to study systems containing a significant number of atoms (i.e. biological macromolecules) are typically based on MM methodologies rather than quantum mechanics (QM), mainly due to the fact that many of such systems are effectively too large to be considered by the later. Indeed, while QM methods deal with the distribution of electrons within a molecular system, in MM the energy of the system is calculated as a function of the nuclear positions only (i.e. by ignoring the electronic motions). This represents a considerable reduction in the number of degrees of freedom of the system (i.e. the number of particles that are considered), thus allowing for much less time-consuming calculations. The fact that this modelling approach can be used to predict the properties of a molecular system depends on the validity of various assumptions and, accordingly, also implies several limitations [**104**]. The most important assumption is probably the Born-Oppenheimer approximation, which enables for electronic and nuclear motions to be decoupled and thereby the former to be averaged out (i.e. considering that the much smaller electrons can rapidly adjust to changes in the positions

[1] See refs. [**102**] and [**103**] for a more thorough description of MM/MD and additional aspects of computer simulation methods.

of the nuclei). However, because the electronic distribution within a molecule is considered to be optimal, processes such as chemical reactions cannot be described in light of these models.

In MM methods, a molecular systems is described as a collection of point masses moving along a potential field, which is generally considered to be conservative (i.e. it only depends on the instantaneous coordinates of the particles). Therefore, the dynamic behaviour of the system is assumed to be governed by the laws of classical mechanics and, consequently, the energy of the system can be predicted based on a rather simple model accounting for the interactions within the system, arising from processes such as stretching of bonds, opening/closing of angles or the rotation about single bonds, to mention a few. Hence, the potential energy function representing a molecular system can be mathematically described as the sum of all intra- and intermolecular interactions contributing to the overall potential energy of the system ($V(\mathbf{r}^N)$), given a particular conformation. It is calculated as a function of the cartesian position vectors of all atoms within the system ($\mathbf{r}^N$), as represented in the following equation:

$$\begin{aligned} V(\mathbf{r}^N) = {} & V_{bonds}(\mathbf{r}^N) + V_{angles}(\mathbf{r}^N) + V_{proper\ dihedrals}(\mathbf{r}^N) + V_{improper\ dihedrals}(\mathbf{r}^N) \\ & + V_{van\ der\ Waals}(\mathbf{r}^N) + V_{electrostatic}(\mathbf{r}^N) \end{aligned} \tag{6.1}$$

In most cases, the potential energy function only comprises the six components shown in **Equation 6.1**, although certain force fields can be found in which additional terms are included. The first four terms describe the contribution of bonded interactions (i.e. those involving covalently bonded atoms), while the last two terms are related to the so-called non-bonded interactions (i.e. between pairs of atoms that either belong to different molecules, or are separated by at least three bonds). The potential energy associated with these interactions is usually modelled according to each of the following mathematical expressions, respectively:

$$V_{bonds}(\mathbf{r}^N) = \sum_{n=1}^{N_b} \frac{1}{2} k_{b_n} (b_n - b_{0_n})^2 \tag{6.2}$$

$$V_{angles}(\mathbf{r}^N) = \sum_{n=1}^{N_\theta} \frac{1}{2} k_{\theta_n} (\theta_n - \theta_{0_n})^2 \tag{6.3}$$

$$V_{proper\ dihedrals}(\mathbf{r}^N) = \sum_{n=1}^{N_\phi} k_{\phi_n} [1 + \cos(m_n \phi_n - \delta_n)] \tag{6.4}$$

$$V_{improper\ dihedrals}(\mathbf{r}^N) = \sum_{n=1}^{N_\xi} \frac{1}{2} k_{\xi_n} (\xi_n - \xi_{0_n})^2 \tag{6.5}$$

$$V_{van\ der\ Waals}(\mathbf{r}^N) = \sum_{i=1}^{N} \sum_{j>i}^{N} 4\epsilon_{ij} \left[\left(\frac{\sigma_{ij}}{r_{ij}} \right)^{12} - \left(\frac{\sigma_{ij}}{r_{ij}} \right)^{6} \right] \tag{6.6}$$

$$V_{electrostatic}(\mathbf{r}^N) = \sum_{i=1}^{N} \sum_{j>i}^{N} \frac{q_i q_j}{4\pi\epsilon_0 \epsilon_r r_{ij}} \tag{6.7}$$

As represented in **Equation 6.2**, the vibrational energy associated with the (two-body) bond stretching between covalently bonded atoms is described by a harmonic potential, where b_n is the bond lenght, b_{0_n} is the equilibrium bond lenght and k_{b_n} is the associated force constant. The interaction due to the (three-body) bond angle bending is also modelled by a harmonic potential, as depicted in **Equation 6.3**, where θ_n is the bond angle, θ_{0_n} is the equilibrium bond angle and k_{θ_n} is the force constant. **Equations 6.4** and **6.5** are related to the energy contributions associated with bond rotation, that is, the (four-body) torsions in the proper and improper dihedral angles, respectively). The latter include dihedral angles within planar groups (i.e. aromatic rings) or others that are not allowed to make transitions (i.e. chirality centers), which are again described by a harmonic potential, where ξ_n is the improper dihedral angle, ξ_{0_n} is the equilibrium improper dihedral angle and k_{ξ_n} is the force constant. Proper dihedrals (i.e. those with unrestricted torsional freedom), in turn, are modelled by a sinusoidal function, where ϕ_n is the proper dihedral angle, m_n is the multiplicity, δ_n is the fase factor and k_{ϕ_n} is the force constant. Finally, **Equations 6.6** and **6.7** represent the potential energies associated with the non-bonded interactions between pairs of atoms. The contribution due to the van der Waals forces is usually modelled using a Lennard-Jones 12-6 potential accounting for both repulsive and attractive interactions, where r_{ij} is the interatomic distance, σ_{ij} is the interatomic distance at which the potential equals zero (collision diameter) and ϵ_{ij} is the potential well depth. The long-range electrostatic interactions are treated according to the Coulomb law, where q_i and q_j are the atomic charges, r_{ij} is again the interatomic distance, ϵ_r is the relative dielectric constant, and ϵ_0 is the vacuum permitivity.

The specific functional form of the potential energy function (i.e. that presented in **Equation 6.1**), along with the set of its intrinsic parameters (i.e. the several constants from each term in **Equations 6.2-6.7**) define a force field. The quality of a force field is determined by its ability to accurately reproduce certain structural properties of a given molecule. For that purpose, force field parametrization is generally based on quantum-level calculations and/or experimental data, rendering them empirical. Hence, although in general a force field is designed so that it can be further applied to a series of related molecules, that is, featuring transferability, it will never be able to model all molecular systems in an universal-fashion. In most force fields, all atoms within the system are explicitly represented in the model. These are often called all-atom force fields, in contrast with the united-atom force fields (i.e. like the one used in this work) where non-polar hydrogen atoms are not treated explicitly. Instead, they are subsumed into the atoms to which they are covalently bonded (usually carbon atoms). This approach dramatically reduces the number of interaction sites in the model and hence the number of non-bonded interactions considered, thus allowing for substantially lower computational costs, without compromising the accuracy of the calculations. However, this methodology cannot be

applied to polar hydrogen atoms (i.e. hydroxy group hydrogen) since these are involved in important non-bonded interactions, namely hydrogen bonding.

The MD simulation method provides a microscopic description of the dynamical behaviour of a molecular system, from which time averages of macroscopic properties can be calculated. In other words, it allows for the preferred conformations of a system to be predicted by exploring its conformational space. A representative ensemble of successive configurations of the system, that is, a trajectory that specifies how the positions and velocities of all particles in the system vary with time, is generated by solving the Newton's equations of motion. This computer simulation method is therefore deterministic, in the sense that the state of the system at any future time can be predicted from its current state. In more detail, the instantaneous forces acting on each particle, given a particular conformation, can be determined from the gradient of the potential energy, according to the following equation:

$$\mathbf{F}_i = -\nabla_{\mathbf{r}_i} V(\mathbf{r}_i), \tag{6.8}$$

where $\nabla_{\mathbf{r}_i} V(\mathbf{r}_i)$ is the gradient of the potential energy, $V(\mathbf{r}_i)$ with respect to the vectorial position of each particle i in the system, $\mathbf{r}_i$, and $\mathbf{F}_i$ is the resulting force acting on each particle. The obtained force can then be combined with the position and velocity of each particle either to search for energy minima, or to calculate its acceleration through the integration of the differential equations embodied in Newton's second law of motion:

$$\mathbf{F}_i = m_i \mathbf{a}_i = m_i \frac{\mathrm{d}\mathbf{v}_i}{\mathrm{d}t} = m_i \frac{\mathrm{d}^2 \mathbf{r}_i}{\mathrm{d}t^2}, \tag{6.9}$$

where m_i is the mass of each particle i in the system and $\mathbf{a}_i$, $\mathbf{v}_i$ and $\mathbf{r}_i$ are the acceleration, velocity and position vectors of the particle, respectively, at each time step t. The new position and velocity of each particle can thus be obtained by solving **Equations 6.8** and **6.9** simulataneously in small time steps (typically 1-10 femtoseconds). However, these equations cannot be solved analytically, since the motions of all particles are coupled, and for that reason several numerical integration algorithms have been developed.

In computer simulations, the correct treatment of boundaries/boundary effects is of great importance since it allows for macroscopic properties to be predicted by simulating relatively small systems. In fact, performing computer simulations on a "realistic" solution of a given concentration is inconceivable due to the extreme complexity of such a model system, in light of the available computational resources. Hence, molecular simulations can be performed using a rather small amount of particles, in such a way that the particles experience forces approximately as if they were within a bulk solution, by using periodic boundary conditions (PBC). This approach consists in the replication of the system in all directions, so that the system is surrounded by periodic images, rendering it infinite in space. In such a periodic system, when-

ever a particle leaves the central box during the simulation its neighbouring periodic image will replace it by entering from the opposide side of the simulation box, due to the absence of physical barriers, and the overall number of particles will remain constant. This process is illustrated in **Figure 6.1** for a two-dimensional periodic system. There are several implications

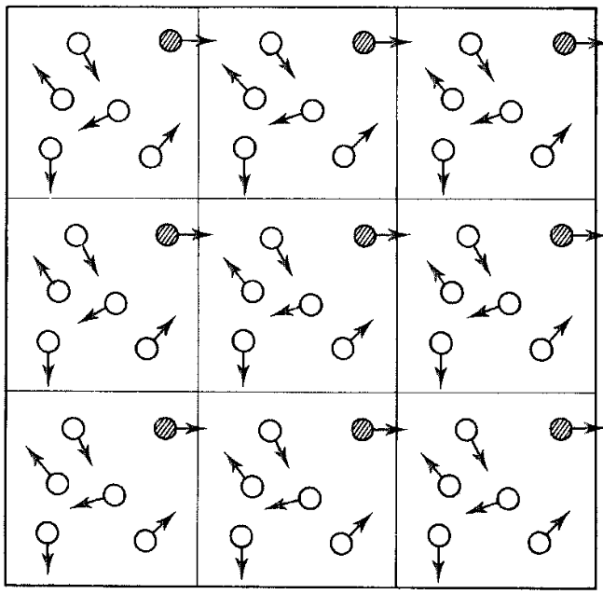

Figure 6.1: Representation of a system of particles with periodic boundary conditions in two dimensions. Image was taken from ref. [**102**].

of using PBC, which depend on the specific system being simulated. In the case of simulations of proteins or surfactant micelles in solution, for instance, it implies an infinite dilution condition. Another example of particular relevance in the context of this work is that of membrane systems, where the existence of PBC along the membrane plane (xy) direction implies that the membrane is infinite in the simulations.

MD simulations are usually performed considering equilibrium conditions of both temperature and pressure, in order to properly mimic biological systems. Therefore, the simulations are carried out in an isothermal-isobaric (NPT) ensemble, where these two external thermodynamic parameters, as well as the number of particles, are kept contant throughout the simulations. There are several methodologies to control temperature and pressure of the system. In the method developed by Berendsen and co-workers, which was used in this work, the temperature and the pressure are maintained by coupling the system to external heat and pressure baths, respectively [**105**]. Temperature adjustments are achieved simply by scaling the velocities at each time step (i.e. the temperature is related to the average kinetic energy of the system), while the pressure is kept constant through adjustments in the volume of the system (i.e. by scaling the simulation box).

Another important methodological aspect in MD simulations is that bond lenghts and angles are contrained in order to allow for an increase in the integration time steps. This type of approxi-

mations is widely used because it allows for much lower computational costs, without affecting significantly the accuracy of the calculations in terms of conformational information. The most commonly employed methods for bond constraining are the SHAKE [**106**] and LINCS [**107**] algorithms, both of which correct bond lenghts to equilibrium values after an unconstrained integration step. The former is an iterative algorithm that can be used to constrain bond angles as well as bond lenghts. In turn, the LINCS algorithm, which is non-iterative and mainly handles bond lenght constraints, is the usually preferred method since it is considered to be more stable and perform faster. The SETTLE [**108**] algorithm, which is an analytical version of SHAKE, is frequently used to treat rigid water molecules since it has been specifically optimized for its bond lenght and angle constraints.

6.2 Objectives

In this part of the project, we aimed at taking advantage of this state-of-the-art molecular modelling technique in order to contribute to the elucidation of the mechanisms governing the antibacterial action assotiated with the family of sugar-based surfactants developed by our research group (refer back to **Section 1.2**).

Experimental data (i.e. surface activity and microbial susceptibility assays) show that, for those alkyl deoxyglycosides exhibiting a bioactive profile, antimicrobial activity is achieved above the respective critical micelle concentration (CMC) and is modulated by the deoxygenation pattern of the sugar moiety, as well as by key features in their structure (i.e. sugar stereochemistry and alkyl side-chain lenght) [**1**–**3**]. Additionally, extensive biological studies have been performed by collaborators in the search for specific biomolecular targets associated with their mechanism of action [2]. In particular, the effect of these compounds on bacterial cell vitality, viability, metabolism and sporulation cycle was evaluated, amongst other studies, using a model strain of *Bacillus cereus*, a set of mutant strains produced by either random transposition or knock-out of several membrane-related targets, and bacterial protoplasts/spheroplasts. From these experiments, it was concluded that glycoside bactericidal effect is most probably not driven by molecular recognition processes involving the interacion of glycosides with specific bacterial proteins. Instead, the results and the data on surface activity suggest a mechanism based on surfactant aggregation into micelles and their interaction with bacterial cell membranes in a detergent-like manner. In fact, many amphiphilic antibiotics are known to target lipid bilayers, through destabilization of their thermotropic properties upon insertion, ultimately leading to membrane disruption. Thus, unraveling the molecular details of glycoside-lipid bilayer interactions is paramount in order to better understand the mechanism of action of these antibiotics, which is the main motivation of this research work.

The methodology involved different sets of atomistic simulations, which were applied to various

[2] João Pais, Ricardo Dias, Rogério Tenreiro and Amélia P. Rauter *et al.*, unpublished results.

glycolipids [3], including some of those whose synthesis was presented in **Part I** (see **Section 7.1** for further details on the methods). Each set of simulations was designed with the purpose of exploiting distinct phenomena and/or properties within the respective system. In **Section 8.1** we studied the self-assembly of glycosides into equilibrated micelles and characterized these aggregates in terms of their structural properties and stability in aqueous media. Then, we investigated the behaviour of glycoside micelles at the interface of a model phospholipid bilayer by monitoring partitioning/fusion events (**Section 8.2**) and subsequently analyzed the effect of glycoside insertion on membrane biophysical properties by simulating glycoside/phospholipid binary mixtures (**Section 8.3**). Finally, the eventual ability of these molecules to induce and/or stabilize membrane pores was also preliminary assessed in **Section 8.4**.

[3] Hereinafter, the term "glycolipid" (GL) will be frequently used in alternative to glycoside.

Chapter 7

Computational methods

7.1 Simulations details

The structures of the studied glycolipids are shown in **Figure 7.1**. Most of the simulations were performed using dodecyl 2,6-dideoxy-α-L-*arabino*-hexopyranoside (A12, **Figure 7.1a**) as model compound, since this is the most potent antibacterial reported so far, for which a substantial amount of experimental data is available [**1**–**3**]. For methodological validation purposes and, particularly, with the intent to evaluate the effect of certain structural modifications on the physical properties of these molecules, as well as on their interaction with model lipid bilayers, other surfactant glycosides were also simulated. Hence, octyl 2,6-dideoxy-α-L-*arabino*-hexopyranoside (A08, **Figure 7.1b**) was chosen aiming at studying the effect of alkyl side-chain lenght, whereas the newly synthesized (see **Part I**) dodecyl α-L-rhamnopyranoside (R12, **Figure 7.1c**) and dodecyl 2-deoxy-α-L-*threo*-pentopyranoside (T12, **Figure 7.1d**) where employed in order to address the importance of deoxygenation at 2-position, and that of the presence of a methylene group at 5-position of the sugar ring, respectively.

The zwitterionic phospholipid 1,2-dimyristoyl-*sn*-glycero-3-phosphocholine (DMPC) was employed in all simulations involving either pure lipid bilayer systems or glycoside/phospholipid binary mixtures in membrane environment. The structural/biophysical properties of its bilayer systems have been thoroughly investigated experimentally [**109**–**123**]. Furthermore, particularly reliable force field parametrization has been developed for this molecule [**124**], making it a suitable model system for our MM/MD studies.

7.1.1 MM/MD settings

All MM/MD simulations were performed using the GROMACS software package (version 4.0.7) [**125**–**127**]. A modified version of the GROMOS 54A7 force field [**128**–**130**] was used, which included parameters for carbohydrates from the recently reported GROMOS 56A$_{\mathrm{CARBO}}$ force

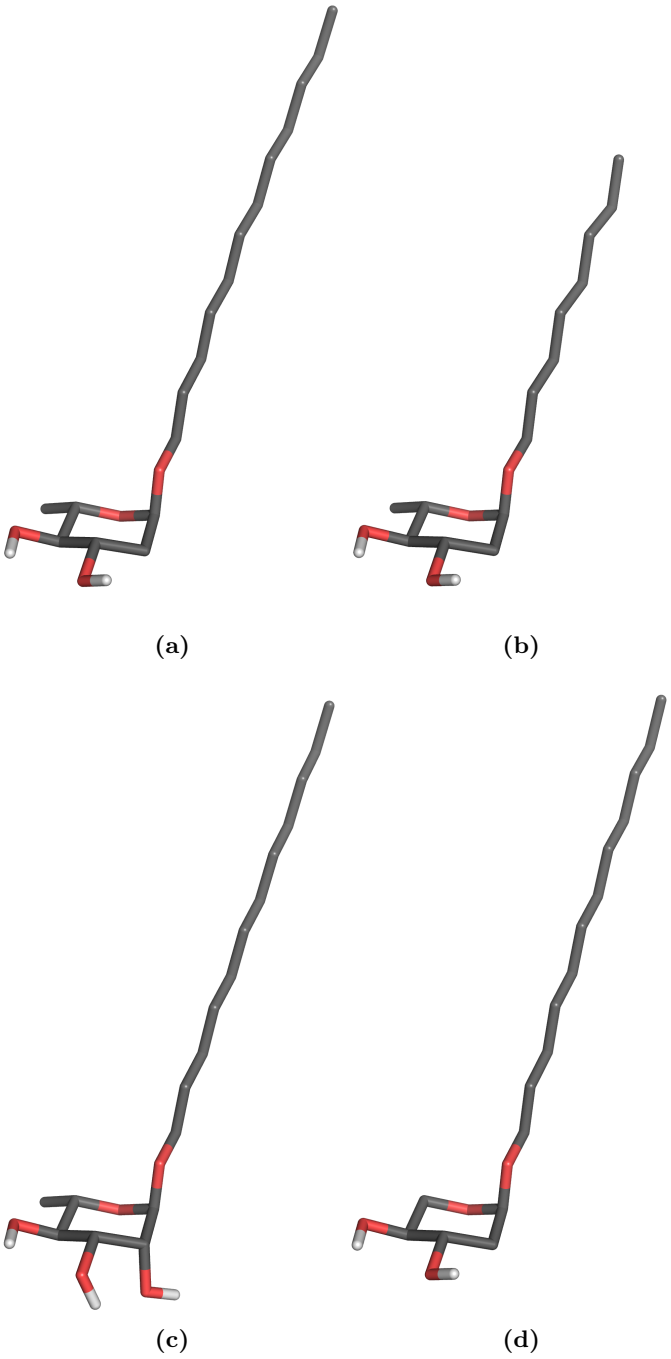

Figure 7.1: Structures of the glycolipids studied in this work. **(a)** Dodecyl 2,6-dideoxy-α-L-*arabino*-hexopyranoside (A12), **(b)** octyl 2,6-dideoxy-α-L-*arabino*-hexopyranoside (A08), **(c)** dodecyl α-L-rhamnopyranoside (R12) and **(d)** dodecyl 2-deoxy-α-L-*threo*-pentopyranoside (T12). Carbon atoms are show in dark gray, oxygens in red, and polar hydrogens in white. All apolar hydrogens were ommited for clarity. Images were rendered using PyMOL [**83**].

field [**131**], and the corrections to phosphatidylcholine parametrization originally implemented in the GROMOS 53A6 force field [**124**]. Initial systems (see **Section 7.1.2**) consisted of variable configurations of glycoside and/or phospholipid molecules explicitly solvated with an adequate number of water molecules from the single point charge (SPC) model [**132**]. A rhombic dodecahedric simulation box was used for micellization studies, whereas in the case of lipid bilayer systems an orthorhombic boxtype was used. Periodic boundary conditions with the minimum image convention were applied in the three dimensions [1]. All simulations were started from pre-equilibrated systems (see **Section 7.1.3**) by applying different sets of initial velocities [2]. The equations of motion were numerically integrated using the leap-frog algorithm [**103–105**] with a time step of 2 fs, with conformations being saved every 10 ps for analysis purposes. Non-bonded interactions were treated using a twin-range method with cutoffs of 8 Å and 14 Å, updating the neighbor pair lists every 10 fs. The reaction field method [**133–135**] was used to treat long-range electrostatic interactions, using a relative dielectric constant of 54.0 [**136**]. All simulations were performed in an isothermal-isobaric (NPT) ensemble using the Berendsen's weak coupling methods [**105**]. Solute and solvent were separately coupled to external heat baths, with temperature set to 308.0 K and a relaxation time of 0.1 ps. Pressure was kept constant at 1 bar, with an isothermal compressibility of 4.5×10^{-5} bar^{-1} and using either an isotropic coupling with a relaxation time of 2.0 ps (for micellization studies), or a semi-isotropic coupling with a relaxation time of 5.0 ps (for lipid bilayer systems). Bond lenghts were constrained applying the parallel version of the linear constraint solver algorithm (P-LINCS) [**107, 137**] in the case of glycoside and/or phospholipid molecules, while the SETTLE algorithm [**108**] was used for constraining water molecules.

7.1.2 Initial configurations

Initial systems were built using the PyMOL software package (version 1.4.1) [**83**] and/or several scripts developed in-house.

Micellization studies (see **Table 7.1**) were carried out starting from a varying number (from n_{GL} = 5 to n_{GL} = 200) of glycolipid molecules (GL = A12, A08), which were randomnly distributed within the solvated simulation box. After energy minimization and initialization (see **Section 7.1.3**), each equilibrated system was simulated in a total of five replicates, 100 ns long each.

For the studies regarding the interaction of glycoside micelles with a model membrane (see **Table 7.2**), previously equilibrated micelles (GL = A12), each containing a different number of monomers (n_{GL} = 10, 30, 60), where placed in the vicinity of a pre-equilibrated lipid bilayer, which was invariably composed of 256 DMPC molecules. For each equilibrated micelle/bilayer system, an initial set of long simulations was performed, corresponding to three replicates with

[1] All systems where built with adequate box vector lenghts in order to ensure that equilibrated micelles and/or lipid bilayers could not see their respective periodic images (along the $x/y/z$-directions and/or z-direction, respectively).

[2] Initial atomic velocities were randomnly generated according to a Maxwell distribution at 308.0 K, during the first initialization step.

Table 7.1: Simulations details of the glycoside micellization systems.

GL	n_{GL}	n_{Water}	$\mathbf{t}_{simulation}$/ ns
A12	5	2126	5 × 100
A12	10	2838	5 × 100
A12	30	4406	5 × 100
A12	50	5971	5 × 100
A12	60	6355	5 × 100
A12	70	6824	5 × 100
A12	100	8181	5 × 100
A12	150	10268	5 × 100
A12	200	12409	5 × 100
A08	5	2125	5 × 100
A08	10	2869	5 × 100
A08	20	3687	5 × 100
A08	30	4515	5 × 100
A08	40	5380	5 × 100
A08	50	6177	5 × 100
A08	60	6567	5 × 100
A08	100	8512	5 × 100

individual run times of either 300 ns (for systems with $n_{GL} = 10$) or 500 ns (for $n_{GL} = 30, 60$). Aiming to maximize the computational efficiency of these studies, another series of simulations was performed starting from smaller systems (containing fewer water molecules). In those cases, seven replicates were run, each with an individual time lenght of 100 ns. Whenever a partitioning/fusion event could be observed during the simulation, the corresponding production run was extended to totalize a simulation time of either 300 ns (for $n_{GL} = 10$) or 500 ns (for $n_{GL} = 30, 60$).

Glycoside/phospholipid binary mixtures (see **Table 7.3**) were constructed starting from a pre-equilibrated lipid bilayer consisting of 256 DMPC molecules and 8821 water molecules, from which a variable number of phospholipids ($n = 2, 10, 30, 60, 128, 192$) was randomly removed and replaced by equal number of glycoside molecules (GL = A12, A08, R12, T12). Equilibrium

Table 7.2: Simulations details of the glycoside micelle/phospholipid bilayer systems.

GL	n_{GL}	n_{DMPC}	n_{Water}	$t_{simulation}$/ ns
A12	10	256	18733	3 × 300
A12	10	256	12183	1 × 300 [a]
A12	10	256	12183	6 × 100
A12	30	256	19721	3 × 500
A12	30	256	13515	1 × 500 [a]
A12	30	256	13515	6 × 100
A12	60	256	21161	3 × 500
A12	60	256	14669	1 × 500 [a]
A12	60	256	14669	6 × 100

[a] After an initial production time of 100 ns, the simulation was prolonged to the indicated final production time (see text above).

configurations of each two-component bilayer system at different molar fractions (GL/PC = 0.8%, 3.9%, 11.7%, 23.4%, 50.0% or 75.0%) were subsequently simulated in triplicate, 100 ns long each. A 100% DMPC bilayer was also simulated, with a production run time of 300 ns (single replicate), as a control for specific analyzes related with the structural properties of DMPC molecules in the two-component membrane environment. Additionally, three replicates of another 23.4% A12/PC bilayer were also simulated (100 ns long each). In this particular system, all 60 glycoside molecules (30 per monolayer) were intentionally placed in a cluster configuration, with the purpose of preliminarily testing the cluster stabilty and its eventual tendency to (spontaneously) promote membrane pore formation. Finally, our methodology was further validated by simulating binary mixtures containing the related dodecyl/octyl β-D-glucopyranosides (G12/G08) and phosphatidylcholine at several molar fractions (see **Table 7.3**), for which comparable experimental data is available **[138, 139]**.

Initial configurations for the membrane pore stability studies were built starting from pre-equilibrated systems which were obtained similarly to the binary mixtures described above, in this case by replacing either 60 or 132 neighbouring phospholipid molecules (30 or 66 per monolayer, respectively) by equal number of glycoside molecules (GL = A12). Removal of 8 glycolipids (4 per monolayer) from the center of each two-component bilayer patch originated two systems featuring a transmembrane cavity and containing final GL/PC molar fractions of 20.1% and 50.0%, respectively (see **Table 7.4**). A three-step simulation procedure was then performed in order to force water molecules to fill the cavity and subsequently allow glycoside

Table 7.3: Simulations details of the glycoside/phospholipid binary mixtures.

GL	n_{GL}	n_{DMPC}	$\%_{GL}$	n_{Water}	$t_{simulation}$/ ns
-	0	256	0.0	8821	1×300 [a]
A12	2	254	0.8	8821	3×100
A12	10	246	3.9	8821	3×100
A12	30	226	11.7	8821	3×100
A12	60	196	23.4	8821	3×100
A12	60	196	23.4	8821	3×100 [b]
A12	128	128	50.0	8821	3×100
A12	192	64	75.0	8821	3×100
A08	2	254	0.8	8821	3×100
A08	10	246	3.9	8821	3×100
A08	30	226	11.7	8821	3×100
A08	60	196	23.4	8821	3×100
A08	128	128	50.0	8821	3×100
A08	192	64	75.0	8821	3×100
R12	2	254	0.8	8821	3×100
R12	10	246	3.9	8821	3×100
R12	30	226	11.7	8821	3×100
R12	60	196	23.4	8821	3×100
R12	128	128	50.0	8821	3×100
R12	192	64	75.0	8821	3×100
T12	2	254	0.8	8821	3×100
T12	10	246	3.9	8821	3×100
T12	30	226	11.7	8821	3×100
T12	60	196	23.4	8821	3×100
T12	128	128	50.0	8821	3×100
T12	192	64	75.0	8821	3×100

[a] A 100% DMPC bilayer was simulated for analysis purposes (see text above).
[b] The glycolipid molecules were intentionally placed in a cluster in the starting configuration (see text above).

Table 7.3: Simulations details of the glycoside/phosphilipid binary mixtures *(continued from previous page).*

GL	n_{GL}	n_{DMPC}	$\%_{GL}$	n_{Water}	$t_{simulation}$/ ns
G12	60	196	23.4	8821	3 × 100
G12	128	128	50.0	8821	3 × 100
G12	192	64	75.0	8821	3 × 100
G08	60	196	23.4	8821	3 × 100
G08	128	128	50.0	8821	3 × 100
G08	192	64	75.0	8821	3 × 100

and/or phospholipid headgroups to move toward the interior of the bilayer, thus leading to a stabilized pore state. First, a 5 ps simulation was done using the microcanonical ensemble (NVE), that is, by keeping both volume and temperature constant. The temperature of the solvent heat bath was increased up to 500.0 K and the positions of all glycoside atoms were restrained by applying force constants of 1000 kJ nm^{-2} mol^{-1} and 10 kJ nm^{-2} mol^{-1} in the bilayer plane (xy) and in the bilayer normal (z) directions, respectively. Phospholipid atoms' positions were restrained using a force constant of 1000 kJ nm^{-2} mol^{-1} in all three directions. In a second simulation, carried out without position restraints to enable free motion of the lipids, the solvent was cooled down to 308.0 K and the pressure was kept constant at 1 bar in the bilayer plane direction and at 100 bar in the bilayer normal direction. The conformations thus obtained after 1.0, 1.5 and 2.0 ns, corresponding to pore states of increased size (and number of water molecules in the interior of the cavity), were employed as starting structures in the next step. During the final 10 ns long simulation, the pressure was kept constant at 1 bar in all three directions but the isothermal compressibility was set to zero in the bilayer plane direction. Because the cross-sectional area of the simulation box cannot be scaled in this direction when using the NPAT ensemble, pore closure is prevented. Each of the six configurations obtained by this procedure, corresponding to pre-formed pores, were then simulated for ∼20-30 ns without further equilibration. Pore stability was evaluated by monitoring the evolution of the system.

7.1.3 Minimization and initialization procedures

All systems were energy minimized prior to MM/MD simulations, following a common three-step procedure which consisted of (i) approximately 10000 steps using the steepest descent algorithm **[103]** (without constraints), followed by (ii) approximately 10000 steps using the limited-memory Broyden-Fletcher-Goldfarb-Shanno (l-BFGS) algorithm **[140]** (also unconstrained) and

Table 7.4: Simulations details of the membrane pore stability systems.

GL	n_{GL}	n_{DMPC}	$\%_{GL}$	n_{Water}	$t_{simulation}$/ ns
A12	52	196	20.1	12095	1×20 [a]
A12	52	196	20.1	12095	1×20 [a]
A12	52	196	20.1	12095	1×20 [a]
A12	124	124	50.0	12071	1×20 [a]
A12	124	124	50.0	12071	1×20 [a]
A12	124	124	50.0	12071	1×20 [a]

[a] Each of the three production runs was started from a different configuration of the system, with variable pore size (see text above).

(iii) a final minimization using the steepest descent algorithm again, but with all bond lenghts contrained. MM/MD simulations were subsequently initiated according to different procedures. The methodologies adopted for each system are briefly described below.

For micellization studies, a first 100 ps simulation was done with all glycolipid atoms position-restrained using a force constant of 1000 kJ nm^{-2} mol^{-1}, which was followed by a second 150 ps simulation with a force constant of 100 kJ nm^{-2} mol^{-1} in the same atoms. For the larger systems ($n_{GL} \geq 150$), an intermediate initiation step (performed between the latter two steps) was required, which consisted of further 150 ps without position restraints while applying the same coulombic charges (+0.05 e) in all atoms. This step ensures that the glycolipids are apart from each other and that no artifical clustering is present. During the last step, which was 200 ps long, only the sugar ring atoms were restrained with a force constant of 100 kJ nm^{-2} mol^{-1}.

In the case of glycoside micelle/phospholipid bilayer systems, the initialization was started by a 100 ps simulation, during which the positions of all glycoside and phospholipid atoms were retrained with a force constant of 1000 kJ nm^{-2} mol^{-1}. A second step was performed for further 100 ps, applying a force constant of 100 kJ nm^{-2} mol^{-1} in all glycoside atoms and a force constant of 1000 kJ nm^{-2} mol^{-1} in phosphorus atoms. A final 50 ps simulation was done with position restraints in the sugar ring atoms and on phosphorus atoms, using force constants of 100 kJ nm^{-2} mol^{-1} and 1000 kJ nm^{-2} mol^{-1}, respectively.

Regarding glycoside/phospholipid binary mixtures , the simulations were also initialized in three steps. The procedure was started by a 50 ps simulation, which was carried out with the positions of all atoms restrained using a force constant of 1000 kJ nm^{-2} mol^{-1}. In the second step, a 300 ps simulation was perfomed with all atoms again position-restrained, but using a force constant of 100 kJ nm^{-2} mol^{-1} instead. Finally, only the sugar ring and phosphorus atoms were restrained

with force constants of 100 kJ nm^{-2} mol^{-1} and 1000 kJ nm^{-2} mol^{-1}, respectively, for further 100 ps.

The equilibrated conformations obtained as described above were used as starting systems for the several simulations performed (with the exception of the membrane pore studies). Production run times and number of replicates, variable depending on the system, are detailed in **Tables 7.1-7.4**.

7.2 Analyses details

All analyzes were performed using tools available from the GROMACS software package [**125–127, 141**] and/or others developed in-house. Rendered structural representations were generated using PyMOL [**83**] and graphics were obtained using the Gnuplot (version 4.4.2) software package [**142**].

Ensemble averages were calculated considering only the contribution of equilibrated segments of the trajectories (variable in time lenght). All plotted data was averaged from at least three replicates, depending on the system (see **Section 7.1.2**). Errors were computed as the correlation-corrected standard deviation in the mean using standard methods based on the time-dependent autocorrelation function of the given property, which was used to estimate the number of independent blocks in the simulations [**102, 103**]. The correlation time was taken as the value at which the autocorrelation function becomes lower than 10%.

7.2.1 Radius of gyration

The radius of gyration (R_g) provides a rough measure of the compactness of a structure and is commonly used for monitoring the equilibration/stability of proteins and other molecular systems, i.e. surfactant micelles. It can be determined as the mass-weighted root mean square distance of the components of an object from its center of mass, according to the following equation:

$$R_g = \sqrt{\frac{\sum_{i=1}^{N} ||\mathbf{r}_i||^2 m_i}{\sum_{i=1}^{N} m_i}}, \tag{7.1}$$

where N is the number of particles, m_i is the mass of each particle and $\mathbf{r}_i$ is the vectorial position of each particle with respect to the center of mass of the object (i.e. molecule/supramolecular aggregate).

7.2.2 Solvent accessible surface area

The solvent accessible surface area (SASA) is the surface area of a molecule that is accessible to the solvent. The accessible surface **[102, 143]** is defined as the surface traced by the center of a spherical probe rolling along the van der Waals surface of the molecule. It was computed using a probe of radius 1.4 Å to represent a water molecule. In this work, it was used to evaluate the relative solvent exposure of all sugar headgroups and hydrocarbon side-chains in the micelle simulations. Since the network of glycolipid-solvent interactions is directly dependent on monomer packing efficiency, in micelles and relatd self-assembled supramolecular systems, this property may provide a rough measure of the overall thermodynamic stability of the aggregates.

7.2.3 Principal moments of inertia

Information regarding micelle shape is usually obtained from molecular simulations by computing the three principal moments of inertia (MOI), I_1, I_2 and I_3, which correspond to the eigenvalues of the diagonalized inertia tensor (see text below) **[144–155]**.

The moment of inertia is a physical property that measures the resistance of a rotating object to angular acceleration, which depends on the mass distribution of the components of the object throughout its shape. For a rotating rigid body, the moment of inertia with respect to a given axis can be defined considering a discrete distribution of mass (i.e. assuming uniform density), as the sum of products of each element of mass in the body and the square of the element's distance from the specified axis **[155]**, according to the following expression:

$$I = \int r^2 dm = \sum_{i=1}^{N} m_i r_i^2, \tag{7.2}$$

where N is the total number of particles, m_i is the mass of each particle and r_i is the perpendicular distance of each particle from the given axis of rotation. In general three-dimensional motion, the moments of inertia correspond to the entries of a symmetric 3×3 matrix, known as the inertia tensor. The three mutually orthogonal axes x, y, and z for which the quantities I_{xy}, I_{yx}, I_{xz}, I_{zx}, I_{yz} and I_{zy} - known as the products of inertia - are zero and the inertia matrix takes the diagonalized form are called the principal axes of inertia, and the quantities I_{xx}, I_{yy} and I_{zz} (also sometimes denoted, respectively, I_x, I_y and I_z, or I_1, I_2 and I_3), corresponding to the diagonal entries of the matrix, are called the principal moments of inertia, which are then given in cartesian coordinates by:

$$I_{xx} = \sum_{i=1}^{N} m_i(y_i^2 + z_i^2), \qquad I_{yy} = \sum_{i=1}^{N} m_i(x_i^2 + z_i^2), \qquad I_{zz} = \sum_{i=1}^{N} m_i(x_i^2 + y_i^2) \tag{7.3}$$

The shape of the globular micelles formed by most surfactants in solution is considered to be well described by ellipsoidal geometries (which often deviate significantly from spherical, depending on the nature of the monomer, i.e. its geometric/packing constraints), as supported by both theoretical studies [**156–158**] and experimental investigations on several model surfactants, including alkyl glycosides [**159, 160**]. Ellipsoids can be classified into different geometric shapes depending on the relative lenghts of the respective three semi-axes, which are directly proportional to the corresponding principal moments of inertia [3] (**Figure 7.2**). Hence, when the lenghts of two of the semi-axes (or two of the principal moments of inertia, by extension) are equal, we have a biaxial ellipsoid which is called either prolate spheroid (**Figure 7.2a**) or oblate spheroid (**Figure 7.2b**) depending on whether the two semi-axes are shorter, or longer than the remaining semi-axis, respectively. In the limit case where the lenghts of the three semi-axes are the same, the ellipsoid is a sphere [4] (**Figure 7.2c**).

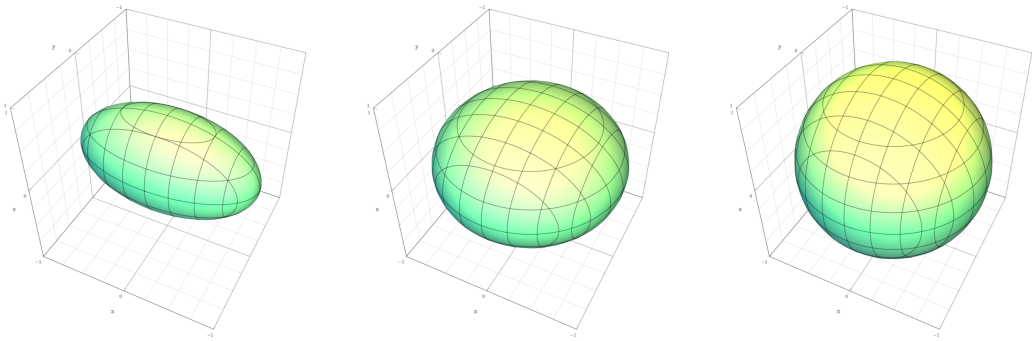

(a) **(b)** **(c)**

Figure 7.2: Representation of different ellipsoidal geometric shapes. **(a)** prolate spheroid ($I_1 > I_2 = I_3$), **(b)** oblate spheroid ($I_1 = I_2 > I_3$) and **(c)** sphere ($I_1 = I_2 = I_3$). Images were taken from ref. [**161**].

Most commonly, micelle shape is usually analyzed by calculating the ratios between the three principal moments of inertia, I_1/I_3, I_1/I_2 and I_2/I_3 [**144–155**], which give a measure of the overall prolate- or oblate-like elliptical shape of the aggregate. In particular, the ratio of the longest to the shortest principal moment of inertia (I_1/I_3) is often assessed since it is indicative of the deviation from an ideal sphere (i.e. a larger I_1/I_3 indicates a more elliptical shape).

[3] An ellipsoid is a quadratic surface which is given in cartesian coordinates by $\frac{x^2}{a^2} + \frac{y^2}{b^2} + \frac{z^2}{c^2} = 1$, where a, b and c are the lenghts of the semi-axes along the x, y, and z directions, respectively (and $a \geq b \geq c$). The principal moments of inertia are then given by $I_1 = \frac{1}{5}M(a^2 + b^2)$, $I_2 = \frac{1}{5}M(a^2 + c^2)$, and $I_3 = \frac{1}{5}M(b^2 + c^2)$, where M is the total mass of the ellipsoid and $I_1 \geq I_2 \geq I_3$ [**144, 155**].

[4] For a sphere, $I_1 = I_2 = I_3 = \frac{2}{5}Mr_i^2$, where r_i is the radius of the sphere.

7.2.4 Area per lipid

The area per lipid (A_L), which gives a direct measure of lipid lateral organization, is probably the most important structural property of lipid bilayers, typically used to characterize the correct liquid phase behaviour of lipid bilayers and for monitoring system equilibration in membrane simulations **[118, 162]**. This parameter is also fundamental in the context of force field validation **[162, 163]**. For single-component bilayer systems, it can be easily determined by evaluating the dimensions of the simulation box along the bilayer plane (xy), according to the following expression:

$$A_L = \frac{x_b \times y_b}{N}, \tag{7.4}$$

where x_b and y_b represent the dimensions of the simulation box over the corresponding cartesian axes, and N is the number of lipid molecules in each monolayer (i.e. half the total number of lipids in the bilayer). It should be noted that this approach can only be applied assuming that the bilayer structure remains intact throughout the simulation.

In the case of more complex bilayer systems consisting of multi-component mixtures or lipids and/or other molecules (i.e. our glycoside/phospholipid binary mixtures), more rigorous formalisms have been proposed based on the definition of the average partial-specific-area for the several bilayer components. This new canonical quantity can be estimated from the relationship between the total area per lipid (easily obtained from computer simulations as described above) and the molar fraction of each lipidic component, given a set of simulations at different molar fractions (see ref. **[164]** for further insight). Although this approach could be particularly interesting when applied to our heterogeneous systems, we decided not to implement such analysis for the purposes of this thesis. Instead, we computed the average total area of the bilayer (later simply referred to as total area) for the several simulations carried out, since it may also provide some indirect information about the area per lipid.

7.2.5 Order parameter

The degree of hydrocarbon chain ordering/disordering in lipid bilayers can be assessed by determining the deuterium order parameter ($|S_{\mathrm{CD}}|$), which measures the orientational anisotropy of each C-D bond with respect to the bilayer normal (z) direction **[165]**, defined as follows:

$$|S_{\mathrm{CD}}| = \frac{1}{2}\langle 3\cos^2\theta - 1\rangle, \tag{7.5}$$

where θ corresponds to the angle between the vector along the C-D bond and the reference axis, and the angular brackets denote an average over time for the entire ensemble, which is calculated separately for each methylene segment. Furthermore, this quantity is often reported

from computer simulations as an average over both *sn*-1 and *sn*-2 chains. The order parameter can be experimentally determined by ^{2}H-NMR spectroscopy (i.e. from its relationship with the deuterium quadrupolar splitting) [**165**]. In computer simulations using united atom force fields (i.e. where non-polar hydrogen atoms are not treated explicitly), in turn, its estimation follows a standard methodology based on the reconstruction of the C-D bond vector from the positions of the neighboring carbon atoms [**165**–**167**].

7.2.6 Bilayer thickness

The lipid bilayer thickness is known to play a key role in several biological processes (i.e. modulation of integral membrane protein function) [**168, 169**]. Therefore, it is considered an important parameter in the context of the structural characterization of model lipid bilayers. Although several other definitions of lipid bilayer thickness can be found in the literature, depending on the technique used for measuring it (i.e. hydrophobic thickness, steric thickness, and overal bilayer thickness), we analyzed the headgroup spacing which can be defined as the distance between the lipid headgroup phosphates. This quantity is commonly determined experimentally using the small-angle X-ray scattering technique [**115, 119**]. More precisely, the bilayer thickness was computed as twice the mean distance between the (z)-positions of all phosphorus atoms and the center of mass of the bilayer, averaging over time and for the entire ensemble.

7.2.7 Lateral diffusion

Lipid bilayers are highly flexible entities where several dynamic phenomena govern not only their structure but also their functional properties, with particular relevance in biological systems. The dynamical processes taking place in lipid membranes cover an impressive range of time-scales (i.e. from picoseconds to even hours) [**170, 171**]. In-plane lateral diffusional motions are probably the most studied experimentally, but very different values are obtained for lateral self-diffusion coefficients depending on both the conditions and the time-scale on which the different techniques operate. For instance, fluorescence recovery after photobleaching (FRAP) is sensitive at the milisecond time-scale [**172**], while neutron scattering experiments lead to measurements at the picosecond time-scale [**173**]. This discrepancy in the experimentally measured lateral diffusion coefficients is interpretated in terms of distinct diffusional movements of the lipid molecules (i.e. fast motions within their microenvironment occuring at shorter time-scales and slower longe-range motions between adjacent sites at longer time-scales) [**171, 174**]. The major advantage of computer simulation techniques is that they cover most of the time-scales of interest. The lateral self-diffusion coefficient (D) of a given particle can be computed from the slope of the mean square displacement (MSD) over time (for the linear portion of the curve), using the Einstein relation in two dimensions [**102, 103, 171**]:

$$D = \lim_{t\to\infty} \frac{1}{4}\frac{d}{dx}\langle[\mathbf{r}(t+t_0) - \mathbf{r}(t_0)]^2\rangle_{t_0}, \tag{7.6}$$

where $\mathbf{r}(t+t_0)$ is the center-of-mass vectorial position of the particle at each time step $(t+t_0)$, $\mathbf{r}(t_0)$ is the vectorial position at each each time origin t_0, and the angular brackets imply averaging over all time origins and for the entire ensemble. This parameter was calculated using all phospholipid phosphorus as reference atoms instead of the center of mass of each molecule for simplification.

Chapter 8

Results and discussion

8.1 Micellization of glycosides in aqueous media

This section is dedicated to the results obtained for the glycoside micellization studies. As we have already introduced (see **Section 6.2**), preliminary biological assays and surface activity data (i.e. adsorption and aggregation parameters) on the family of sugar-based surfactants developed by Rauter and co-workers [**1**–**3**] are indicative that the antibacterial activity displayed by these molecules is governed by glycoside micelle-bacterial cell membrane interaction phenomena. In this context, our first set of simulations focused on studying the microscopic behaviour and features of alkyl deoxyglycoside micelles in aqueous media. The main goals, then, were (i) to preliminarily investigate the dynamics of glycoside self-assembling into micelles, as well as to evaluate their kinetic stability at different aggregation numbers (**Section 8.1.1**); and (ii) to further characterize the structural/physical properties of these aggregates in solution (i.e. micelle size, shape, and relative thermodynamic stability) at the molecular level (**Section 8.1.2**). Ultimately, we intended to obtain different equilibrated conformations to be later employed in the glycoside micelle/phospholipid bilayer interaction studies (see **Section 8.2** further ahead).

In contrast with many studies reported in the literature for other surfactant systems [**149, 152**–**154, 175**], including related alkyl glycopyranosides [**144**–**148**], in which pre-assembled micelles were used as starting configurations, we decided to start the simulations from random configurations of glycolipids within the solvated simulation box [**150, 151, 176**–**178**], both due to the practical aspects of this methodology and because it allowed us to study the self-assembly process. This approach was applied to two of the glycolipids (A12 and A08), which were simulated at different concentrations/aggregation numbers as described in **Section 7.1.2** (see **Table 7.1**). The rigorous treatment of nominal concentration and/or concentration-dependent effects (i.e. interactions between multiple aggregates) is particularly challenging in micelle simulations, mainly due to the restrictions imposed by both the periodic boundary conditions (i.e. micelles cannot see their periodic images) and the size of the systems that may be studied. In fact, although concentration is expected to influence the behaviour of the system during the initial

stages of the simulations (where the range concentrations is extremely high), once assembled (and equilibrated), the micelles are modelled in an infinite dilution condition where concentration has a negligible effect on the properties of the system [**144**]. Hence, a comprehensive study of the effecs of concentration (i.e. through modelling several micelles within the same simulation box, at different concentrations) is beyond the scope of this work since it would be not only methodologically difficult, but also - and most importantly - unfeasible due to the large computational cost it would require.

8.1.1 Micelle formation/equilibration

System equilibration was monitored through inspection of the time-course of the radius of gyration, the total potential energy, and by visual inspection of each trajectory. The former is shown in **Figures B.1-B.2** and **B.3-B.4** for all replicates of the A12 and A08 systems simulated, respectively, differing in the aggregation number. In all cases, a decrease in the radius of gyration takes places very abruptly in a short time-scale (i.e. invariably whitin the initial 10 ns) in the range of concentrations simulated, after which an equilibrium value is reached (variable depending on the aggregation number). This variation corresponds to the self-assembly of glycoside monomers into micelles, which is illustrated in **Figure 8.1**. In some cases this process may be complete just after a few nanoseconds, depending on whether multiple pre-micellar aggregates of smaller size are produced prior to the formation of the final, larger micelle or not.

It can be observed in **Figures B.1-B.4** that the instantaneous value of the radius of gyration remains stable over the course of most of the simulations, with the exception of the A08 systems simulated at lower aggregation numbers of $n_{GL} = 5$ and 10, for which fluctuations of relatively large amplitude take place occasionally (see **Figures B.3a** and **B.3b**, repectively). These fluctuations are due to single glycolipid exchanges with the bulk solution and/or partial aggregate dissociation events that occur rapidly in the sub-nanosecond time-scale, demonstrating that solvation of the sugar headgroups is a process that significantly competes with aggregation at lower aggregation numbers, when the glycoside exhibits a less hydrophobic octyl side-chain. Notwithstanding, nearly all micelles were considered to be equilibrated (i.e. presenting optimal aggregate compactness/size and shape), and kinetically stable throughout the last 90 ns of production and hence that segment of each trajectory (including for the two systems referred above) was subjected to structural analysis. It should be also noted that for the larger systems with aggregation numbers of $n_{GL} \geq 100$, single glycolipid diffusion from the micelle's surface to its hydrophobic interior is often observed when visually inspecting the trajectories. Although in most of the simulations these events do not compromise micelle structural integrity, in two of the replicates of the A12 system at an aggregation number of $n_{GL} = 200$ a considerable number of glycolipids (≥ 10) migrate to the interior of the micelle, occasionaly with simultaneous penetration of high-energy water molecules, which become trapped in the hydrophobic core of the micelle over the course of the simulations (see replicates 3 and 5 in **Figure B.2d**). As these

events lead to an overall decrease in the radius of gyration (and should affect other structural properties likewise), the referred replicates were discarded for analysis purposes. Moreover, this result suggests that the optimal number of monomers for micelles of this particular glycoside probably lies below $n_{GL} = 200$ and, consequently, at such high aggregation number transition to more complex aggregate structures - the study of which is beyond the scope of this work - should be preferred.

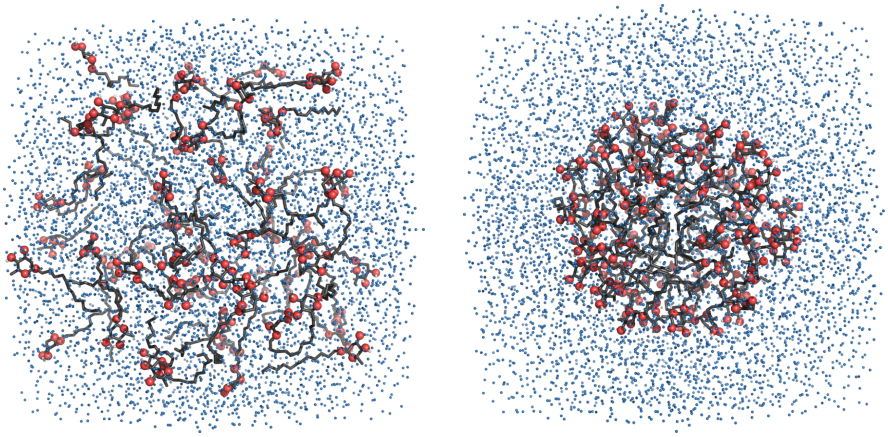

(a) $\mathbf{t_{simulation}} = 0$ ns **(b)** $\mathbf{t_{simulation}} = 100$ ns

Figure 8.1: Representative snapshots for the self-assembly of 60 glycolipids (GL = A12) in aqueous media. **(a)** Initial configuration of the system and **(b)** equilibrated micelle after 100 ns production. GL molecules are shown as dark gray sticks (carbon atoms), red spheres (oxygen atoms) and white sticks (hydroxy group hydrogens); water oxygens are represented as light blue spheres. All apolar and water hydrogens were omitted for clarity. Images were rendered using PyMOL [**83**].

8.1.2 Structural analysis

Micelle structure was briefly characterized in terms of the aggregation number dependence of three important properties, which could be easily computed from the MD trajectories: the radius of gyration, the solvent accessible surface area (SASA) and the principal moments of inertia (MOI). The most relevant results obtained will now be presented.

Figure 8.2 shows the radius of gyration for the glycoside micelle simulations at different aggregation numbers, now averaged over each trajectory. The mean value of the radius of gyration incresases with the number of monomers, indicating that larger aggregates are formed. It can also be observed that the size of the dodecyl glycoside micelles is larger than that of the corresponding octyl counterparts, as expected since the latter present shorter hydrocarbon side-chains. More importantly, the fact that there is a non-linear relationship between the radius of gyration, which gives a measure of the overall compactness of the micelle structures, and the aggregation number suggests that the shape of the micelles should vary according to the number of monomers.

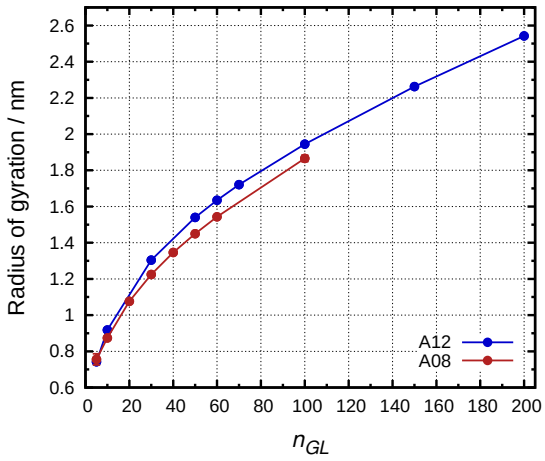

Figure 8.2: Radius of gyration as a function of the aggregation number averaged from the simulations of glycolipid micelles.

In the search for a structural property that would allow us to compare different micelles with respect to their relative thermodynamic stability, we then analyzed the solvent accessible surface area (SASA, **Figure 8.3**), which provides a measure of the solvent exposure of a molecule. The total SASA is herein reported per glycolipid molecule, instead of the overall absolute value for each aggregate, since the former gives an idea of the accessible area of every monomer within each micelle which, in turn, depends on monomer packing efficiency. It results from the contribution of a hydrophilic and a hydrophobic component, that is, the SASA due to the sugar headgroup and to the hydrocarbon side-chain, respectively. **Figures 8.3a** and **8.3b** show the variation of the total SASA per glycolipid with the aggregation number for the A12 and A08 micelle simulations performed, respectively. In both cases, the total SASA per glycolipid decreases when the number of monomers increases in the range of aggregation numbers simulated, suggesting that larger aggregates present greater thermodynamic stability in solution. Inspection of **Figures 8.3c** and **8.3d**, which represent the relative contribution of the sugar headgroups and hydrocarbon side-chains to the total SASA (for A12 and A08 micelles, respectively), reveals that this result arises from a lower solvent exposure of surfactant hydrophobic tails - the driving force for micelle formation in light of the hydrophobic effect **[179, 180]** - when aggregate size increases. Nevertheless, it is interesting to note that there is a significant contribution of surfactant tailgroups to the total SASA (ranging from ∼51% to ∼28% and from ∼43% to ∼25% for A12 and A08 micelles, respectively), demonstrating that the hydrocarbon side-chains are not optimally excluded from the water interface. In fact, visual examination of the trajectories shows that glycoside micelles present a rather rough, irregular-shaped surface exhibiting several hydrophobic tailgroups exposed to the solvent, similarly to what has been described for related alkyl glycosides in the literature **[144–148]**. Also noteworthy is the fact that the observed decrease in total SASA per glycolipid with the increasing aggregation number is not a linear dependence again. In fact, while for lower numbers of monomers an abrupt decrease can be observed, there is a particular range of aggregation numbers ($n_{GL} \approx$ 50-60 and $n_{GL} \approx$

30-40 for A12 and A08 micelles, respectively) from which this tendency is much less significant and hence all micelles present a considerably greater stability. Finally, comparison of the data obtained for both dodecyl and octyl glycoside micelles shows that the latter feature lower values of total SASA per glycolipid, which is due to less exposuse of glycolipid tailgroups in that case. This results from the lower lenght of the octyl hydrocarbon side-chain when compared to the dodecyl counterpart and, consequently, higher headgroup-to-tailgroup area ratio. Therefore, the relative stability of dodecyl and octyl glycoside micelles cannot be rigorously discussed without normalizing the SASA values herein presented, which merits further investigation.

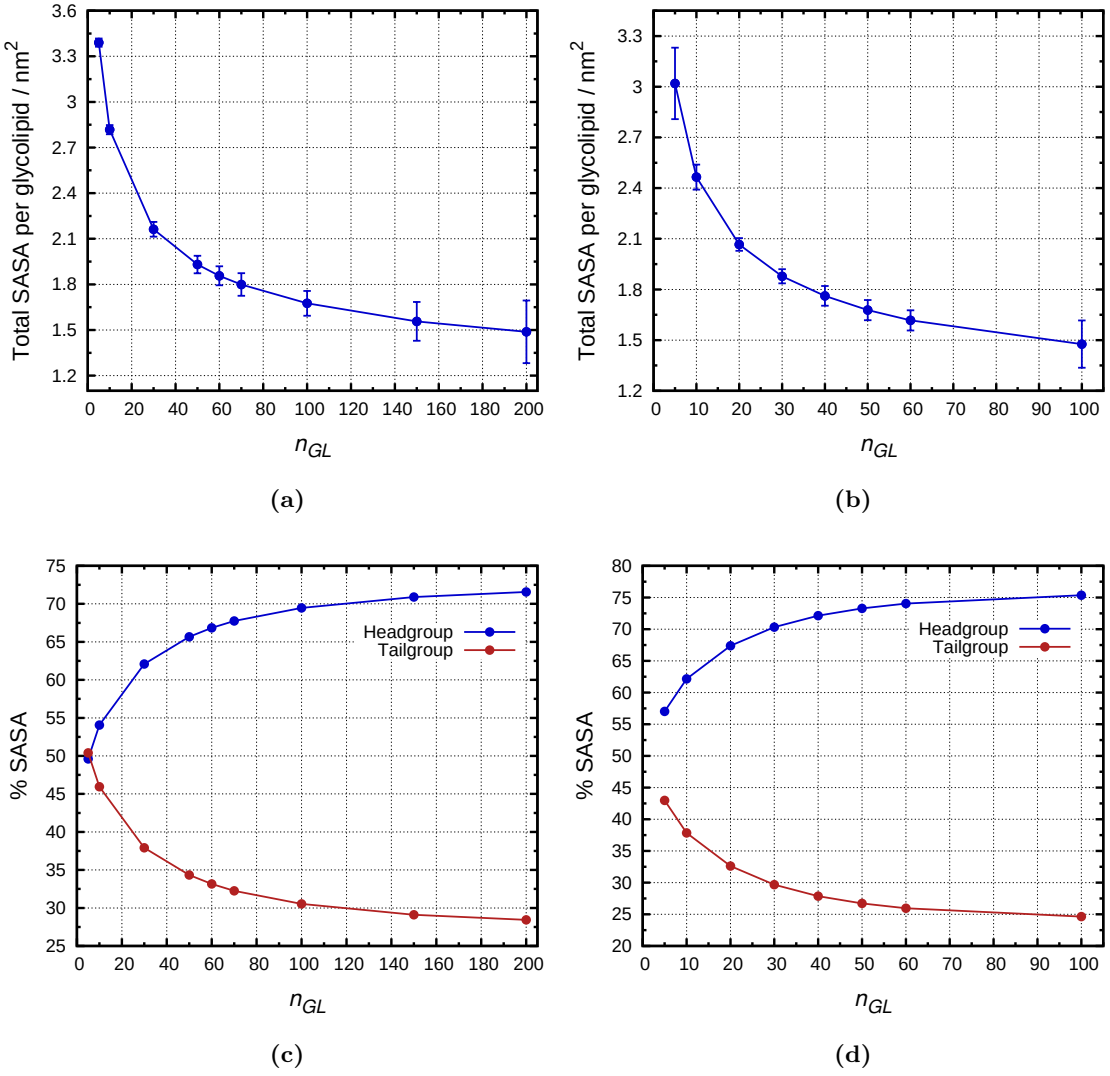

Figure 8.3: Solvent accessible surface area (SASA) analysis for the simulated glycolipid micelles at different aggregation numbers. **(a)**, **(b)** Average total SASA per glycolipid for the A12 and A08 glycoside micelles, respectively; **(c)**, **(d)** Relative contribution of the sugar headgroups and hydrocarbon side-chains in percentage for the A12 and A08 glycoside micelles, respectively.

For the characterization of glycoside micelles with regard to their shape, we analyzed the principal moments of inertia (MOI, **Figure 8.4**). As discussed earlier (see **Section 7.2.3**), examining

the ratios for the three principal MOIs provides a measure of the elliptical shape of globular structures. In particular, the ratio of the longest to the shortest MOI, I_1/I_3, is probably the most important since it describes the deviation from an ideal sphere. The three ratios I_1/I_3, I_1/I_2 and I_2/I_3 were computed as a function of the aggregation number, and the results are shown in **Figures 8.4a** and **8.4b**, for the A12 and A08 micelle simulations, respectively. Firstly,

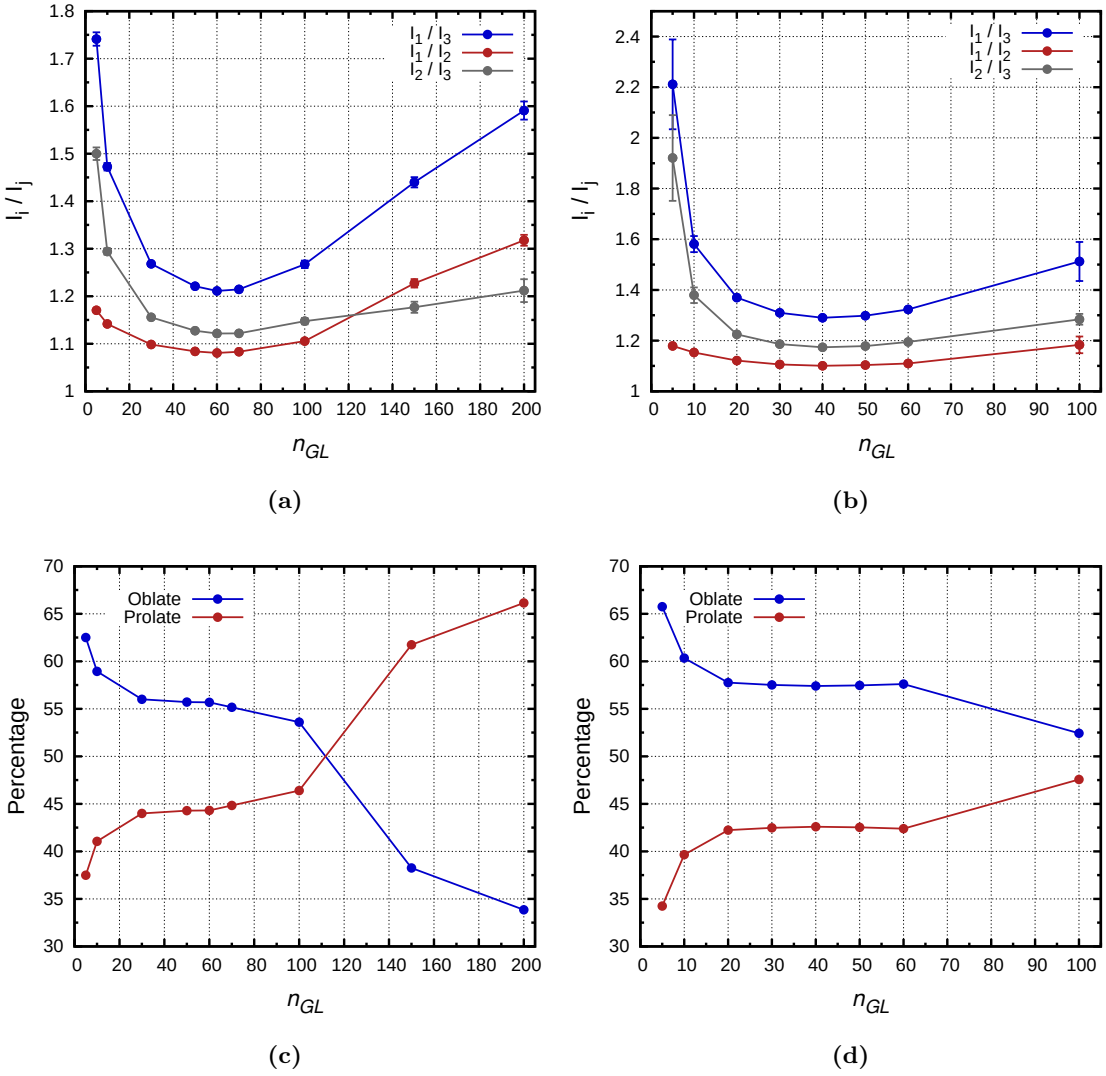

Figure 8.4: Principal moments of inertia (MOI) analysis for the simulated glycolipid micelles at different aggregation numbers. **(a)**, **(b)** Average MOI ratios for the A12 and A08 glycoside micelles, respectively; **(c)**, **(d)** Relative population of oblate- and prolate-like spheroids in percentage for the A12 and A08 glycoside micelles, respectively.

the results demonstrate that the average shape deviates significantly from spherical for all micelles (with I_1/I_3 values ranging from ∼1.2 to ∼1.7 and from ∼1.3 to ∼2.4 for the A12 and A08 micelles, respectively). It may also be noticed that octyl glycoside micelles are relatively more elliptical when compared to their dodecyl counterparts. Moreover, the lower limits obtained for I_1/I_3 indicate that micelles are more spherical at aggregation numbers of $n_{GL} = 60$ and 40,

for the A12 and A08 glycoside micelles, respectively. In order to further distinguish micelles' elliptical shape betweeen either oblate- or prolate-like, we calculated the relative population of each spheroid from the principal MOIs, which is given in percentage according to the following equation:

$$\%_{oblate} = \frac{(I_2 - I_3) \times 100}{I_1 - I_3}, \qquad \%_{prolate} = 100 - \%_{oblate} \tag{8.1}$$

The values determined for the different aggregation numbers are represented in **Figures 8.4c** and **8.4d**. The results show that for numbers of monomers up to $n_{GL} = 100$ micelle's average elliptical shape is oblate-like, whereas in the case of larger aggregates ($n_{GL} > 100$) the prolate-like shape is more populated, as indicated by the results obtained for the dodecyl glycoside. Finally, it should be also noted that, although we were able to characterize the average shape of the simulated glycoside micelles, significant fluctuations in the principal MOIs (and their ratios, consequently) occur frequently in the sub-nanosecond time-scale (data not shown), emphasizing the dynamic behaviour of glycoside micelle's shape in solution.

8.2 Interaction of glycoside micelles with a model membrane

In the previous section, different deoxyglycoside micelles were simulated and preliminarily analyzed with respect to their relative stabilities and configurations in solution. Pursuing our computational project, we will focus from now in the study of glycoside-phospholipid bilayer interactions, which should provide relevant molecular insight into their mechanism of action.

First, we report on the results from a series of simulations performed starting from several equilibrated conformations of glycoside micelles (obtained as described in **Section 8.1**) at the interface of a model phosphatidylcholine (DMPC) membrane. This approach allowed us to study the adsoption properties of these molecules, through monitoring (i) glycoside partitioning from micelles in solution to the lipid bilayer at the interface and/or (ii) glycoside micelle-lipid bilayer fusion events. Typically, such molecular processes (generally involving very large (bio)molecular systems, i.e. up to the micrometer-lenght scale) are associated with high potential energy barriers and thus may be only efficiently sampled in rather long time-scales (i.e. from nanoseconds to miliseconds). For that reason, coarse-grained simulations [1] are often applied in related computer simulations, i.e. studies on complex surfactant systems [**181**–**183**], biological systems [**184**] and drug-membrane interactions [**185**–**187**]. Although these models usually require more affordable calculation time, they also have the disavantage of providing much less molecular detail when compared to atomistic simulations. Furthermore, in most cases a specific coarse-grained model has to be implementated for each particular study-system.

[1] In coarse-grained models, a molecular system may be simplified by averaging out a number of non-essential degrees of freedom, that is, through the representation of groups of atoms as single beads.

In order to overcome the above-referred limitations, we decided to perform multiple long time-scale (i.e. either 100/300 ns or 100/500 ns long each, depending on the size of the system) atomistic simulations as described in **Section 7.1.2** (see **Table 7.2** for further detail). In these particular studies, only the lead compound (A12) was employed as model glycolipid and a pre-equilibrated DMPC bilayer containing 256 phospholipid molecules was used in all cases. Three series of ten simulations were performed essentially differing in the size of the system (and, consequently, also on production time-lenghts), which featured glycoside micelles containing either 10, 30, or 60 monomers. In light of the results discussed in **Section 8.1.2**, these micelles display increasing thermodynamic stabilities. Hence, it could be antecipated that glycoside micelles with higher aggregation numbers would need to cross larger energy barriers (i.e. longer simulation run times) for monomer partitioning and/or glycoside micelle-phospholipid bilayer fusion events to be observed during our simulations. Although it would be interesting to perform simulations with glycoside micelles presenting higher aggregation numbers, those simulations would also require using larger phospholipid bilayers (i.e. containing 512 DMPC molecules), mainly due to the restrictions imposed by the periodic boudary conditions. Thus, our simulations were designed essentially taking into account two limitations: (i) the eventually slow kinetics and (ii) the unfeasible computational cost that could both compromise the success of our studies, if the simulated systems were too large. The full results obtained from this set of simulations are then summarized in **Table 8.1**.

As an initial remark, it should be noted that adsorption of glycoside micelles into the surface of the phospholipid bilayer at their interface was found to occur rapidly in our simulations, that is, invariably during the initial 10 ns (see **Figures 8.5a** and **8.5b** for illustrative snapshots regarding **Simulation #11** in **Table 8.1**). Moreover, this is an irreversible process in the sense that the glycoside micelle-phospholipid bilayer complex interaction remains stable throughout all the simulations, and independently of eventual insertion events taking place thereafter. More importantly, **Table 8.1** shows that, as intended, several glycolipid partitioning events could be captured in our simulations, ranging from the insertion of only a few number of monomers (see **Simulations #4**, **#14** and **#24** in **Table 8.1**) to the complete fusion of glycolipid micelles into the interior of the phospholipid bilayer (**Simulations #1** and **#11**). The latter process is illustrated in **Figure 8.5** for **Simulation #11**, which is an interesting example where all 30 glycolipids were completely inserted in the phopsholipid bilayer after $<$ 400 ns of production time. Without exception, whenever these partitioning events could be observed, the first glycolipid was completely inserted within the phospholipid bilayer during the initial 100 ns of the simulation. However, in most cases further partitioning events were observed only after many hundreds of nanoseconds (see **Simulations #11**, **#14** and **#24**), except for **Simulation #1** where complete micelle fusion occured as a synchronous process within $<$ 100 ns of production time. Furthermore, the outcome of these glycolipid micelle-phospholipid bilayer interactions seems to be dependent on micelle size/stability, once complete insertion of all glycolipids could be captured only for the smaller micelles presenting aggregation numbers of $n_{GL} = 10$ and 30 (**Simulations #1** and **#11**), whereas in the case of the more stable micelle

Table 8.1: Summary of the results obtained for the glycoside micelle/phospholipid bilayer interaction studies [a]. Entries corresponding to insertion events are highlighted.

Simulation	n_{GL}	$n_{inserted\ GL}$	$t_{insertion}$/ ns	$t_{simulation}$/ ns
#1	10	10	66−78 [b]	300
#2	10	-	-	300
#3	10	-	-	300
#4	10	1	39	300 [c]
#5	10	-	-	100
#6	10	-	-	100
#7	10	-	-	100
#8	10	-	-	100
#9	10	-	-	100
#10	10	-	-	100
#11	30	30	92 [d], 310 [e], 340−388 [b]	500
#12	30	-	-	500
#13	30	-	-	500
#14	30	2	94 [d], 463 [e]	500 [c]
#15	30	-	-	100
#16	30	-	-	100
#17	30	-	-	100
#18	30	-	-	100
#19	30	-	-	100
#20	30	-	-	100
#21	60	-	-	500
#22	60	-	-	500
#23	60	-	-	500
#24	60	2	89 [d], 327 [e]	500 [c]
#25	60	-	-	100
#26	60	-	-	100
#27	60	-	-	100
#28	60	-	-	100
#29	60	-	-	100
#30	60	-	-	100

[a] GL = A12 was used in all simulations.
[b] Time interval for the overall insertion of either all or the remaining glycolipids.
[c] After 100 ns, the simulation was prolonged to the indicated final production time (see **section 7.1.2**).
[d] Simulation time until complete insertion of the 1st glycolipid.
[e] Simulation time until complete insertion of the 2nd glycolipid.

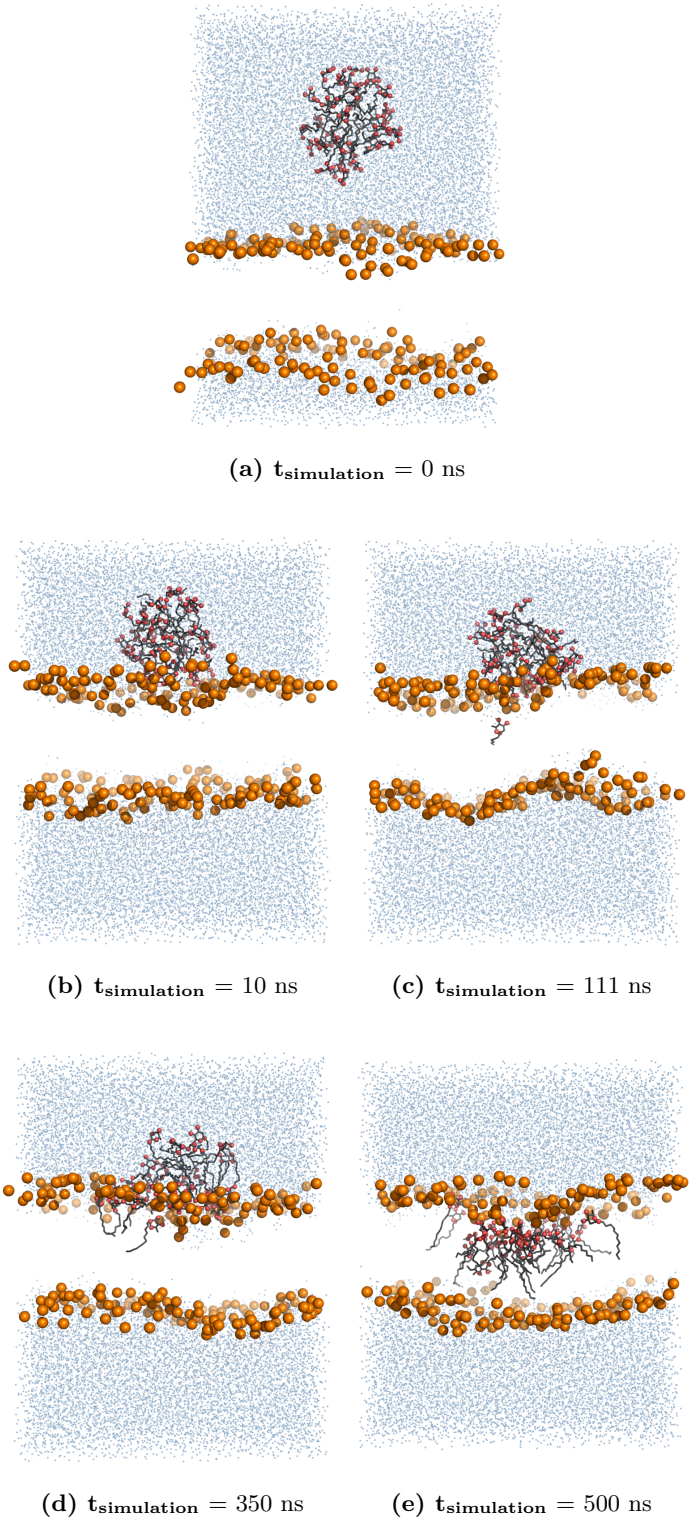

(a) $\mathbf{t_{simulation}}$ = 0 ns

(b) $\mathbf{t_{simulation}}$ = 10 ns

(c) $\mathbf{t_{simulation}}$ = 111 ns

(d) $\mathbf{t_{simulation}}$ = 350 ns

(e) $\mathbf{t_{simulation}}$ = 500 ns

Figure 8.5: Representative snapshots for the full insertion of 30 glycolipids (GL = A12) into a phospholipid bilayer consisting of 256 DMPC molecules (**Simulation #11** in **Table 8.1**). **(a)** Initial configuration of the system and configurations obtained after **(b)** 10 ns, **(c)** 111 ns, **(d)** 350 ns and **(e)** 500 ns production time. GL molecules are shown as dark gray sticks (carbon atoms), red spheres (oxygen atoms) and white sticks (hydroxy group hydrogens); phospholipid molecules phosphorus are shown as orange spheres and water oxygens as light blue spheres. Phospholipid carbon atoms, oxygens and nitrogens, and all apolar and water hydrogens were omitted for clarity. Images were rendered using PyMOL [**83**].

containing 60 glycolipids we were able to sample the insertion of only two monomers. It should be mentioned that significant perturbations in bilayer structure (i.e pronounced curvature) could be detected throughout the trajectories (data not shown), especially in the case of glycoside micelles with higher aggregation numbers of $n_{GL} = 30$ and 60, which indicates that the tight micelle-membrane interaction induces mechanical stress on the bilayer surface. Also noteworthy is the fact that upon partitioning, glycolipid tranverse diffusion (i.e. from one leaflet of the bilayer into the other) was never observed during our sub-microsecond simulations, indicating that such diffusional movements - often referred to as *flip-flop* - should take place in longer time-scales for these neutral surfactants, similarly to phospholipid molecules. This is most probably due to (i) strong interactions between the sugar headgroups and the phospholipid hydrophilic region, as well as (ii) the network of hydrogen bonds involving the cluster-configurated sugar headgroups, both of which can be clearly observed in our simulations (see **Figures 8.5c-e**).

In summary, we were able to capture several examples of glycolipid partitioning from micelles in solution into a model phospholipid bilayer at their interface, using atomistic simulations. Notwithstanding, we must stress the fact that these events could be observed only in a couple of simulations. Moreover, both single glycolipid insertion and/or complete micelle fusion events were captured within comparable time-scales. Altogether, these results highlight the complexity of the potential energy landscapes, that is, the unfavorable kinetics that we had already antecipated. This is a result of very large potential energy barriers which, in turn, probably are driven by solvation effects (i.e. water molecules must be excluded from the micelle-membrane interface in order for insertion events to take place). Therefore, a much more extensive conformational sampling would be required for these events to be quantitatively analyzed. Moreover, it should also be noted that each insertion event promotes an imbalance in the system (i.e. the number of lipids in the inner and outer monolayers becomes different), which also represents a barrier for further internalization events to be captured during our simulations. In fact, it would take longer time-scales for the initial symmetry of the system to be re-established (i.e. via glycolipid and/or phospholipid *flip-flop* movements, see discussion above), thereby hampering any attempt to quantify the number of insertion events observed by the end of our sub-microsecond simulations.

8.3 Glycoside/phospholipid binary mixtures

The computational simulations presented and discussed in the previous section allowed us to verify that glycoside micelles interact tightly with phospholipid bilayers, ultimately leading to the irreversible insertion of glycosides into the model membranes. The following step of our project was to investigate the effect of these sugar-based surfactants on the biophysical properties/structural integrity of lipid bilayers upon partioning, which was accomplished through the simulation of glycoside-phospholipid binary mixtures at different molar fractions. Hence, our approach to assess the eventual destabilization of lipid bilayers by alkyl deoxyglycosides at the

microscopic level was based on simulating increasing glycolipid concentrations [2], focusing now strictly on the viewpoint of the membrane.

All simulations were performed using now the four target glycolipids (A12, A08, R12, and T12) and again starting from a fully-hydrated phospholipid bilayer initially containing 256 DMPC molecules, as described in **Section 7.1.2**. Final GL/PC molar fractions ranged from 0.8% to 75.0%, and a 100% DMPC bilayer was simulated in order to be employed as a control (see **Table 7.3**). In this section, the simulations were further extended to the related dodecyl/octyl β-D-glucopyranosides (G12/G08) (see **Table 7.3**), because the effect of non-ionic detergents from this class on the ordering of phosphatidylcholine bilayers has already been investigated by experimental techniques (i.e solid-state ^{2}H- and ^{31}P-NMR spectroscopy) **[138, 139]**. These sugar-based detergents have been the subject of extensive research **[188, 189]**, particularly the octyl β-D-glucopyranoside (G08) which has found widespread biochemical applications (i.e. in biomembrane research), mainly due to its superior physico-chemical properties for membrane solubilization and simultaneous non-denaturating effect on proteins, when compared to other detergents (i.e. ionic surfactants) **[138, 139, 190–194]**. Although the deutereum order parameters ($|S_{CD}|$) reported in the literature have been determined from multilamellar bilayer dispersions containing 1,2-dipalmitoyl-*sn*-glycero-3-phosphocholine (DPPC) **[138]**, which exhibits longer-lenght fatty acyl chains when compared with our model phospholipid (DMPC), we expect such experimental data to be comparable and thus provide information on the reliability of our force field parametrization. An additional 23.4% A12/PC bilayer simulation was performed (also in triplicate) featuring all glycolipid molecules in a cluster configuration in the beginning of the simulation (refer back again to **Section 7.1.2** and **Table 7.3**). This system was simulated aiming at qualitatively evaluating the ability of these molecules to induce the formation of membrane pores, and thus was not considered for quantitative analysis.

8.3.1 Equilibration

Equilibration of the glycoside/phospholipid binary mixture simulations was followed through the temporal evolution of the total cross-sectional area along the bilayer plane (herein after simply referred to as total area) of each two-component lipidic system over the corresponding trajectory, which was computed as described in **Section 7.2.4**. The results are shown in **Figures B.5**, **B.6**, **B.7**, **B.8**, **B.9** and **B.10**, for all replicates of the A12, A08, R12, T12, G12 and G08 simulations, respectively. It can be clearly observed that equilibration occurs nearly instantly for the lipidic systems containing lower molar fractions of glycolipid, while in the case of the simulations performed at higher molar fractions a significant decrease in the total area takes place whitin the initial 20 ns of production time. For that reason, that segment

[2] In the case of multi-component bilayer simulations, increasing the molar fraction of one lipidic component corresponds to an increase in its local concentration within the membrane. However, it should be clarified that a direct relationship between this local concentration and the nominal surfactant concentration in solution (i.e. from experiments) cannot be established since the latter is a macroscopic property. In order to overcome that limitation, we tested a large range of concentrations in our simulations.

of each trajectory was discarded and only the final 80 ns of production time were considered for analysis. In most cases, after this initial decrease, the total area then converges into a stable value, this process corresponding to system equilibration. An illustrative snapshot of a fully-equilibrated 23.4% A12/PC binary mixture (taken after 100 ns of production time) is represented in **Figure 8.6**. In the particular case of the octyl glycoside simulations performed at higher molar fractions of $x_{GL} = 75\%$, stabilization of this structural property is not observed. Instead, the total area decreases throughout the simulations, as shown in **Figures B.6f** and **B.10c** corresponding to the A08/PC and G08/PC two-component bilayer systems. This process leads to very pronounced distortions in the lipid bilayers, as indicated by visual inspection of the trajectories (data not shown). Although in these cases the bilayer structural intergrity

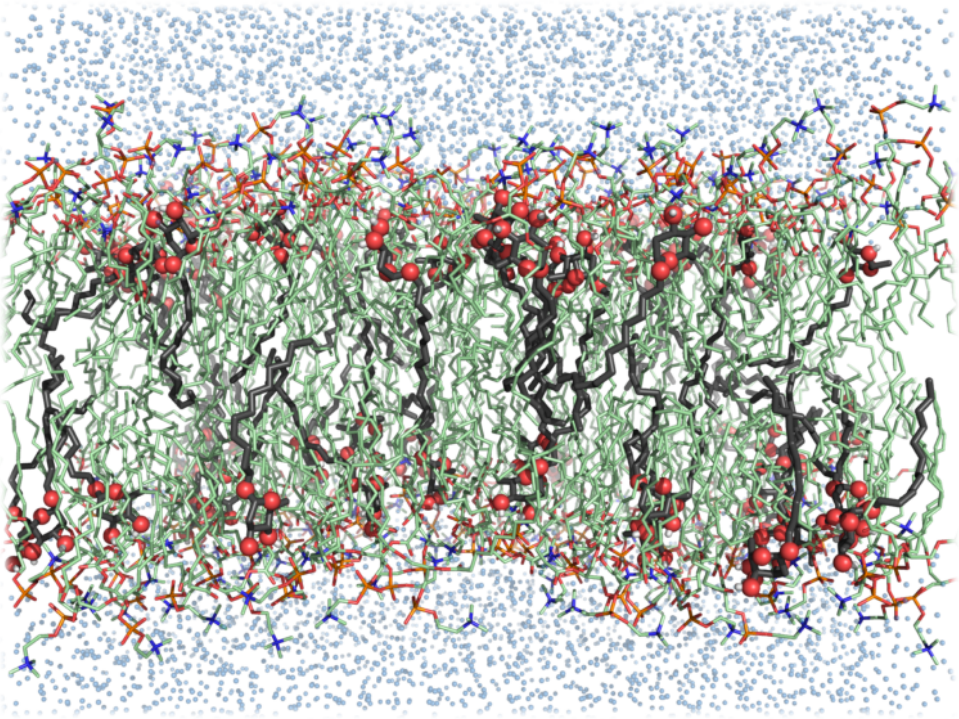

Figure 8.6: Lateral view of an equilibrated binary mixture consisting of glycolipid (GL = A12) and phospholipid (DMPC) molecules (GL/PC = 23.4%) obtained from our simulations. GL molecules are shown as dark gray sticks (carbon atoms), red spheres (oxygen atoms) and white sticks (hydroxy group hydrogens); phospholipids are represented as light green sticks (carbon atoms), red sticks (oxygen atoms), orange sticks (phosphorus) and blue sticks (nitrogen); water oxygens are represented as light blue spheres. All apolar and water hydrogens were omitted for clarity. Image was rendered using PyMOL [**83**].

was greatly compromised by the end of the simulations, we decided not to discard them for analysis purposes at this stage and hence these results will be also disclosed in **Section 8.3.2**. However, their interpretation should be careful and take into account the fact that simulations performed at such molar fractions of glycolipid most probably do not represent any system of biological/physical relevance. In fact, they correspond to extremely high local concentrations of glycolipid within the membrane patches being simulated, probably above the nominal

concentrations at which all these compounds excert their bactericidal and/or citotoxic effects. Furthermore, at such high nominal concentrations these molecules are known to aggregate into micelles rather than form bilayer-like structures. Hence, we believe that the reason why these membrane defects were only observed in the octyl glycoside simulations relies in an overstabilization of the bilayer structure in the case of their larger chain-lenght dodecyl counterparts, where glycolipid-phospholipid packing efficiency is much stronger.

Finally, in the simulations performed starting from a glycolipid-cluster configuration, pore formation was not observed. Instead, lateral diffusion of the glycolipid molecules led to the formation of a quite heterogeneous glycolipid-phospholipid binary mixture, with the two-components randomly distributed. This resuly does not necessarily implies that these surfactants are not able to assist membrane pore formation/stabilization, since other concentrations and/or simulation time-lenghts may be required in order for such a process to be captured via computer simulations. Thus, in spite of the fact that these preliminary results suggest that membrane pore formation is not likely to occur, this problem will be further exploited through a different approach further ahead in **Section 8.4**.

8.3.2 Structural analysis

In this section, we evaluated several structural properties of our glycoside-phospholipid bilayer simulations, namely: the total area, the deuterium order parameter, membrane thickness and phospholipid lateral diffusion. All these properties are commonly assessed, both experimentally and computationally, in order to describe lipid bilayers [**115, 165, 166, 172, 195, 196**], as well as surfactant-phospholipid binary systems [**197, 198**], in terms of their liquid-phase behaviour in solution.

The average total area of the bilayer was computed for all binary mixtures as a function of the glycolipid molar fraction. **Figure 8.7** shows that this property decreases considerably when the molar fraction of glycolipid increases, and a nealy linear relationship between the two variables may be established. Moreover, this effect seems to be independent on the structural nature of the glycolipid since only negligible differences are observed amongst the six surfactants tested, especially at lower molar fractions. This result was quite expected because the area per lipid of each glycoside is significantly lower than that presented by the phosphatidylcholine molecules they replace in our two-component systems. Notwithstanding the relevance of this overall effect, an increase in the glycolipid molar fraction may eventually lead to a concomitant decrease in the area per lipid of all phospholipid molecules, as a result of the newly-formed network of intermolecular interactions. In fact, the presence of sugar headgroups featuring several hydroxy and/or hydroxymethyl groups most probably decreases the electrostatic repulsion involving neighbor phosphate groups via hydrogen bonding. However, this eventual decrease in the phospholipid area could only be verified by computing the average partial-specific area for each lipidic component which is a rather complicated task due to the heterogeneous nature of our

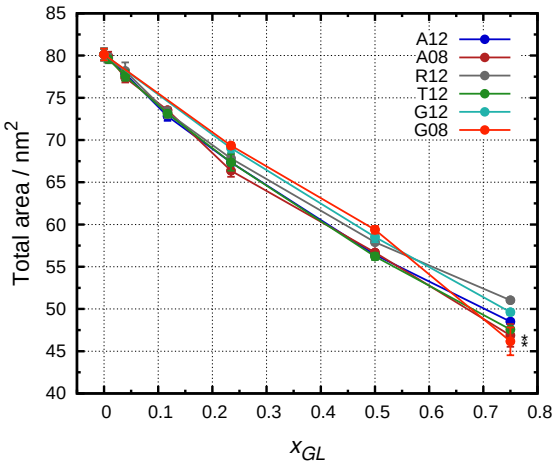

Figure 8.7: Total area of the bilayer as a function of the glycolipid molar fraction averaged from the binary mixture simulations. *The bilayer structure distorts significantly for octyl glycoside systems at $x_{GL} = 0.75$ (see **Section 8.3.1**).

systems, as already discussed in **Section 7.2.4**. It is important to notice that our control - the 100% DMPC bilayer starting configuration - has an average total area of ∼80.12 ± 0.70 nm^2, which corresponds to an area per lipid of ∼0.626 ± 0.005 nm^2. This value is within the experimental range (∼0.58−0.65 nm^2) **[109–123]** and in good agreement with the value of 0.599 ± 0.012 nm^2 at 30 °C (which may be interpolated to ∼0.605-0.610 nm^2 at ∼35 °C) that has been recently reported by Kučerka and co-workers for fluid DMPC bilayers in the liquid-crystalline lamellar (L_α) phase, also known as liquid-disordered (L_d) phase **[115]**. Furthermore, our results also reproduce with reasonable accuracy those obtained in other bilayer simulations with lower number of phospholipid molecules **[195, 199]**.

The ordering of the phospholipid hydrocarbon side-chains was assessed by computing the deuterium order parameter ($|S_\mathrm{CD}|$) for all phospholipid methylene groups of our binary mixtures (averaging over both *sn*-1 and *sn*-2 chains, as described in **Section 7.2.5**). The results are shown in **Figure 8.8** for all glycolipid-phospholipid bilayer systems at the different glycolipid molar fractions tested. The calculated deuterium order parameters exhibit a typical profile, featuring a plateau value at around the sixth methylene group following the ester groups, which varies only slightly depending on the glycolipid molar fraction. In all cases, this plateau value is followed by a pronounced decrease in the order parameter with the increasing carbon number towards the terminal methyl group, indicating that the acyl chains are much more disordered nearby the center of the bilayer **[165]**, where conformational flexibility is less constrained. Also important is the fact that the order parameter profile obtained for the 100% DMPC bilayer is in good agreement with experimental values (when extrapolated to the temperature of our simulations) **[120]** and also with those reported in the literature for other membrane simulations **[165, 195, 199]** (data not shown). Regarding the effect of glycolipid partitioning into our model membrane, it can be clearly observed that it leads to an increase in the order parameters

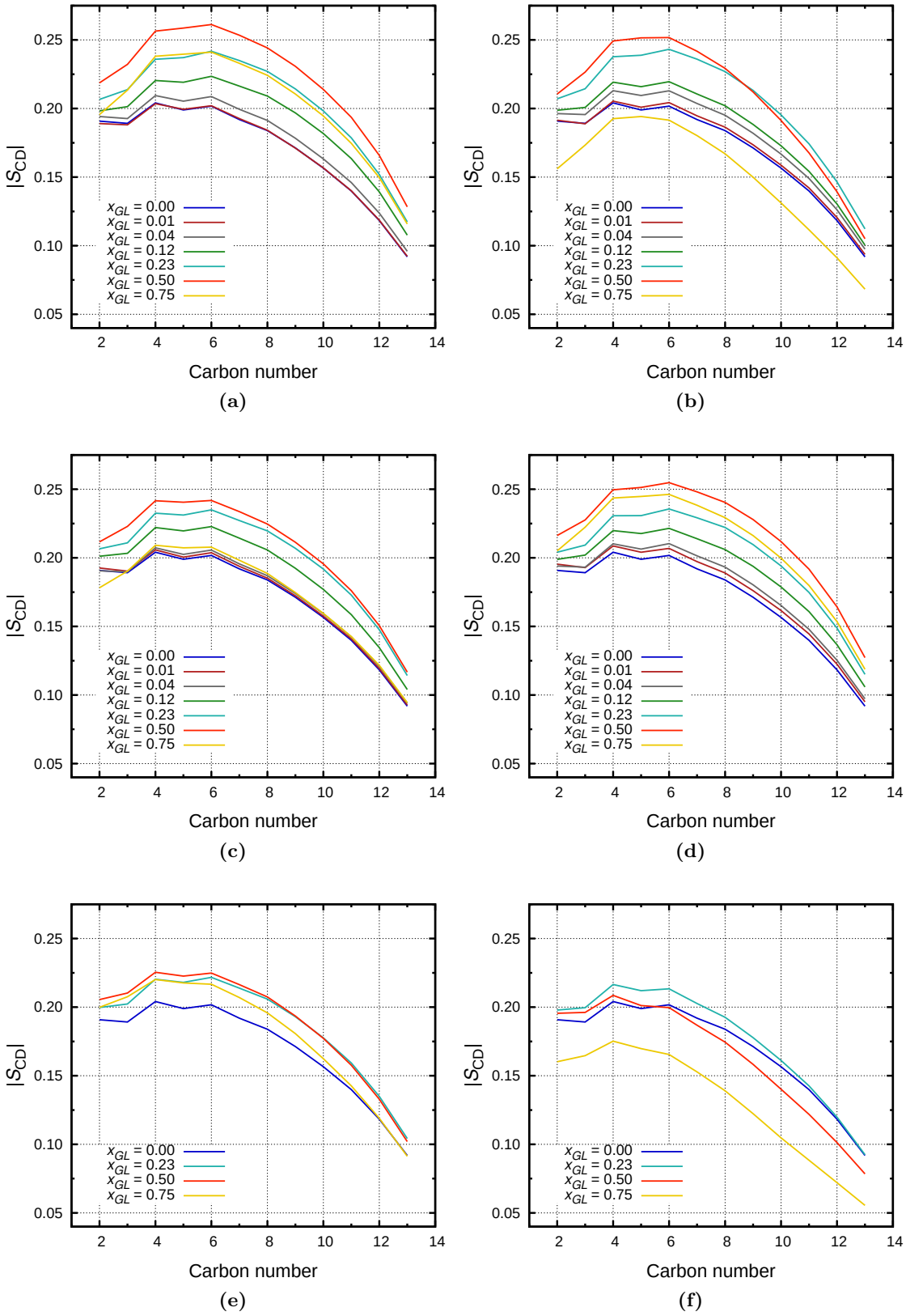

Figure 8.8: Deuterium order parameters averaged over the *sn*-1 and *sn*-2 phospholipid hydrocarbon chains for the simulated binary mixtures at different glycolipid molar fractions. **(a)** GL = A12, **(b)** GL = A08, **(c)** GL = R12, **(d)** GL = T12, **(e)** GL = G12, **(f)** GL = G08.

for glycolipid molar fractions up to $x_{GL} = 50\%$. However, when the glycolipid molar fraction is raised to $x_{GL} = 75\%$, phospholipid hydrocarbon chain order apparently decreases. Altogether, these results suggest that partitioning of glycosides into a phospholipid bilayer promotes an overall ordering within the hydrocarbon region of the membrane, probably due to the efficient packing between both phospholipid and glycolipid hydrocarbon chains that arises from the cooperative effect of the large number of hydrophobic interactions that may be established. The fact that this tendency is counteracted at higher glycolipid molar fractions of $x_{GL} = 75\%$ should be carefully interpreted taking into account the considerations discussed in **Section 8.3.1**. Indeed, such high molar fractions represent local concentrations that greatly compromise the bilayers' structural integrity, especially in the case of the octyl glycoside systems for which the above-mentioned hydrocarbon chain desordering effect was much more pronounced (see **Figures 8.8b** and **8.8f** for the A08 and G08 binary mixture simulations, respectively). Therefore, we conclude that the only microscopic effect that should be considered relevant, from the biophysical point of view, is that of phospholipid hydrocarbon chain ordering which could be observed for lower glycolipid molar fractions $\leq x_{GL} = 50\%$. In order to better analyze this effect, we plotted the average order parameters calculated for the plateau observed at the sixth methylene group, and also those obtained for the seventh methylene group, since comparable experimental data is available for the octyl glucoside (G08) at the latter segment **[138]** (see **Figures 8.9a** and **8.9b**, respectively). The results shown in **Figure 8.9a** clearly support our interpretation of the

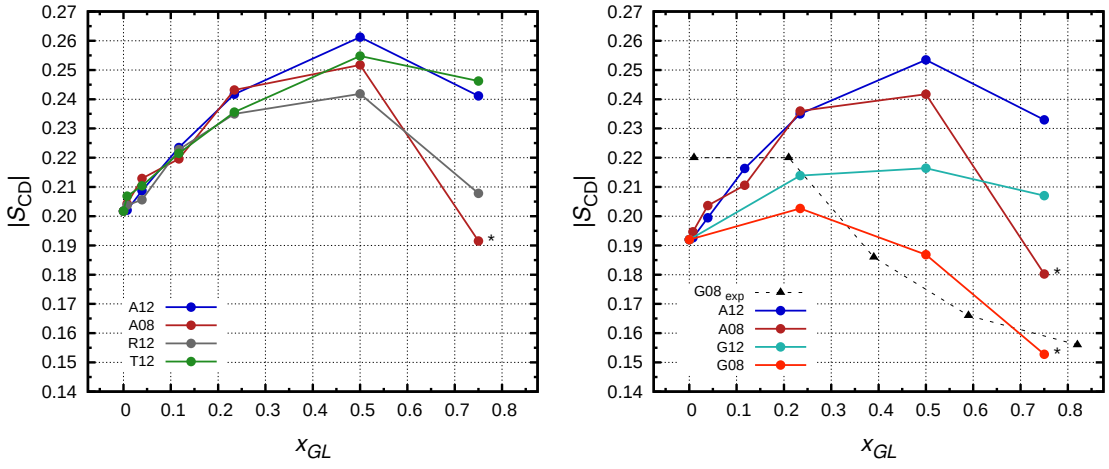

Figure 8.9: Deuterium order parameter of the phospholipid hydrocarbon chains as a function of the glycolipid molar fraction averaged from the binary mixture simulations. **(a)** Computed values for the sixth methylene group and **(b)** for the seventh methylene group. Experimental data was taken from ref. **[138]**. *The bilayer structure distorts significantly for octyl glycoside systems at $x_{GL} = 0.75$ (see **Section 8.3.1**).

ordering effect of glycosides over phospholipid acyl chains. However, these results did not reveal any substantial difference amongst the four deoxyglycosides tested, indicating that other factors should influence their distinguished antimicrobial activity, i.e. solvation and/or solubility

effects that are likely to govern the relative stabilities of the aggregates they form in solution, prior to their eventual membrane internalization. On the other hand, inspection of the results shown in **Figures 8.9a** and **8.9b** demonstrates that the phospholipid hydrocarbon chain ordering effect is significantly greater for the deoxyglycosides than for the two glucosides tested. In fact, this tendency seems to be counteracted in the latter case, with only little increase in the order parameter for the binary mixtures containing the dodecyl glucoside (G12) and an overall decrease for those featuring the octyl glucoside (G08) (**Figure 8.9b**). We may rationalize these results in terms of unfavorable interactions between the much more polar headgroup of these glucose-based surfactants (i.e. presenting a larger number of hydroxy groups and β-anomeric configuration) and the phosphatidylcholine hydrophilic region, which may eventually induce a disordering effect over the acyl side-chains. This reduction in the order parameter in the case of the octyl glucoside is in reasonable agreement with experimental data from Meier and Seelig (**Figure 8.9b**), who have shown that the addition of alkyl β-D-glucopyranosides leads to a disordering of membrane lipids, this effect being more pronounced for the detergents bearing shorter alkyl chain lenghts **[138]**. However, it should be mentioned that the order parameters computed from our simulations are not directly comparable to these experimental results, since the latter were obtained for a different system and temperature (i.e. DPPC bilayers at 45 °C). Nevertheless, the fact that we were able to roughly capture this disordering trend for the octyl glucoside reinforces the reliability of our force field parametrization and emphasizes the clearly different results obtained between the deoxyglycosides and the glucosides studied. As a final note, the phospholipid acyl chain ordering observed for the deoxyglycosides is similar to the well-known effect of cholesterol in fluid lipid bilayers **[165, 200–204]**.

In order to evaluate a possible phase-transition into a more liquid-ordered (L_o) phase, we analyzed the membrane thickness, which is another important property of lipid bilayers (see **Section 7.2.6** for methodological aspects). **Figure 8.10** presents all DMPC thickness distribution histograms and also the glycolipid distribution along the bilayer normal. The results confirm that the bilayers' structural integrity is retained upon addition of glycosides, with the exception of the two octyl glycosides at molar fractions of $x_{GL} = 75\%$ (**Figures 8.10b** and **8.10f**), as mentioned previously. The glycolipid distribution profiles suggest that the DMPC membrane loading capacity is limited, since increasing molar fractions induce glycolipid headgroups to sample the outter regions of the bilayer, and this effect is more pronounced for the glycosides with more polar headgroups. The DMPC bilayer thickness is also sensitive to the molar fraction of glycosides (**Figure 8.11**). Interestingly, the dependence of the average thickness with the glycolipid molar fraction is in very good agreement with the results obtained for the plateau of the order paramenter (refer back to **Figure 8.9**).

Finally, we also looked at the lateral diffusion coefficients of DMPC molecules at different glycolipid molar fractions (**Tables B.1** and **B.1**). These were computed using the Einstein relation, by measuring the slope of the linear part of the mean square displacement (MSD) over time (**Figure B.11**), as described in **Section 7.2.7**. In **Figure 8.12** is shown the dependence of the lateral diffusion coefficients on the glycolipid molar fraction. In contrary to what was

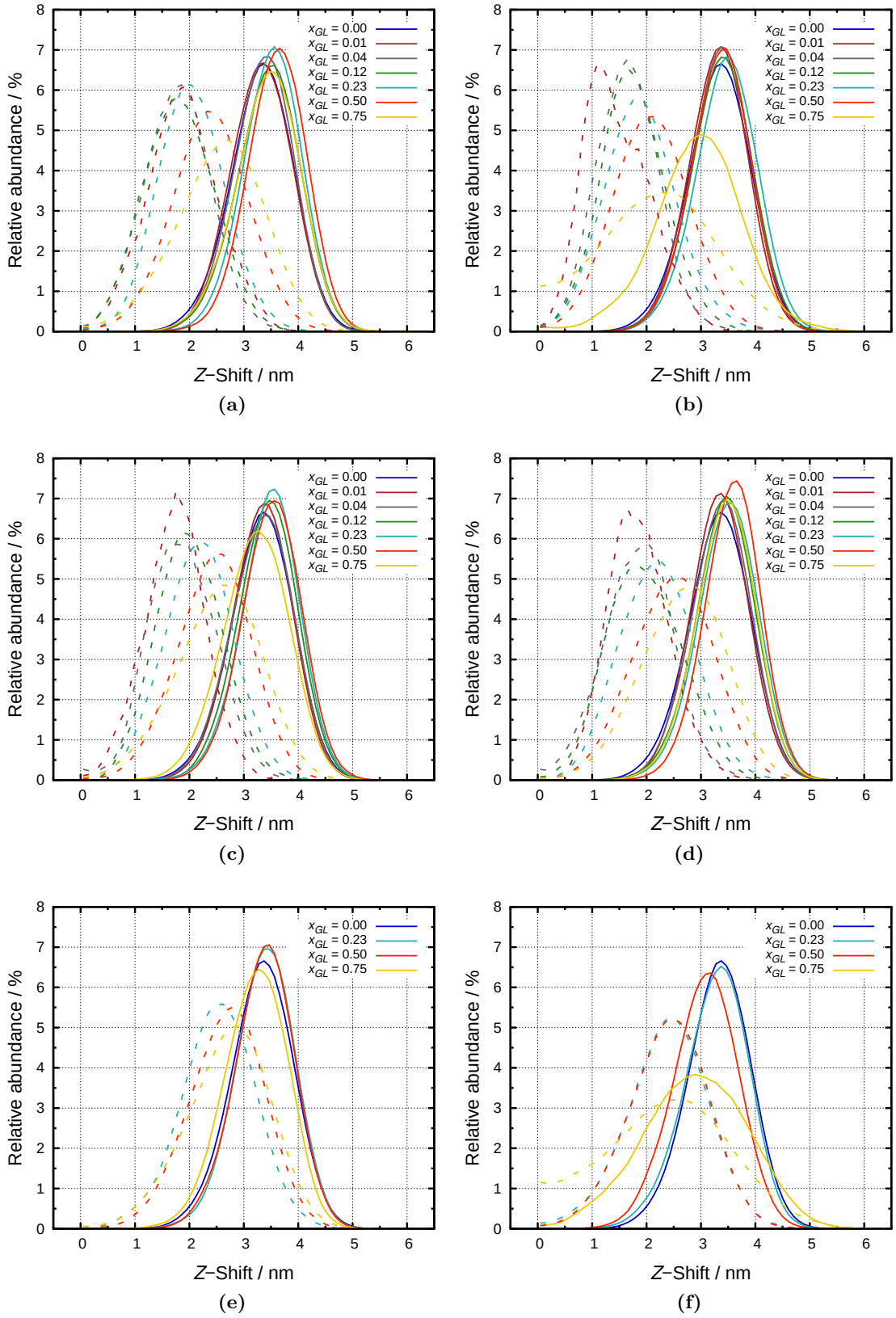

Figure 8.10: Lipid bilayer thickness distribution histograms for the simulated binary mixtures at different glycolipid molar fractions calculated using all phospholipid phosphorus as reference atoms. The z-shift distribution histograms calculated using the glycolipid endocyclic oxygen atoms as reference are shown in dashed lines. **(a)** GL = A12, **(b)** GL = A08, **(c)** GL = R12, **(d)** GL = T12, **(e)** GL = G12, **(f)** GL = G08.

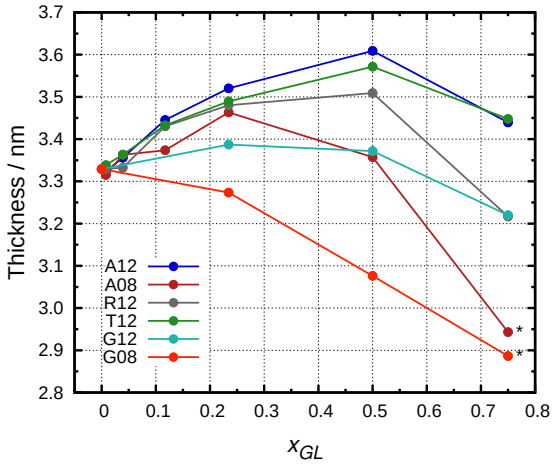

Figure 8.11: Membrane thickness as a function of the glycolipid molar fraction averaged from the binary mixture simulations calculated using all phospholipid phosphorus as reference atoms. *The bilayer structure distorts significantly for octyl glycoside systems at $x_{GL} = 0.75$ (see **Section 8.3.1**).

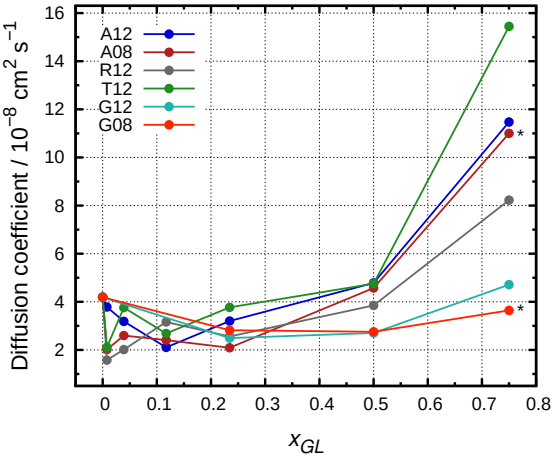

Figure 8.12: Lateral diffusion coefficient as a function of the glycolipid molar fraction averaged from the binary mixture simulations. *The bilayer structure distorts significantly for octyl glycoside systems at $x_{GL} = 0.75$ (see **Section 8.3.1**).

observed for the order parameter and the membrane thickness results, the diffusion coefficients were not significantly affected by the addition of glycosides up to a molar fraction of $x_{GL} = 50\%$. The fact that the diffusion coefficients did not decrease, suggests that the observed hydrocarbon chain ordering did not hinder the lateral motions of DMPC molecules. However, this may also be interpretated an indirect effect resulting from a high diffusion rate of the glycolipid molecules. The large increase in the diffusion coefficients observed at $x_{GL} = 75\%$ is probably related with the instability of the bilayers, as previously mentioned, but also due to the fact that at such high glycolipid concentrations there is a scarce number of DMPC molecules available for the MSD

measurements. This results in greater uncertainty in the calculation of the diffusion coefficients beacuse this property is rather sensitive to sampling issues [**205**]. The experimental range for the diffusion coefficient of pure DMPC bilayers is 5-10 $\times$ 10^{-8} cm^2 s^{-1} [**172**], which is slightly higher than the value calculated from our simulations (4.19 $\pm$ 0.17$\times$ 10^{-8} cm^2 s^{-1}).

8.4 Membrane pore stability

In this section, we investigated the ability of our deoxyglycosides to promote membrane pore formation, which is a common mechanism of action for several membrane-active drugs, i.e. antimicrobial peptides [**206–208**]. Membrane pores/defects are also known to be transiently generated under physiological conditions (i.e. induced by mechanical stress) and subsequently repaired by several mechanisms [**209–211**]. However, these processes often take place in rather long time-scales which are difficult to access by coventional molecular dynamics simulations, although many aspects related to pore formation in membranes have been successfully tackled by computational studies either by extending the time-scales of atomistic simulations [**212–215**], through the development of improved sampling methods [**214, 216**] or by simplifying the system using coarse-grained models [**185, 186, 217**]. In order to overcome this major limitation,

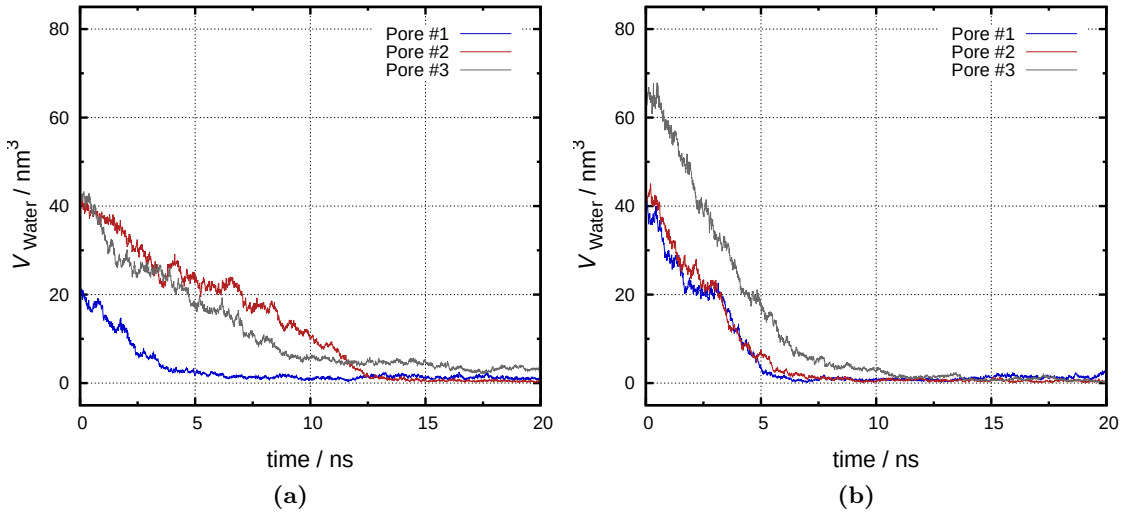

Figure 8.13: Volume of water molecules inside the glycoside (GL = A12)/phospholipid bilayer as a function of time computed from the membrane pore simulations. The third methylene group of one of the phospholipid hydrocarbon chains (atom C2D) was used as reference in all calculations. **(a)** GL/PC = 20.1% and **(b)** GL/PC = 50.0% in all simulations. Note that each of the three simulations in **(a)** and **(b)** was started from a different configuration of the system, with variable pore size (refer back to **Table 7.4** in **Section 7.1.2**).

we devised a computational protocol where we artificially built membrane pores of different sizes surrounded by significant amounts of glycolipid molecules (see **Section 7.1.2**, **Table 7.4** for further detail), and evaluated their stabilities over time with unrestrained molecular dynamics

simulations. A simple way to measure the pore size is to calculate the number of water molecules in the interior of the bilayer in each case. **Figure 8.13** shows the estimated volume of several membrane pores at ∼20% and ∼50% A12/PC molar fractions. We observed complete pore closure after 20 ns in most of the simulations, with the exception of the larger ∼20% A12/PC system (**Pore #3** in **figure 8.13a**). In this case, a very small water tunnel corresponding to a metastable pore-state was kept over 100 ns, after which it eventually closed (see **Figure 8.14** for an illustration of the closure process). These results indicate that the A12/PC mixtures tested were not able to stabilize any of our pre-formed membrane pores. Altogether, it seems that this glycolipid does not exert its antibacterial action through the promotion of membrane pores.

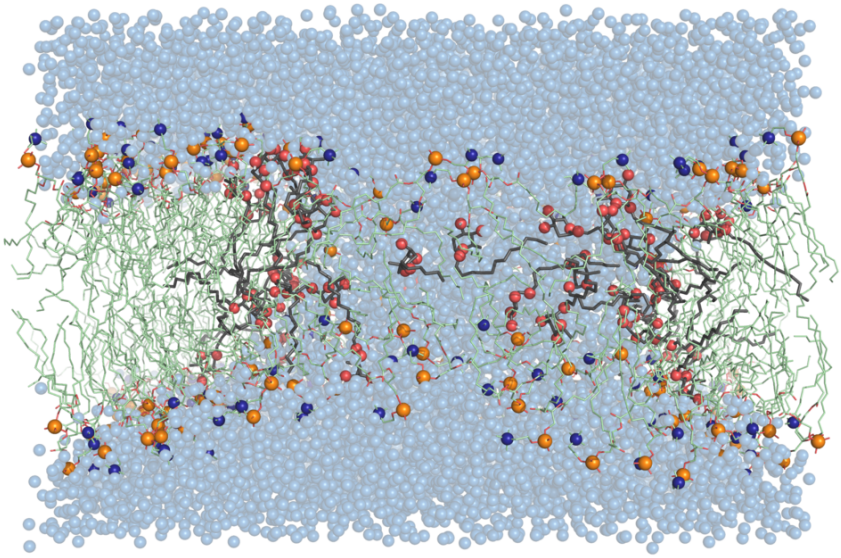

(a) $\mathbf{t_{simulation}}$ = 0 ns

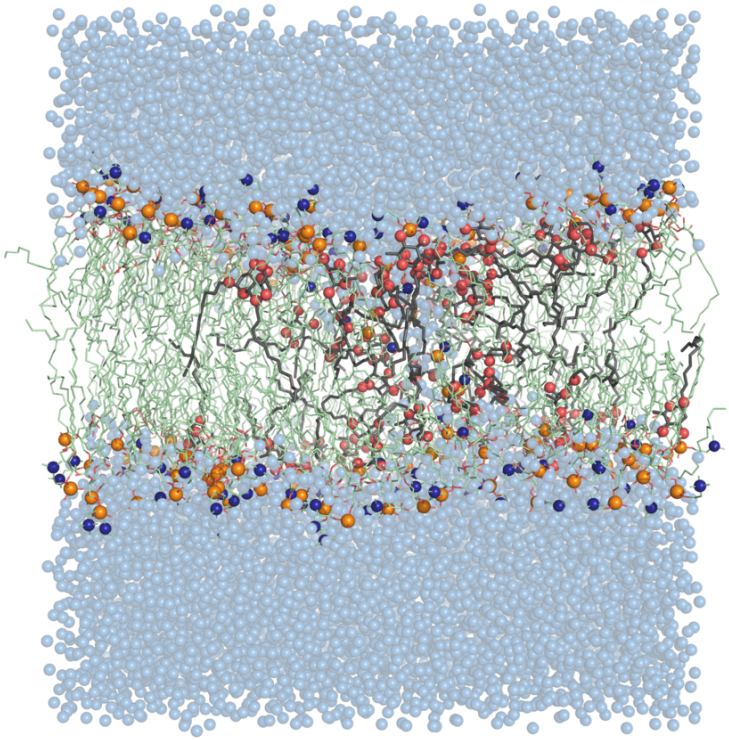

(b) $\mathbf{t_{simulation}}$ = 20 ns

Figure 8.14: Representative snapshots from a membrane pore simulation consisting of 52 glycolipid (GL = A12) and 196 phospholipid (DMPC) molecules (**Pore #3** in **Figure 8.13a**). Lateral view of **(a)** the initial system configuration and after **(b)** 20 ns, **(c)** 60 ns, and **(d)** 150 ns production time (complete pore closure). GL molecules are shown as gray sticks (carbon atoms), red spheres (oxygen atoms) and white sticks (hydroxy group hydrogens); phospholipids are represented as light green sticks (carbon atoms), red sticks (oxygen atoms), orange spheres (phosphorus) and dark blue spheres (nitrogen); water oxygens are represented as light blue spheres. All apolar and water hydrogens were omitted for clarity. Images were rendered using PyMOL **[83]**.

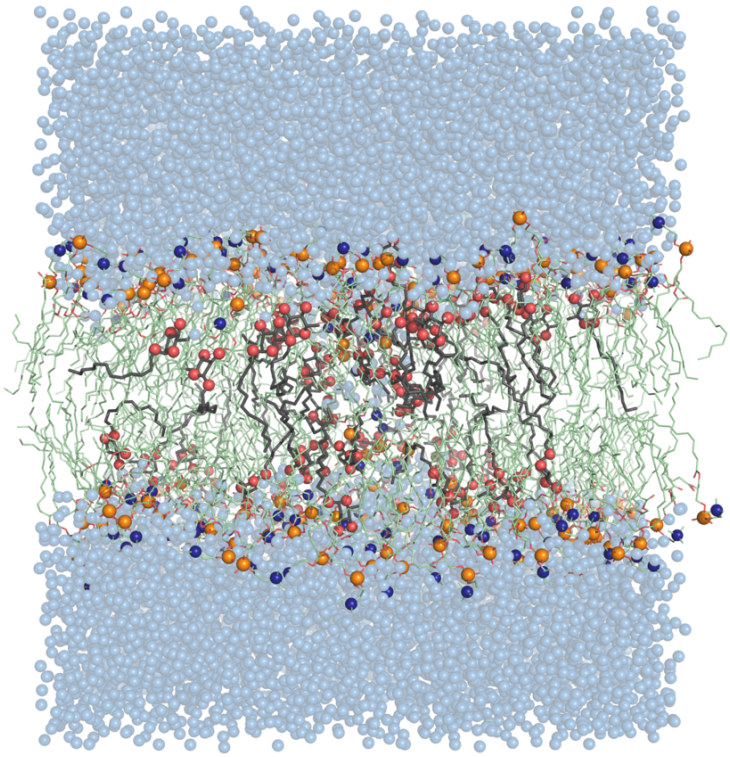

(c) $\mathbf{t_{simulation}} = 60$ ns

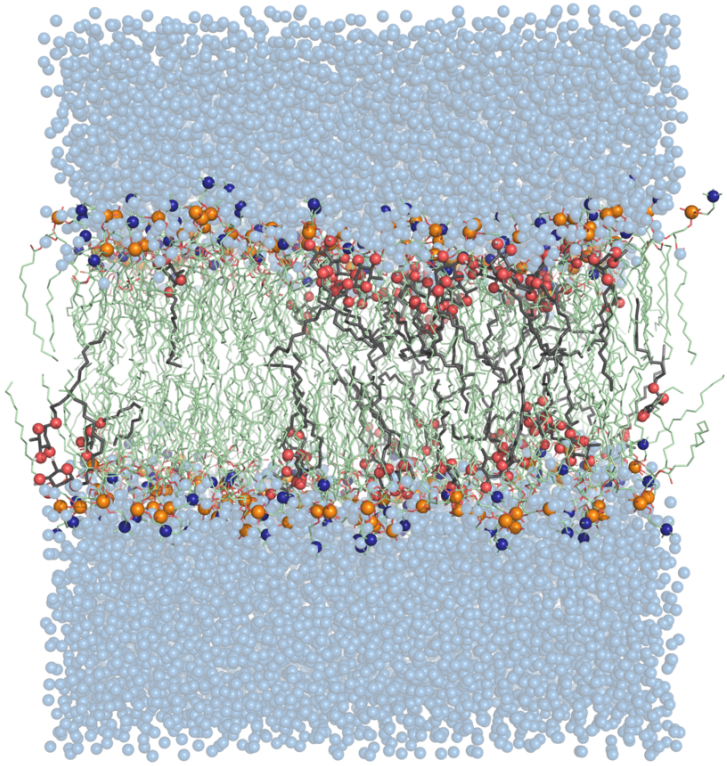

(d) $\mathbf{t_{simulation}} = 150$ ns

Figure 8.14: *(continued from previous page).*

Chapter 9

Conclusion

In this part of the work, we used molecular dynamics simulations in order to perform a conformational study on a series of alkyl deoxyglycosides [**1**–**3**] and the aggregates they form in solution, as well as to investigate the effect of these molecular entities on the biophysical properties of a model lipid bilayer, in the attempt to provide molecular insight into their antibacterial mechanism of action.

In our simulations, all studied glycosides aggregated rapidly into a single micelle in aqueous media. Topologically, these structures are heterogeneous regarding both their size/shape and the surfactant moieties that are exposed to the solvent. Micelles exhibit ellipsoidal shapes, where at lower aggregation numbers the mostly adopted shape is oblate-like, and at higher numbers ($n_{GL} > 100$) a more prolate-like geometry is preferred. The most spherical-like micelles, in turn, were obtained at aggregation numbers of $n_{GL} = 60$ and 40, for the dodecyl and octyl deoxyglycosides, respectively. The increasing aggregation number leads to a decrease in the solvent exposure of the glycolipid hydrocarbon chains, indicating a higher thermodynamic stability for the larger aggregates. Therefore, the micelles simulated at lower aggregation numbers are merely representative of metastable systems with little physical relevance.

These sugar-based surfactants are expected to exert their antimicrobial activity by a bacterial membrane-targeted mechanism. However, not much is known about the relevant glycoside-phospholipid interactions at the molecular level. In this context, we studied the behaviour of glycoside micelles featuring different aggregation numbers ($n_{GL} = 10$, 30, and 60) at the interface of a phospholipid (DMPC) bilayer, using the lead compound as a model. The results from our simulations demonstrated that all micelles have a high affinity for the lipid bilayer, since de-adsoption events were never observed. Furthermore, we captured several membrane internalization events, ranging from single monomer insertions to the complete fusion of the micelle. These processes took place in the hundreds of nanoseconds time-scale, rendering them very difficult to sample quantitatively using atomistic simulations. Nevertheless, our results suggest that these glycosides, given enough time, should prefer the lipid phase.

The effect of these glycoside surfactants on the structural properties of phospholipid bilayers upon insertion was investigated by simulating binary mixtures containing glycosides and phospholipid molecules at several molar fractions. The results showed that increasing the molar fraction of glycolipid (up to $x_{GL} = 50\%$) leads to a thickening of the phospholipid bilayer and to a higher ordering of its hydrocarbon chains, similar to the known condensing effect of cholesterol [**165, 200–204**]. This decrease in membrane fluidity was not observed for the related alkyl glucosides (in agreement with the available experimental data), suggesting that deoxygenation of the sugar headgroup is pivotal for their membrane-activity. In contrast, phospholipid lateral diffusion was not significantly affected by the neighbouring glycolipid molecules. However, the accuracy in the determination of diffusion coefficients may be compromised by both the limited time-scale of our simulations and the sampling variability at different glycolipid molar fractions. Hence, we consider that this property should be further investigated.

Finally, since many antimicrobial agents are known to promote membrane pore formation [**206–208**], we also preliminarily explored the eventual ability of deoxy glycosides to stabilize preformed membrane pore configurations (again using the lead compound as a model). In all simulations, pore closure was observed in a relatively short time-scale. Notwithstanding the limited sampling of these studies (only a single replicate was simulated for each of the six starting systems), the results suggest that the membrane pore formation/stabilization in probably not involved in the mechanism of action for this family of compounds.

Chapter 10

Final remarks

The work presented in this thesis was motivated by a project already in progress within our research group, which was mainly intended at developing new sugar-based antibacterial agents with innovative mechanisms of action, as potential candidates for application in therapeutics. The starting point was the family of alkyl deoxy glycosides introduced by Rauter and co-workers [**1**–**3**], some of which exhibited very potent and selective antibacterial activity towards *Bacillus* spp. The small library of analogues synthesized provided a better understanting of how key structural features such as deoxygenation/fluorination patterns, as well as conformational properties, are able to tune bioactivity. Furthermore, some of these compounds were as active as the previously reported lead compound against *B. anthracis*, showing their potential usefulness for application in the field of biosecurity. The *in silico* studies gave us new insights on the molecular details of the interaction between these compounds and membrane models. The effects observed on the phospholipid bilayer suggest that these sugar-based surfactants are able to exert their mechanism of action by inducing membrane ordering and stiffening. To evaluate the impact of these structural alterations on membrane stability and, ultimately, on cell viability, experimental (i.e. molecular biophysics) studies are required. This interdisciplinary work developed in our research unit demonstrates the advantadge of employing complementary areas of research towards problem-solving approaches. Organic synthesis and computational methodologies succeeded in finding new antibiotics with new mechanisms of action to overcome antibiotic resistance.

Appendix A

NMR spectra

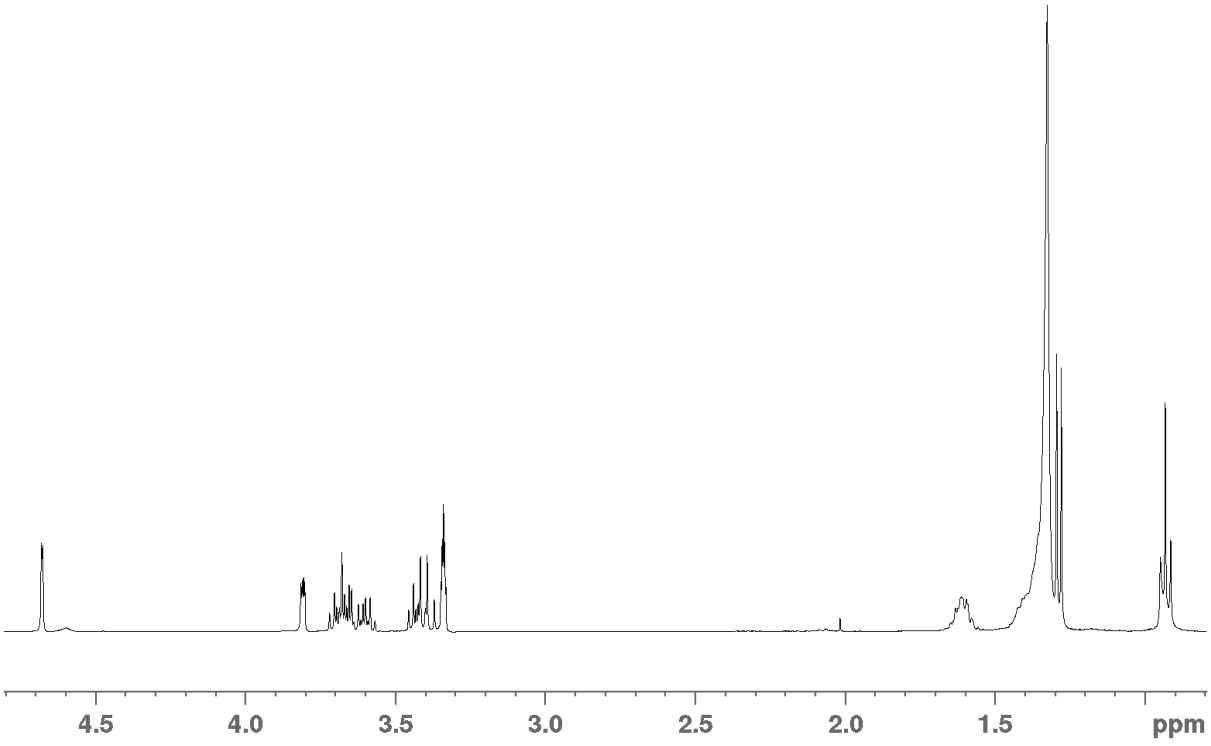

Figure A.1: ^{1}H NMR (400 MHz, $CDCl_3$) spectrum of dodecyl α-L-rhamnopyranoside **(2)**.

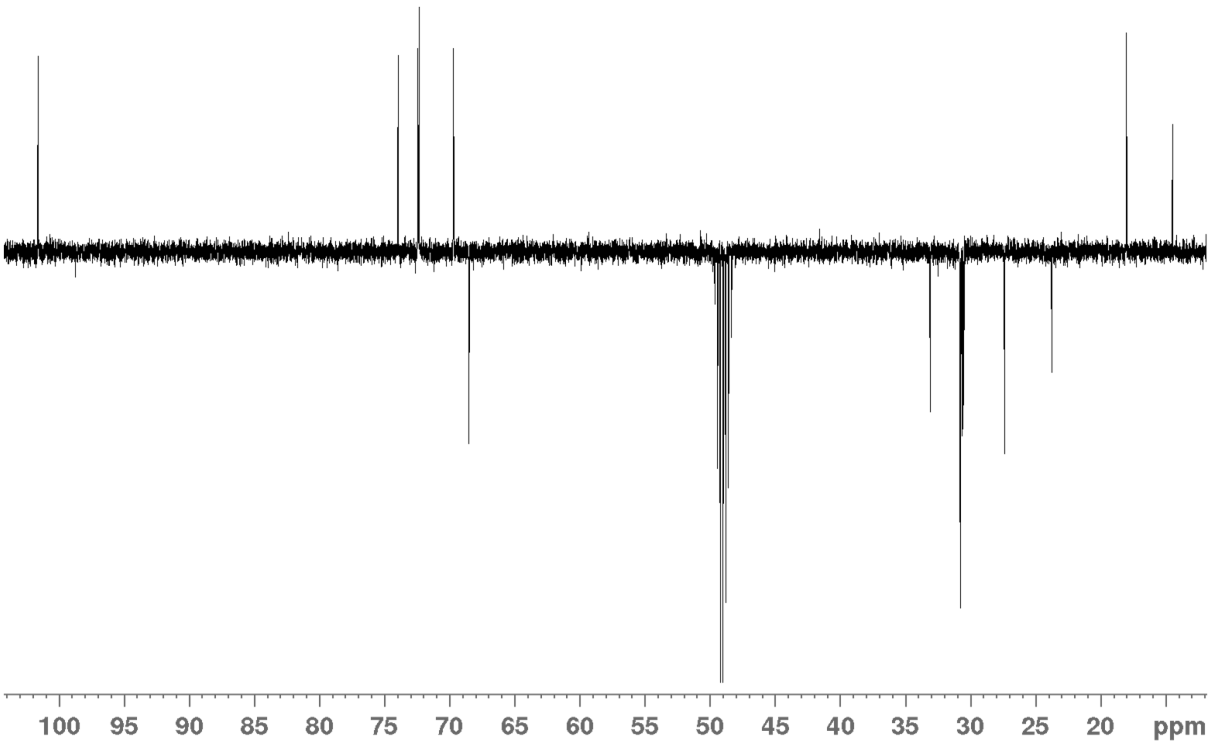

Figure A.2: ^{13}C NMR (100 MHz, $CDCl_3$) spectrum of dodecyl α-L-rhamnopyranoside **(2)**.

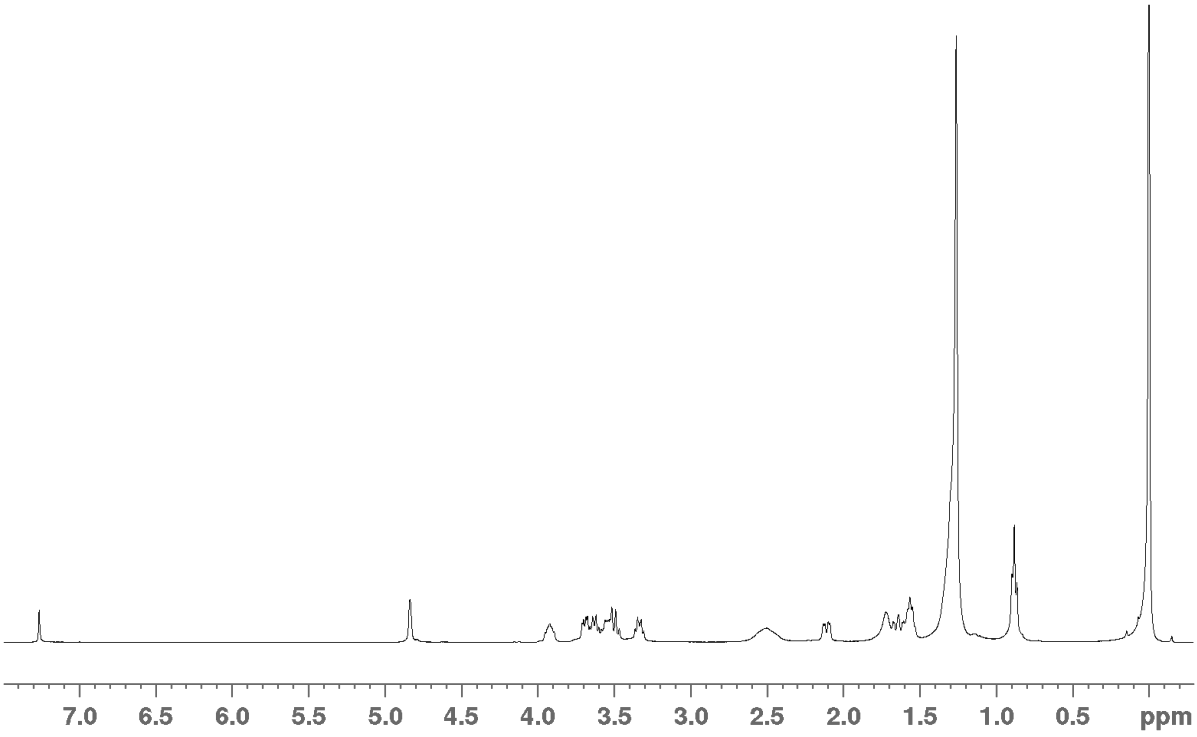

Figure A.3: ^{1}H NMR (400 MHz, $CDCl_3$) spectrum of dodecyl 2-deoxy-α-L-*threo*-pentopyranoside **(3)**.

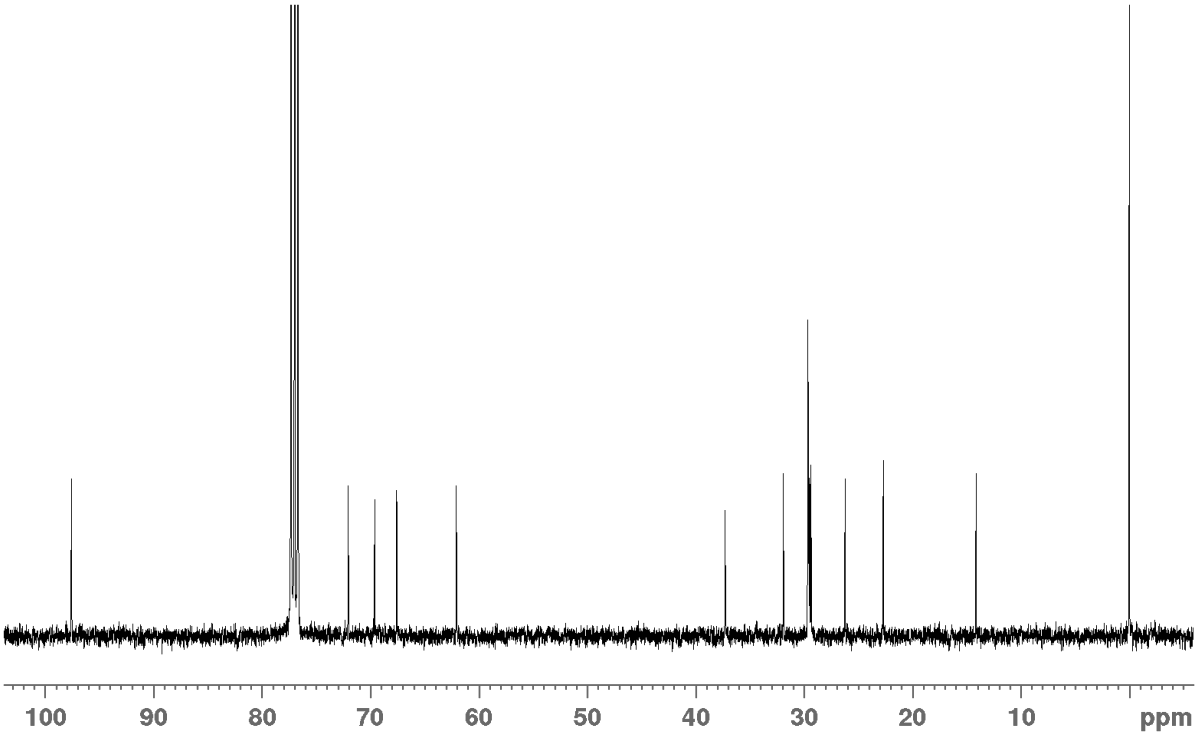

Figure A.4: ^{13}C NMR (100 MHz, $CDCl_3$) spectrum of dodecyl 2-deoxy-α-L-*threo*-pentopyranoside **(3)**.

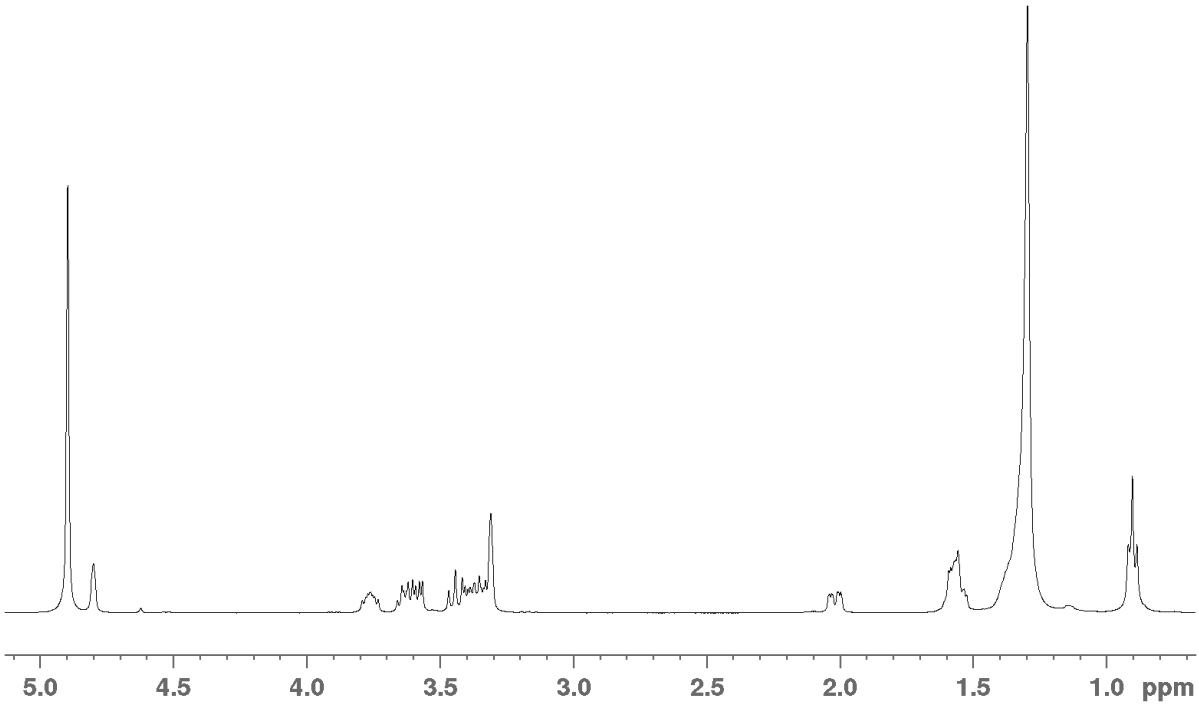

Figure A.5: ^{1}H NMR (400 MHz, MeOD) spectrum of dodecyl 2-deoxy-α-L-*threo*-pentopyranoside **(3)**.

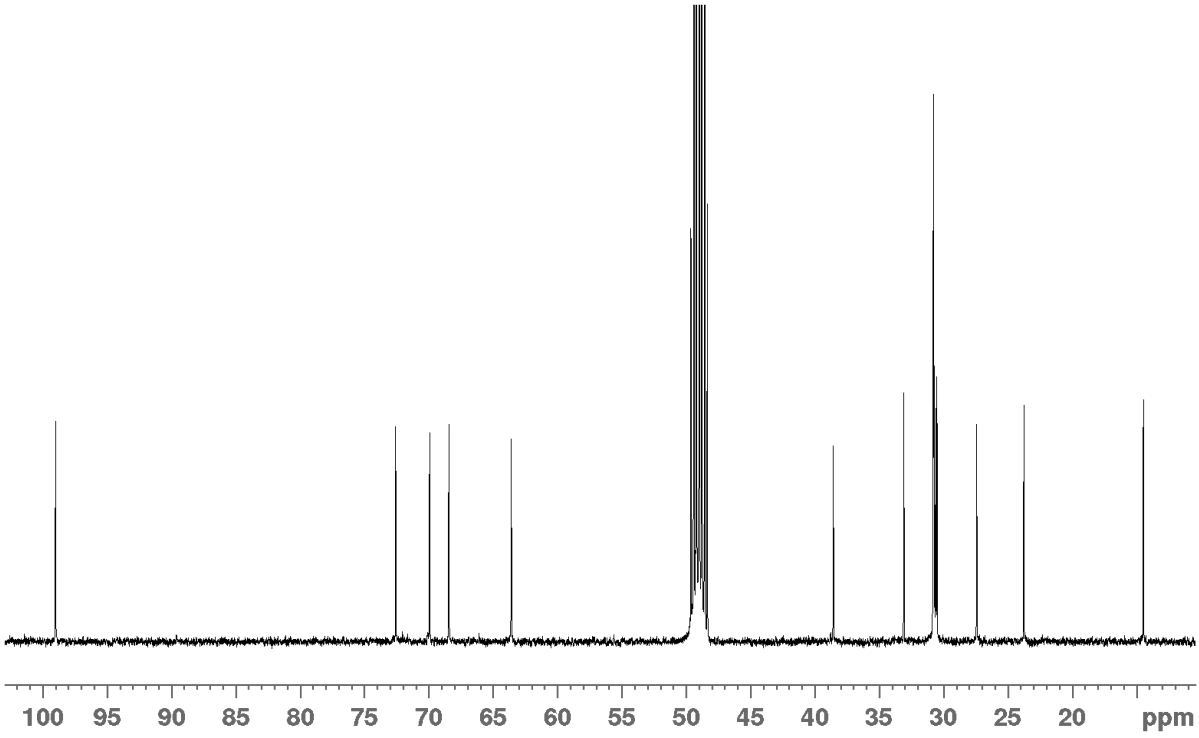

Figure A.6: ^{13}C NMR (100 MHz, MeOD) spectrum of dodecyl 2-deoxy-α-L-*threo*-pentopyranoside **(3)**.

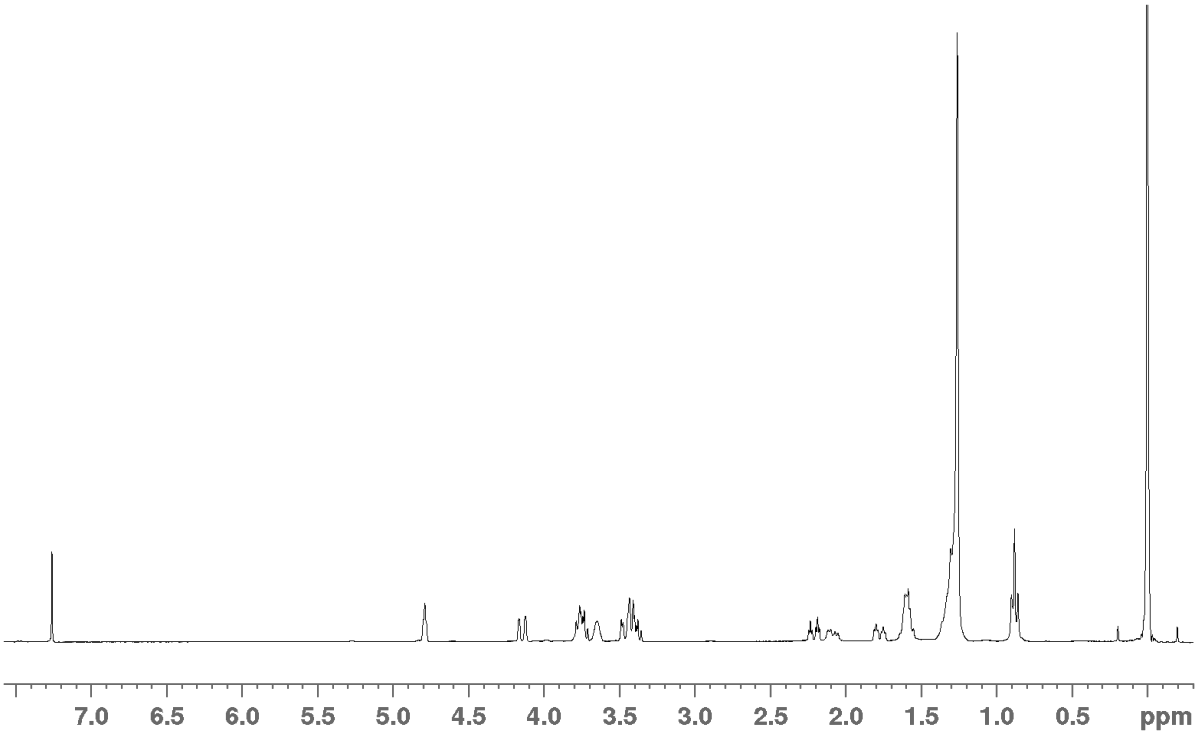

Figure A.7: ^{1}H NMR (400 MHz, $CDCl_3$) spectrum of dodecyl 2-deoxy-β-L-*threo*-pentopyranoside **(18)**.

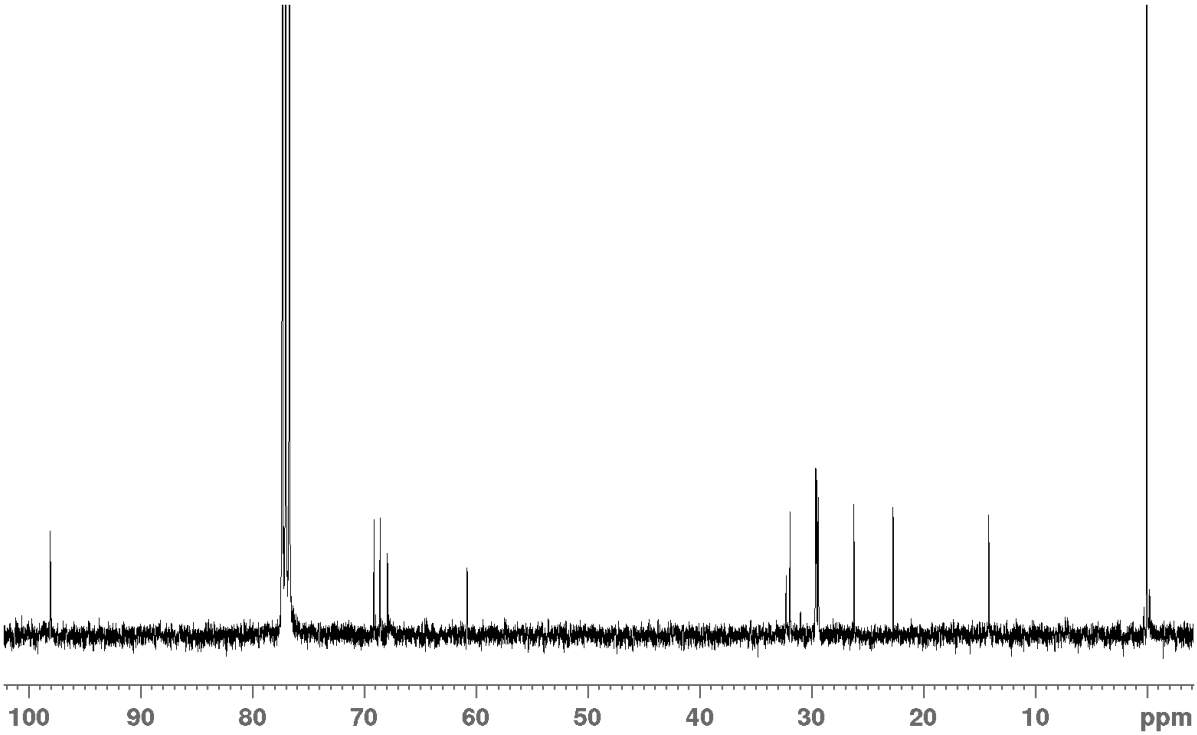

Figure A.8: ^{13}C NMR (100 MHz, $CDCl_3$) spectrum of dodecyl 2-deoxy-β-L-*threo*-pentopyranoside **(18)**.

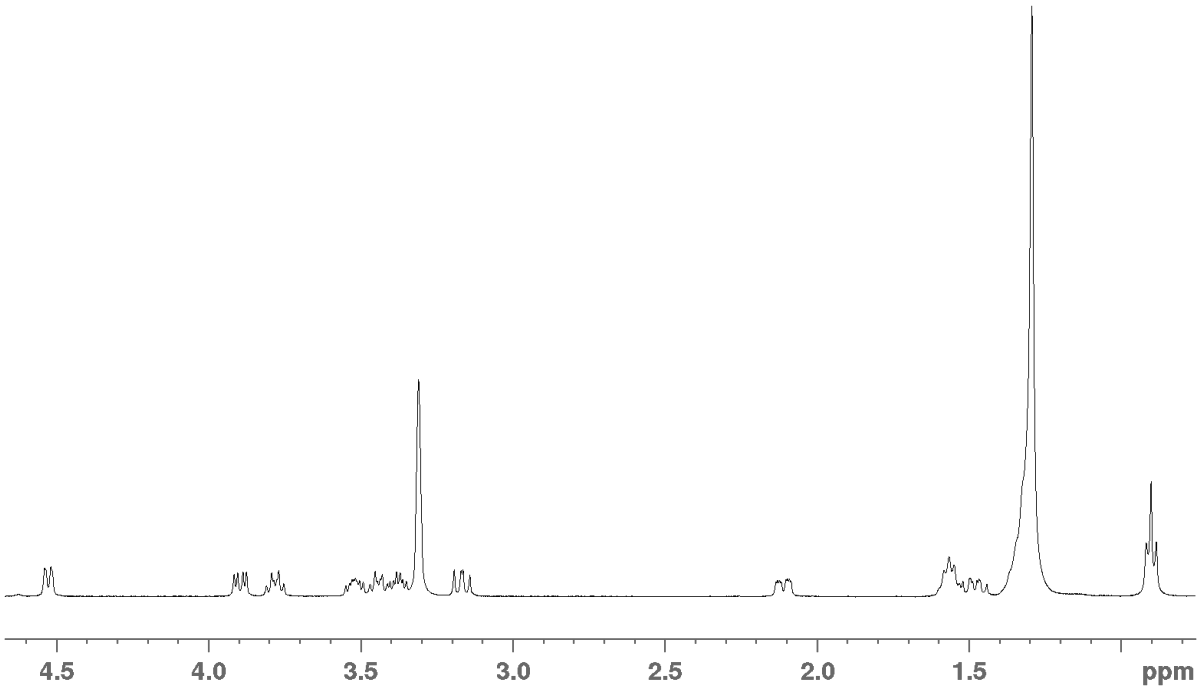

Figure A.9: ^{1}H NMR (400 MHz, MeOD) spectrum of dodecyl 2-deoxy-β-L-*threo*-pentopyranoside **(18)**.

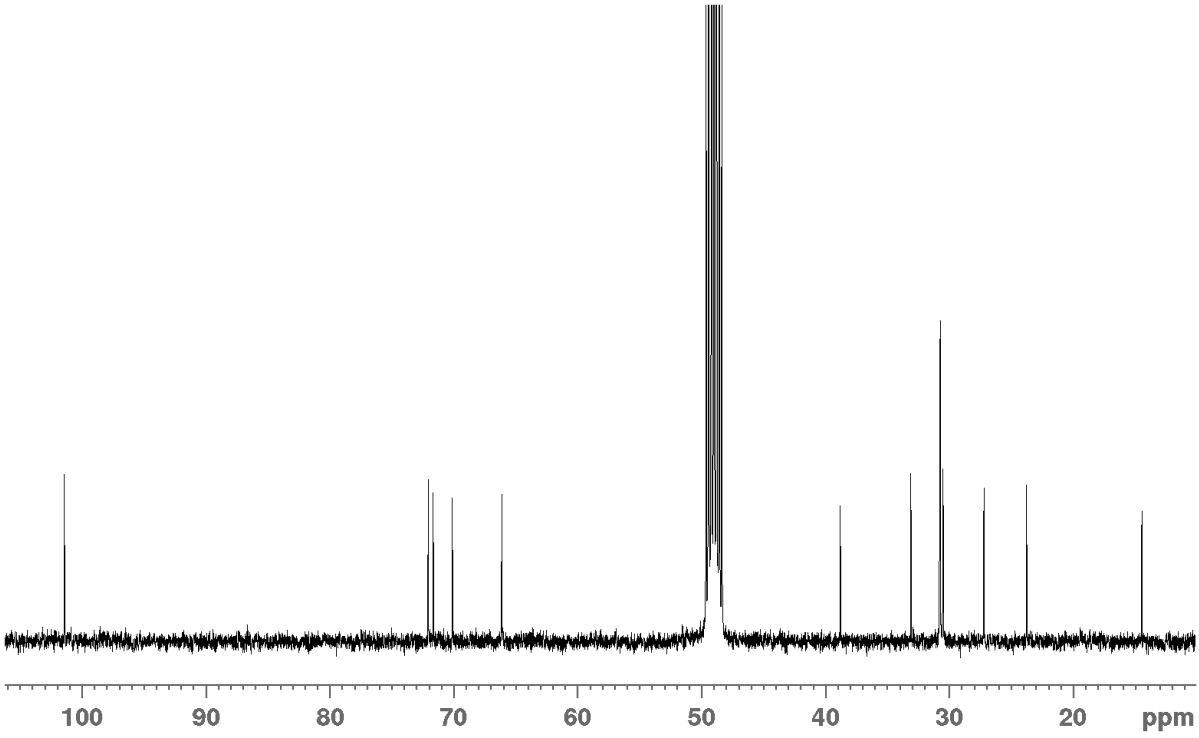

Figure A.10: ^{13}C NMR (100 MHz, MeOD) spectrum of dodecyl 2-deoxy-β-L-*threo*-pentopyranoside **(18)**.

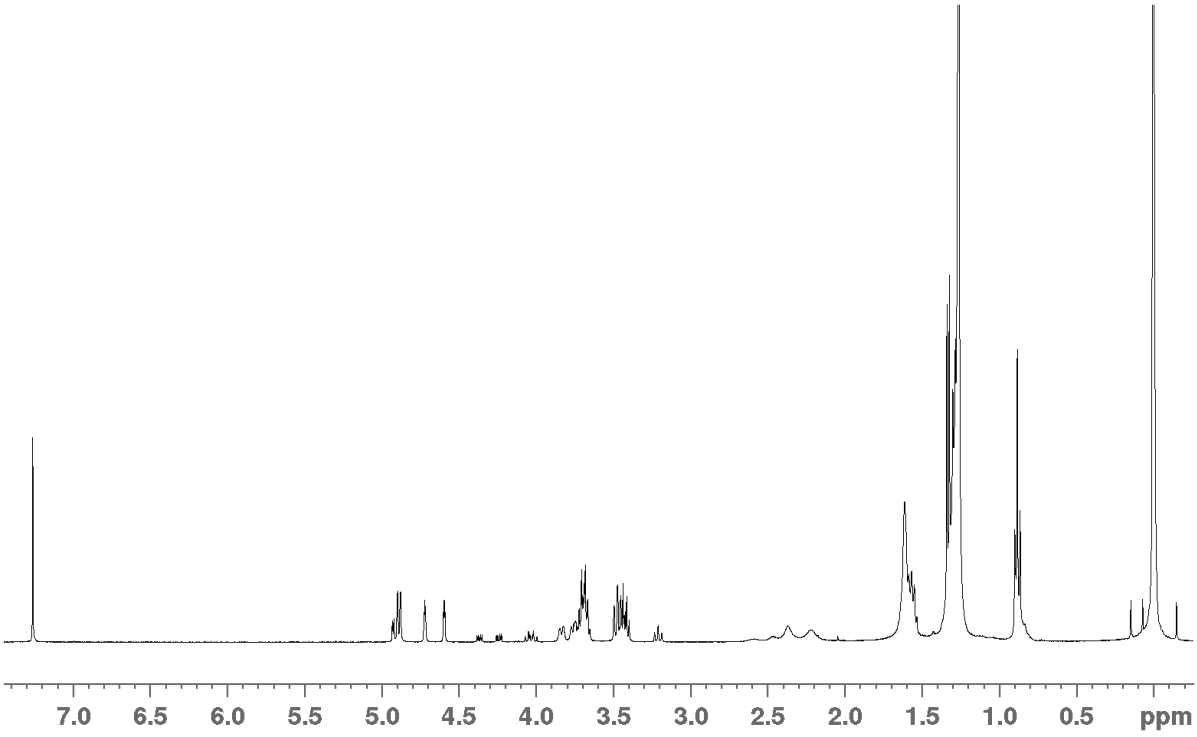

Figure A.11: ^{1}H NMR (400 MHz, $CDCl_3$) spectrum of dodecyl 2,6-dideoxy-2-fluoro-α-L-glucopyranoside **(4)** and dodecyl 2,6-dideoxy-2-fluoro-α-L-mannopyranoside **(5)**.

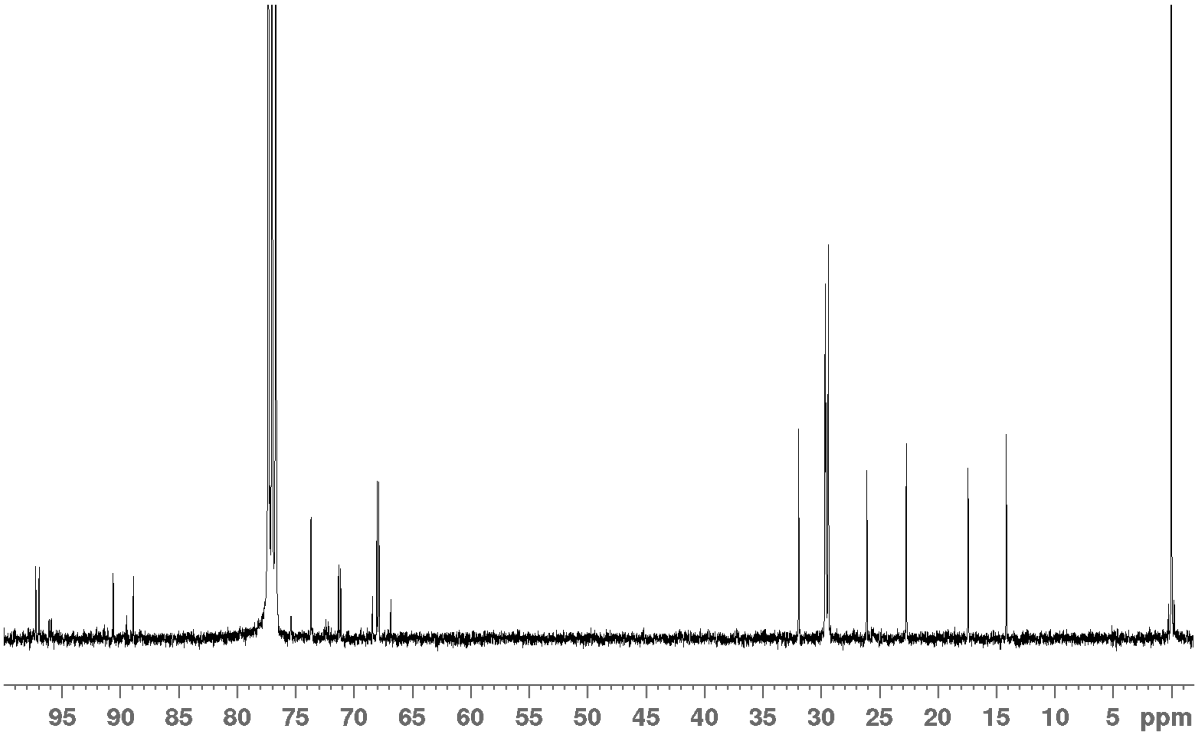

Figure A.12: ^{13}C NMR (100 MHz, $CDCl_3$) spectrum of dodecyl 2,6-dideoxy-2-fluoro-α-L-glucopyranoside **(4)** and dodecyl 2,6-dideoxy-2-fluoro-α-L-mannopyranoside **(5)**.

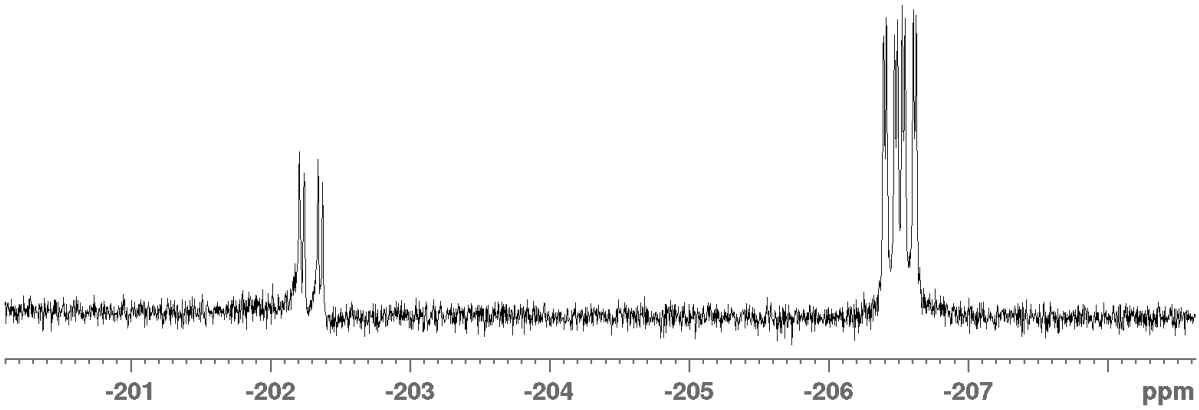

Figure A.13: ^{19}F NMR (376 MHz, $CDCl_3$) spectrum of dodecyl 2,6-dideoxy-2-fluoro-α-L-glucopyranoside **(4)** and dodecyl 2,6-dideoxy-2-fluoro-α-L-mannopyranoside **(5)**.

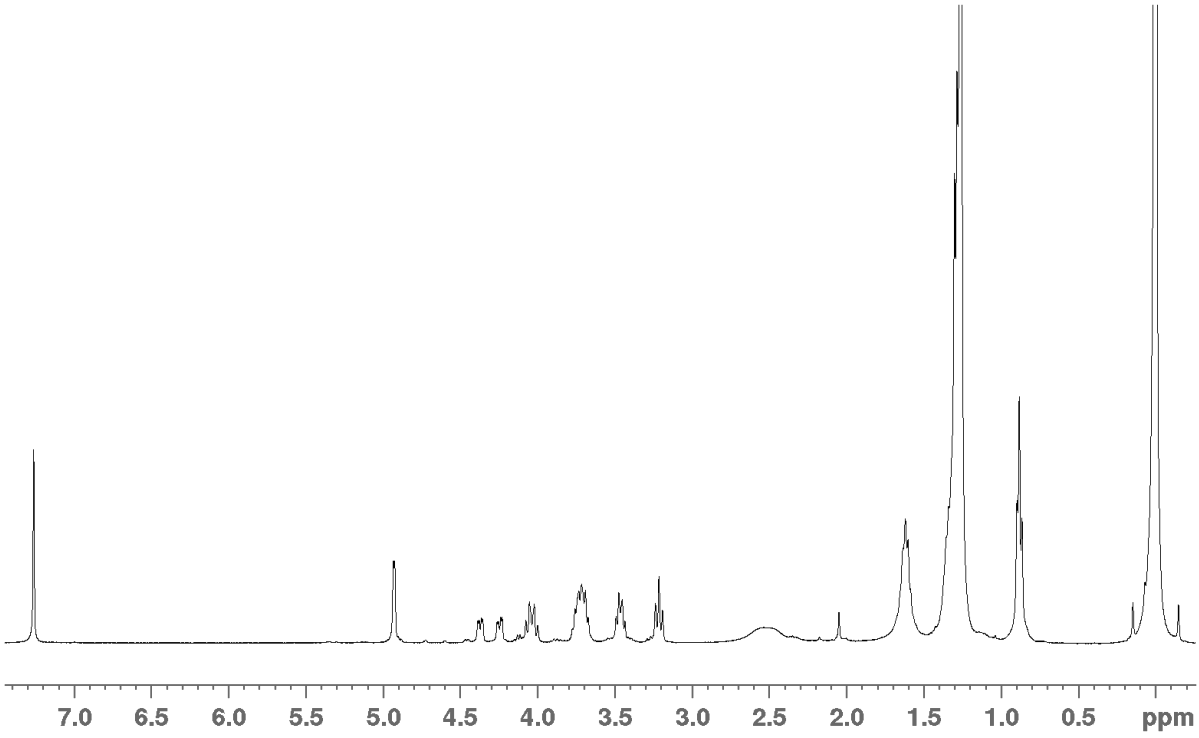

Figure A.14: ^{1}H NMR (400 MHz, $CDCl_3$) spectrum of dodecyl 2,6-dideoxy-2-fluoro-α-L-glucopyranoside **(4)**.

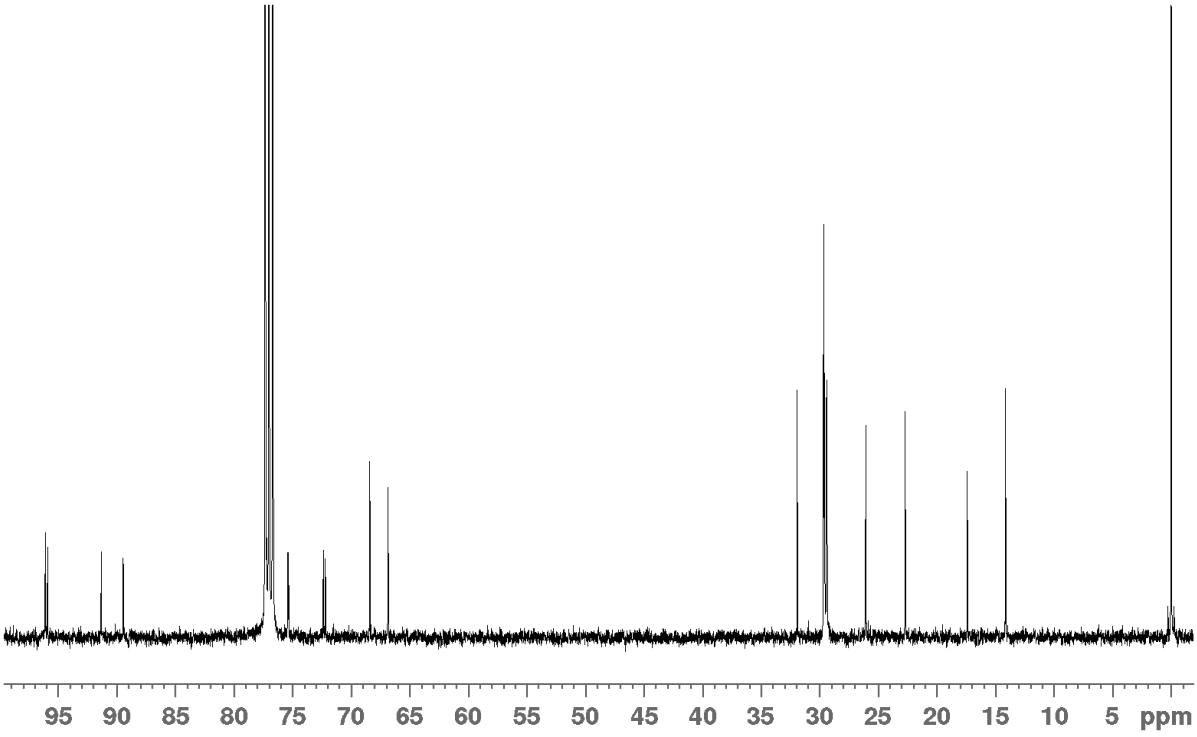

Figure A.15: ^{13}C NMR (100 MHz, $CDCl_3$) spectrum of dodecyl 2,6-dideoxy-2-fluoro-α-L-glucopyranoside **(4)**.

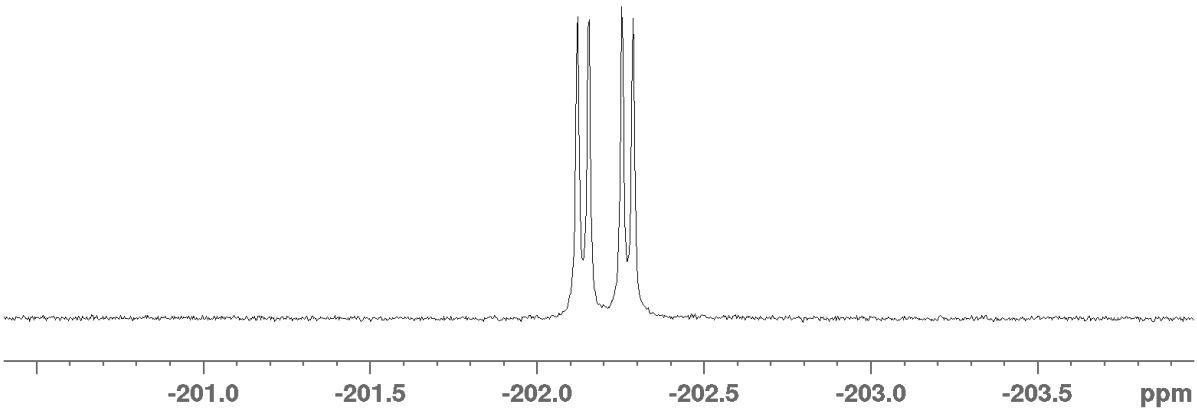

Figure A.16: ^{19}F NMR (376 MHz, $CDCl_3$) spectrum of dodecyl 2,6-dideoxy-2-fluoro-α-L-glucopyranoside **(4)**.

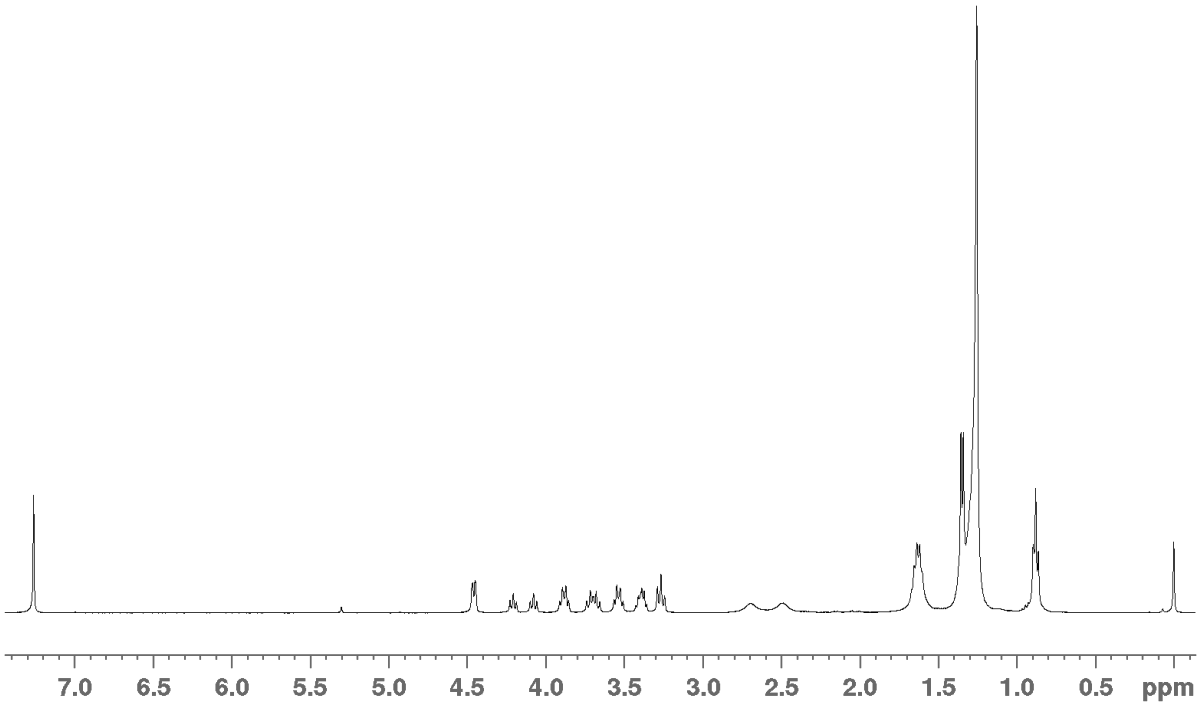

Figure A.17: ^{1}H NMR (400 MHz, $CDCl_3$) spectrum of dodecyl 2,6-dideoxy-2-fluoro-β-L-glucopyranoside **(31)**.

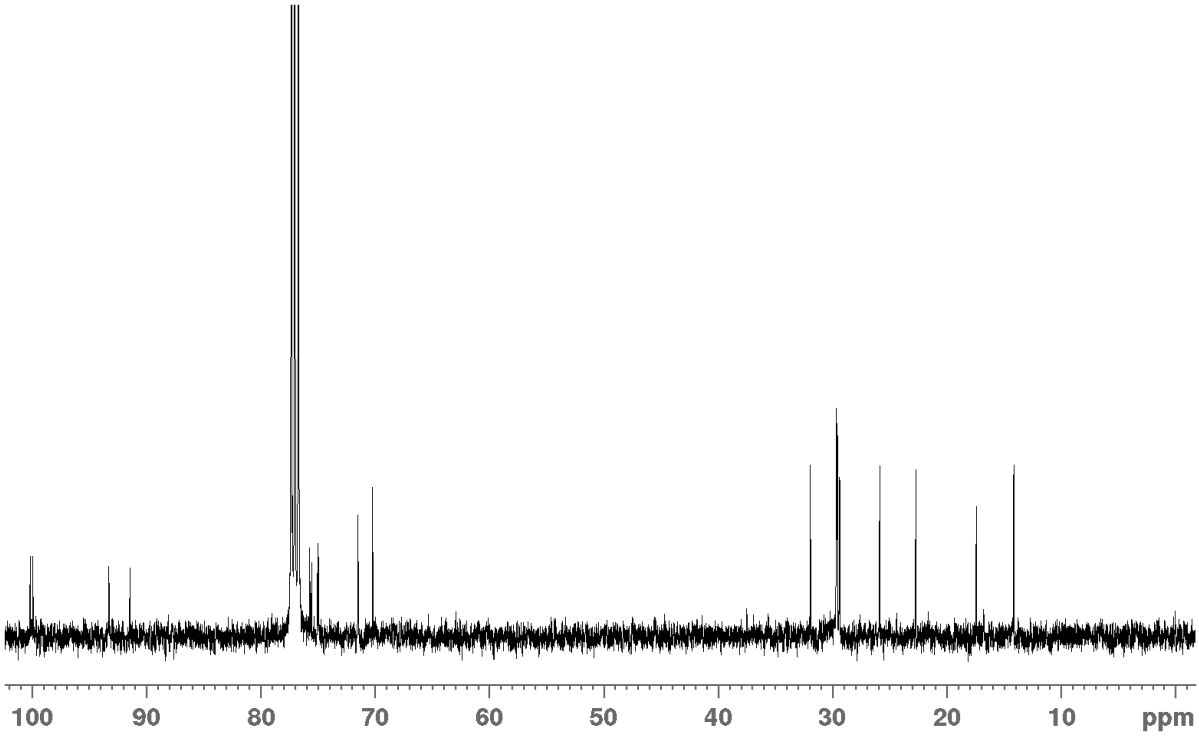

Figure A.18: ^{13}C NMR (100 MHz, $CDCl_3$) spectrum of dodecyl 2,6-dideoxy-2-fluoro-β-L-glucopyranoside **(4)**.

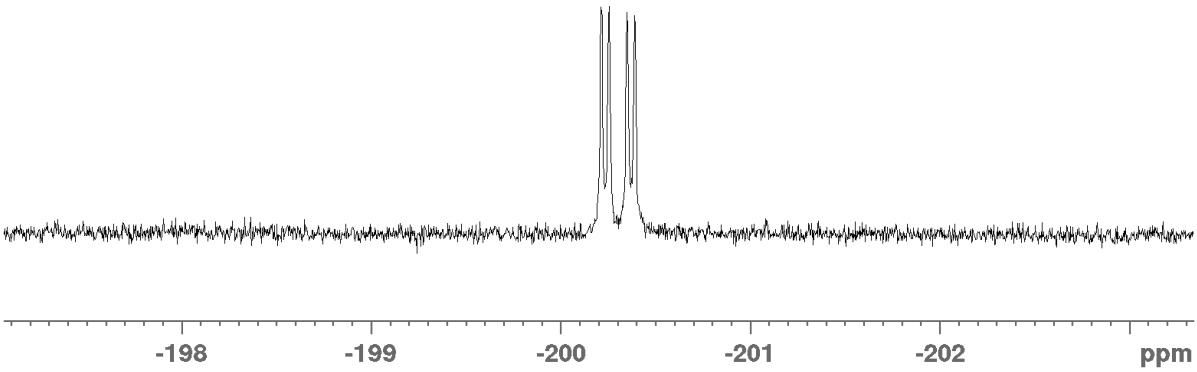

Figure A.19: ^{19}F NMR (376 MHz, $CDCl_3$) spectrum of dodecyl 2,6-dideoxy-2-fluoro-β-L-glucopyranoside **(31)**.

Appendix B

Auxiliary figures and tables

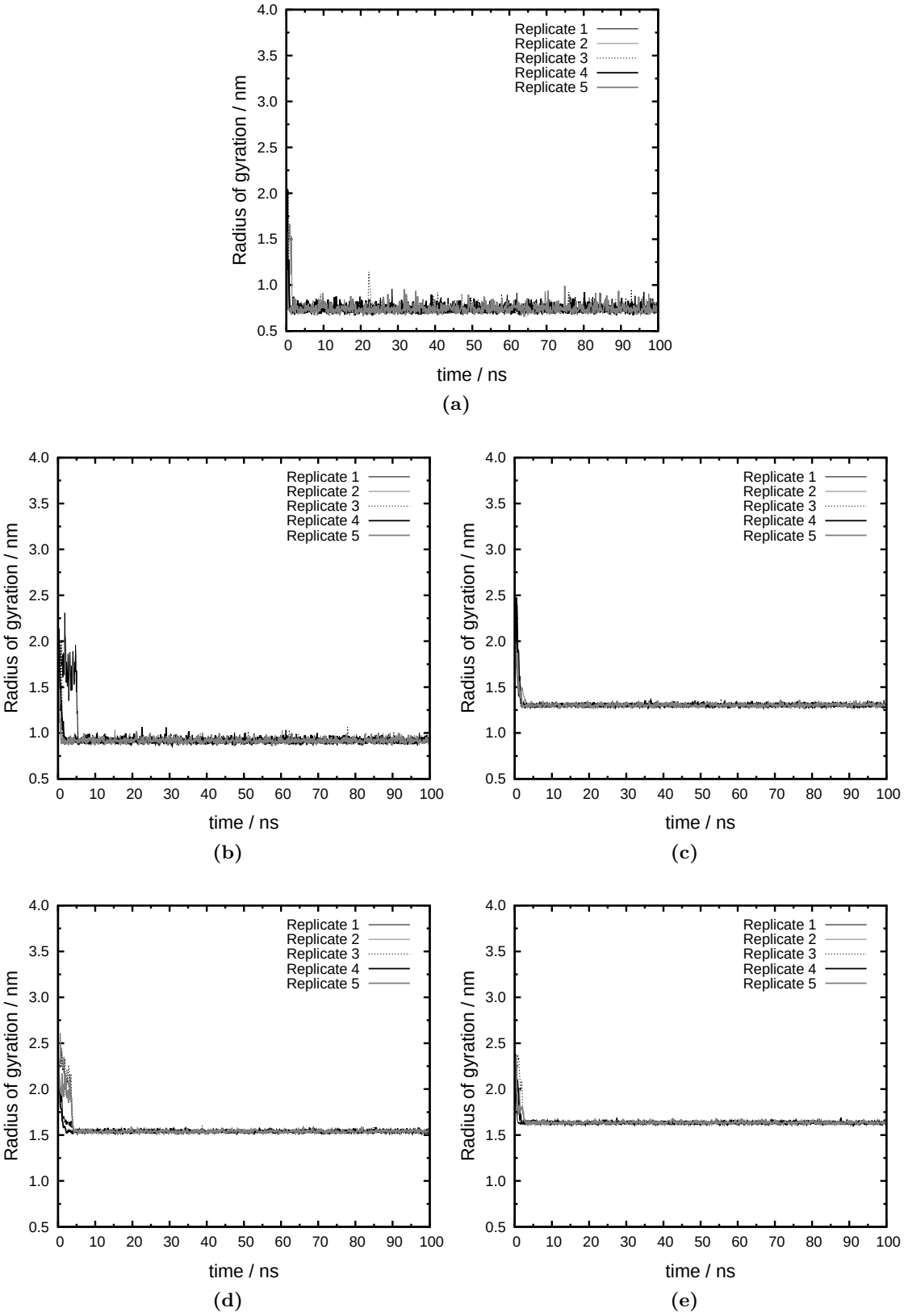

Figure B.1: Radius of gyration as a function of time computed from the simulations of glycolipid (GL = A12) micelles at different aggregation numbers. **(a)** $n_{GL} = 5$, **(b)** $n_{GL} = 10$, **(c)** $n_{GL} = 30$, **(d)** $n_{GL} = 50$, **(e)** $n_{GL} = 60$.

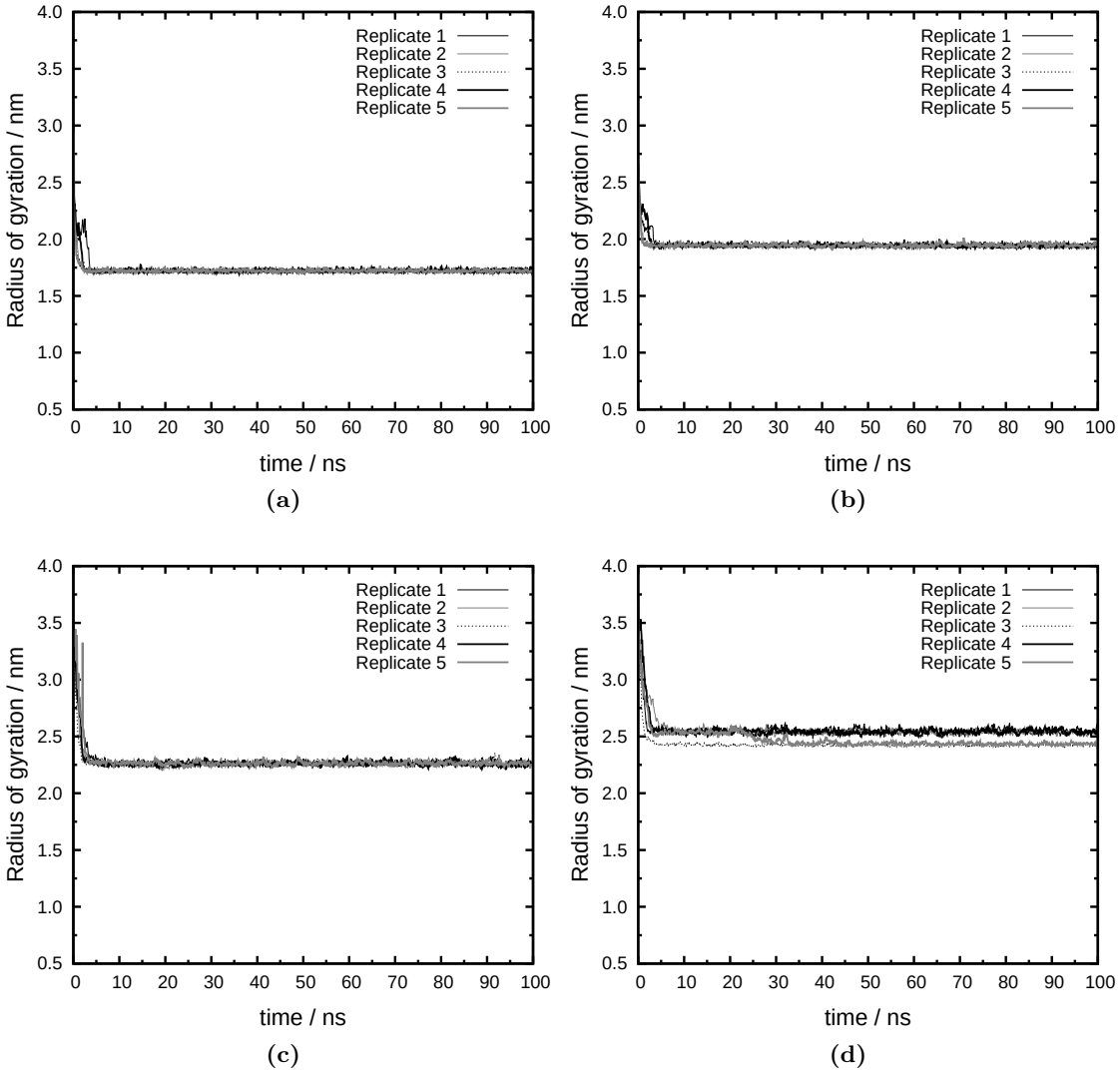

Figure B.2: Radius of gyration as a function of time computed from the simulations of glycolipid (GL = A12) micelles at different aggregation numbers. **(a)** $n_{GL} = 70$, **(b)** $n_{GL} = 100$, **(c)** $n_{GL} = 150$, **(d)** $n_{GL} = 200$.

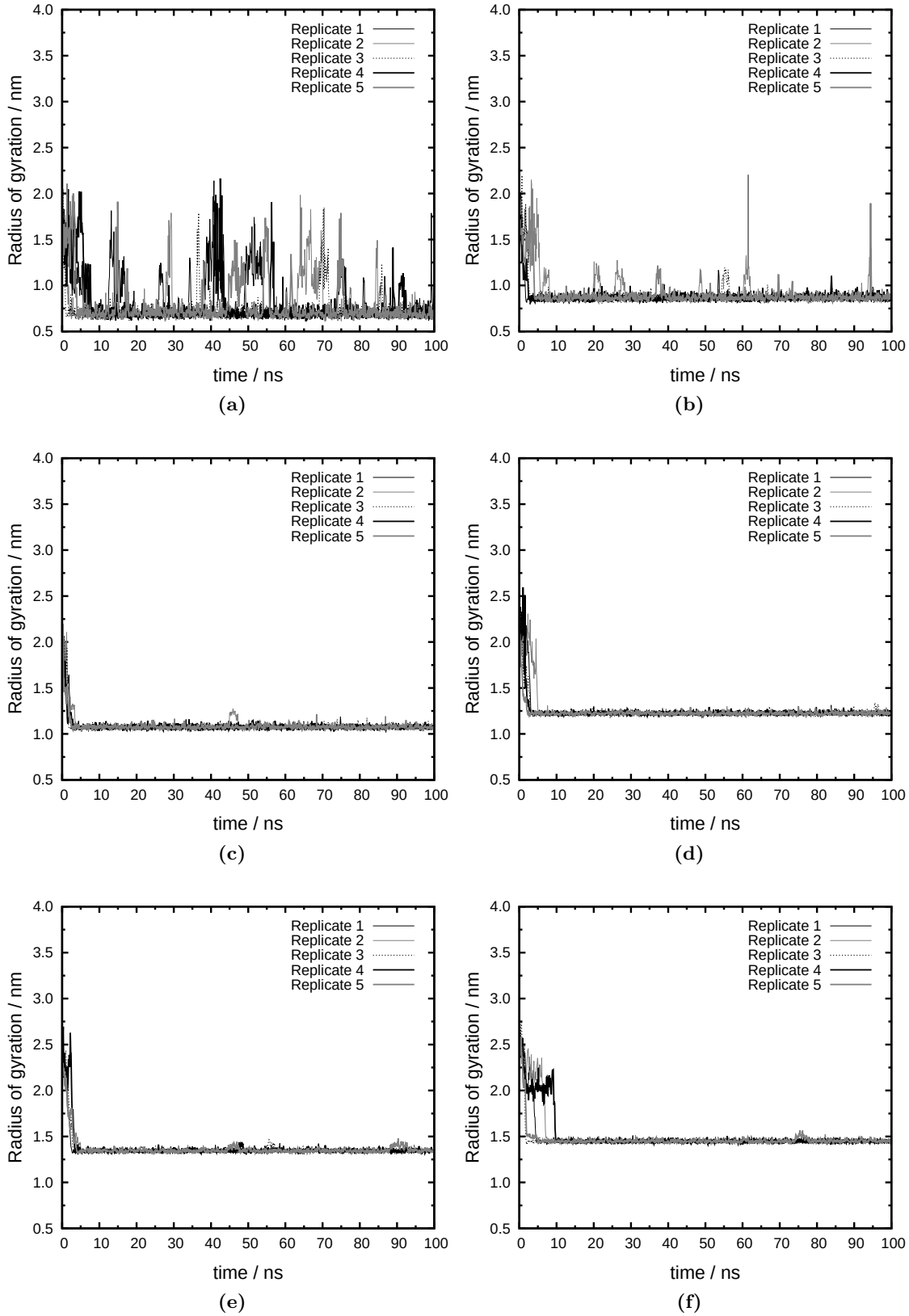

Figure B.3: Radius of gyration as a function of time computed from the simulations of glycolipid (GL = A08) micelles at different aggregation numbers. **(a)** $n_{GL} = 5$, **(b)** $n_{GL} = 10$, **(c)** $n_{GL} = 20$, **(d)** $n_{GL} = 30$, **(e)** $n_{GL} = 40$, **(f)** $n_{GL} = 50$.

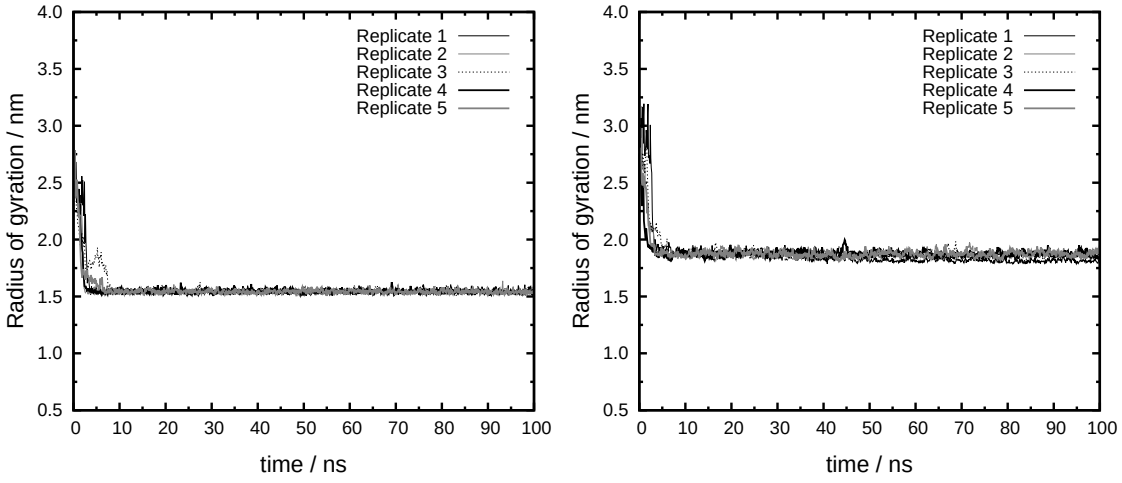

Figure B.4: Radius of gyration as a function of time computed from the simulations of glycolipid (GL = A08) micelles at different aggregation numbers. **(a)** $n_{GL} = 60$, **(b)** $n_{GL} = 100$.

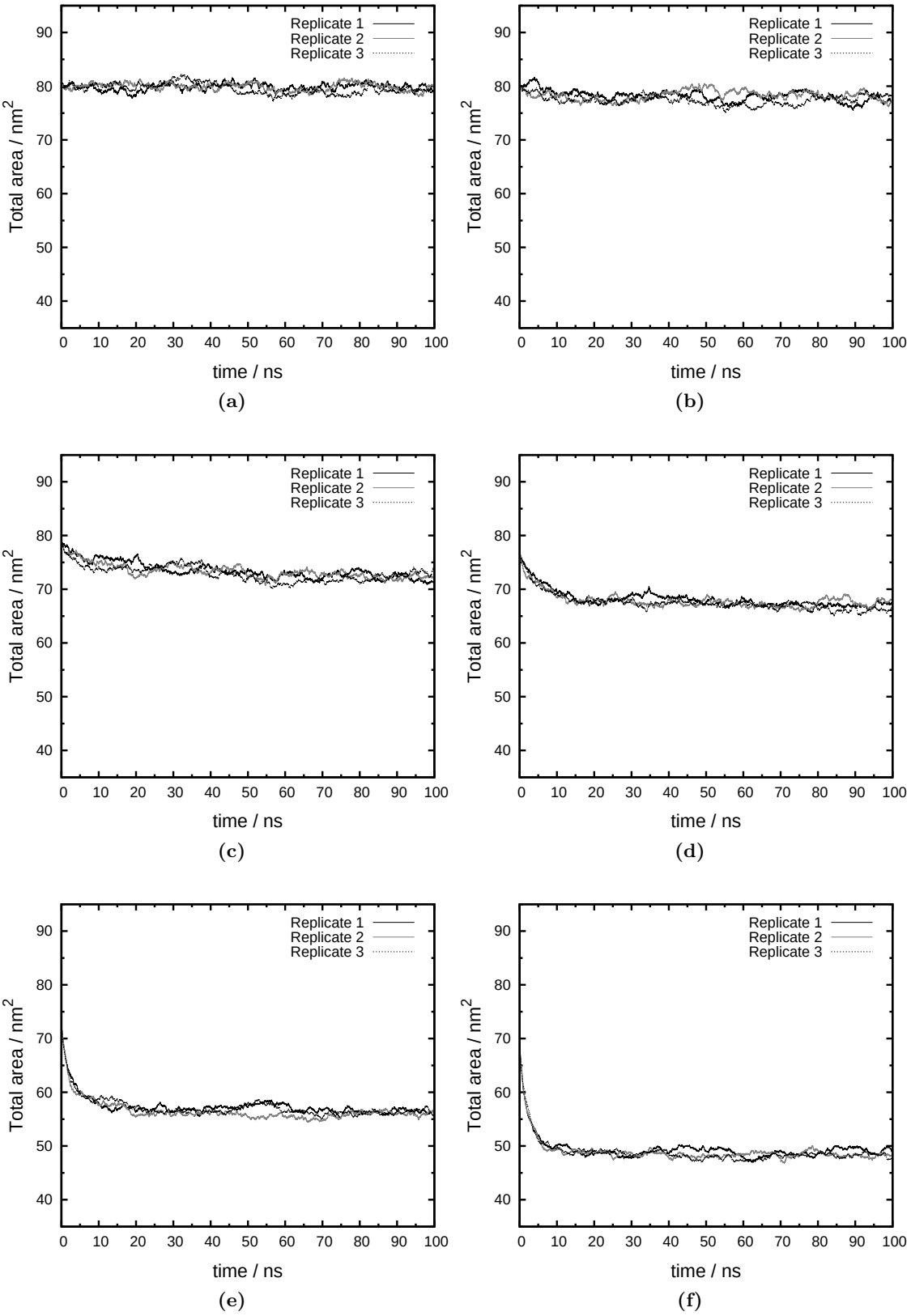

Figure B.5: Total area of the lipid bilayer as a function of time computed from the simulated binary mixtures at different glycolipid (GL = A12) molar fractions. **(a)** $x_{GL} = 0.01$, **(b)** $x_{GL} = 0.04$, **(c)** $x_{GL} = 0.12$, **(d)** $x_{GL} = 0.23$, **(e)** $x_{GL} = 0.50$, **(f)** $x_{GL} = 0.75$.

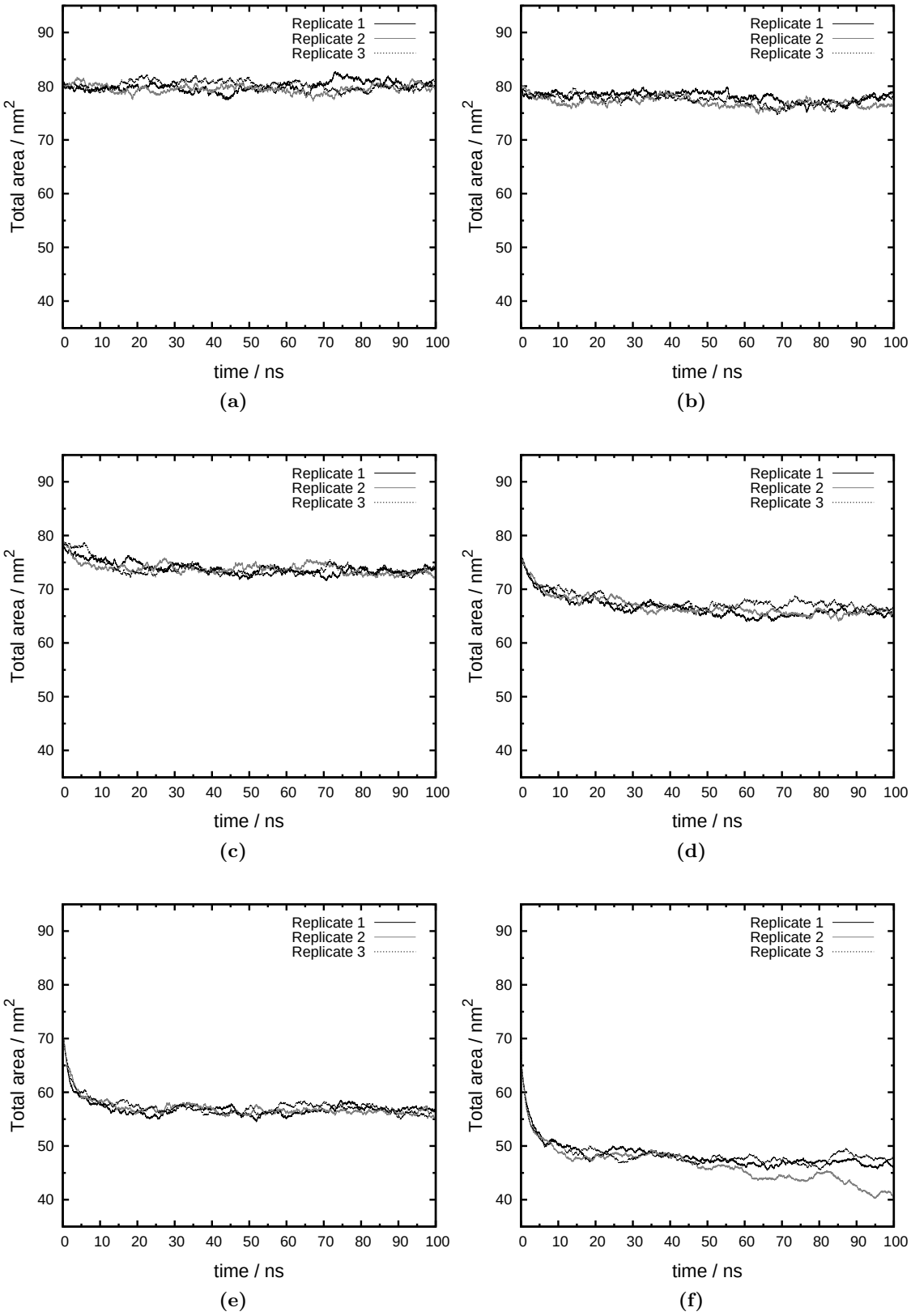

Figure B.6: Total area of the lipid bilayer as a function of time computed from the simulated binary mixtures at different glycolipid (GL = A08) molar fractions. **(a)** $x_{GL} = 0.01$, **(b)** $x_{GL} = 0.04$, **(c)** $x_{GL} = 0.12$, **(d)** $x_{GL} = 0.23$, **(e)** $x_{GL} = 0.50$, **(f)** $x_{GL} = 0.75$.

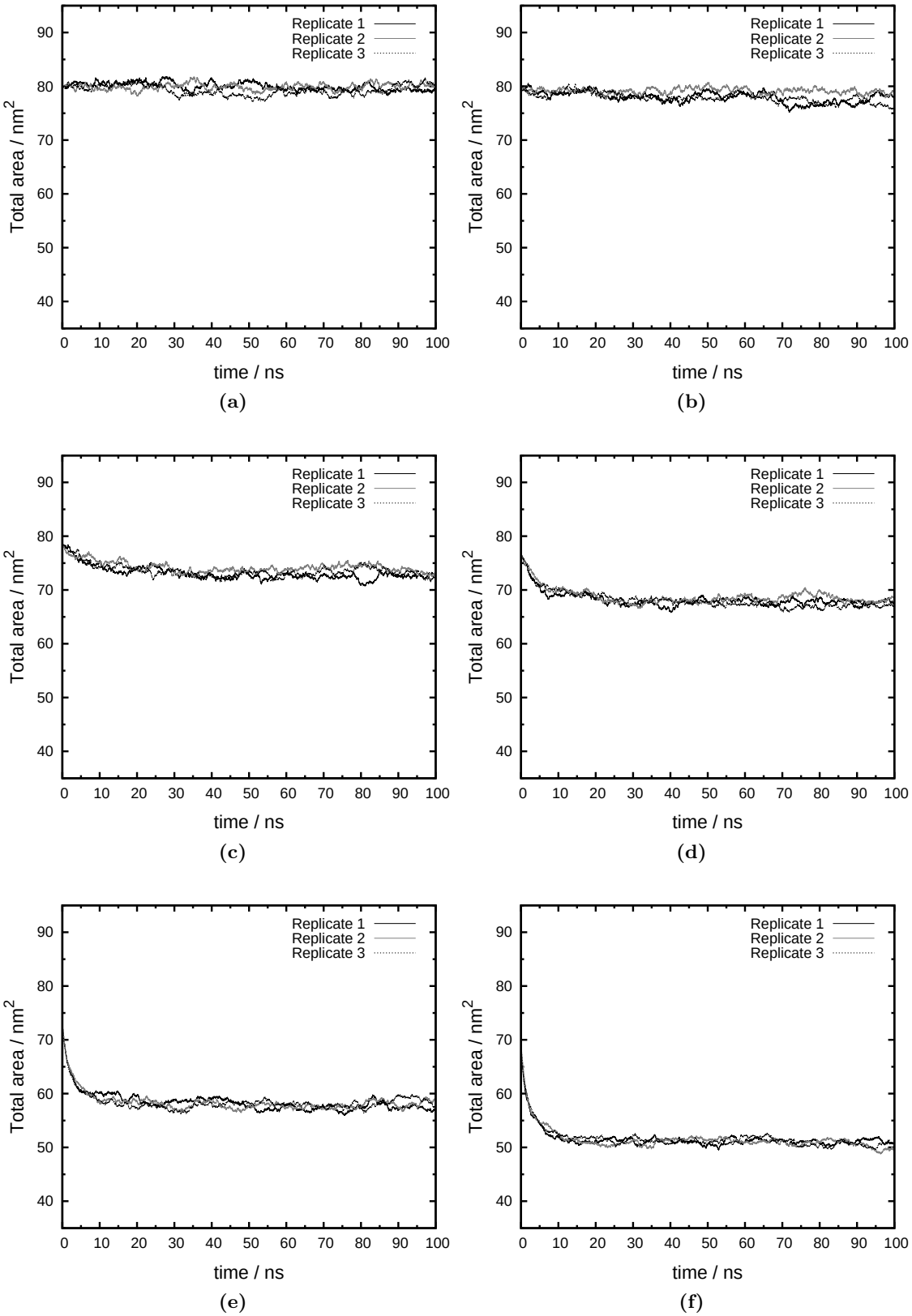

Figure B.7: Total area of the lipid bilayer as a function of time computed from the simulated binary mixtures at different glycolipid (GL = R12) molar fractions. **(a)** $x_{GL} = 0.01$, **(b)** $x_{GL} = 0.04$, **(c)** $x_{GL} = 0.12$, **(d)** $x_{GL} = 0.23$, **(e)** $x_{GL} = 0.50$, **(f)** $x_{GL} = 0.75$.

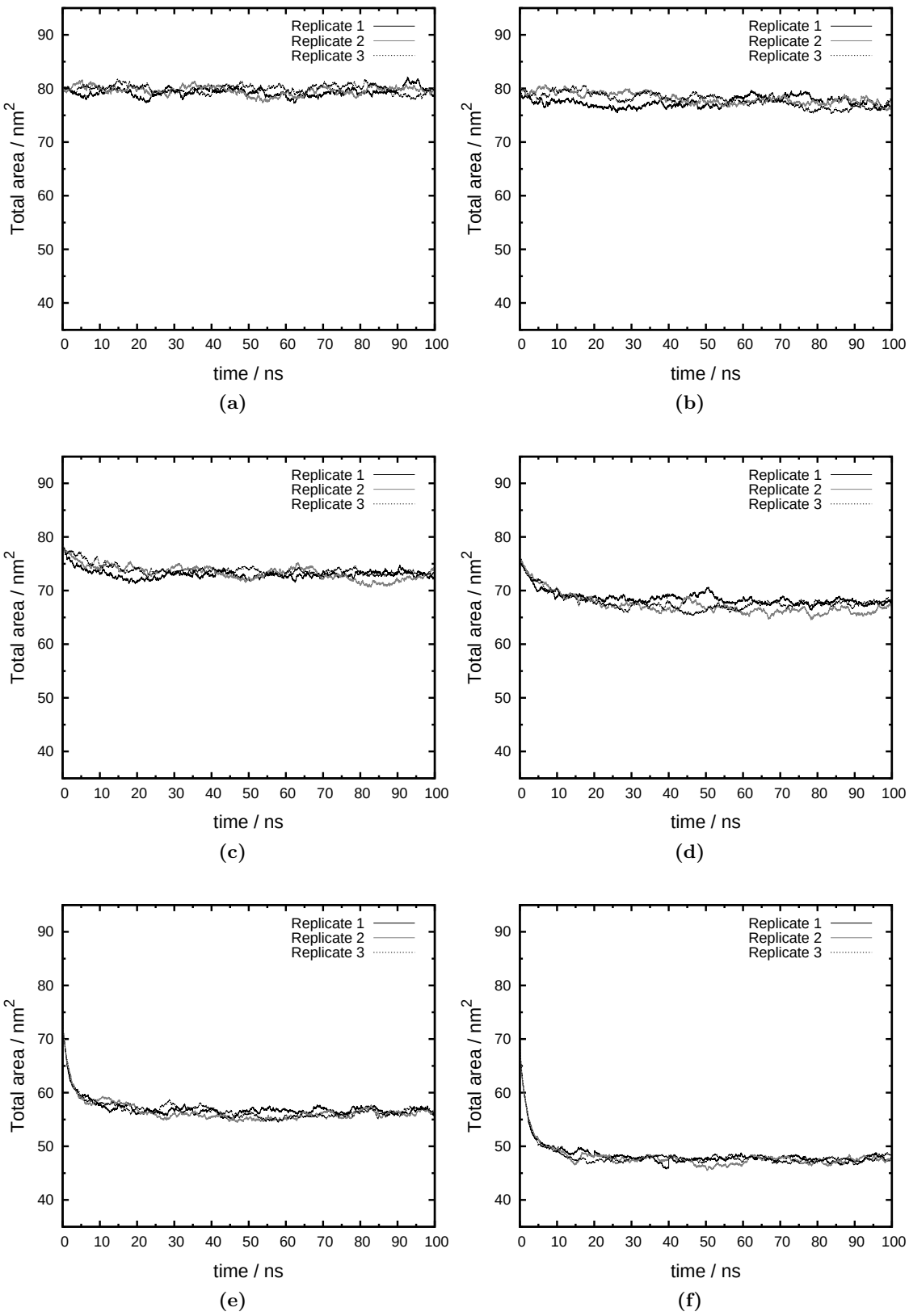

Figure B.8: Total area of the lipid bilayer as a function of time computed from the simulated binary mixtures at different glycolipid (GL = T12) molar fractions. **(a)** $x_{GL} = 0.01$, **(b)** $x_{GL} = 0.04$, **(c)** $x_{GL} = 0.12$, **(d)** $x_{GL} = 0.23$, **(e)** $x_{GL} = 0.50$, **(f)** $x_{GL} = 0.75$.

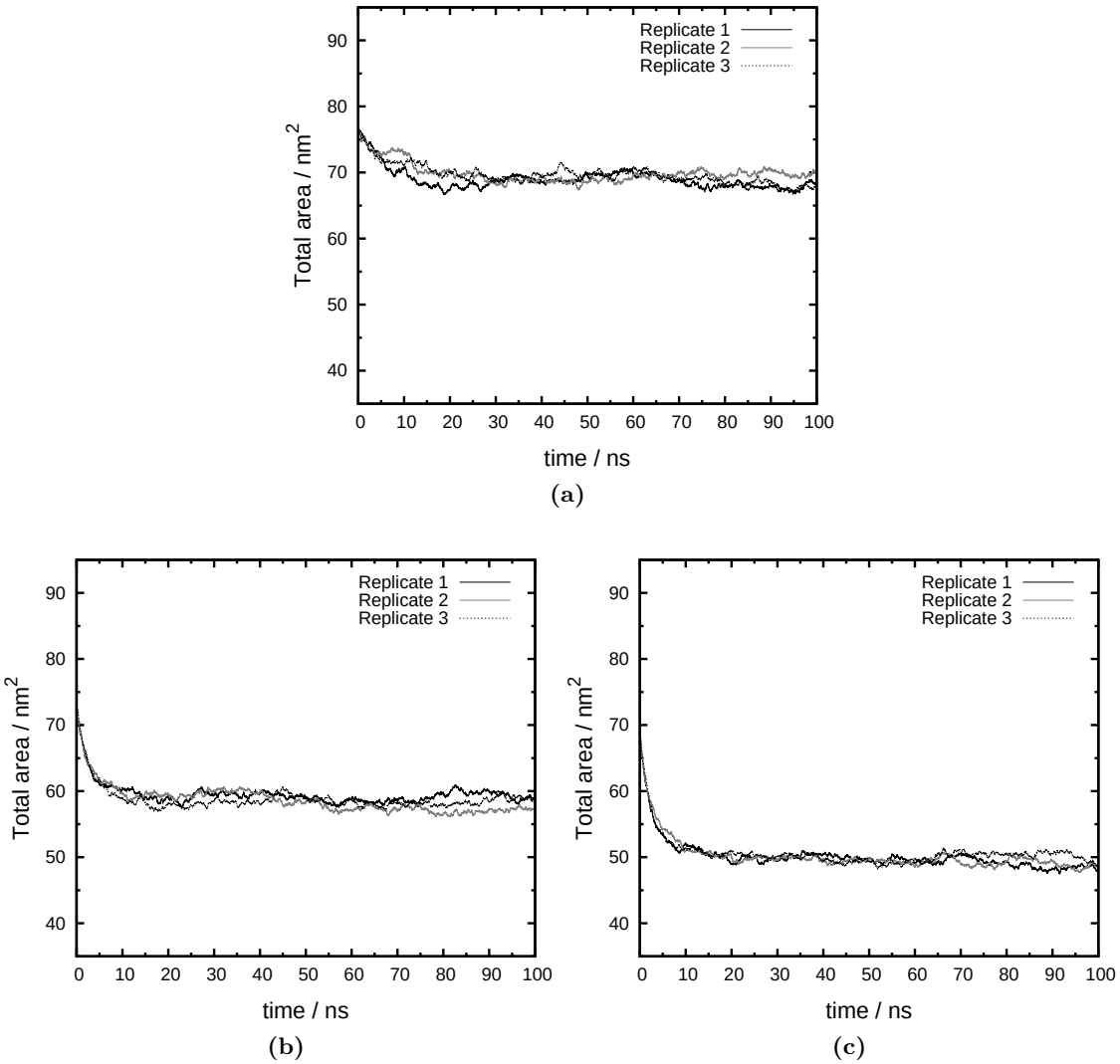

Figure B.9: Total area of the lipid bilayer as a function of time computed from the simulated binary mixtures at different glycolipid (GL = G12) molar fractions. **(a)** $x_{GL} = 0.23$, **(b)** $x_{GL} = 0.50$, **(c)** $x_{GL} = 0.75$.

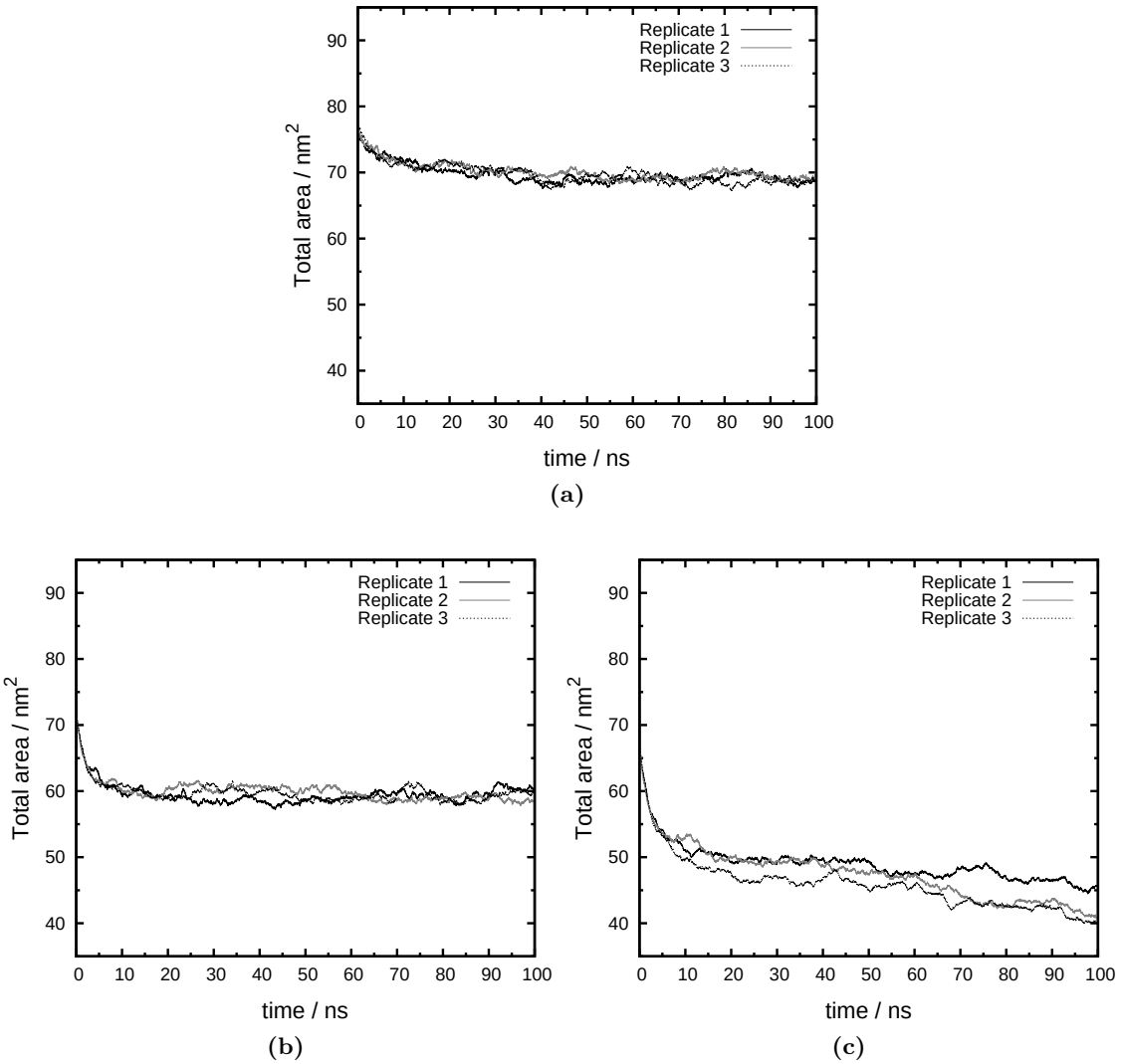

Figure B.10: Total area of the lipid bilayer as a function of time computed from the simulated binary mixtures at different glycolipid (GL = G08) molar fractions. **(a)** $x_{GL} = 0.23$, **(b)** $x_{GL} = 0.50$, **(c)** $x_{GL} = 0.75$.

Table B.1: Lateral diffusion coefficients determined for the glycoside/phospholipid binary mixtures [a].

GL	n_{GL}	n_{DMPC}	$\%_{GL}$	D/ 10^{-8} cm^2 s^{-1}
-	0	256	0.0	4.19 ± 0.17
A12	2	254	0.8	3.78 ± 0.45
A12	10	246	3.9	3.18 ± 0.01
A12	30	226	11.7	2.10 ± 0.22
A12	60	196	23.4	3.20 ± 0.32
A12	128	128	50.0	4.78 ± 0.10
A12	192	64	75.0	11.5 ± 1.16
A08	2	254	0.8	2.01 ± 0.05
A08	10	246	3.9	2.59 ± 0.29
A08	30	226	11.7	2.40 ± 0.08
A08	60	196	23.4	2.09 ± 0.20
A08	128	128	50.0	4.57 ± 0.39
A08	192	64	75.0	11.0 ± 0.23 [b]
R12	2	254	0.8	1.58 ± 0.16
R12	10	246	3.9	2.01 ± 0.18
R12	30	226	11.7	3.16 ± 0.24
R12	60	196	23.4	2.55 ± 0.30
R12	128	128	50.0	3.85 ± 0.11
R12	192	64	75.0	8.23 ± 0.25
T12	2	254	0.8	2.11 ± 0.09
T12	10	246	3.9	3.76 ± 0.11
T12	30	226	11.7	2.68 ± 0.26
T12	60	196	23.4	3.77 ± 0.16
T12	128	128	50.0	4.75 ± 0.30
T12	192	64	75.0	15.4 ± 1.32

[a] Errors were computed as the highest difference between the reported diffusion coefficient and the coefficient obtained using each of the two equal halves of the time interval.

[b] The bilayer structure distorts significantly for octyl glycoside systems at $x_{GL} = 0.75$ (see **Section 8.3.1**).

Table B.1: Lateral diffusion coefficients determined for the glycoside/phospholipid binary mixtures *(continued from previous page)* [a].

GL	n_{GL}	n_{DMPC}	$\%_{GL}$	D/ 10^{-8} cm^2 s^{-1}
-	0	256	0.0	4.19 ± 0.17
G12	60	196	23.4	2.49 ± 0.09
G12	128	128	50.0	2.70 ± 0.14
G12	192	64	75.0	4.71 ± 0.31
G08	60	196	23.4	2.82 ± 0.17
G08	128	128	50.0	2.75 ± 0.17
G08	192	64	75.0	3.64 ± 0.30 [b]

[a] Errors were computed as the highest difference between the reported diffusion coefficient and the coefficients obtained using each of the two equal halves of the time interval.

[b] The bilayer structure distorts significantly for octyl glycoside systems at $x_{GL} = 0.75$ (see **Section 8.3.1**).

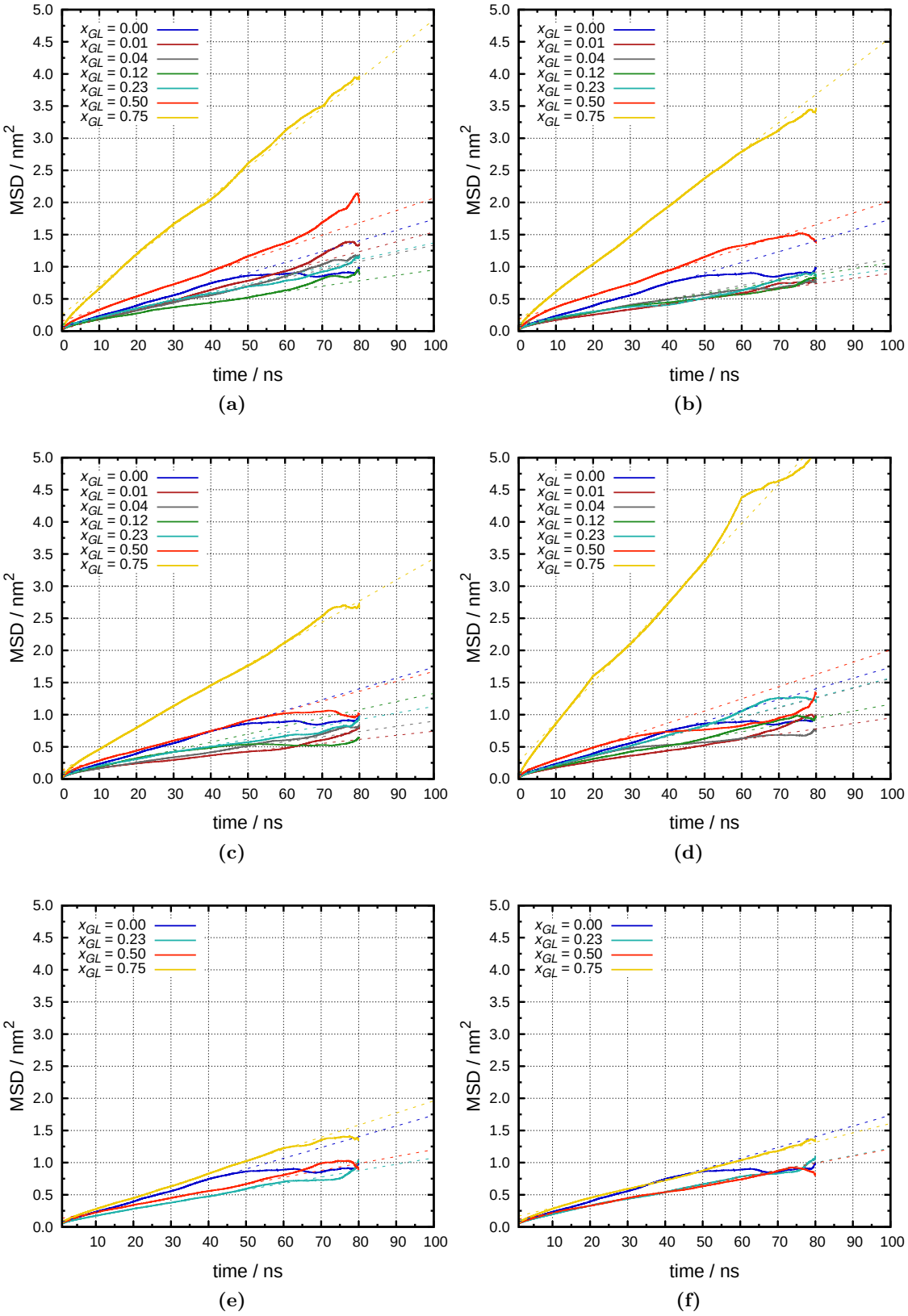

Figure B.11: Mean square displacement (MSD) as a function of time for the phospholipid phosphorus atoms averaged from the simulated binary mixtures at different glycolipid molar fractions. Lateral diffusion coefficients were computed from the slope of the linear part of the curves (shown in dashed lines). **(a)** GL = A12, **(b)** GL = A08, **(c)** GL = R12, **(d)** GL = T12, **(e)** GL = G12, **(f)** GL = G08.

Bibliography

[1] AP Rauter, S Lucas, T Almeida, D Sacoto, V Ribeiro, J Justino, A Neves, FVM Silva, MC Oliveira, MJ Ferreira, M-S Santos, and E Barbosa. Synthesis, surface active and antimicrobial properties of new alkyl 2,6-dideoxy-L-*arabino*-hexopyranosides. *Carbohydr. Res.*, 340(2):191–201, 2005.

[2] FVM Silva, M Goulart, J Justino, A Neves, F Santos, J Caio, S Lucas, A Newton, D Sacoto, E Barbosa, M-S Santos, and AP Rauter. Alkyl deoxy-*arabino*-hexopyranosides: Synthesis, surface properties, and biological activities. *Bioorg. Med. Chem.*, 16(7):4083–4092, 2008.

[3] A Martins, MS Santos, C Dias, P Serra, V Cachatra, J Pais, J Caio, VH Teixeira, M Machuqueiro, MS Silva, A Pelerito, J Justino, M Goulart, FV Silva, and AP Rauter. Tuning the bioactivity of tensioactive deoxy glycosides to structure: Antibacterial activity versus selective cholinesterase inhibition rationalized by molecular docking. *Eur. J. Org. Chem.*, 2013(8):1448–1459, 2013.

[4] I Radecka, C Martin, and D Hill. *Novel Antimicrobial Agents and Strategies 1st Ed.*, chapter 1, pages 1–16. Wiley-VCH, Weinheim, Germany, 2015.

[5] L Zaffiri, J Gardner, and LH Toledo-Pereyra. History of antibiotics. From salvarsan to cephalosporins. *J. Invest. Surg.*, 25(2):67–77, 2012.

[6] A Fleming. On the antibacterial action of cultures of a penicillium, with special reference to their use in the isolation of *B. influenzae*. *Brit. J. Exp. Pathol*, 10(3):226, 1929.

[7] MA Kohanski, DJ Dwyer, and JJ Collins. How antibiotics kill bacteria: From targets to networks. *Nat. Rev. Microbiol.*, 8(6):423–435, 2010.

[8] DJ Payne, MN Gwynn, DJ Holmes, and DL Pompliano. Drugs for bad bugs: Confronting the challenges of antibacterial discovery. *Nat. Rev. Drug Discov.*, 6(1):29–40, 2007.

[9] Otto Cars, Anna Hedin, and Andreas Heddini. The global need for effective antibiotics—Moving towards concerted action. *Drug Resist. Update.*, 14(2):68–69, 2011.

[10] RC Moellering. Discovering new antimicrobial agents. *Int. J. Antimicrob. Ag.*, 37(1):2–9, 2011.

[11] JMA Blair, MA Webber, AJ Baylay, DO Ogbolu, and LJV Piddock. Molecular mechanisms of antibiotic resistance. *Nat. Rev. Microbiol.*, 13(1):42–51, 2015.

[12] GD Wright. Molecular mechanisms of antibiotic resistance. *Chem. Comm.*, 47(14):4055–4061, 2011.

[13] RM Epand and RF Epand. Lipid domains in bacterial membranes and the action of antimicrobial agents. *Biochem. Biophys. Acta Rev. Biomembranes*, 1788(1):289–294, 2009.

[14] RM Epand and RF Epand. Bacterial membrane lipids in the action of antimicrobial agents. *J. Pept. Sci.*, 17(5):298–305, 2011.

[15] N Papo and Y Shai. Can we predict biological activity of antimicrobial peptides from their interactions with model phospholipid membranes? *Peptides*, 24(11):1693–1703, 2003.

[16] RF Epand, PB Savage, and RM Epand. Bacterial lipid composition and the antimicrobial efficacy of cationic steroid compounds (ceragenins). *Biochem. Biophys. Acta Rev. Biomembranes*, 1768(10):2500–2509, 2007.

[17] A Som and GN Tew. Influence of lipid composition on membrane activity of antimicrobial phenylene ethynylene oligomers. *J. Phys. Chem. B*, 112(11):3495–3502, 2008.

[18] Y-M Zhang and CO Rock. Membrane lipid homeostasis in bacteria. *Nat. Rev. Microbiol.*, 6(3):222–233, 2008.

[19] B Ernst and JL Magnani. From carbohydrate leads to glycomimetic drugs. *Nat. Rev. Drug Discov.*, 8(8):661–677, 2009.

[20] NM Xavier and AP Rauter. Enantioselective synthesis in carbohydrate-based drug discovery: Imino sugars, alkaloids and macrolide antibiotics. *Curr. Top. Med. Chem*, 14(10):1235–1243, 2014.

[21] NM Xavier and AP Rauter. Environmentally friendly approaches to the synthesis of new antibiotics from sugars. *Pure Appl. Chem.*, 84(3):803–816, 2012.

[22] NM Xavier, M Goulart, A Neves, J Justino, S Chambert, AP Rauter, and Y Queneau. Synthesis of sugars embodying conjugated carbonyl systems and related triazole derivatives from carboxymethyl glycoside lactones. Evaluation of their antimicrobial activity and toxicity. *Bioorg. Med. Chem.*, 19(2):926–938, 2011.

[23] AP Rauter, T Almeida, AI Vicente, V Ribeiro, JC Bordado, JP Marques, F Ramôa Ribeiro, MJ Ferreira, C Oliveira, and M Guisnet. Reactions of N-, S-and O-nucleophiles with 3,4,6-tri-*O*-benzyl-D-glucal mediated by triphenylphosphane hydrobromide versus those with HY zeolite. *Eur. J. Org. Chem*, 2006(10):2429–2439, 2006.

[24] DB Jernigan, PL Raghunathan, BP Bell, R Brechner, EA Bresnitz, JC Butler, M Cetron, M Cohen, T Doyle, M Fischer, C Greene, KS Griffith, J Guarner, JL Hadler, JA Hayslett, R Meyer, LR Petersen, M Phillips, R Piner, T Popovic, CP Quinn, J Reefhuis, D Reissman, N Rosenstein, A Schuchat, W-J Shieh, L Siegal, DL Swerdlow, FC Tenover, M Traeger, JW Ward, I Weisfuse, S Wiersma, K Yeskey, S Zaki, DA Ashford, BA Perkins, S Ostroff, J Hughes, D Fleming, JP Koplan, JL Gerberding, and the National Anthrax Epidemiologic Investigation Team. Investigation of bioterrorism-related anthrax, United States, 2001: Epidemiologic findings. *Emerg. Infect. Dis.*, 8(10):1019, 2002.

[25] J Frean, KP Klugman, L Arntzen, and S Bukofzer. Susceptibility of *Bacillus anthracis* to eleven antimicrobial agents including novel fluoroquinolones and a ketolide. *J. Antimicrob. Chemoth.*, 52(2):297–299, 2003.

[26] VA Luna, DS King, J Gulledge, AC Cannons, PT Amuso, and J Cattani. Susceptibility of *Bacillus anthracis*, *Bacillus cereus*, *Bacillus mycoides*, *Bacillus pseudomycoides* and *Bacillus thuringiensis* to 24 antimicrobials using sensititre® automated microbroth dilution and etest® agar gradient diffusion methods. *J. Antimicrob. Chemoth.*, 60(3):555–567, 2007.

[27] B Nammalwar, RA Bunce, KD Berlin, CR Bourne, PC Bourne, EW Barrow, and WW Barrow. Synthesis and biological activity of substituted 2,4-diaminopyrimidines that inhibit *Bacillus anthracis*. *Eur. J. Med. Chem.*, 54:387–396, 2012.

[28] A Tripathi, MM Schofield, GE Chlipala, PJ Schultz, I Yim, SA Newmister, TD Nusca, JB Scaglione, PC Hanna, G Tamayo-Castillo, and DH Sherman. Baulamycins A and B, broad-spectrum antibiotics identified as inhibitors of siderophore biosynthesis in *Staphylococcus aureus* and *Bacillus anthracis*. *J. Am. Chem. Soc.*, 136(4):1579–1586, 2014.

[29] KH Jang, S-J Nam, JB Locke, CA Kauffman, DS Beatty, LA Paul, and W Fenical. Anthracimycin, a potent anthrax antibiotic from a marine-derived actinomycete. *Angew. Chem. Int. Ed.*, 52(30):7822–7824, 2013.

[30] E Helgason, OA Økstad, DA Caugant, HA Johansen, A Fouet, M Mock, I Hegna, and A-B Kolstø. *Bacillus anthracis*, *Bacillus cereus*, and *Bacillus thuringiensis* — One species on the basis of genetic evidence. *Appl. Environ. Microbiol.*, 66(6):2627–2630, 2000.

[31] AR Hoffmaster, J Ravel, DA Rasko, GD Chapman, MD Chute, CK Marston, BK De, CT Sacchi, C Fitzgerald, LW Mayer, MCJ Maiden, FG Priest, M Barker, L Jiang, RZ Cer, J Rilstone, SN Peterson, RS Weyant, DR Galloway, TD Read, T Popovic, and CM Fraser. Identification of anthrax toxin genes in a *Bacillus cereus* associated with an illness resembling inhalation anthrax. *Proc. Nat. Acad. Sci. U.S.A.*, 101(22):8449–8454, 2004.

[32] LO Ticknor, A-B Kolstø, KK Hill, P Keim, MT Laker, M Tonks, and PJ Jackson. Fluorescent amplified fragment length polymorphism analysis of norwegian *Bacillus cereus* and *Bacillus thuringiensis* soil isolates. *Appl. Environ. Microbiol.*, 67(10):4863–4873, 2001.

[33] D Daffonchio, A Cherif, and S Borin. Homoduplex and heteroduplex polymorphisms of the amplified ribosomal 16S-23S internal transcribed spacers describe genetic relationships in the "*Bacillus cereus* group". *Appl. Environ. Microbiol.*, 66(12):5460–5468, 2000.

[34] A Cherif, L Brusetti, S Borin, A Rizzi, A Boudabous, H Khyami-Horani, and D Daffonchio. Genetic relationship in the '*Bacillus cereus* group'by rep-PCR fingerprinting and sequencing of a *Bacillus anthracis*-specific rep-PCR fragment. *J. Appl. Microbiol.*, 94(6):1108–1119, 2003.

[35] AD McNaught. Nomenclature of carbohydrates (Recommendations 1996). *Pure Appl. Chem.*, 68(10):1919–2008, 1996.

[36] PM Collins and RJ Ferrier. *Monosaccharides: Their Chemistry and Their Roles in Natural Products.* John Wiley & Sons, 1996.

[37] BG Davis and AJ Fairbanks. *Carbohydrate Chemistry.* Oxford University Press, New York, US, 2002.

[38] DE Levy and P Fügedi. *The Organic Chemistry of Sugars.* CRC Press, Taylor & Francis Group, US, 2006.

[39] AP Davis and RS Wareham. Carbohydrate recognition through noncovalent interactions: a challenge for biomimetic and supramolecular chemistry. *Angew. Chem. Int. Ed.*, 38(20):2978–2996, 1999.

[40] A Varki. Biological roles of oligosaccharides: all of the theories are correct. *Glycobiol.*, 3(2):97–130, 1993.

[41] RA Dwek. Glycobiology: toward understanding the function of sugars. *Chem. Rev.*, 96(2):683–720, 1996.

[42] L-X Wang and BG Davis. Realizing the promise of chemical glycobiology. *Chem. Sci.*, 4(9):3381–3394, 2013.

[43] C-Y Wu and C-H Wong. Chemistry and glycobiology. *Chem. Comm.*, 47(22):6201–6207, 2011.

[44] GW Hart and RJ Copeland. Glycomics hits the big time. *Cell*, 143(5):672–676, 2010.

[45] RV Stick. *Carbohydrates: The Sweet Molecules of Life.* Academic Press, UK, 2001.

[46] ML Sinnott. *Carbohydrate Chemistry and Biochemistry: Structure and Mechanism.* Royal Society of Chemistry, Cambridge, UK, 2007.

[47] I Tvaroŝka and T Bleha. Anomeric and exo-anomeric effects in carbohydrate chemistry. *Adv. Carbohydr. Chem. Biochem.*, 47:45–123, 1989.

[48] B Xu, L Unione, J Sardinha, S Wu, M Ethève-Quelquejeu, AP Rauter, Y Blériot, Y Zhang, S Martín-Santamaría, D Díaz, J Jiménez-Barbero, and M Sollogoub. *gem*-difluorocarbadisaccharides: restoring the *exo*-anomeric effect. *Angew. Chem. Int. Ed.*, 53(36):9597–9602, 2014.

[49] RU Lemieux. Effects of unshared pairs of electrons and their solvation on conformational equilibria. *Pure Appl. Chem.*, 25(3):527–548, 1971.

[50] E Juaristi and G Cuevas. Recent studies of the anomeric effect. *Tetrahedr.*, 48(24):5019–5087, 1992.

[51] Y Mo. Computational evidence that hyperconjugative interactions are not responsible for the anomeric effect. *Nat. Chem.*, 2(8):666–671, 2010.

[52] EJ Cocinero, P Çarçabal, TD Vaden, JP Simons, and BG Davis. Sensing the anomeric effect in a solvent-free environment. *Nat.*, 469(7328):76–79, 2011.

[53] C Wang, F Ying, W Wu, and Y Mo. How solvent influences the anomeric effect: Roles of hyperconjugative versus steric interactions on the conformational preference. *J. Org. Chem.*, 79(4):1571–1581, 2014.

[54] AV Demchenko. *Handbook of Chemical Glycosylation: Advances in Stereoselectivity and Therapeutic Relevance.* Wiley-VCH, Weinheim, Germany, 2008.

[55] RA Laine. A calculation of all possible oligosaccharide isomers both branched and linear yields 1.05×10^{12} structures for a reducing hexasaccharide: the isomer barrier to development of single-method saccharide sequencing or synthesis systems. *Glycobiol.*, 4(6):759–767, 1994.

[56] SC Ranade and AV Demchenko. Mechanism of chemical glycosylation: focus on the mode of activation and departure of anomeric leaving groups. *J. Carbohydr. Chem.*, 32(1):1–43, 2013.

[57] LK Mydock and AV Demchenko. Mechanism of chemical *O*-glycosylation: from early studies to recent discoveries. *Org. Biomol. Chem.*, 8(3):497–510, 2010.

[58] D Crich. Mechanism of a chemical glycosylation reaction. *Acc. Chem. Res.*, 43(8):1144–1153, 2010.

[59] X Zhu and RR Schmidt. New principles for glycoside-bond formation. *Angew. Chem. Int. Ed.*, 48(11):1900–1934, 2009.

[60] C-C Wang, J-C Lee, S-Y Luo, SS Kulkarni, Y-W Huang, C-C Lee, K-L Chang, and S-C Hung. Regioselective one-pot protection of carbohydrates. *Nat.*, 446(7138):896–899, 2007.

[61] M Huang, P Retailleau, L Bohé, and D Crich. Cation clock permits distinction between the mechanisms of α-and β-*O*–and β-*C*-glycosylation in the mannopyranose series: evidence for the existence of a mannopyranosyl oxocarbenium ion. *J. Am. Chem. Soc.*, 134(36):14746–14749, 2012.

[62] T Hosoya, T Takano, P Kosma, and T Rosenau. Theoretical foundation for the presence of oxacarbenium ions in chemical glycoside synthesis. *J. Org. Chem.*, 79(17):7889–7894, 2014.

[63] RJ Ferrier and JO Hoberg. Synthesis and reactions of unsaturated sugars. *Adv. Carbohydr. Chem. Biochem.*, 58:55–121, 2003.

[64] H-J Böhm, D Banner, S Bendels, M Kansy, B Kuhn, K Müller, U Obst-Sander, and M Stahl. Fluorine in medicinal chemistry. *ChemBioChem*, 5(5):637–643, 2004.

[65] J Wang, M Sánchez-Roselló, JL Aceña, C del Pozo, AE Sorochinsky, S Fustero, VA Soloshonok, and H Liu. Fluorine in pharmaceutical industry: Fluorine-containing drugs introduced to the market in the last decade (2001–2011). *Chem. Rev.*, 114(4):2432–2506, 2013.

[66] PT Nyffeler, SG Durón, MD Burkart, SP Vincent, and C-H Wong. Selectfluor: mechanistic insight and applications. *Angew. Chem. Int. Ed.*, 44(2):192–212, 2005.

[67] MD Burkart, Z Zhang, S-C Hung, and C-H Wong. A new method for the synthesis of fluorocarbohydrates and glycosides using selectfluor. *J. Am. Chem. Soc.*, 119(49):11743–11746, 1997.

[68] M Albert, K Dax, and J Ortner. A novel direct route to 2-deoxy-2-fluoro-aldoses and their corresponding derivatives. *Tetrahedr.*, 54(19):4839–4848, 1998.

[69] SP Vincent, MD Burkart, C-Y Tsai, Z Zhang, and C-H Wong. Electrophilic fluorination-nucleophilic addition reaction mediated by selectfluor: Mechanistic studies and new applications. *J. Org. Chem.*, 64(14):5264–5279, 1999.

[70] J Ortner, M Albert, H Weber, and K Dax. Studies on the reaction of D-glucal and its derivatives with 1-chloromethyl-4-fluoro-1,4-diazoniabicyclo[2.2.2]octane salts. *J. Carbohydr. Chem.*, 18(3):297–316, 1999.

[71] TK Lindhorst. *Essentials of Carbohydrate Chemistry and Biochemistry.* Wiley-VCH, Weinheim, Germany, 2000.

[72] AMP van Steijn, JP Kamerling, and JFG Vliegenthart. Synthesis of a spacer-containing repeating unit of the capsular polysaccharide of *Streptococcus pneumoniae* type 23F. *Carbohydr. Res.*, 211(2):261–277, 1991.

[73] D Lafont, M-N Bouchu, A Girard-Egrot, and P Boullanger. Syntheses and interfacial behaviour of neoglycolipid analogues of glycosyl ceramides. *Carbohydr. Res.*, 336(3):181–194, 2001.

[74] J Zhang and F Kong. A general method for the synthesis of oligosaccharides consisting of α-(1→2)- and α-(1→3)-linked rhamnan backbones and GlcNAc side chains. *Tetrahedr.*, 59(9):1429–1441, 2003.

[75] HM Branderhorst, R Kooij, A Salminen, LH Jongeneel, CJ Arnusch, RMJ Liskamp, J Finne, and RJ Pieters. Synthesis of multivalent *Streptococcus suis* adhesion inhibitors by enzymatic cleavage of polygalacturonic acid and 'click' conjugation. *Org. Biomol. Chem.*, 6(8):1425–1434, 2008.

[76] B Coxon. Developments in the karplus equation as they relate to the NMR coupling constants of carbohydrates. *Adv. Carbohydr. Chem. Biochem.*, 62:17–82, 2009.

[77] R Šardzík, GT Noble, MJ Weissenborn, A Martin, SJ Webb, and SL Flitsch. Preparation of aminoethyl glycosides for glycoconjugation. *Beilstein J. Org. Chem.*, 6(1):699–703, 2010.

[78] J Zhao, S Wei, X Ma, and H Shao. A simple and convenient method for the synthesis of pyranoid glycals. *Carbohydr. Res.*, 345(1):168–171, 2010.

[79] M Hunsen, DA Long, CR D'Ardenne, and AL Smith. Mild one-pot preparation of glycosyl bromides. *Carbohydr. Res.*, 340(17):2670–2674, 2005.

[80] SJ Angyal. The composition and conformation of sugars in solution. *Angew. Chem. Int. Ed.*, 8(3):157–166, 1969.

[81] RG Parr and W Yang. *Density-Functional Theory of Atoms and Molecules*. Oxford University Press, New York, US, 1989.

[82] JW Ochterski. *Thermochemistry in Gaussian*. Gaussian Inc. Pittsburgh PA, 2000.

[83] WL DeLano. The PyMOL molecular graphics system, 2002.

[84] AV Marenich, CJ Cramer, and DG Truhlar. Universal solvation model based on solute electron density and on a continuum model of the solvent defined by the bulk dielectric constant and atomic surface tensions. *J. Phys. Chem. B*, 113(18):6378–6396, 2009.

[85] M Michalik, M Hein, and M Frank. NMR spectra of fluorinated carbohydrates. *Carbohydr. Res.*, 327(1):185–218, 2000.

[86] WP Aue, J Karhan, and RR Ernst. Homonuclear broad band decoupling and two-dimensional *J*-resolved NMR spectroscopy. *J. Chem. Phys.*, 64(10):4226–4227, 1976.

[87] TDW Claridge. *High-Resolution NMR Techniques in Organic Chemistry; Tetrahedron Organic Chemistry Series Volume 19*. Elsevier Ltd., Oxford, UK, 1999.

[88] M Findeisen and S Berger. *50 and More Essential NMR Experiments: A Detailed Guide*. Wiley-VCH, Weinheim, Germany, 2014.

[89] H Dohi, R Périon, M Durka, M Bosco, Y Roué, F Moreau, S Grizot, A Ducruix, S Escaich, and SP Vincent. Stereoselective glycal fluorophosphorylation: Synthesis of ADP-2-fluoroheptose, an inhibitor of the LPS biosynthesis. *Chem. Eur. J.*, 14(31):9530–9539, 2008.

[90] EJ Corey and A Venkateswarlu. Protection of hydroxyl groups as *tert*-butyldimethylsilyl derivatives. *J. Am. Chem. Soc.*, 94(17):6190–6191, 1972.

[91] PGM Wuts and TW Greene. *Greene's Protective Groups in Organic Synthesis, Fourth Edition.* John Wiley & Sons, New Jersey, US, 2006.

[92] Clinical and Laboratory Standards Institute. *Methods for Dilution Antimicrobial Susceptibility Tests for Bacteria That Grow Aerobically; Approved Standard - Seventh Edition.* CLSI document M07-A7. CLSI, Wayne, PA, USA, 2005.

[93] Clinical and Laboratory Standards Institute. *Methods for Antimicrobial Dilution and Disk Susceptibility Testing of Infrequently Isolated or Fastidious Bacteria; Approved Guideline.* CLSI document M45. CLSI, Wayne, PA, USA, 2006.

[94] R Miethchen and M Hein. Liquid crystals based on fluorinated carbohydrates. *Carbohydr. Res.*, 327(1):169–183, 2000.

[95] MD Hanwell, DE Curtis, DC Lonie, T Vandermeersch, E Zurek, and GR Hutchison. Avogadro: An advanced semantic chemical editor, visualization, and analysis platform. *J. Cheminf.*, 4:17, 2012.

[96] TA Halgren. MMFF VI. MMFF94s option for energy minimization studies. *J. Comput. Chem.*, 20(7):720–729, 1999.

[97] MJ Frisch, GW Trucks, HB Schlegel, GE Scuseria, MA Robb, JR Cheeseman, G Scalmani, V Barone, B Mennucci, GA Petersson, H Nakatsuji, M Caricato, X Li, HP Hratchian, AF Izmaylov, J Bloino, G Zheng, JL Sonnenberg, M Hada, M Ehara, K Toyota, R Fukuda, J Hasegawa, M Ishida, T Nakajima, Y Honda, O Kitao, H Nakai, T Vreven, JA Montgomery, Jr, JE Peralta, F Ogliaro, M Bearpark, JJ Heyd, E Brothers, KN Kudin, VN Staroverov, R Kobayashi, J Normand, K Raghavachari, A Rendell, JC Burant, SS Iyengar, J Tomasi, M Cossi, N Rega, JM Millam, M Klene, JE Knox, JB Cross, V Bakken, C Adamo, J Jaramillo, R Gomperts, RE Stratmann, O Yazyev, AJ Austin, R Cammi, C Pomelli, JW Ochterski, RL Martin, K Morokuma, VG Zakrzewski, GA Voth, P Salvador, JJ Dannenberg, S Dapprich, AD Daniels, Ö Farkas, JB Foresman, JV Ortiz, J Cioslowski, and DJ Fox. Gaussian 09 Revision D.01. Gaussian Inc. Wallingford CT, 2009.

[98] C Adamo and V Barone. Toward reliable density functional methods without adjustable parameters: The PBE0 model. *J. Chem. Phys.*, 110(13):6158–6170, 1999.

[99] R Krishnan, JS Binkley, R Seeger, and JA Pople. Self-consistent molecular orbital methods. XX. A basis set for correlated wave functions. *J. Chem. Phys.*, 72(1):650–654, 1980.

[100] G Scalmani and MJ Frisch. Continuous surface charge polarizable continuum models of solvation. I. General formalism. *J. Chem. Phys.*, 132(11):114110, 2010.

[101] GA Zhurko and DA Zhurko. Chemcraft: Graphical program for working with quantum chemistry results, version 1.6, 2009.

[102] AR Leach. *Molecular modelling: Principles and applications, 2nd Ed.* Pearson Education Ltd, Edinburgh, UK, 2001.

[103] MP Allen and DJ Tildesley. *Computer simulation of liquids.* Oxford University Press, New York, USA, 1987.

[104] WF van Gunsteren and HJC Berendsen. Computer simulation of molecular dynamics: Methodology, applications, and perspectives in chemistry. *Angew. Chem. Int. Ed. Eng.*, 29(9):992–1023, 1990.

[105] HJC Berendsen, JPM Postma, WF van Gunsteren, A DiNola, and JR Haak. Molecular dynamics with coupling to an external bath. *J. Chem. Phys.*, 81(8):3684–3690, 1984.

[106] J-P Ryckaert, G Ciccotti, and HJC Berendsen. Numerical integration of the cartesian equations of motion of a system with constraints: Molecular dynamics of *n*-alkanes. *J. Comput. Phys.*, 23(3):327–341, 1977.

[107] B Hess, H Bekker, HJC Berendsen, and JGEM Fraaije. LINCS: A linear constraint solver for molecular simulations. *J. Comput. Chem.*, 18(12):1463–1472, 1997.

[108] S Miyamoto and PA Kollman. Settle: An analytical version of the SHAKE and RATTLE algorithm for rigid water models. *J. Comput. Chem.*, 13(8):952–962, 1992.

[109] P Balgavỳ, M Dubničková, N Kučerka, MA Kiselev, SP Yaradaikin, and D Uhríková. Bilayer thickness and lipid interface area in unilamellar extruded 1,2-diacylphosphatidylcholine liposomes: A small-angle neutron scattering study. *Biochem. Biophys. Acta Biomembranes*, 1512(1):40–52, 2001.

[110] SC Costigan, PJ Booth, and RH Templer. Estimations of lipid bilayer geometry in fluid lamellar phases. *Biochem. Biophys. Acta Biomembranes*, 1468(1):41–54, 2000.

[111] MJ Janiak, DM Small, and GG Shipley. Temperature and compositional dependence of the structure of hydrated dimyristoyl lecithin. *J. Biol. Chem.*, 254(13):6068–6078, 1979.

[112] BW Koenig, HH Strey, and K Gawrisch. Membrane lateral compressibility determined by NMR and X-ray diffraction: Effect of acyl chain polyunsaturation. *Biophys. J.*, 73(4):1954–1966, 1997.

[113] N Kučerka, MA Kiselev, and P Balgavỳ. Determination of bilayer thickness and lipid surface area in unilamellar dimyristoylphosphatidylcholine vesicles from small-angle neutron scattering curves: A comparison of evaluation methods. *Eur. Biophys. J.*, 33(4):328–334, 2004.

[114] N Kučerka, Y Liu, N Chu, HI Petrache, S Tristram-Nagle, and JF Nagle. Structure of fully hydrated fluid phase DMPC and DLPC lipid bilayers using X-ray scattering from oriented multilamellar arrays and from unilamellar vesicles. *Biophys. J.*, 88(4):2626–2637, 2005.

[115] N Kučerka, M-P Nieh, and J Katsaras. Fluid phase lipid areas and bilayer thicknesses of commonly used phosphatidylcholines as a function of temperature. *Biochem. Biophys. Acta Biomembranes*, 1808(11):2761–2771, 2011.

[116] BA Lewis and DM Engelman. Lipid bilayer thickness varies linearly with acyl chain length in fluid phosphatidylcholine vesicles. *J. Mol. Biol.*, 166(2):211–217, 1983.

[117] LJ Lis, M McAlister, N Fuller, RP Rand, and VA Parsegian. Interactions between neutral phospholipid bilayer membranes. *Biophys. J.*, 37(3):657, 1982.

[118] JF Nagle and S Tristram-Nagle. Structure of lipid bilayers. *Biochem. Biophys. Acta Rev. Biomembranes*, 1469(3):159–195, 2000.

[119] HI Petrache, S Tristram-Nagle, and JF Nagle. Fluid phase structure of EPC and DMPC bilayers. *Chem. Phys. Lipids*, 95(1):83–94, 1998.

[120] HI Petrache, SW Dodd, and MF Brown. Area per lipid and acyl length distributions in fluid phosphatidylcholines determined by ^{2}H NMR spectroscopy. 79(6):3172, 2000.

[121] RP Rand and VA Parsegian. Hydration forces between phospholipid bilayers. *Biochem. Biophys. Acta Biomembranes*, 988(3):351–376, 1989.

[122] JM Smaby, MM Momsen, HL Brockman, and RE Brown. Phosphatidylcholine acyl unsaturation modulates the decrease in interfacial elasticity induced by cholesterol. *Biophys. J.*, 73(3):1492–1505, 1997.

[123] LR De Young and KA Dill. Solute partitioning into lipid bilayer membranes. *Biochemistry-US*, 27(14):5281–5289, 1988.

[124] D Poger, WF van Gunsteren, and AE Mark. A new force field for simulating phosphatidylcholine bilayers. *J. Comput. Chem.*, 31(6):1117–1125, 2010.

[125] HJC Berendsen, D van der Spoel, and R van Drunen. GROMACS: A message-passing parallel molecular dynamics implementation. *Comput. Phys. Commun.*, 91(1):43–56, 1995.

[126] D van der Spoel, E Lindahl, B Hess, G Groenhof, AE Mark, and HJC Berendsen. GROMACS: fast, flexible, and free. *J. Comput. Chem.*, 26(16):1701–1718, 2005.

[127] B Hess, C Kutzner, D van der Spoel, and E Lindahl. GROMACS 4: algorithms for highly efficient, load-balanced, and scalable molecular simulation. *J. Chem. Theory Comput.*, 4(3):435–447, 2008.

[128] WF van Gunsteren, X Daura, and AE Mark. GROMOS force field. *Encyclopedia of Computational Chemistry*, 1998.

[129] WRP Scott, PH Hünenberger, IG Tironi, AE Mark, SR Billeter, J Fennen, AE Torda, T Huber, P Krüger, and WF van Gunsteren. The GROMOS biomolecular simulation program package. *J. Phys. Chem. A*, 103(19):3596–3607, 1999.

[130] N Schmid, AP Eichenberger, A Choutko, S Riniker, M Winger, AE Mark, and WF van Gunsteren. Definition and testing of the GROMOS force-field versions 54A7 and 54B7. *Eur. Biophys. J.*, 40(7):843–856, 2011.

[131] HS Hansen and PH Hünenberger. A reoptimized GROMOS force field for hexopyranose-based carbohydrates accounting for the relative free energies of ring conformers, anomers, epimers, hydroxymethyl rotamers, and glycosidic linkage conformers. *J. Comput. Chem.*, 32(6):998–1032, 2011.

[132] J Hermans, HJC Berendsen, WF van Gunsteren, and JPM Postma. A consistent empirical potential for water–protein interactions. *Biopolymers*, 23(8):1513–1518, 1984.

[133] L Onsager. Electric moments of molecules in liquids. *J. Am. Chem. Soc.*, 58(8):1486–1493, 1936.

[134] JA Barker and RO Watts. Monte Carlo studies of the dielectric properties of water-like models. *Mol. Phys.*, 26(3):789–792, 1973.

[135] M Neumann. Dipole moment fluctuation formulas in computer simulations of polar systems. *Mol. Phys.*, 50(4):841–858, 1983.

[136] PE Smith and WF van Gunsteren. Consistent dielectric properties of the simple point charge and extended simple point charge water models at 277 and 300 K. *J. Chem. Phys.*, 100(4):3169–3174, 1994.

[137] B Hess. P-LINCS: A parallel linear constraint solver for molecular simulation. *J. Chem. Theory Comput.*, 4(1):116–122, 2008.

[138] M Meier and J Seelig. Lipid and peptide dynamics in membranes upon insertion of *n*-alkyl-β-D-glucopyranosides. *Biophys. J.*, 98(8):1529–1538, 2010.

[139] MR Wenk, T Alt, A Seelig, and J Seelig. Octyl-β-D-glucopyranoside partitioning into lipid bilayers: Thermodynamics of binding and structural changes of the bilayer. *Biophys. J.*, 72(4):1719, 1997.

[140] RH Byrd, P Lu, J Nocedal, and C Zhu. A limited memory algorithm for bound constrained optimization. *SIAM J. Sci. Comput.*, 16(5):1190–1208, 1995.

[141] D van der Spoel, E Lindahl, B Hess, AR van Buuren, E Apol, PJ Meulenhoff, DP Tieleman, ALTM Sijbers, KA Feenstra, R van Drunen, and HJC Berendsen. *Gromacs user manual version 4.0*. www.gromacs.org, 2005.

[142] T Williams and C Kelley. *Gnuplot 4.4: An interactive plotting program*. www.gnuplot.info, 2011.

[143] B Lee and FM Richards. The interpretation of protein structures: Estimation of static accessibility. *J. Mol. Biol.*, 55(3):379–IN4, 1971.

[144] S Bogusz, RM Venable, and RW Pastor. Molecular dynamics simulations of octyl glucoside micelles: Structural properties. *J. Phys. Chem. B*, 104(23):5462–5470, 2000.

[145] S Bogusz, RM Venable, and RW Pastor. Molecular dynamics simulations of octyl glucoside micelles: Dynamic properties. *J. Phys. Chem. B*, 105(35):8312–8321, 2001.

[146] P Konidala, L He, and B Niemeyer. Molecular dynamics characterization of *n*-octyl-β-D-glucopyranoside micelle structure in aqueous solution. *J. Mol. Graph. Model.*, 25(1):77–86, 2006.

[147] TT Chong, R Hashim, and RA Bryce. Molecular dynamics simulation of monoalkyl glycoside micelles in aqueous solution: Influence of carbohydrate headgroup stereochemistry. *J. Phys. Chem. B*, 110(10):4978–4984, 2006.

[148] S Abel, F-Y Dupradeau, EP Raman, AD MacKerell Jr, and M Marchi. Molecular simulations of dodecyl-β-maltoside micelles in water: Influence of the headgroup conformation and force field parameters. *J. Phys. Chem. B*, 115(3):487–499, 2011.

[149] DP Tieleman, D van der Spoel, and HJC Berendsen. Molecular dynamics simulations of dodecylphosphocholine micelles at three different aggregate sizes: Micellar structure and chain relaxation. *J. Phys. Chem. B*, 104(27):6380–6388, 2000.

[150] S Abel, F-Y Dupradeau, and M Marchi. Molecular dynamics simulations of a characteristic DPC micelle in water. *J. Chem. Theory Comput.*, 8(11):4610–4623, 2012.

[151] S Lee, A Tran, M Allsopp, JB Lim, J Hénin, and JB Klauda. CHARMM36 united atom chain model for lipids and surfactants. *J. Phys. Chem. B*, 118(2):547–556, 2014.

[152] X Gao and TC Wong. Molecular dynamics simulation of adrenocorticotropin (1–10) peptide in a solvated dodecylphosphocholine micelle. *Biopolymers*, 58(7):643–659, 2001.

[153] S Garde, L Yang, JS Dordick, and ME Paulaitis. Molecular dynamics simulation of C_8E_5 micelle in explicit water: Structure and hydrophobic solvation thermodynamics. *Mol. Phys.*, 100(14):2299–2306, 2002.

[154] H Kuhn, B Breitzke, and H Rehage. A molecular modeling study of pentanol solubilized in a sodium octanoate micelle. *J. Colloid Interf. Sci.*, 249(1):152–161, 2002.

[155] ST Thornton and JB Marion. *Classical Dynamics of Particles and Systems, 5^{th} Ed.* Thomson-Brooks/Cole, Belmont, USA, 2004.

[156] C Tanford. Micelle shape and size. *J. Phys. Chem.*, 76(21):3020–3024, 1972.

[157] JN Israelachvili, DJ Mitchell, and BW Ninham. Theory of self-assembly of hydrocarbon amphiphiles into micelles and bilayers. *J. Chem. Soc. Farad. T. 2*, 72:1525–1568, 1976.

[158] J Iyer and D Blankschtein. Are ellipsoids feasible micelle shapes? An answer based on a molecular-thermodynamic model of nonionic surfactant micelles. *J. Phys. Chem. B*, 116(22):6443–6454, 2012.

[159] RC Oliver, J Lipfert, DA Fox, RH Lo, S Doniach, and L Columbus. Dependence of micelle size and shape on detergent alkyl chain length and head group. *PLoS ONE*, 8(5), 2013.

[160] JA Long, BM Rankin, and D Ben-Amotz. Micelle structure and hydrophobic hydration. *J. Am. Chem. Soc.*, 137(33):10809–10815, 2015.

[161] Quadric — Wikipedia, The Free Encyclopedia, 2015. (https://en.wikipedia.org/wiki/Quadric; accessed 22 September 2015).

[162] AP Lyubartsev and AL Rabinovich. Recent development in computer simulations of lipid bilayers. *Soft Matter*, 7(1):25–39, 2011.

[163] D Poger and AE Mark. On the validation of molecular dynamics simulations of saturated and *cis*-monounsaturated phosphatidylcholine lipid bilayers: A comparison with experiment. *J. Chem. Theory Comput.*, 6(1):325–336, 2009.

[164] O Edholm and JF Nagle. Areas of molecules in membranes consisting of mixtures. *Biophys. J.*, 89(3):1827–1832, 2005.

[165] LS Vermeer, BL de Groot, V Réat, A Milon, and J Czaplicki. Acyl chain order parameter profiles in phospholipid bilayers: Computation from molecular dynamics simulations and comparison with ^{2}H NMR experiments. *Eur. Biophys. J.*, 36(8):919–931, 2007.

[166] P van der Ploeg and HJC Berendsen. Molecular dynamics simulation of a bilayer membrane. *J. Chem. Phys.*, 76(6):3271–3276, 1982.

[167] M Patra, M Karttunen, MT Hyvönen, E Falck, P Lindqvist, and I Vattulainen. Molecular dynamics simulations of lipid bilayers: Major artifacts due to truncating electrostatic interactions. *Biophys. J.*, 84(6):3636–3645, 2003.

[168] AG Lee. How lipids affect the activities of integral membrane proteins. *Biochem. Biophys. Acta Rev. Biomembranes*, 1666(1):62–87, 2004.

[169] N Kucerka, M-P Nieh, J Pencer, JN Sachs, and J Katsaras. What determines the thickness of a biological membrane. *Gen. Physiol. Biophys.*, 28:117–125, 2009.

[170] U Essmann and ML Berkowitz. Dynamical properties of phospholipid bilayers from computer simulation. *Biophys. J.*, 76(4):2081–2089, 1999.

[171] J Wohlert and O Edholm. Dynamics in atomistic simulations of phospholipid membranes: Nuclear magnetic resonance relaxation rates and lateral diffusion. *J. Chem. Phys.*, 125(20):204703, 2006.

[172] PFF Almeida and WLC Vaz. *Handbook of Biological Physics*, volume 1, chapter 6, pages 305–357. Elsevier, Amsterdam, Netherlands, 1995.

[173] J Tabony and B Perly. Quasielastic neutron scattering measurements of fast local translational diffusion of lipid molecules in phospholipid bilayers. *Biochem. Biophys. Acta Rev. Biomembranes*, 1063(1):67–72, 1991.

[174] WL Vaz and PF Almeida. Microscopic versus macroscopic diffusion in one-component fluid phase lipid bilayer membranes. *Biophys. J.*, 60(6):1553, 1991.

[175] GB Goh, DM Eike, BP Murch, and CL Brooks. Accurate modeling of ionic surfactants at high concentration. *J. Phys. Chem. B*, 2015.

[176] SJ Marrink, DP Tieleman, and AE Mark. Molecular dynamics simulation of the kinetics of spontaneous micelle formation. *J. Phys. Chem. B*, 104(51):12165–12173, 2000.

[177] M Sammalkorpi, S Sanders, AZ Panagiotopoulos, M Karttunen, and M Haataja. Simulations of micellization of sodium hexyl sulfate. *J. Phys. Chem. B*, 115(6):1403–1410, 2011.

[178] SA Sanders, M Sammalkorpi, and AZ Panagiotopoulos. Atomistic simulations of micellization of sodium hexyl, heptyl, octyl, and nonyl sulfates. *J. Phys. Chem. B*, 116(8):2430–2437, 2012.

[179] C Tanford. The hydrophobic effect and the organization of living matter. *Science*, 200(4345):1012–1018, 1978.

[180] L Maibaum, AR Dinner, and D Chandler. Micelle formation and the hydrophobic effect. *J. Phys. Chem. B*, 108(21):6778–6781, 2004.

[181] B Smit, PAJ Hilbers, K Esselink, LAM Rupert, NM van Os, and AG Schlijper. Computer simulations of a water/oil interface in the presence of micelles. *Nature*, 348(6302):624–625, 1990.

[182] JC Shelley and MY Shelley. Computer simulation of surfactant solutions. *Curr. Opin. Colloid In.*, 5(1):101–110, 2000.

[183] YM Li, GY Xu, YJ Chen, YX Luan, and SL Yuan. Computer simulations of surfactants and surfactant/polymer assemblies. *Comp. Mat. Sci.*, 36(4):386–396, 2006.

[184] ML Klein and W Shinoda. Large-scale molecular dynamics simulations of self-assembling systems. *Science*, 321(5890):798–800, 2008.

[185] H Lee and RG Larson. Molecular dynamics simulations of PAMAM dendrimer-induced pore formation in DPPC bilayers with a coarse-grained model. *J. Phys. Chem. B*, 110(37):18204–18211, 2006.

[186] L Chen, X Li, L Gao, and W Fang. Theoretical insight into the relationship between the structures of antimicrobial peptides and their actions on bacterial membranes. *J. Phys. Chem. B*, 119(3):850–860, 2014.

[187] A De Nicola, S Hezaveh, Y Zhao, T Kawakatsu, D Roccatano, and G Milano. Micellar drug nanocarriers and biomembranes: How do they interact? *Phys. Chem. Chem. Phys.*, 16(11):5093–5105, 2014.

[188] A Capalbi, G Gente, and C La Mesa. Solution properties of alkyl glucosides, alkyl thioglucosides and alkyl maltosides. *Colloid. Surface. A*, 246(1):99–108, 2004.

[189] PH Thiesen, H Rosenfeld, P Konidala, VM Garamus, L He, A Prange, and B Niemeyer. Glycolipids from a colloid chemical point of view. *J. Biotechnol.*, 124(1):284–301, 2006.

[190] MN Jones. Surfactant interactions with biomembranes and proteins. *Chem. Soc. Rev.*, 21(2):127–136, 1992.

[191] Z Wasylewski and A Kozik. Protein—non-ionic detergent interaction. *Eur. J. Biochem.*, 95(1):121–126, 1979.

[192] GW Stubbs, HG Smith, and BJ Litman. Alkyl glucosides as effective solubilizing agents for bovine rhodopsin. A comparison with several commonly used detergents. *Biochem. Biophys. Acta Biomembranes*, 426(1):46–56, 1976.

[193] M Almgren. Mixed micelles and other structures in the solubilization of bilayer lipid membranes by surfactants. *Biochem. Biophys. Acta Biomembranes*, 1508(1):146–163, 2000.

[194] M le Maire, P Champeil, and JV Møller. Interaction of membrane proteins and lipids with solubilizing detergents. *Biochem. Biophys. Acta Biomembranes*, 1508(1):86–111, 2000.

[195] VH Teixeira, D Vila-Viçosa, AM Baptista, and M Machuqueiro. Protonation of DMPC in a bilayer environment using a linear response approximation. *J. Chem. Theory Comput.*, 10(5):2176–2184, 2014.

[196] M Sega, R Vallauri, P Brocca, and S Melchionna. Molecular dynamics simulation of a GM3 ganglioside bilayer. *J. Phys. Chem. B*, 108(52):20322–20330, 2004.

[197] S Bandyopadhyay, JC Shelley, and ML Klein. Molecular dynamics study of the effect of surfactant on a biomembrane. *J. Phys. Chem. B*, 105(25):5979–5986, 2001.

[198] Y Andoh, S Muraoka, and S Okazaki. Molecular dynamics study of changes in physico-chemical properties of DMPC lipid bilayers by addition of nonionic surfactant $C_{12}E_{10}$. *Mol. Simulat.*, 41(10–12):955–960, 2014.

[199] M Machuqueiro, SRR Campos, CM Soares, and AM Baptista. Membrane-induced conformational changes of kyotorphin revealed by molecular dynamics simulations. *J. Phys. Chem. B*, 114(35):11659–11667, 2010.

[200] OG Mouritsen and MJ Zuckermann. What's so special about cholesterol? *Lipids*, 39(11):1101–1113, 2004.

[201] H Ohvo-Rekilä, B Ramstedt, P Leppimäki, and JP Slotte. Cholesterol interactions with phospholipids in membranes. *Prog. Lipid Res.*, 41(1):66–97, 2002.

[202] M Bonn, S Roke, O Berg, LBF Juurlink, A Stamouli, and M Müller. A molecular view of cholesterol-induced condensation in a lipid monolayer. *J. Phys. Chem. B*, 108(50):19083–19085, 2004.

[203] SW Chiu, E Jakobsson, and HL Scott. Combined monte carlo and molecular dynamics simulation of hydrated lipid-cholesterol lipid bilayers at low cholesterol concentration. *Biophys. J.*, 80(3):1104–1114, 2001.

[204] T Róg and M Pasenkiewicz-Gierula. Cholesterol effects on a mixed-chain phosphatidylcholine bilayer: A molecular dynamics simulation study. *Biochimie*, 88(5):449–460, 2006.

[205] G Pranami and MH Lamm. Estimating error in diffusion coefficients derived from molecular dynamics simulations. *J. Chem. Theory Comput.*, 2015. ASAP, DOI:10.1021/acs.jctc.5b00574.

[206] Kim A Brogden. Antimicrobial peptides: Pore formers or metabolic inhibitors in bacteria? *Nat. Rev. Microbiol.*, 3(3):238–250, 2005.

[207] C-C Lee, Y Sun, S Qian, and HW Huang. Transmembrane pores formed by human antimicrobial peptide LL-37. *Biophys. J.*, 100(7):1688–1696, 2011.

[208] CJ Arnusch, RJ Pieters, and E Breukink. Enhanced membrane pore formation through high-affinity targeted antimicrobial peptides. *PLoS ONE*, 7(6):e39768–e39768, 2012.

[209] I Gozen and P Dommersnes. Pore dynamics in lipid membranes. *Eur. Phys. J.-Spec. Top.*, 223(9):1813–1829, 2014.

[210] PL McNeil and RA Steinhardt. Loss, restoration, and maintenance of plasma membrane integrity. *J. Cell Biol.*, 137(1):1–4, 1997.

[211] PL McNeil and T Kirchhausen. An emergency response team for membrane repair. *Nat. Rev. Mol. Cell Biol.*, 6(6):499–505, 2005.

[212] DP Tieleman, H Leontiadou, AE Mark, and S-J Marrink. Simulation of pore formation in lipid bilayers by mechanical stress and electric fields. *J. Am. Chem. Soc.*, 125(21):6382–6383, 2003.

[213] H Leontiadou, AE Mark, and SJ Marrink. Antimicrobial peptides in action. *J. Am. Chem. Soc.*, 128(37):12156–12161, 2006.

[214] WFD Bennett, N Sapay, and DP Tieleman. Atomistic simulations of pore formation and closure in lipid bilayers. *Biophys. J.*, 106(1):210–219, 2014.

[215] WFD Bennett and DP Tieleman. The importance of membrane defects - Lessons from simulations. *Accounts Chem. Res.*, 47(8):2244–2251, 2014.

[216] V Mirjalili and M Feig. Density-biased sampling: A robust computational method for studying pore formation in membranes. *J. Chem. Theory Comput.*, 11(1):343–350, 2014.

[217] M Fuhrmans, G Marelli, YG Smirnova, and M Müller. Mechanics of membrane fusion/pore formation. *Chem. Phys. Lipids*, 185:109–128, 2015.